

Issue 10
December 2015

DOI : 10.12762/2015.AL10

Publisher
Stéphane Andrieux

Editor in Chief
Alain Appriou

Editorial Board
Stéphane Andrieux
Alain Appriou
Philippe Bidaud
Esteban Busso
Laurent Jacquin
Pierre Touboul

Production
ONERA Scientific
Information Department

On line
www.aerospacelab-journal.com
Webmaster ONERA

Contact
E-mail: aerospacelab@onera.fr

Produced by
ONERA - BP 80100
Chemin de la Hunière
et des Joncherettes
91123 PALAISEAU CEDEX
France
www.onera.fr

ISSN: 2107-6596

P l a s m a s f o r A e r o n a u t i c s

AL10-00 - Plasmas for Aeronautics
D. Packan

AL10-01 - Plasma Aerodynamics: Current Status and Future Direction
J. Poggie, T. Mc Laughlin, S. Leonov

AL10-02 - A Short Review of Microwave and Laser Discharges for Supersonic Flow Control
D. Knight

AL10-03 - Numerical Simulations on the Effect and Efficiency of Long Linear Energy Deposition Ahead of a Supersonic Blunt Body: Toward a Laser Spike
P.Q. Elias

AL10-04 - Plasmas for High Speed Flow Control
R. Jousset, S. Coumar, V. Lago

AL10-05 - Numerical Modeling of Dielectric Barrier Discharge based Plasma Actuators for Flow Control: the COPAIER/CEDRE Example
G. Dufour, F. Rogier

AL10-06 - Applications of Dielectric Barrier Discharges and Plasma Synthetic Jet Actuators at ONERA
F. Chedeveigne, G. Casalis, O. Léon, M. Forte, F. Laurendeau, N. Szulga, O. Vermeersch, E. Piot

AL10-07 - Mechanisms of Ethylene Flame Propagation Enhancement by $O_2(a^1\Delta_g)$
T. Ombrello, N. Popov

AL10-08 - Experiments on Plasma-Assisted Combustion in a Supersonic Flow: Optimization of Plasma Position in Relation to the Fuel Injector
K.V. Savelkin, D.A. Yarantsev, S.B. Leonov

AL10-09 - Ignition of Lean Air / Hydrocarbon Mixtures at Low Temperature by a Single Corona Discharge Nanosecond Pulse
S. Bentaleb, N. Blin-Simiand, P. Jeanney, L. Magne, N. Moreau, S. Pasquiers, P. Tardiveau



Denis Packan
(ONERA)

Research Scientist, Plasmas Applications
and Electric Propulsion, Physics
and Instrumentation Department

DOI : 10.12762/2015.AL10-00

Plasmas for Aeronautics

The potential of plasmas for aerodynamics and combustion has been known for many years, but a dedicated research domain has only started to significantly develop over the past 20 years (Ref. [1]). Based either on new technological advances, on enhanced numerical capabilities, or on new needs created by the aeronautical industry's quest for higher performance, the development of plasma actuators has now reached a point where an industrial application is within grasp. This tenth issue of the Aerospace Lab journal will present an overview of the research in this field. Due to the great diversity of the plasmas and of the applications studied in laboratories around the world, this overview is necessarily limited in its scope, but the main research areas will nevertheless be illustrated.

Plasmas are generally created by causing an electrical current to flow through a gas. The energy deposited results in effects such as chemical reactions, radiation, forces or heating in the gas, which can combine in different ways depending on the physical conditions and on the electrical discharge parameters. Numerical simulations are still challenging nowadays, because of the non-equilibrium nature of the physics involved. Indeed, the electrons are the main vector for the interaction with the gas (they excite, dissociate, heat-up, etc.), yet they are very complex to model: they generally are much hotter than the heavy species and their temperature is sometimes even not defined when they do not follow a Boltzmann distribution. This complexity also renders experiments difficult to interpret. However, distinct advantages of plasmas for aerodynamics and combustion have long been observed and are being studied.

For aerodynamics, plasma actuators have the unique capability of injecting momentum into an air flow without any mechanical movement. Beyond the cost / reliability advantage, this enables the use of high pulsed repetition rates, which can be tuned to a physical frequency of the flow, in order to achieve a resonant enhancement. Both supersonic (Ref. [2], [3], [4]) and subsonic flows (Ref. [5], [6]) are targeted, with plasmas that can vary widely in nature, from cold plasma such as coronas and Dielectric Barrier Discharges or DBDs, which act as "momentum injectors" mostly in subsonic flows (Ref. [5], [6]), to thermal plasmas used as "energy injectors" (Ref. [2], [3], [4], [6]). Plasma actuators are being developed to tackle important issues, such as aerodynamic instabilities, drag reduction (and hence fuel efficiency), or sonic bang attenuation, and the variety and complexity of the physics and of the experiments is a challenge that will be illustrated in all of the contributions to this issue.

Combustion is also a crucial issue in aeronautics, as jet engines seek ever higher combustion stability, fuel efficiency or startup flexibility, and plasmas have specific properties that make them well suited to address these issues. Whether plasmas are used for ignition or flame stabilization, several phenomena are at play. Combustion processes can be affected in particular by chemical kinetics enhancement, due to the creation of reactive species (Ref. [7], [9]) or by heating of the gas (Ref. [8]). In parallel, the actuations on the flow can improve fuel mixing or create stabilizing recirculation zones. These effects are often difficult to distinguish experimentally and even more difficult to model, which explains why maturity has not arrived yet. However, mastering all of them with plasma actuators could potentially lead to a breakthrough in such hot topics of jet engine combustion as lean combustion stabilization (for pollution reduction), supersonic combustion (for high speed transportation), low temperature ignition (for reliable in-flight restart) or even pulsed detonation engines (new technologies) ■

References

- [1] J. POGGIE, T. MC LAUGHLIN, S. LEONOV - *Plasma Aerodynamics : Current Status and Future Direction*. Aerospace Lab Journal Issue 10, January 2016
- [2] D. KNIGHT - *A Short Review of Microwave and Laser Discharges for Supersonic Flow Control*. Aerospace Lab Journal Issue 10, December 2015
- [3] P.Q. ELIAS - *Numerical Simulations on the Effect and Efficiency of Long Linear Energy Deposition Ahead of a Supersonic Blunt Body: Toward a Laser Spike*. Aerospace Lab Journal Issue 10, December 2015
- [4] R. JOUSSOT, S. COUMAR, V. LAGO - *Plasmas for High Speed Flow Control*. Aerospace Lab Journal Issue 10, December 2015
- [5] G. DUFOUR, F. ROGIER - *Numerical Modeling of Dielectric Barrier Discharge Based Plasma Actuators for Flow Control : the COPAIER/CEDRE Example*. Aerospace Lab Journal Issue 10, December 2015
- [6] F. CHEDEVERGNE, G. CASALIS, O.LÉON, M. FORTE, F. LAURENDEAU, N. SZULGA, O.VERMEERSCH, E. PIOT - *Applications of Dielectric Barrier Discharges and Plasma Synthetic Jet Actuators at ONERA*. Aerospace Lab Journal Issue 10, December 2015
- [7] T. OMBRELLO, N. POPOV - *Mechanisms of Ethylene Flame Propagation Enhancement by $O_2(a^1\Delta_g)$* . Aerospace Lab Journal Issue 10, December 2015
- [8] K.V. SAVELKIN, D. A. YARANTSEV, S. B. LEONOV - *Experiments on Plasma-Assisted Combustion in a Supersonic Flow: Optimization of Plasma Position in Relation to Fuel Injector*. Aerospace Lab Journal Issue 10, December 2015
- [9] S. BENTALEB, N. BLIN-SIMIAND, P. JEANNEY, L. MAGNE, N. MOREAU, S. PASQUIERS, P. TARDIVEAU - *Ignition of Lean Air / Hydrocarbon Mixtures at Low Temperature by a Single Corona Discharge Nanosecond Pulse*. Aerospace Lab Journal Issue 10, December 2015

J. Poggie

(US Air Force Research Laboratory)

T. McLaughlin

(US Air Force Academy)

S. Leonov

(The Ohio State University)

E-mail: jonathan.poggie@wpafb.af.mil

DOI: 10.12762/2015.AL10-01

Plasma Aerodynamics: Current Status and Future Directions

Plasma aerodynamics can trace its origin to the beginning of the space age, and in particular to a time when designers realized that plasmas could have a significant influence on reentry flows. From the 1950s to the 1970s, there was considerable work on magnetohydrodynamic reentry systems and related technology. The recent resurgence in the field was stimulated by the disclosure of the Soviet AJAX vehicle concept in the mid-1990s. This led to an extraordinary international collaboration that has now lasted almost twenty years. Plasma-based flow control seems quite feasible, particularly for local flow control applications where power consumption is low. Plasma-based devices have a low profile, and can provide actuation over short time scales. Plasma-enhanced combustion is a very promising area for both low- and high-speed regimes. Discharges are already being used to break down fuels, enhance ignition, provide flameholding, and promote combustion efficiency. There are a number of potential breakthrough areas in the field that could have strong technological impact on the aerospace industry. Industry seems to be receptive to the adoption of plasma-based technology, but has reservations about technical risk, performance, reliability, and integration. There is a need to identify applications where plasma devices are significantly better than competing technologies, and to demonstrate prototypes in an operational environment. With a century of atmospheric flight and half a century of spaceflight behind us, the aerospace sciences remain a vigorous and exciting field. The new field of plasma aerodynamics contributes to this excitement, and supports diverse aerospace technology needs, from energy efficiency to space access.

Introduction

Although plasma aerodynamics has a history that dates to the beginning of the space age, a surge of activity has occurred in the field since the mid-1990s. There has been strong research interest in plasma-based flow and flight control, plasma-assisted combustion, on-board electrical power generation, and magnetohydrodynamic heat shields. As the field has matured, some of the older concepts are receiving less attention, and emphasis is being placed on different areas like small-scale plasma actuators. The present white paper summarizes the current status of the field, and identifies promising directions for scientific research and technology development.

In 1994, Russian scientists introduced a novel hypersonic flight vehicle concept, AJAX or AYAKS, into the open literature. AJAX was a scramjet-powered vehicle, which incorporated plasma-based technology to enhance combustion and aerodynamic performance. Work had begun on AJAX and its predecessor concept vehicles in the former Soviet Union before 1985, but this work was not made public at

the time. In response to AJAX, the US Air Force, through the Air Force Research Laboratory (AFRL) and the European Office of Aerospace Research and Development (EOARD) established the Weakly Ionized Gases (WIG) Program in the former Soviet Republics. The WIG program was created to foster US – Eastern Bloc cooperative research exchange, and has been a strong influence on the recent resurgence of interest in plasma aerodynamics.

Initial research in the United States was directed at understanding the role of plasmas in the performance of the AJAX vehicle. Arguably the most captivating aspect of the plasma effects was the so-called “plasma magic,” the weakening of hypersonic shock waves by plasmas. The Air Force Arnold Engineering and Development Center (AEDC) performed ballistic projectile experiments to attempt to reproduce early (ca. 1978) Russian experiments. Their results generally confirmed the Russian observations. Subsequently, the Air Force Office of Scientific Research (AFOSR) assembled a team to

conduct modeling and experiments. Plasma magic was eventually explained as a plasma-based heating effect, albeit a result of complex and subtle physics. Research on aerospace plasma technology has now expanded far beyond these initial efforts, and includes a broad international collaboration.

Weakly ionized plasmas offer significant potential benefits for flight vehicles. The plasma technologies of interest fall into two main categories: plasma actuators for aerodynamic control, and plasma assisted combustion for propulsion.

As flush-mounted electronic devices with no moving parts, plasma actuators offer the possibility of very fast response times and low profile. Use of these actuators has been explored for re-attachment of separated flow, supersonic and transonic shock mitigation, control of shock-shock and shock-boundary layer interactions, delay of laminar-to-turbulent transition, and other effects that reduce drag, enhance lift, and eliminate undesirable transient phenomena in off-design conditions. In reentry flight, where plasma is generated through aerodynamic heating, the plasma layer can be manipulated with on-board magnets for electrical power generation, flight control, and heat transfer mitigation.

Plasma-assisted combustion technologies can shorten ignition time, enhance fuel-air mixing, increase flame speed, provide stable flame-holding, and enable reliable operation with lean mixtures. The application of plasma torches to scramjets allows the possibility of ignition over a wide range of conditions. Near-term applications will lie with localized discharges, because of low energy requirements and ease of integration within a harsh environment. Short-pulse discharges (nanosecond and below) are well suited to high-speed environments because they have the ability to couple energy into the flow on short time scales. Laser ignition, in which a tightly-focused beam generates localized plasma, is a promising alternative approach.

Research in academia, industry, and government has produced interesting and promising results. The mechanisms of plasma effects on aerodynamics and propulsion are now fairly well understood, but the Technology Readiness Level (TRL) is still relatively low. For the most mature technologies, component or prototype validation has been carried out in a relevant environment (TRL 5-6), but many concepts have not yet been brought to that stage maturity. For plasma technology transition to application on flight vehicles, a number of additional issues have to be addressed. The critical issues include relative control authority of plasma devices, electrical power requirements, overall weight of the plasma systems, technology integration issues, and environmental factors. Near-term application of plasma technology will come in the form of modifications to improve the performance of existing platforms. Nonetheless, the greatest benefits of plasma technology will come when it is incorporated at the conceptual design stage, with the design paradigm focused on this new approach.

Plasma-Based Flow Control

Over the past several decades, a number of control techniques have been developed to create or maintain a desired flow pattern. Flow control techniques are chosen based on several factors, including the flow configuration, Mach number, and Reynolds number. Successful endeavors always require an understanding of both the flow physics and the actuation technique.

A flow control device may be passive or active. Passive control almost always involves geometrical modifications, such as vortex generators on a wing or chevrons on an exhaust nozzle. Passive control devices are always in operation, regardless of need or performance penalty. Active flow control, on the other hand, involves the regulated addition of energy or momentum to the flow. Active control can be turned on or off as needed, but it involves significant effort and cost.

Actuators are at the heart of active flow control implementation, and have been the weakest link in the development of flow control technology. Plasma actuators are able to address some of this deficiency; they offer the possibility of low weight, low profile, no moving parts, energy efficiency, durability, ease of use, scalability, high amplitude, wide bandwidth, and rapid response.

Research and development on plasma actuators has included direct current, alternating current, radio frequency, microwave, arc, corona, and spark discharge actuators. The two primary mechanisms of plasma-based flow control include generation of a body force (electrohydrodynamic and magnetohydrodynamic interactions) and thermal effects (Joule heating and relaxation of internal energy states). The field is still evolving, and a variety of actuator concepts are currently being explored. Flow control using four of the more-studied actuators will be briefly discussed here.

Alternating current, dielectric barrier discharge (AC-DBD) plasma actuators impose a force on the flow through electrohydrodynamic interaction, and have been used primarily to control flow separation. Their application was initially limited to low-speed flows, but has recently been extended to a somewhat higher speed regime. In recent years, these AC-DBDs have been applied to boundary layer transition control, with successful in-flight demonstration. Continued improvement of these actuators is anticipated with new electrode configurations, optimized dielectrics, and optimized high voltage driving waveforms.

Nanosecond-pulse, dielectric barrier discharge (ns-DBD) plasma actuators are similar in configuration to AC-DBD actuators, but their input waveform is a short pulse instead of a sinusoidal waveform. Their flow control effect is primarily a result of heating; the body force generated by current ns-DBD designs is only a small fraction of that of an AC-DBD. The rapid heating of the air near the actuator generates compression waves and introduces streamwise vorticity. In flow over an airfoil, these perturbations can trip a laminar boundary layer to turbulence, which can mitigate separation. Further, an ns-DBD actuator can attach separated flows under stall conditions by exciting the instabilities in the separated shear layer. This concept shows promise for improving aircraft performance in takeoff and approach.

Localized arc filament plasma actuators (LAFPAs) also operate through gas heating, and have a flow effect similar to that obtained with ns-DBDs. They use a spark discharge across pin electrodes to generate high amplitude, short-duration perturbations to the flow. An alternative configuration introduces transverse plasma filaments into the flow, with a repetition frequency tuned to flow instabilities. They have been successfully used in a wide variety of flows with inherent instabilities, including subsonic and supersonic cold or hot jets, shock / boundary-layer interaction, and cavity flows.

The spark jet, or pulsed plasma jet, is a hybrid actuator. It employs a spark discharge across electrodes housed in a small cavity. When the actuator fires, the rapid heating generates a synthetic jet out of

the cavity, which injects high-momentum fluid into the flow. These actuators can introduce a strong perturbation into the flow, and have been successfully applied to shock-wave / boundary-layer interaction control.

While plasma actuators have been demonstrated to be very effective in laboratory environments, they are subject to reliability and scalability concerns that have inhibited their widespread adoption for flight applications. Some of the chief concerns include electromagnetic interference, weather effects, durability, and maintenance. For many actuator designs, performance deteriorates over time through electrode erosion and plasma-initiated chemical degradation of the dielectrics, which must remain relatively pristine to avoid high voltage arcs and failure. Steady progress is being made, but additional emphasis needs to be placed on addressing such concerns.

Future efforts in plasma-based flow control must balance emphasis on specific applications and fundamental physics. In the former, the focus must be on reliability, scaling, efficiency, and miniaturization. This will require collaboration among experts in fluid dynamics, plasma physics, power supply engineering, and materials science. More fundamental research will serve to provide a more thorough understanding of the actuators and their influence on the flow field, leading to better designs, targeting specific applications. Study of applications and fundamentals must be closely linked for long-term success.

Plasma-Enhanced Combustion

Today, 85% of primary energy conversion processes are based on combustion, and this fraction is expected to remain stable in the foreseeable future. Because of the increasing financial cost and environmental impact of fossil fuels, however, industry faces ever more stringent challenges to improve combustion efficiency, reduce pollutant emissions, control combustion instabilities, and develop novel propulsion systems. Plasmas have long been used in combustion, beginning 150 years ago with the spark ignition system invented by Belgian engineer Etienne Lenoir. But the AJAX project (see Section 1) triggered interest in the use of plasma discharges as a means to provide in-place, on-demand enhancement of fuel-air reactivity, and thus launched the new field of plasma-assisted combustion.

Over the past two decades, the worldwide plasma-assisted combustion research community has been able to achieve great progress in the understanding of the fundamental physico-chemical effects of various types of plasma discharges in combustion, and has carried out successful demonstrations with laboratory-scale devices. Today, plasma-assisted combustion is seen as one of the most promising combustion strategies, and a key field for novel applications of high-pressure plasma discharges.

Since the mid-1990s, several successful proof-of-concept experiments have been conducted in small- to large-scale laboratory devices, and clear beneficial effects of plasma-assisted combustion have been demonstrated. For example, reduced ignition delays and enhanced flame stabilization in supersonic flows have been achieved by applying direct-current (DC), microwave (MW), or nanosecond repetitively pulsed (NRP) discharges to both flat plates and cavity-based flame holders. "Rail gun" plasma spark plugs, based on a self-induced magnetic field, have been shown to improve ignition and reduce electrode wear, and are currently being marketed for automotive,

turbine, and pulse detonation engine applications. Ignition delay times have been reduced by several orders of magnitude with nanosecond discharges, allowing, for example, the operation of Pulse Detonation Engines (PDE) at higher frequencies, and thus increased thrust and higher performance.

Flame stabilization, particularly in lean premixed regimes where lower burnt-gas temperatures lead to reduced formation of nitrogen oxide compounds (NO_x), has been achieved with NRP discharges for a wide variety of fuels (from natural gas and propane to kerosene) at pressures up to several bars. The ability of plasma discharges to enhance the ignition of ultra-lean fuel-air mixtures, or mixtures with increased exhaust gas recirculation (EGR) fractions, has also been demonstrated. This has the potential to increase the efficiency of gasoline engines and to reduce NO_x emissions in diesel engines.

Active plasma control of thermoacoustic combustion instabilities in the range of hundreds of hertz is being investigated as a method to reduce NO_x emissions, reduce the propensity for flashback and blowoff, increase heat transfer, mitigate structural fatigue or damage, simplify combustor design, and expand operability. Compared with mechanical or acoustic control devices, plasma discharges offer the advantages of relatively easy practical implementation (they can often be created across conventional spark plug electrodes), and fast temporal response and high actuation bandwidth. In most of these applications, the beneficial effects have been obtained with low power discharge consumption, typically with less than 1% of the power released by the flame.

Study of liquid and liquid-vapor interface plasmas has intensified considerably over the last few years. Some of the features of these plasmas may also have a significant potential for aerospace applications. One example is rapid pressure rise during pulsed breakdown in a liquid fuel, which may generate transient supercritical conditions and have a strong effect on the dynamics of fuel injection, atomization, and mixing with the flow.

These many opportunities for improvement of combustion processes present a compelling picture. The nearest term applications are most likely in ignition, with some concepts already being tested in realistic environments. These applications have the potential to improve ignition reliability, achieve more complete combustion, and minimize electrode erosion. Cold startup performance may also be improved. With enhanced reliability, the use of leaner fuel-air mixtures becomes practical, and operation with repeated pulses may enable combustion to proceed at extinction levels below those previously achievable.

Applications in high-pressure environments associated with internal combustion diesel and gasoline engines, natural gas and liquid hydrocarbon fueled turbines, and electrical power generators will be especially important, given the ubiquity of that equipment for mobile and stationary power. Even a small improvement in performance or reliability will be a great achievement, and the reduction of emissions will have a wide impact. Implementation in atmospheric pressure environments, such as natural gas and oil fired home heating and hot water heating units, may lead to reduction of pollution and improved efficiency through leaner, lower-temperature combustion.

An important long-range payoff may be the augmentation and control of high-speed ramjet and scramjet engines and of jet afterburners. Relevant plasma-based technologies show promise for volumetric

ignition, flame holding, increased mixing, flame speed enhancement, and acoustic control. For many applications, existing combustor designs may be utilized and the plasma effects introduced through advanced spark plug technology or injector and fuel delivery modifications.

Supporting Science

In order to make continued progress in plasma aerodynamics, certain supporting scientific areas require development. In particular, there is a need to improve the simulation and measurement of aerospace plasmas.

There are two main challenges for numerical simulation of aerospace plasmas. The first is the disparity in the time and length scales for an electrical discharge in a large-scale gas flow. Important physics occurs on the scale of molecules, the actuator, the air vehicle, and the flight path. Thus, the time scales involved range from sub-nanosecond molecular processes to several hours of flight time. Spatial scales range from nanometer molecular scales to megameter global flight paths. Significant progress has been made in multiscale computations through the use of unstructured meshes with a dynamic range in spatial resolution of 10^4 , time-slicing techniques which enable a dynamic range in timescales of 10^9 , and kinetic-fluid hybrid models that enable accurate representation of non-equilibrium processes. These techniques need to be refined to address the conditions of interest. These multiscale challenges have also motivated the use of reduced-order models, but there is a need to corroborate their accuracy with experiment and high-fidelity computations.

The accuracy of numerical modeling also depends strongly on the chemical kinetic model. The kinetics of plasmas in air and air-fuel mixtures is extremely complex, and care must be taken in calculations to stay within the bounds of validity of a plasma kinetic model. There is a lack of detailed experimental data to compare with new kinetic mechanisms. In general, there is a compelling need for consistent effort to establish the accuracy of plasma aerodynamic modeling.

Kinetic processes in nonequilibrium air and fuel-air plasmas remain far from understood, in spite of considerable experimental and kinetic modeling advances achieved over the last two decades. For example, the importance of rapid thermalization of internal energy on a sub-acoustic time scale, which generates high-amplitude, high bandwidth pressure perturbations, has been recognized only recently. Several aerospace technology areas that would benefit from detailed insight into plasma energy transfer processes and chemical kinetics include high-speed flow control, fuel injection and reforming, and combustion.

Quantitative insight into coupling between low-temperature plasma kinetics and combustion chemistry also remains a challenge. Conventional combustion chemistry mechanisms have been developed and validated for relatively high temperature conditions. Applicability of such mechanisms at temperatures below ignition temperature, common in plasma-assisted combustion environments, is uncertain at best. It must still be determined whether they can be used as a basis for a predictive plasma-assisted combustion chemistry mechanism. Quantitative insight into kinetics of nonequilibrium plasma assisted flow control, fuel oxidation, ignition, combustion, flameholding, and fuel reforming will not be feasible without detailed kinetic modeling.

Truly predictive analysis of air plasma and fuel-air plasma kinetics, even in relatively simple geometries, remains a formidable challenge.

Multi-fluid models, including separate modeling of the motion of electrons, ions, and species with different internal energy states, are also under study. The fundamental physics may also include kinetic effects, which can lead to phase space dynamics that manifest in large-scale effects of the flow dynamics. Additional work on rigorously formulating the governing equations and boundary conditions is still needed.

The inherent complexity of plasma-aerodynamic flows poses unique measurement challenges. In particular, prediction from first principles requires detailed knowledge of the partitioning of plasma energy between translational, rotational, vibrational, and chemical internal energy modes of flow constituents, as well as the ability to predict the coupling of this non-equilibrium fluid state to the gas dynamics of the flow field. The last twenty years have seen enormous growth in new aerodynamic measurement technologies, however, and the community is now poised to make significant advances. Carefully constructed, coupled experimental and computational campaigns, where high-fidelity computer simulations are validated by the available experimental measurements, could also significantly advance our understanding.

Three particularly important challenges should be noted. First, there is a need to develop new approaches for non-intrusive measurement in the aerodynamic environment of fundamental plasma properties, in particular the electric field, electron density, and electron temperature. Second, there is need for new technologies and methodologies that can provide data with space and time resolution at scales of interest for unsteady turbulent flows. Finally, there is the need to develop the capability to capture quantitative data in three dimensions. The last decade has seen extremely rapid advances in laser and optical technology, which researchers are exploiting to provide revolutionary new capability for aerodynamic measurement.

Potential Breakthrough Areas

Breakthroughs in aerodynamic plasma technology will come from the improvement of devices that are currently under study, from the implementation of new concepts, and from the development of new experimental facilities and materials. Significant advances in plasma-assisted combustion, plasma-enhanced aerodynamics, and measurement technologies are anticipated.

Plasma-based methods are currently under development for flame speed enhancement, volumetric ignition, reduction of nitric oxide formation, mixing enhancement, stabilization of combustion at reduced equivalence ratio, control of acoustic modes, and low temperature combustion. Breakthroughs in these areas are to be expected as better modeling provides better understanding of the most effective mechanisms for interaction, and as more effective actuator configurations and energy deposition mechanisms are developed. Such developments may include sub-nanosecond high voltage pulse capabilities for the creation of discharges suitable for operational combustors, and efficient, open-cavity, high-power pulsed microwave systems for the control of flame propagation speeds in turbulent combustion environments. Laser and nanosecond-pulse guided microwave energy

deposition may provide methods for more direct control of ignition location and temperature, and high voltage, nanosecond-pulse ignition methods may lead to greater combustion stability, volumetric ignition, reduced nitric oxide emission, and low equivalence ratio operation.

For aerodynamic processes, plasmas can be created on or off the surface. Surface discharges are being studied for the control of boundary layer separation, control of laminar to turbulent transition, drag reduction, and suppression of local heating. Off-body and volumetric plasmas are being studied for drag reduction, reduction of heat transfer rates, vehicle steering, power extraction, and reduction of sonic boom.

New methods for magnetohydrodynamic (MHD) control and power extraction are already leading to innovative designs for hypersonic vehicles. Flight control and reduced surface heating can be achieved through the use of a magnetic field interacting with the bow shock, and the concept is currently being implemented for flight tests. Power extraction during reentry may also be possible through the use of MHD interactions with internal or external flows. Internal flows benefit from shock interactions for ionization, and for these flows the technology is potentially applicable at lower Mach numbers.

Increased effectiveness of surface plasma actuators is anticipated with new electrode configurations, optimized dielectrics, and optimized high voltage driving waveforms. Breakthroughs are expected to occur with multi-electrode configurations for thrust generation and shock wave focusing. Further breakthroughs may arise from new surface materials that allow changes in the fundamental structure or the temporal evolution of the discharge. Additional surface-based concepts can make use of plasma arrays that are capable of generating shock waves that propagate away from the surface and coalesce to generate vorticity or drive acoustic waves for control of near-surface flows. Plasma-generated far-ultraviolet radiation may also be of use for rapid near-surface energy addition through direct absorption and molecular dissociation of oxygen.

Laser plasma ignition is of growing interest in a number of applications including reciprocating engines (mobile or stationary), ground based turbines, aero-turbines, rocket engines, and scramjet engines. Existing laser-ignition approaches are already showing benefit for extending the lean limit and improving reliability in aero-turbines. New approaches using multiple laser pulses to tailor the plasma are being investigated. Examples of approaches that could lead to breakthroughs include use of an overlapped nanosecond pulse to sustain the plasma filament generated from a femtosecond laser, and use of an initial pre-ionization pulse followed by energy addition and heating by a second pulse. Such approaches, which decouple the initial ionization from the subsequent energy addition (avalanche), may allow increased volume of the ignition kernel, formation of partially ionized plasmas with controlled temperature (for thermal ignition), or plas-

mas with longer lifetime, and/or reduced pulse energy requirements (allowing use of smaller, less powerful sources). These new means of laser plasma formation may also benefit other applications, including waveguides for microwave transmission, stand-off detection of hazardous agents, and lightning protection.

Breakthrough technologies in the measurement area will be enabled by the development of new devices that are capable of interacting with air and combustion environments in ways that are not feasible or practical today. Perhaps the most promising of these is the rapid progress toward the development of efficient, very short-pulsed, precision controllable, high-power, high repetition rate lasers. These lasers will open up new methods for real time data acquisition as well as off-body energy addition, efficient volume ionization methods for MHD applications, and volumetric, selective radical production for combustion reaction and ignition control. With more compact, higher efficiency lasers, operation in flight will be a practical reality.

Summary and Conclusions

Plasma aerodynamics can trace its origin to the beginning of the space age, and in particular to a time when designers realized that plasmas could have a significant influence on reentry flows. From the 1950s to the 1970s, there was considerable work on magnetohydrodynamic reentry systems and related technology. The recent resurgence in the field was stimulated by the disclosure of the Soviet AJAX vehicle concept in the mid-1990s. This led to an extraordinary international collaboration that has now lasted almost twenty years.

Plasma-based flow control seems quite feasible, particularly for local flow control applications where power consumption is low. Plasma-based devices have a low profile, and can provide actuation over short time scales. Plasma-enhanced combustion is a very promising area for both low- and high-speed regimes. Discharges are already being used to break down fuels, enhance ignition, provide flameholding, and promote combustion efficiency.

There are a number of potential breakthrough areas in the field that could have strong technological impact on the aerospace industry. Industry seems to be receptive to the adoption of plasma-based technology, but has reservations about technical risk, performance, reliability, and integration. There is a need to identify applications where plasma devices are significantly better than competing technologies, and to demonstrate prototypes in an operational environment.

With a century of atmospheric flight and half a century of spaceflight behind us, the aerospace sciences remain a vigorous and exciting field. The new field of plasma aerodynamics contributes to this excitement, and supports diverse aerospace technology needs, from energy efficiency to space access ■

Acknowledgements and Disclaimers

This document consolidates a survey of opinions from participants in the AIAA Plasma Aerodynamics Discussion Group. It does not necessarily represent the official policy of the institutions of any of the contributors, nor does it imply unanimous agreement among the participants. The material provided has been cleared for public release by the institutions of the contributors.



Sergey Leonov received his Ph.D. from Baltic State University in 1990, and a senior Doctor of Science degree from the Russian Academy of Sciences in 2006. He worked in the Joint Institute for High Temperature where he was a Head of Department, and, concurrently, Moscow Open University where he was a Professor. Currently he is a Research Professor at the University of Notre Dame, USA. His expertise is in weakly ionized plasmas, plasma aerodynamics, aerothermodynamics, and active flow control.



Jonathan Poggie received his Ph.D. in Mechanical and Aerospace Engineering from Princeton University in 1995. Since graduation, he has worked for the U.S. Air Force Research Laboratory, where he is currently Technical Advisor for the Hypersonic Sciences Branch. He has very broad experience, with research publications in the experimental, computational, and theoretical sides of high-speed flow and plasmadynamics. Poggie is a fellow of the ASME and an Associate Fellow of the AIAA.



Thomas McLaughlin received his Ph.D. in Aerospace Engineering Sciences at the University of Colorado in 1992. He is the director of the Aeronautics Research Center at the U.S. Air Force Academy, responsible for all research operations in the Department of Aeronautics. An Associate Fellow of AIAA, Dr. McLaughlin works on aerodynamic flow control and experimental aerodynamics.

Lead Contributors

History of the EOARD WIG Program: J. Tishkoff, US Air Force Office of Scientific Research
 Plasma-Based Flow Control: M. Samimy, The Ohio State University
 Plasma-Enhanced Combustion: C. Laux, Ecole Centrale Paris, France
 Plasma Chemical Kinetics: I. Adamovich, The Ohio State University
 Numerical Simulations: D. Knight, Rutgers University
 Measurement Techniques: W. Lempert, The Ohio State University
 Potential Breakthrough Areas: R. Miles, Princeton University
 Technology Transition: S. Macheret, Lockheed Martin Corporation

Contributors and Reviewers

T. Abe, JAXA, Japan
 N. Aleksandrov, Moscow Institute of Physics and Technology, Russia
 N. Bisek, US Air Force Research Laboratory
 C. Bruno, UTRC
 M. Cappelli, Stanford University
 C. Carter, US Air Force Research Laboratory
 N. Clemens, University of Texas at Austin
 T. Corke, University of Notre Dame
 S. Coulombe, MacGill University, Canada
 B. Cybyk, Johns Hopkins University
 Y. Ju, Princeton University
 J. D. Kelley
 W. Kim, United Technologies Research Center
 D. Konigorski, Airbus Group, Germany
 M. Kushner, University of Michigan
 S. Lawton, The Boeing Corporation
 J. Little, University of Arizona
 E. Moreau, University of Poitiers, France
 M. Mortazavi, Rutgers University
 T. Ombrello, US Air Force Research Laboratory
 S. Pasquiers, Université Orsay Paris Sud, France
 S. Popkin, Johns Hopkins University
 U. Shumlak, University of Washington
 J. Silkey, The Boeing Corporation
 T. Sommerer, GE
 S. Starikovskaya, Ecole Polytechnique, France
 A. Starikovskiy, Princeton University
 C. Tropea, Technical University of Darmstadt, Germany
 D. Veynante, Ecole Centrale Paris, France
 A. Vincent, ONERA, France
 A. Yalin, Colorado State University
 R. Yetter, Pennsylvania State University

A Short Review of Microwave and Laser Discharges for Supersonic Flow Control

D. Knight
(Rutgers, The State University of New Jersey)

E-mail: doyleknight@gmx.com

DOI : 10.12762/2015.AL10-02

Energy deposition by electromagnetic discharge (*e.g.*, arc, laser, microwave) is an emerging field of research in flow and flight control. Major advantages of this approach include fast response time, capability for customization of discharge, and off-body modification of the flow. Recent computational and experimental research in energy deposition are described and future needs identified.

Introduction

Energy deposition by pulsed laser and microwave discharge has received significant interest in the past several decades as a promising technique for flow control at high speeds. In this article we present a brief review of selected experimental and theoretical studies to illustrate the potential of this emerging technology. Additional information may be obtained from several recent reviews including Zheltovodov [30], Fomin *et al.* [7], and Knight [12].

Microwave Discharge

Introduction

The phenomenon of pulsed microwave discharge (breakdown) in air is characterized by a bright flash of light and formation of a complex plasma structure depending on the microwave frequency (wavelength) and ambient pressure. An example of the variety of plasma shapes is presented in figure 1 from Kolesnichenko [13]. The Paschen curve (MacDonald [19], Fridman and Kennedy [8]) defines the breakdown electric field strength E as a function of the product of the ambient pressure p and microwave wavelength λ . An extensive literature on microwave discharge is available; for example, see Lebedev [17, 18].

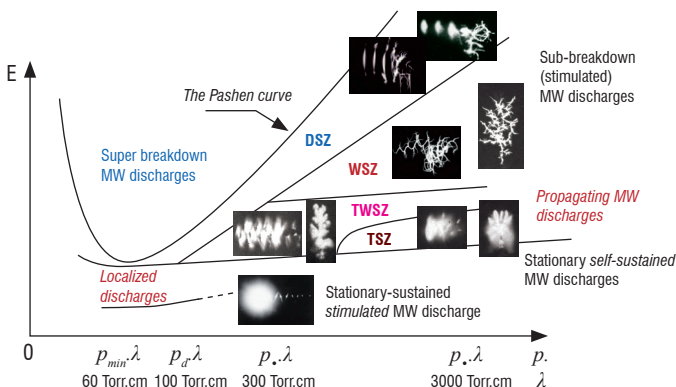


Figure 1 – Types of microwave discharges [13]. DSZ: discharge with straight channels, WSZ: discharge with curved channels, TWSZ, TSZ: variant of WSZ

We summarize the results of three experiments on the interaction of a microwave discharge with a test model in supersonic flow. The flow conditions are summarized in table 1. Kolesnichenko *et al.* [15] and Lashkov *et al.* [16] performed experiments at St. Petersburg State University, Russian Federation. Exton *et al.* [6] conducted experiments at NASA Langley Research Center, Hampton, Virginia.

Quantity	K2001	E2001	L2004
<i>Mach number</i>	1.7	6.0	2.1
<i>Stagnation pressure (kPa)</i>	39.5	631	30.5
<i>Stagnation temperature (K)</i>	316	574	300
<i>MW frequency (GHz)</i>	9	16	9
<i>MW peak power (kW)</i>	210	425	210
<i>MW pulse (μs)</i>	1.2 - 2.2	3.5	1.2

Table 1 – K2001: Kolesnichenko *et al.* [15]. E2001: Exton *et al.* [6]. L2004: Lashkov *et al.* [16]

Kolesnichenko et al. 2001

Kolesnichenko *et al.* [15] conducted a series of experiments to examine the interaction of a microwave-generated plasma on the drag of a blunt cylinder at Mach 1.7 at a freestream static pressure $p_\infty = 8$ kPa and static temperature $T_\infty = 200$ K. The microwave pulse was generated by a klystron operating at 9 GHz with peak power of 210 kW and pulse duration $\tau = 1.2$ to $2.2 \mu s$. The estimated reduced field E/N (where E is the magnitude of the electric field and N is the particle concentration) is 80 to 100 Townsend. The discharge generated multiple plasmoids (up to three) upstream of the blunt cylinder which convected downstream at approximately the freestream velocity. The plasmoids were initially formed on the centerline of the cylinder upstream of the blunt body shock.

Schlieren images of the interaction are shown in figures 2(a) and 2(b) where the flow is from right to left. The blunt body shock generated by the blunt cylinder is visible. At $t=21\mu s$ the plasmoid has reached the blunt body shock causing a lensing forward (*i.e.*, upstream) of the shock. The experimental surface pressure on the cylinder face at the centerline vs time is shown in figures 3(a) and 3(b) for air and CO_2 , respectively, for models of differing diameter. In all cases a dramatic reduction in surface pressure is observed resulting in a momentary reduction in drag.

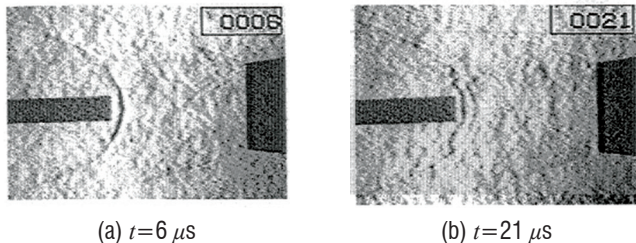


Figure 2 – Schlieren images of microwave discharge [15]

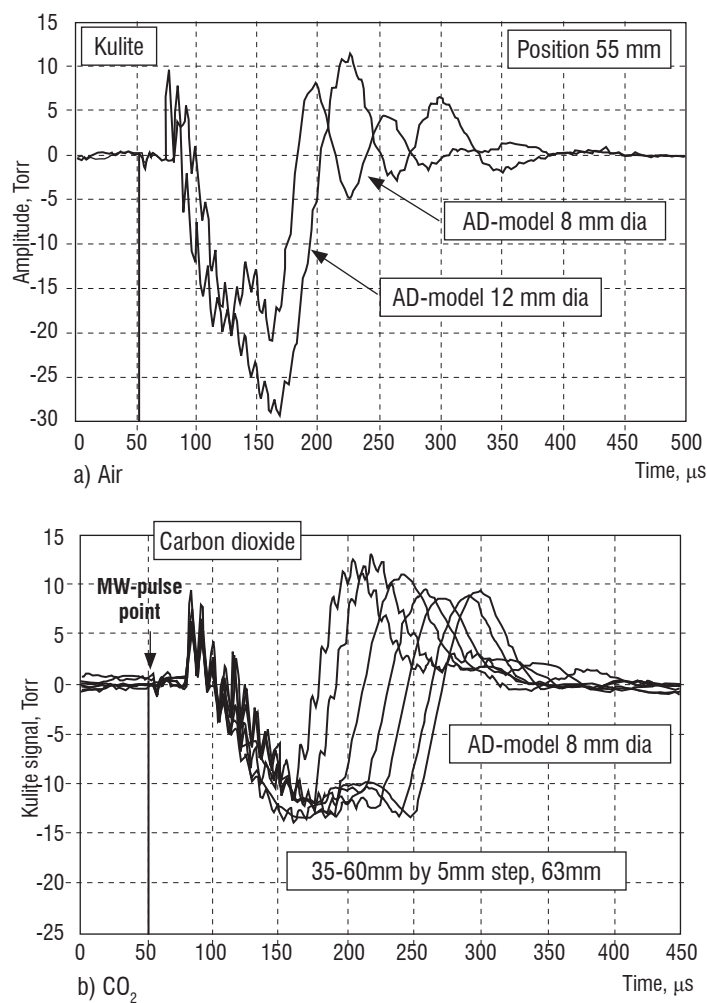


Figure 3 – Surface pressure vs time for microwave discharge (AD means “aerodynamic”) [15]

Exton 2001

Exton *et al.* [6] conducted an experiment to examine the interaction of a microwave-generated plasma with a blunt cylinder at Mach 6 at a freestream static pressure $p_\infty=0.4$ kPa and static temperature $T_\infty=70$ K. The microwave pulse was generated by a Ku-band klystron (15.8 – 17.3 GHz) with a peak power of 425 kW and pulse duration $\tau\leq 3.5\mu s$. A 10-

mCi⁹⁰Sr radioactive source emitting 0.54 MeV electrons was used as an initiator for the discharge. The experimental configuration is shown in figure 4. The duty cycle was 0.001 implying no interaction between individual pulses. Figure 5 displays a time-averaged Schlieren image. The microwave discharge is focused just upstream of the shock wave, and has no apparent effect on the shock standoff distance. The plasma becomes reflective to microwave radiation during the early stages of the microwave pulse due to the increase in the electron concentration, thereby creating an effective plasma mirror.

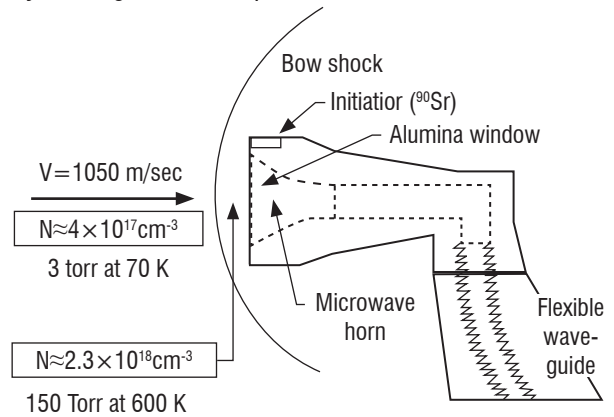
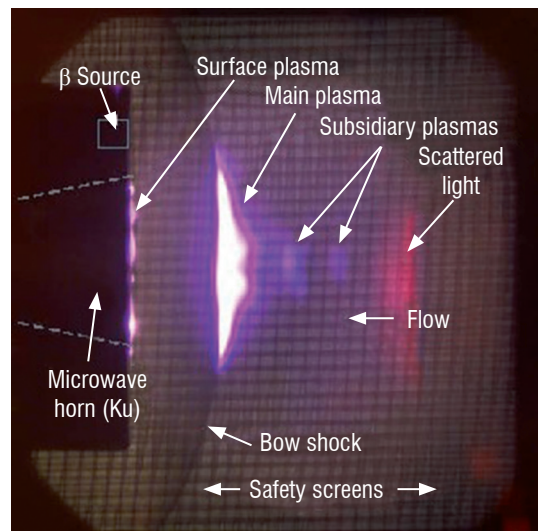


Figure 4 – Experimental configuration for microwave discharge [6]



Precursor Plasma at Mach 6

Figure 5 – Schlieren image for microwave discharge [6]

Lashkov *et al.* 2004

Lashkov *et al.* (2004)[16] conducted experiments to evaluate the interaction of a microwave discharge on blunt and hemisphere cylinders at Mach 2.1 in air at a freestream static pressure $p_\infty=3.3$ kPa and static temperature $T_\infty=159$ K. The microwave generator described in Kolesnichenko *et al.* [15] was used. The plasmoids were similarly formed initially on the centerline of the cylinder upstream of the blunt body shock.

Schlieren images for the interaction of the microwave-generated plasma with the blunt cylinder are presented in figure 6 for $t=20\mu s$ to $140\mu s$. The lensing forward of the shock seen in figures 6(c) to 6(f). The shock standoff distance at the centerline increases to nearly twice the undisturbed distance. The experimental pressure on the cylinder centerline, shown in figure 8(a), decreases from 28.7 kPa prior to the interaction to 9.3 kPa at $t=150\mu s$ due to the interaction, resulting in a significant momentary reduction in pressure drag on the cylinder.

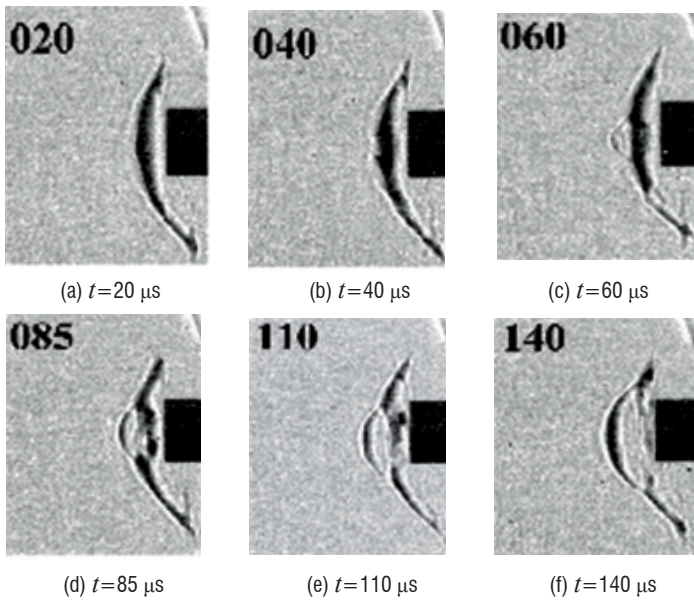


Figure 6 – Schlieren images for microwave discharge upstream of blunt cylinder [16]

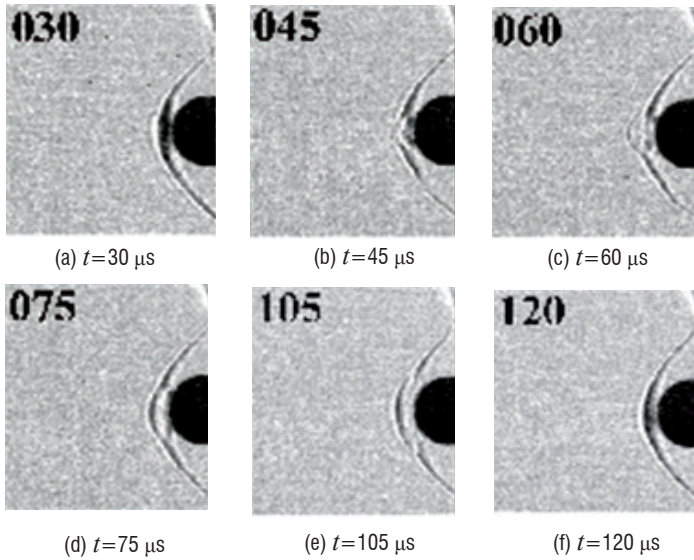


Figure 7 – Schlieren images microwave discharge upstream of hemisphere cylinder [16]

Schlieren images of the interaction of the microwave-generated plasma with the hemisphere cylinder are shown in figure 7. The interaction is similar to the blunt cylinder experiment of Kolesnichenko *et al.* [15]. The plasma causes the blunt body shock to lens forward beginning at $t=60 \mu\text{s}$. The centerline pressure (figure 8(b)) displays a similar dramatic decrease at $t=100 \mu\text{s}$ due to the interaction of the plasma with the blunt body shock.

The effect of off-centerline initial location of the microwave-generated plasma was examined. Off-axis displacement up to D (where D is the cylinder diameter) were considered for the blunt cylinder. An impulse function was defined

$$I = \int_0^{t_f} (p_{CL}(t) - p_o(t)) A dt \quad (1)$$

where $p_{CL}(t)$ is the time-dependent centerline pressure on the cylinder due to the interaction, p_o is the undisturbed centerline pressure, A is the cylinder frontal area and t_f is the duration of the interaction. It was observed that $I < 0$ for displacements less than $0.15D$ (*i.e.*, drag reduction) and $I > 0$ for displacements greater than $0.15D$ (*i.e.*, drag increase).

Laser Discharge

Introduction

The phenomenon of pulsed laser discharge (breakdown) was discovered in the 1960s [4, 20, 21, 22, 23]. The discharge is characterized by a bright flash of light at the focus of the laser beam and a sharp noise (“crack”). Three successive phases occur in the discharge which is typically tens of nanoseconds to microseconds in duration. The first phase is multi-photon ionization wherein multiple photons are absorbed by gas atoms resulting in ionization and release of electrons [10]. The second phase is inverse bremsstrahlung and cascade ionization wherein the free electrons gain energy by absorption of photons and ionize neutral particles leading to a cascade growth of free electrons and ions. The final phase is the formation of a plasma (ionization) wave due to the heating of the gas by the incident laser radiation and propagates towards the laser source [26].

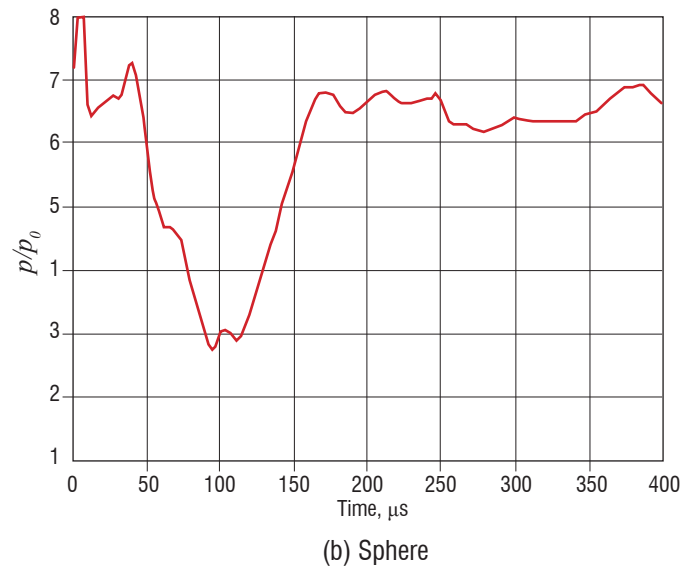
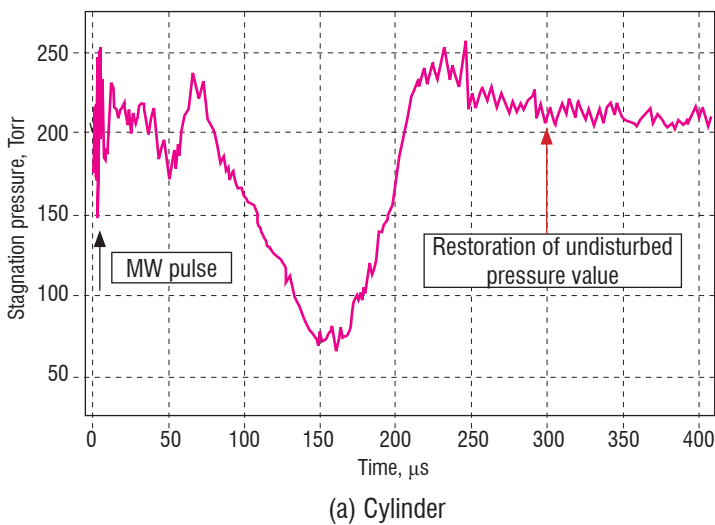


Figure 8 – p vs t on centerline of body for microwave discharge [16]

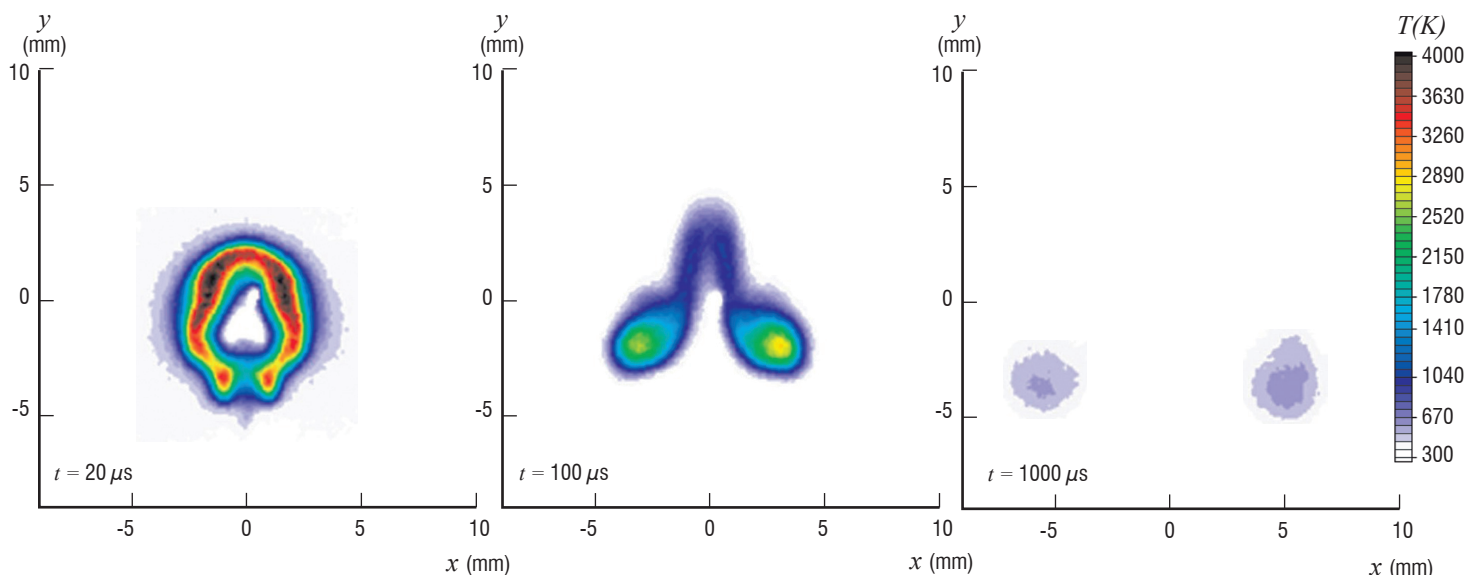


Figure 9 – T at $t=20 \mu\text{s}$ to $1000 \mu\text{s}$ for laser discharge [9]

Subsequent to the discharge phase, a blast wave forms due to the high pressure and temperature generated by the laser discharge. The blast wave becomes spherical at distances large compared to the laser discharge focal volume and the pressure rise decreases with distance from the discharge. The plasma wave formed during the discharge generates a jet directed toward the laser source forming a toroidal vortex. The temperature in the plasma decreases in time due to mixing and radiation. Figure 9 from Glumac *et al.* [9] displays the measured temperature for a 150 mJ Nd:YAG (532 nm) discharge of 6.5 ns in air at ambient conditions. Detailed reviews of laser discharge in gases are presented in Raizer [27], Ostrovskaya and Zaidel [25] and Morgan [24].

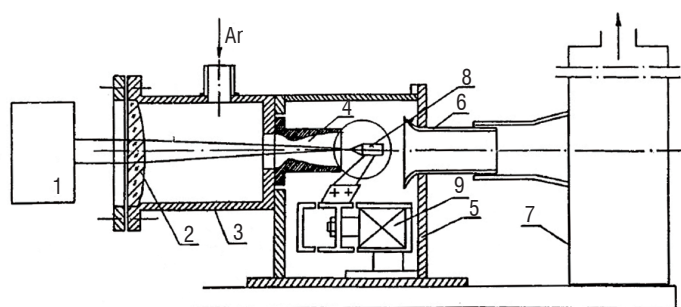
We summarize the results of three experiments on the interaction of a laser discharge with a test model in supersonic flow. The flow conditions are summarized in table 2. Tretyakov *et al.* [29] performed experiments at the Khristianovich Institute of Theoretical and Applied Mechanics in Novosibirsk, Russian Federation. Adलगren *et al.* [1] conducted experiments at Rutgers, The State University of New Jersey. Schülein *et al.* [28] performed experiments at the German Aerospace Center DLR in Göttingen, Germany.

Quantity	T1996	A2005	S2010
<i>Mach number</i>	2	3.45	2.0
<i>Stagnation pressure (kPa)</i>	450	1400	180
<i>Stagnation temperature (K)</i>	293	290	270
<i>Laser pulse frequency (kHz)</i>	12.5 to 100	n/a	n/a
<i>Laser pulse duration (ns)</i>	1200	10	5
<i>Body diameter (mm)</i>	6.0	25.4	60

Table 2 – T1996: Tretyakov *et al.* [29]. A2005: Adलगren *et al.* [1]. S2010: Schülein *et al.* [28]

Tretyakov *et al.* 1996

Tretyakov *et al.* [29] measured the drag on a cone-cylinder and hemisphere-cylinder at $M_\infty=2$ in argon using a high frequency CO_2 laser discharge upstream of the body. The experimental configuration is shown in figure 10 and the experimental conditions are indicated in table 2.



1– CO_2 laser 2– focusing lens 3– plenum chamber 4– nozzle unit 5– working chamber 6– diffuser 7– exhaust chamber 8– model 9– aerodynamic window

Figure 10 – Experimental configuration for laser discharge [29]

The distance l of the focal point of the laser discharge from the test model was varied between one and two diameters upstream on the centerline. The measured drag (figure 11) shows a substantial reduction up to 45%. The parameter L is the distance of the body from the nozzle exit. The effect of the location and frequency of the laser discharge can be understood by replottting the data in terms of the dimensionless pulse period

$$\tau = \frac{U_\infty}{fl} \quad (2)$$

where f is the pulse repetition frequency, U_∞ is the freestream velocity and l is the distance of the laser focus to the test model. The parameter τ is the ratio of the elapsed time between pulses to the time required for the freestream flow to travel between the pulse location and the leading edge of the body. Results shown in figure 12 indicate that the maximum drag reduction is achieved at $\tau \approx 1$.

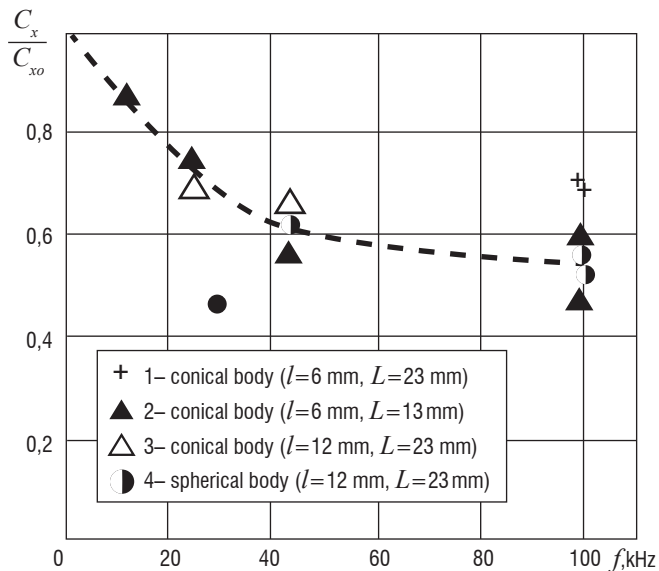


Figure 11 – Drag coefficient ratio vs frequency for laser discharge [29]

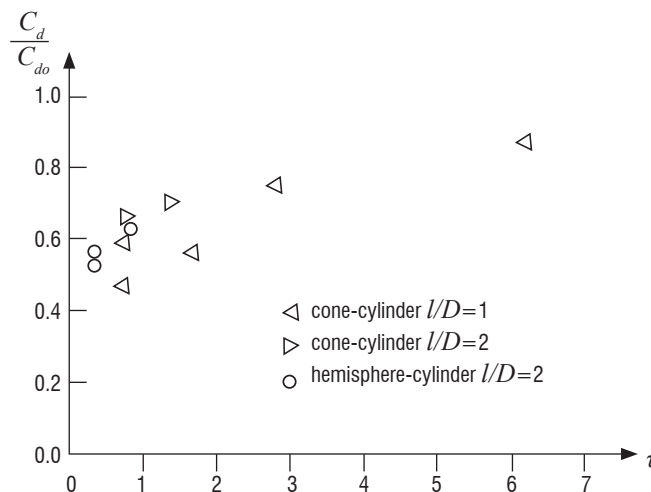


Figure 12 – Drag coefficient vs τ for laser discharge [29]

Adelgren *et al.* 2005

Adelgren *et al.* [1] investigated the interaction of a laser discharge in air with a sphere at Mach 3.45. The experimental configuration is illustrated in figure 13 and the experimental conditions are listed in table 2. An Nd:YAG (532 nm) laser was focused upstream of a hemisphere cylinder on the centerline. The focal volume is approximately 3.0 mm³. Discharge energies from 13 mJ to 283 mJ were considered. Experiments were performed with and without an impinging oblique shock wave (generated by the 15° compression ramp indicated in figure 13) intersecting the blunt body shock generated by the sphere.

Results for the interaction of a 283 mJ laser pulse with the sphere are shown in figure 14. The bright spot indicates the location of the laser discharge (figure 14(a)) and remains in all subsequent images due to saturation of the CCD camera. The blast wave generated by the discharge impacts the sphere at $t=30\mu\text{s}$ (figure 14(b)). The heated plasma intersects the blunt body shock causing it to lens upstream while a toroidal vortex forms (figure 14(c)). Eventually the plasma convects downstream and the flow returns to steady state (figure 14(d)).

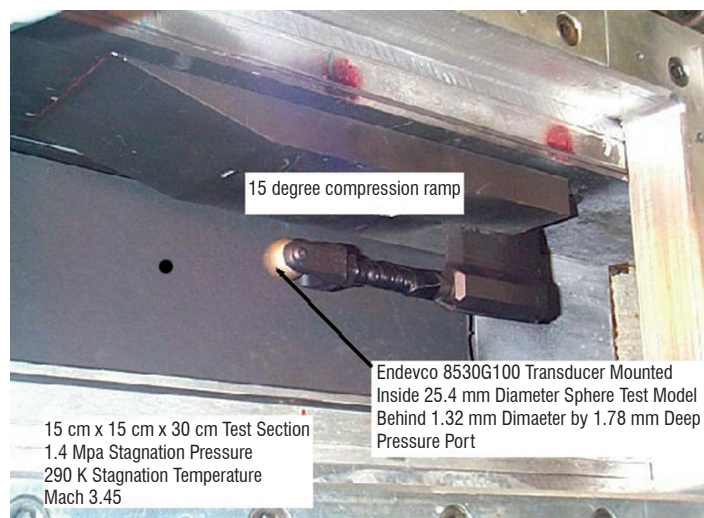


Figure 13 – Experimental configuration for laser discharge [1]

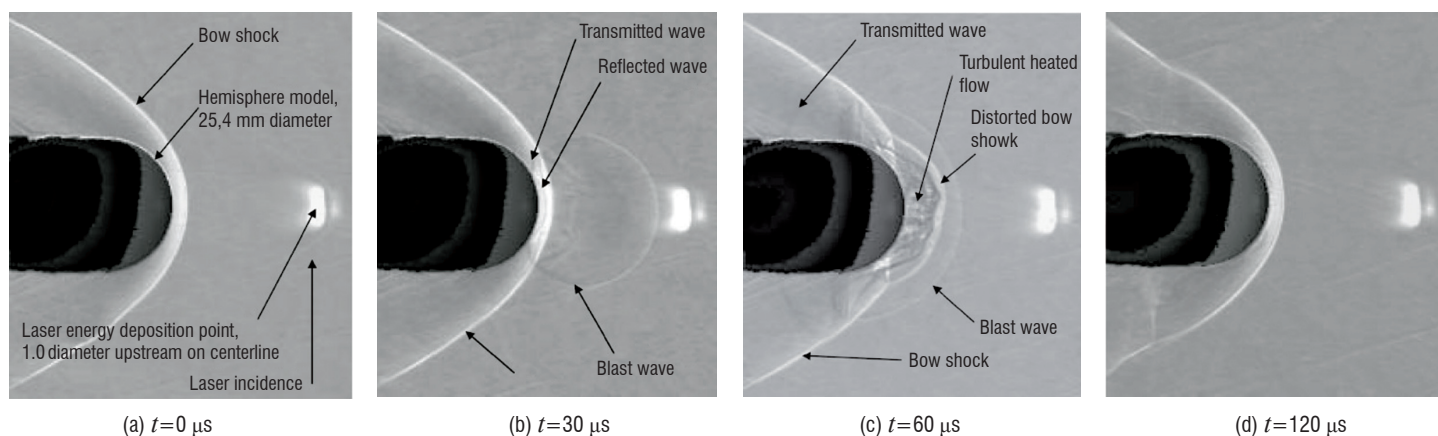


Figure 14 – Schlieren images of interaction of laser discharge (283 mJ) with sphere [1]

Figure 15 displays the surface pressure on the forward face of the hemisphere vs time where the surface pressure is normalized by the stagnation pressure p_{o_2} on the sphere in the absence of the laser discharge. The impact of the blast wave on the sphere results in an initial pressure rise $\tau \approx 30 \mu\text{s}$ followed by a sudden expansion. The interaction of the plasma with the blunt body shock generates a recompression and the pressure relaxes to its steady state distribution. The temporal history of the centerline pressure for three different energy pulses is shown in figure 16. The initial peak pressure associated with the impact of the blast on the sphere increases with laser discharge energy; however, the minimum pressure achieved during the expansion is insensitive to the laser discharge energy.

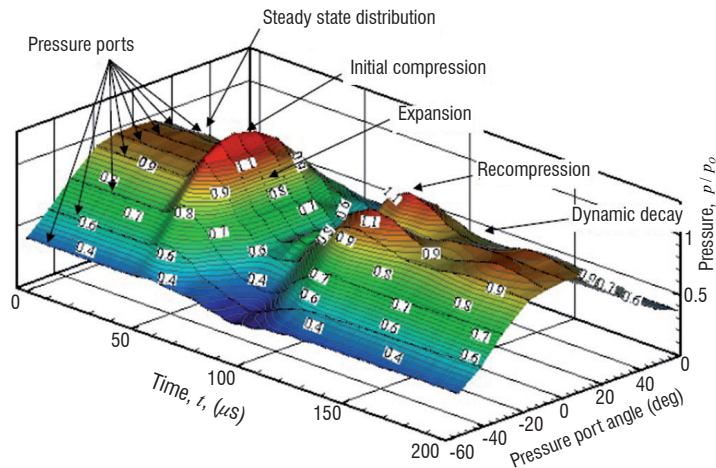


Figure 15 – p/p_o vs t on front surface for interaction of laser discharge with sphere [1]

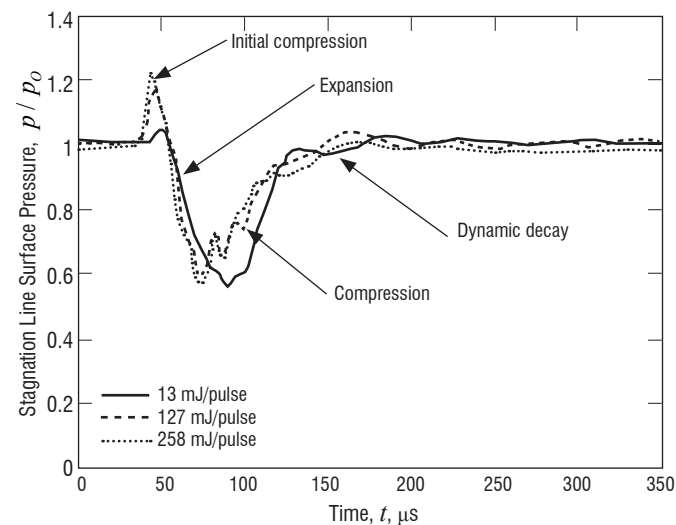


Figure 16 – Centerline pressure vs time for different laser pulse energy [1]

Schüleïn *et al.* 2010

Schüleïn *et al.* [28] performed an experimental investigation of the interaction of single- and double-pulsed laser discharge in air with a hemisphere cylinder at Mach 2. The experimental configuration is shown in figure 17 and the experimental conditions listed in table 2. An Nd:YAG (532nm) laser was focused through the centerline of the hemisphere cylinder to a point upstream. The focal volume is approximately ellipsoidal with major axis of 1 mm and minor axes of 0.2 mm. Discharge energies from 151 mJ to 666 mJ were considered.

Experimental shadowgraphs for $Q=333\text{mJ}$ are shown in figure 18. Figure 18(a) indicates the heated region formed by the laser discharge,

the blast wave which has rapidly assumed a spherical shape and the blunt body shock ahead of the hemisphere. The blast wave expands radially outwards from the initial location of the laser discharge. Figure 18(b) shows the instant of blast wave impact on the centerline. At instant earlier the blast wave intersected the blunt body shock and a transmitted shock propagated into the space between the blunt body shock and the hemisphere. Note that the plasma has not yet reached the blunt body shock. Figure 18(c) shows the instant of intersection of the plasma with the blunt body shock which lenses forward due to the lower Mach number of the heated region. Figure 18(d) displays the toroidal vortex formed by the Richtmyer-Meshkov instability associated with the intersection of the boundary of the heated region with the blunt body shock.

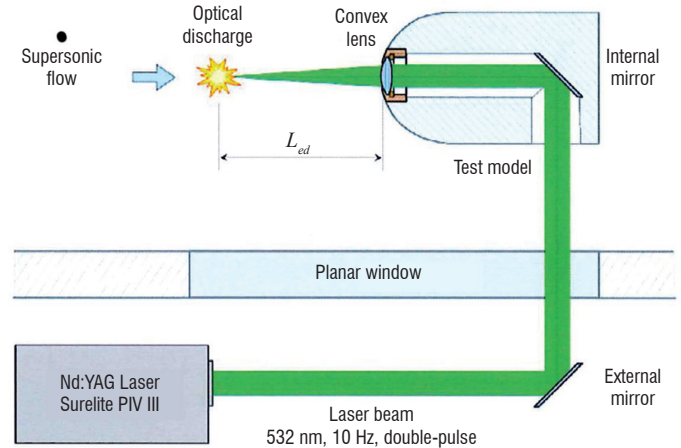


Figure 17 – Experimental configuration for laser discharge [28]

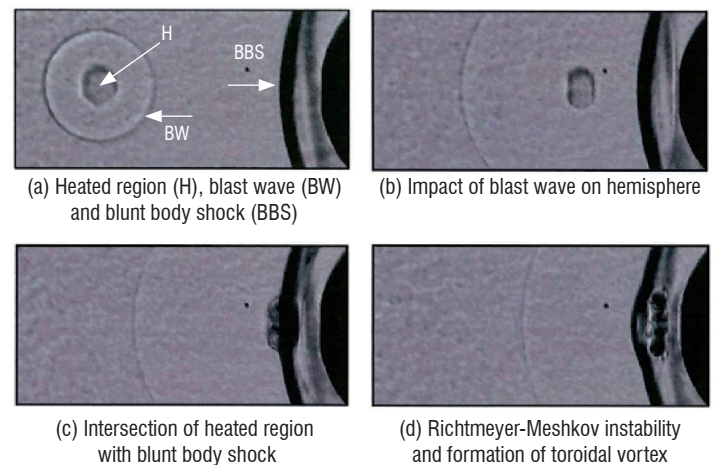


Figure 18 – Experimental shadowgraphs for single laser discharge $Q=333\text{mJ}$ [28]

Modeling

Introduction

The physical processes associated with pulsed laser or microwave discharge in air are complex, involving finite rate chemical reactions, real gas effects, radiation and plasma dynamics. A complete description of these phenomena is therefore difficult, and therefore modeling of such pulsed discharges is typically simplified based upon a variety of assumptions. We present three selected examples of models. Kandala and Candler [11] developed a realistic model of laser discharge and applied the model to the simulation of the interaction of the discharge plasma with a hemisphere and an Edney IV interaction. Azarova *et al.* [3] and Anderson and Knight [2] applied a simpler perfect gas model to the interaction of a microwave discharge with a blunt cylinder.

Kandala and Candler [11] simulated the interaction of a laser discharge with a sphere and an Edney IV interaction (Edney [5]) corresponding to the experiments of Adelgren *et al.* [1]. The laser discharge model assumes the existence of a small concentration of electrons (*i.e.*, assumes multi-photon ionization has occurred) and approximates the inverse-bremsstrahlung absorption by absorptivity coefficient κ_a . The intensity I of the laser radiation in the beam direction x is

$$\frac{dI}{dx} = -\kappa_a I \quad (3)$$

The absorption coefficient is

$$\kappa_a = \Sigma N_e (1 - e^{-hc/\lambda k T_e}) \quad (4)$$

where Σ is the characteristic interaction cross-sectional area, N_e is the electron concentration, h is Planck's constant, c is the speed of light, λ is the laser wavelength, k is Boltzmann's constant and T_e is the electron temperature. Since the laser-generated plasma becomes opaque to the radiation with increase in the electron concentration, a reflectivity coefficient is implemented

$$\kappa_r = A(\log Z + B) \quad (5)$$

where $0 < \kappa_r < 1$ and Z is the degree of ionization. The values of Σ , A and B are determined by comparison of the computed and experimental blast wave

for the laser discharge in ambient air. The laser radiation model was coupled with an eleven species model for air (N_2 , O_2 , NO , N , O , N^{+2} , O^{+2} , NO^+ , N^+ , O^+ and electrons). The governing equations include the conservation of mass for each specie and mass-averaged momentum, and conservation of vibrational, electronic and total energy.

Kandala and Candler simulated a 160mJ Nd:YAG laser discharge and its interaction with a sphere at Mach 3.45 corresponding to the experiment of Adelgren *et al.* [1]. The laser discharge was focused upstream of the sphere on the centerline. Figure 19 displays the computed surface pressure and heat transfer on the centerline vs time where p_o and q_o are the centerline pressure and heat transfer in the undisturbed flow. The initial increase in pressure and heat transfer at $t=25 \mu s$ corresponds to the impact of the blast wave on the sphere. The subsequent reduction in both pressure and heat transfer is due to the interaction of the plasma with the blunt body shock resulting in a lensing forward of the shock and expansion wave impacting the sphere. As the plasma convects towards the sphere the surface pressure increases; however, a significant spike in heat transfer is noted.

Kandala and Candler performed several simulations of a laser discharge and its interaction with an Edney IV flowfield at Mach 3.45 corresponding to the experimental configuration of Adelgren *et al.* [1]. Different focal locations of the laser discharge were considered (figure 20) to determine the effect on the surface pressure and heat transfer. A typical result for the surface pressure and heat transfer on the centerline is shown in figure 21. The behavior is similar to the interaction with the sphere alone. Results for different laser focal locations are presented in figure 22 and suggest that an optimal location for the laser discharge may be obtained.

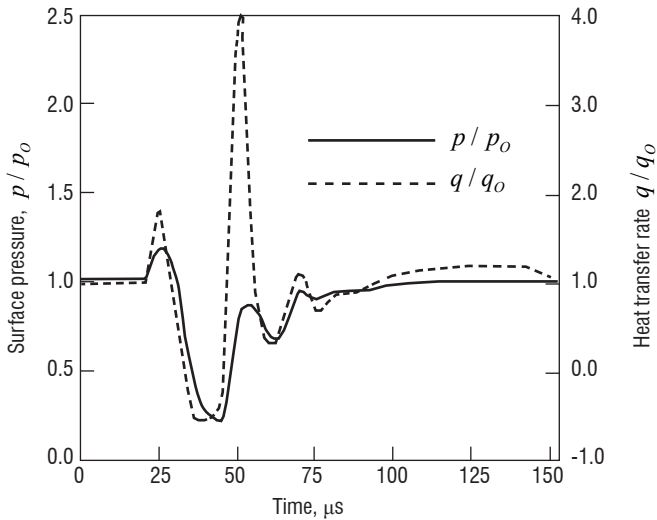


Figure 19 – p/p_o and q/q_o vs t for laser discharge [11]

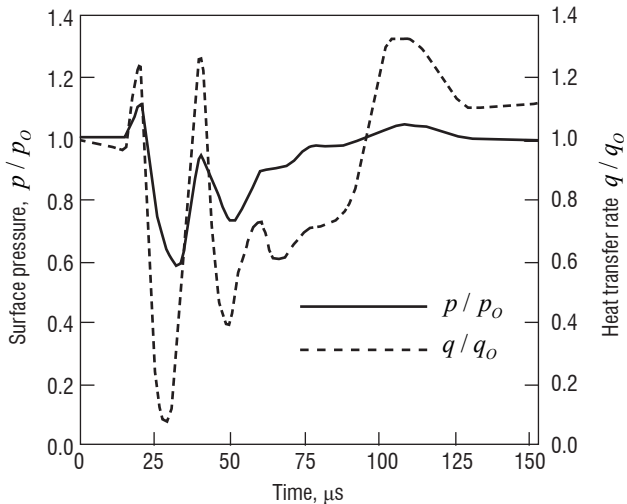


Figure 21 – p/p_o and q/q_o vs t for laser discharge [11]

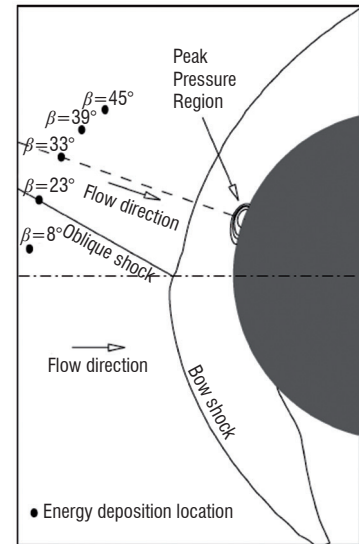


Figure 20 – Laser discharge [11]

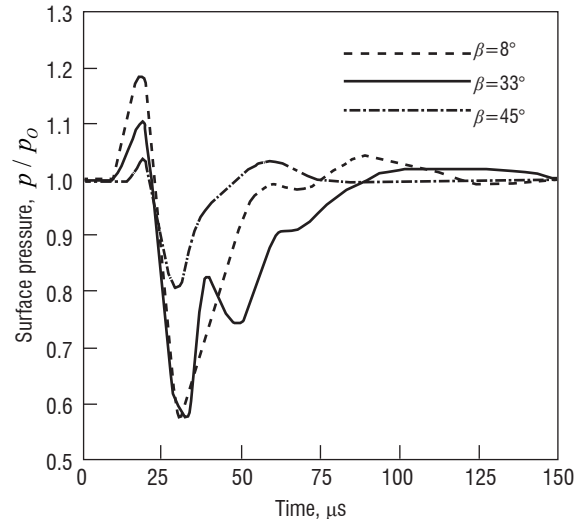


Figure 22 – p/p_o and q/q_o vs t for laser discharge [11]

Anderson and Knight [2] simulated the interaction of pulsed heated filaments with a blunt cylinder at Mach 1.89. The flow configuration is shown in figure 23. The flow parameters (table 3) were selected to correspond to the microwave discharge experiments of Kolesnichenko *et al.* [14]. The microwave-generated plasmas were modeled as instantaneously generated filaments defined by density ratio ρ_f/ρ_∞ , diameter d/D , length l/D and period L/D where D is the diameter of the cylinder. The simulations were based upon the compressible laminar Navier-Stokes equations for a perfect gas.

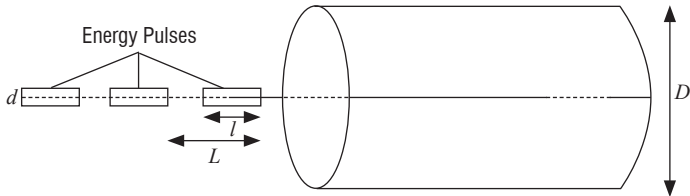


Figure 23 – Flow configuration [2]

Quantity	Symbol	Value
Mach number	M_∞	1.89
Reynolds number	Re_D	$7.0 \cdot 10^4$
Density ratio	α	0.5
Filament diameter	d/D	0.1
Filament length	l/D	1.0
Filament period	L/D	1.0 to 4

Table 3 – Flow Parameters

Simulations were performed for four different filament frequencies L/D with a fixed filament length $l/D=1$, diameter $d/D=0.1$ and density ratio α (table 3). Figures 24 to 27 display instantaneous numerical schlieren images (left) and time-averaged streamlines and velocity magnitude contours (right) for four different filament discharge frequencies L/D . The instantaneous images display the lensing upstream of the blunt body shock, formation of a free shear layer due to the interaction of the density interface of the filament with the blunt body shock, and Kelvin-Helmholtz instability. The time-averaged streamlines display the formation of a recirculation region upstream of the cylinder face, and in the particular case $L/D=4/3$ the movement of the stagnation point off the cylinder centerline.

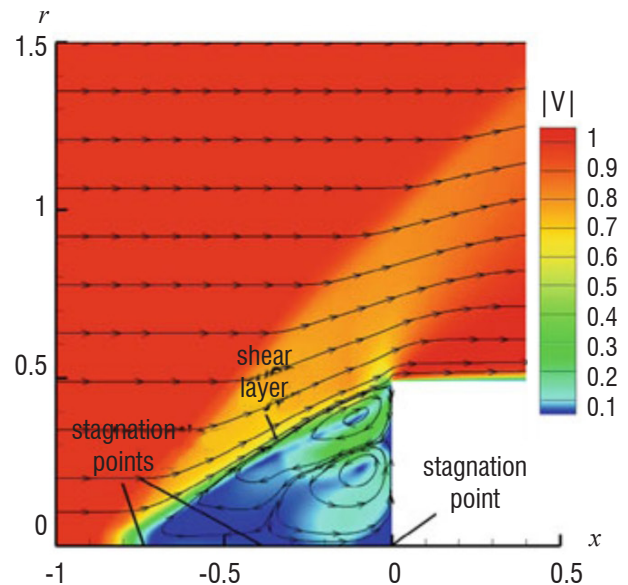
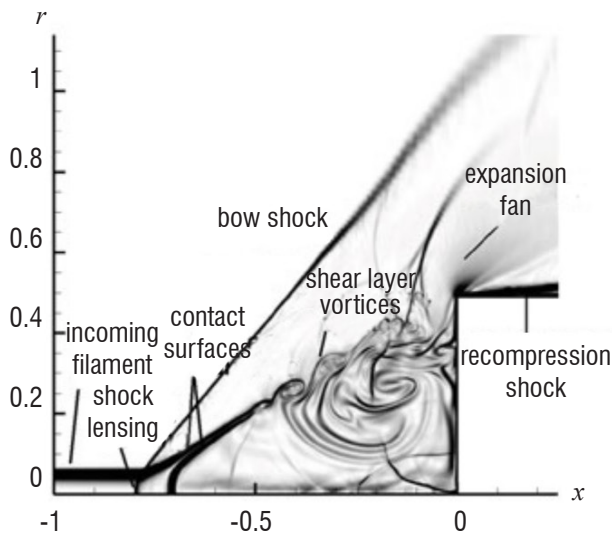


Figure 24 – $L/D=1$ (infinitely long) filament [2]

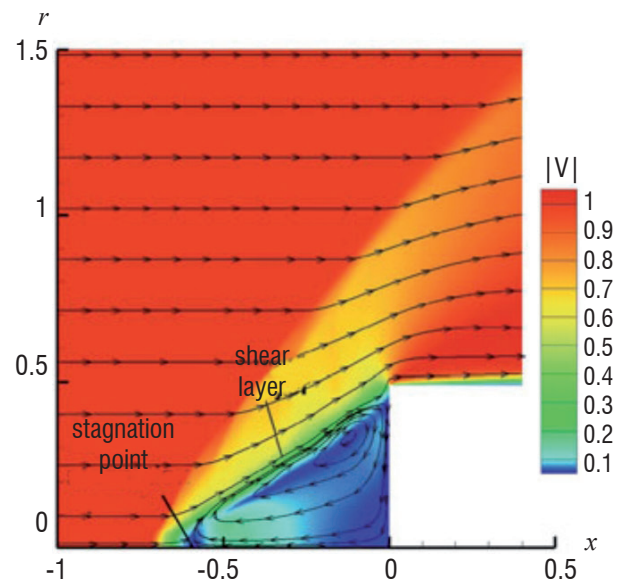
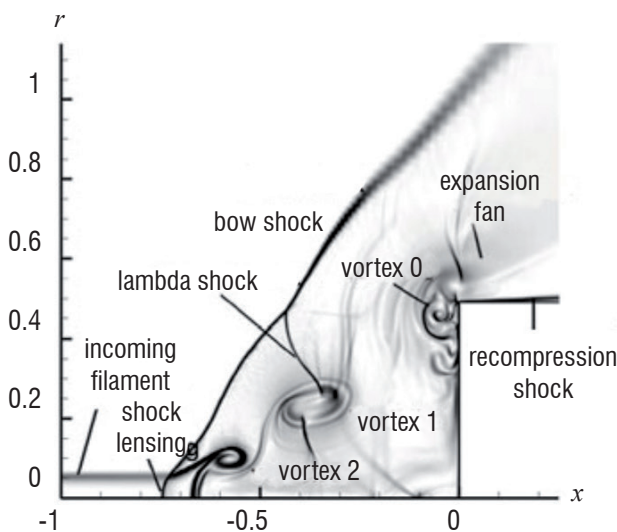


Figure 25 – $L/D=4/3$ filament [2]

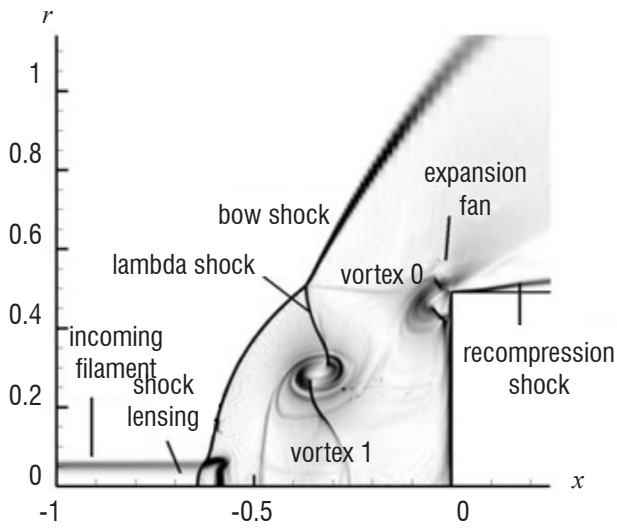


Figure 26 – $L/D=2$ filament [2]

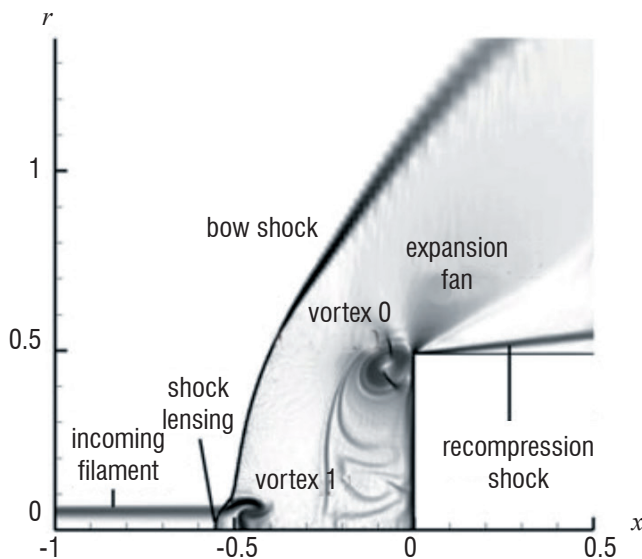
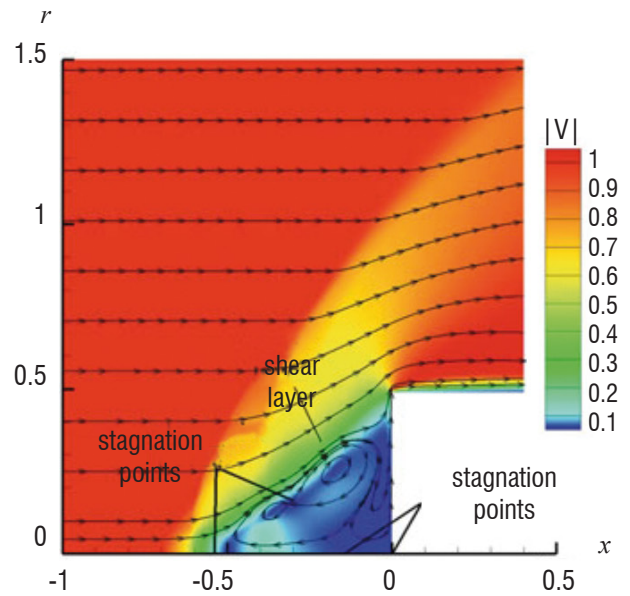
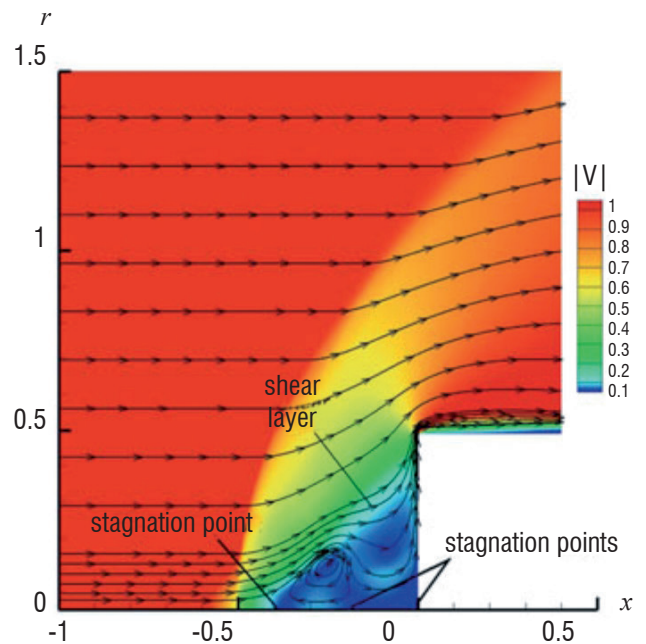


Figure 27 – $L/D=4$ filament [2]



The interaction of the pulsed filaments with the blunt cylinder results in an average reduction in frontal drag at a significant savings in energy. Figure 28 displays the effectiveness ζ defined as the ratio of the average reduction in frontal drag to the baseline (undisturbed flow) drag. Drag reduction up to 40% is observed, with decreasing effectiveness with increasing filament period L/D . Figure 29 shows the efficiency defined as the ratio of the average energy saved due to frontal drag reduction to the energy required to generate the filaments. Efficiencies of a factor of 100 are obtained. Although the filament temperatures are higher than the ambient freestream temperature, there is no detrimental effect on the surface heat transfer to the cylinder face. Figure 30 presents the ratio of the average heat transfer to the cylinder face due to the interaction of the filaments to the undisturbed heat transfer to the cylinder face. Indeed, the average heat transfer is reduced for $L/D=4/3$ due to the movement of the stagnation point off the cylinder face (figure 25).

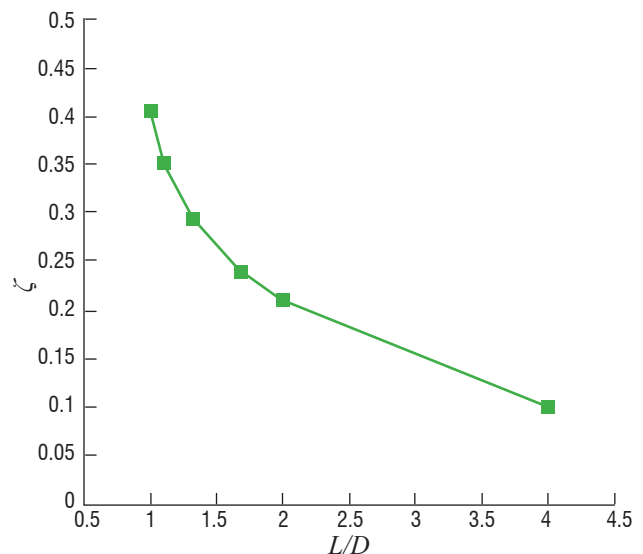


Figure 28 – Effectiveness vs L/D [2]

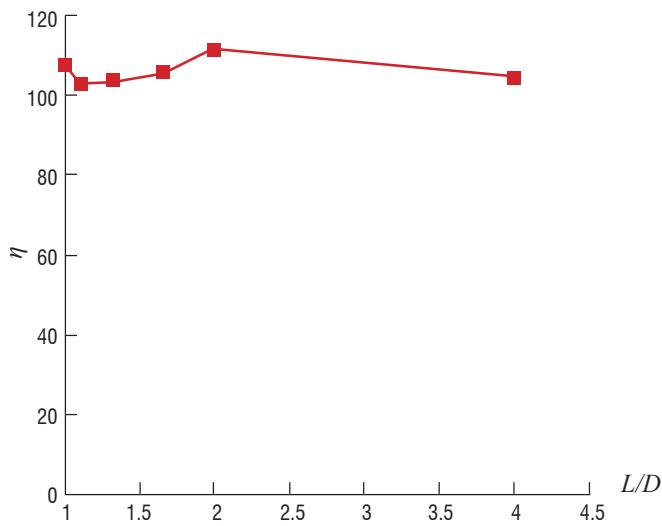


Figure 29 – Efficiency vs L/D [2]

Azarova, Knight and Kolesnichenko

Azarova *et al.* [3] performed a series of simulations of the interaction of an infinitely long heated filament with a blunt cylinder similar to figure 23. The infinitely long filament models repetitive microwave discharges and is characterized by the density ratio ρ_f/ρ_∞ and diameter d/D where D is the cylinder diameter. The flow conditions are indicated in table 4. The computations were based on the compressible Euler equations.

Quantity	Symbol	Value
Mach number	M_∞	1.89 and 3
Density ratio	α	0.4 to 0.6
Filament diameter	d/D	0.1, 0.125, 0.25
Filament length	l/D	∞

Table 4 – Flow Parameters

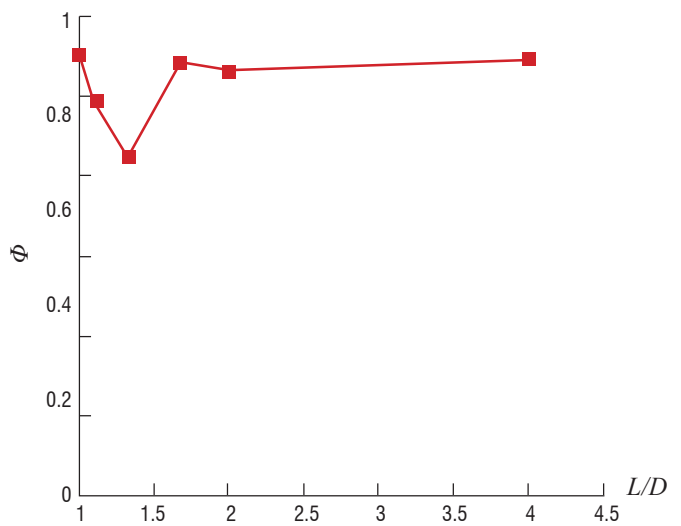


Figure 30 – Heat transfer parameter vs L/D [2]

Contours of density contours at specific times are shown in figure 31 for $M_\infty=1.89$, $\alpha=0.5$ and $d/D=0.25$. A Richtmyer-Meshkov instability develops due to the intersection of the heated filament with the blunt body shock (figure 31 (a)) forming a single toroidal vortex (V) and lambda shock (P). The bow shock (BS) moves upstream due to the lower Mach number in the filament ($M_f=\sqrt{\alpha} M_\infty=1.34$). As the filament penetrates to the cylinder, a Kelvin-Helmholtz (KH) instability develops due to the slip line (contact discontinuity) generated at the intersection of the boundary of the filament with the blunt body shock. Thereafter a spatially periodic train of vortices forms along the contact discontinuity due to the Kelvin-Helmholtz instability.

A periodic instability forms subsequent to the initial transient. Figure 32(a) shows the location of the blunt body shock on the cylinder axis $X_w(t)$ (note the absolute scale in figure 31 (a) and the location of the blunt body shock (BS) on the cylinder axis). The mean shock standoff distance on the centerline due to the filament $\Delta_f=1.6 \Delta$ where Δ is the shock standoff distance in undisturbed flow. The amplitude of oscillation of the shock standoff distance is approximately 0.16Δ . The location $X_{T_{max}}$ and magnitude of the maximum static temperature T_{max} are also shown. The periodic behavior of the drag force is also evident (figure 32(b)).

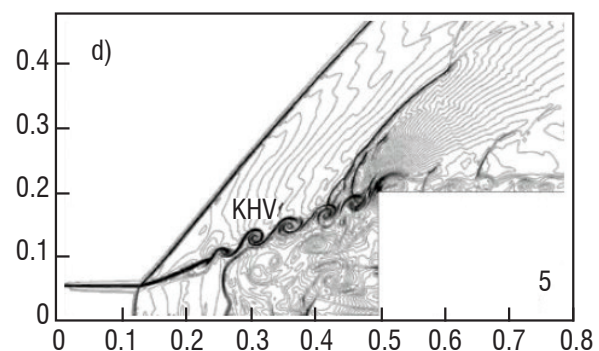
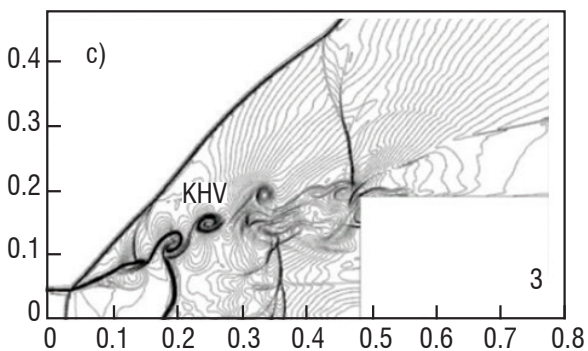
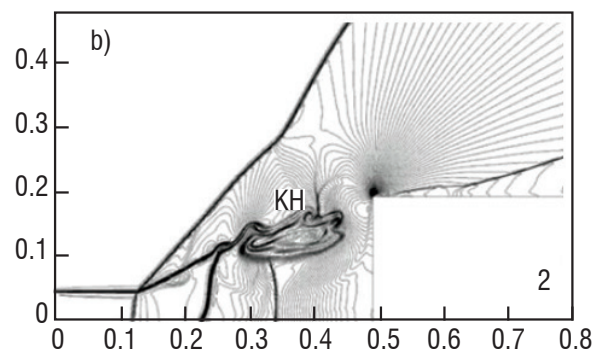
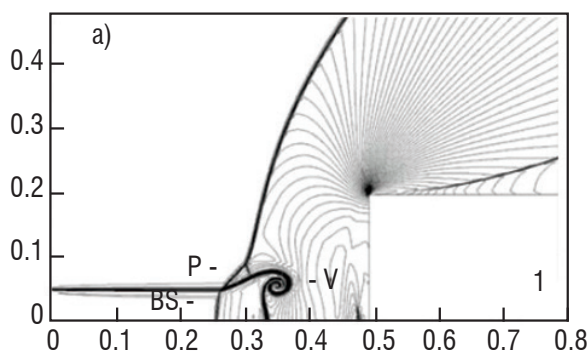


Figure 31 – Density contours for $M_\infty=1.89$, $\alpha=0.5$, $d/D=0.25$ [3]

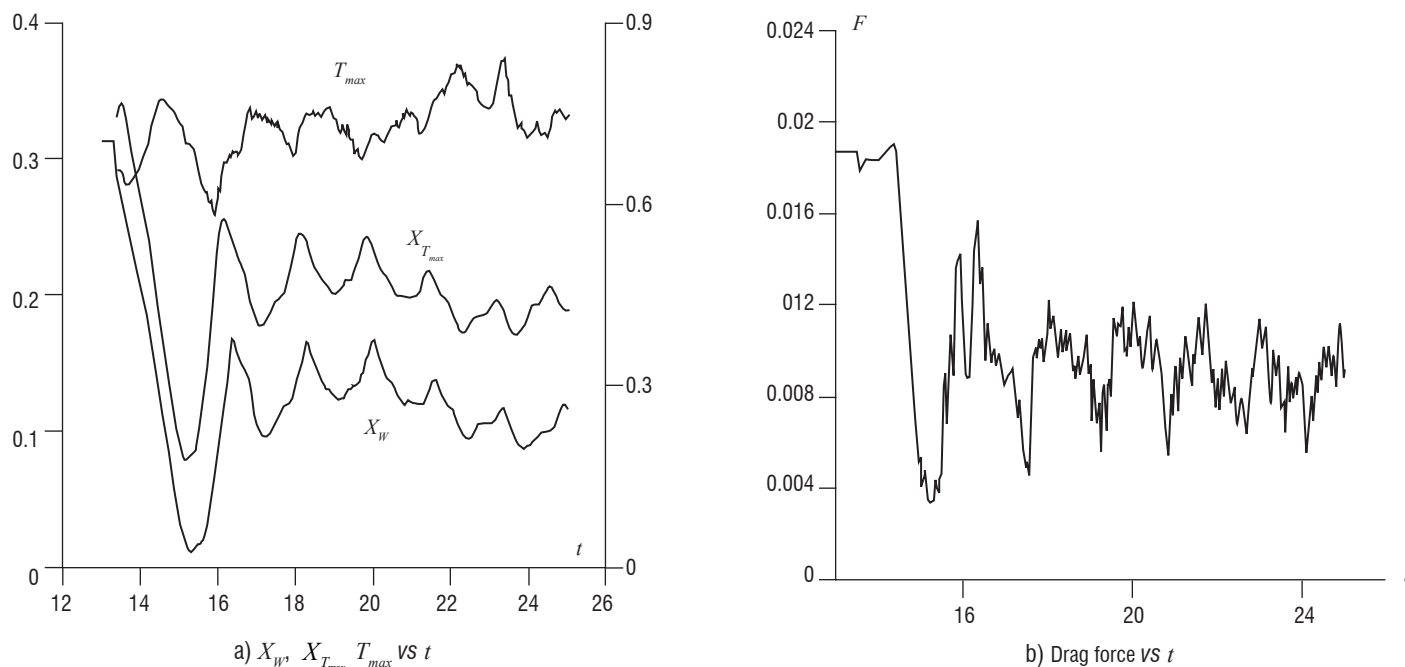


Figure 32 – Instabilities at $M_\infty=1.89$, $\alpha=0.5$, $d/D=0.25$ [3]

Conclusions

Energy deposition by pulsed laser and microwave discharge is an important area of research for supersonic flow control. Experimental and computational studies have demonstrated the capability for significant reduction in drag on simple geometries. The energy required for the discharge is typically quite small compared to the energy saved through drag reduction.

Future research can focus on applications of pulsed laser and microwave discharge for flight control of supersonic and hypersonic vehicles. The capability to substantially modify the wave structure surrounding a vehicle by energy deposition enables new approaches to flight control. Rather than the conventional method of deforming the vehicle shape (*e.g.*, by means of aileron, elevator, rudder, etc.), the instantaneous pressure distribution on the vehicle can be changed by modifying the wave structure through interaction of pulsed electromagnetic discharges ■

References

- [1] R. ADELGREN, H. YAN, G. ELLIOTT, D. KNIGHT, T. BEUTNER and A. ZHELTOVODOV – *Control of Edney IV Interaction by Pulsed Laser Energy Deposition*. AIAA Journal, 43(2):256–269, 2005.
- [2] K. ANDERSON and D. KNIGHT – *Interaction of Heated Filaments with a Blunt Cylinder in Supersonic Flow*. Shock Waves, 21:149–161, 2011.
- [3] O. AZAROVA, D. KNIGHT and Y. KOLESNICHENKO – *Pulsating Stochastic Flows Accompanying Microwave Filament/Supersonic Shock Layer Interaction*. Shock Waves, 21:439–450, 2011.
- [4] E. DAMON and R. TOMLINSON – *Observation of Ionization of Gases by a Ruby Laser*. Applied Optics, 2(5):546–547, May 1963.
- [5] B. EDNEY – *Anomalous Heat Transfer and Pressure Distributions on Blunt Bodies at Hypersonic Speeds in the Presence of an Impinging Shock*. FAA Report 115, Aeronautical Research Institute of Sweden, 1968.
- [6] R. EXTON, R. BALLA, B. SHIRINZADEH, G. BRAUCHMANN, G. HERRING, J. FUGITT, C. LAZARD and K. KHODATAEV – *On-board Projection of a Microwave Plasma Upstream of a Mach 6 Bow Shock*. Physics of Plasmas, 8(11):5013–5017, 2001.
- [7] V. FOMIN, P. TRETYAKOV and J.-P. TARAN – *Flow Control Using Various Plasma and Aerodynamic Approaches (Short Review)*. Aerospace Science and Technology, 8:411–421, 2004.
- [8] A. FRIDMAN and L. KENNEDY – *Plasma Physics and Engineering*. Taylor & Francis, New York, 2004.
- [9] N. GLUMAC, G. ELLIOTT and M. BOGUSZKO – *Temporal and Spatial Evolution of the Thermal Structure of a Laser Spark in Air*. AIAA Journal, 43(9):1984–1993, September 2005.
- [10] A. GOLD and B. BEBB. *Theory of Multiphoton Ionization*. Physical Review Letters, 14(3):60–63, 1965.
- [11] R. KANDALA and G. CANDLER – *Numerical Studies of Laser-Induced Energy Deposition for Supersonic Flow Control*. AIAA Journal, 42(11):2266–2275, 2004.
- [12] D. KNIGHT – *Survey of Aerodynamic Drag Reduction at High Speed by Energy Deposition*. Journal of Propulsion and Power, 24(6):1153–1167, November–December 2008.
- [13] Y. KOLESNICHENKO – *Microwave Discharge in Free Space*. Thematic Workshop on Fundamentals of Aerodynamic Flow and Combustion Control by Plasmas, Villa Monastero, Varenna, Italy, EUCASS Aerospace Thematic Workshop (ATW) on Plasmas, May 2007.
- [14] Y. KOLESNICHENKO, V. BROVKIN, O. AZAROVA, V. GRUDNITSKY, V. LASHKOV and I. MASHEK – *Microwave Energy Deposition for Aerodynamic Application*. AIAA Paper 2003-0361, American Institute of Aeronautics and Astronautics, January 2003.
- [15] Y. KOLESNICHENKO, V. BROVKIN, S. LEONOV, A. KRYLOV, V. LASHKOV, I. MASHEK, A. GORYNYA and M. RYVKIN. *Investigation of AD-Body Interaction with Microwave Discharge Region in Supersonic Flows*. AIAA Paper 2001-0345, American Institute of Aeronautics and Astronautics, January 2001.

- [16] I. LASHKOV, I. MASHEK, Y. ANISIMOV, V. IVANOV, Y. KOLESNICHENKO, M. RYVKIN and A. GORYNYA. *Gas Dynamic Effect of Microwave Discharge on Supersonic Cone-Shaped Bodies*. AIAA Paper 2004-0671, American Institute of Aeronautics and Astronautics, January 2004.
- [17] Y. LEBEDEV (editor) – *IV International Workshop on Microwave Discharges: Fundamentals and Applications*. United Physical Society of the Russian Federation, Yanus-K., ISBN 5-8037-0066-5, Moscow, 2001.
- [18] Y. LEBEDEV (editor) – *VI International Workshop on Microwave Discharges: Fundamentals and Applications*. United Physical Society of the Russian Federation, Yanus-K. ISBN 5-8037-0343-5, Moscow, 2006.
- [19] A. MACDONALD. *Microwave Breakdown in Gases*. Wiley Series in Plasma Physics. John Wiley & Sons, New York, NY, 1966.
- [20] P. MAKER, R. TERHUNE and C. SAVAGE – *Optical Third Harmonic Generation*. Proceedings of the 3rd International Conference on Quantum Electronics, Columbia University Press, P. GRIVET and N. BLOEMBERGEN (editors), New York, 1963.
- [21] R. MEYERAND and A. HAUGHT – *Gas Breakdown at Optical Frequencies*. Physical Review Letters, 11(9):401–403, 1963.
- [22] R. MEYERAND and A. HAUGHT – *Optical-Energy Absorption and High-Density Plasma Production*. Physical Review Letters, 13(1):7–9, 1964.
- [23] R. MINCK – *Optical Frequency Electrical Discharges in Gases*. Journal of Applied Physics, 35(1):252–254, January 1964.
- [24] C. C. MORGAN – *Laser-Induced Breakdown of Gases*. Rep. Prog. Phys., 38:621–665, 1975.
- [25] G. OSTROVSKAYA and A. ZAIDEL – *Laser Spark in Gases*. Soviet Physics Uspekhi, 16(6):834–855, 1974.
- [26] Y. RAIZER – *Heating of a Gas by a Powerful Light Pulse*. Soviet Physics JETP, 21(5):1009–1017, 1965.
- [27] Y. RAIZER – *Breakdown and Heating of Gases Under the Influence of a Laser Beam*. Soviet Physics Uspekhi, 8(5):650–673, 1966.
- [28] E. SCHÜLEIN, A. ZHELTOVODOV, E. PIMONOV and M. LOGINOV – *Experimental and Numerical Modeling of the Bow Shock Interaction with Pulse-Heated Air Bubbles*. International Journal of Aerospace Innovations, 2(3):165–187, 2010.
- [29] P. TRETYAKOV, A. GARANIN, V. KRAYNEV, A. TUPIKIN and V. YAKOVLEV – *Investigation of Local Laser Energy Release Influence on Supersonic Flow by Methods of Aerophysical Experiments*. International Conference on Methods of Aerophysical Research, Novosibirsk, Russia, 1996.
- [30] A. ZHELTOVODOV – *Development of the Studies on Energy Deposition for Application to the Problems of Supersonic Aerodynamics*. Preprint 10-2002, Institute of Theoretical and Applied Mechanics, Novosibirsk, Russia, 2002.

Acronym

MW (Microwave)

AUTHOR



Doyle Knight received his PhD in Aeronautics from the California Institute of Technology in 1974. Following two years service in the United States Air Force as an Aeronautical Engineer, and one year Postdoctoral Fellowship in Applied Mathematics at the California Institute of Technology, he joined the faculty of the Department of Mechanical and Aerospace

Engineering at Rutgers – The State University of New Jersey. He is Distinguished Professor of Aerospace and Mechanical Engineering. His research interests include gas dynamics and design optimization. His research in gas dynamics includes shock wave boundary layer interaction, incipient separation on pitching airfoils, turbulence model development, high speed inlet unstart and effects of unsteady energy deposition in supersonic flows. His research activity in design optimization focuses on the application of computational fluid dynamics to the automated optimal design of high speed air vehicles.

P.-Q. Elias
(ONERA)

E-mail: Paul-Quentin.Elias@onera.fr

DOI : 10.12762/2015.AL10-03

Numerical Simulations on the Effect and Efficiency of Long Linear Energy Deposition Ahead of a Supersonic Blunt Body: Toward a Laser Spike

The effect of single or repetitive linear energy depositions in front of a supersonic blunt body is computed using the CEDRE flow solver. The CFD Code models the effect of a laser-induced energy deposition, as obtained for example using the long filaments created by a femtosecond laser. Single energy depositions show that significant transient drag reductions are obtained, due to the interaction of the heated core, created by the energy release, with the bow shock. When the deposition is repeated, cumulative effects are important and quasi-steady or unsteady flow regimes are obtained, depending on the power and repetition frequency. This behavior is similar to that obtained with supersonic spiked blunt bodies, acting like a laser spike. This system can lead to 15%-20% fuel savings, depending on the energy deposition efficiency.

Introduction

There has been a substantial amount of experimental and theoretical work devoted to the use of plasma-based devices for flow control [1]–[4]. Plasmas mainly act on the flow through two channels: gas heating and volume force in the region where the plasma is not quasi-neutral or where a magnetic field exists. The location of the forcing action of the plasma depends on its generation mechanism. There are two main ways of creating the plasma. First, it can be generated by electrodes exposed to the flow, or partly exposed (with dielectric barriers). In this case, the generated plasma is most of the time confined in the vicinity of the body; this means that the forcing is close to the body surface. Second, the plasma can be generated with an intense electromagnetic radiation focused in the flow. When the radiation is intense enough, gas breakdown occurs and a plasma is generated. In this case, the generation can be near a surface, but also in the volume of the flow and, more interestingly, possibly upstream of the body. This plasma couples with the incoming radiation and heats up, enabling the deposition of energy in the flow ahead of the body.

This possibility has led several authors to study the use of laser-induced or microwave-induced energy deposition upstream of a supersonic body for flow control. For example, it was shown experimentally that laser-induced plasma created upstream of a supersonic body could trigger the transition from a regular to a Mach reflection, or temporarily decrease the wall heat flux in an Edney type IV shock interaction [5] [6]. The use of laser energy deposition has also been

considered to reduce the supersonic drag of blunt bodies. Indeed, it is known that supersonic blunt bodies can have their wave drag significantly decreased when using mechanical spike or counter-flowing jets. Using repetitively pulsed laser sources, several authors have shown the possibility of decreasing the drag of blunt bodies with repetitive point energy deposition [7] [8]. For example, Sakai et al have studied the effect of pulsed laser energy deposition upstream of a blunt body. They have shown numerically and experimentally that there is a 25% drag reduction, for a repetition frequency of $f=60$ kHz, in front of a cylinder at $M=2$ [9] [10].

These works have demonstrated the ability of pulsed repetitive point energy deposition to significantly reduce the drag. However, a key point for this reduction to be applicable is the overall efficiency. This efficiency quantifies the fuel savings taking into account the whole drag reduction system, with the energy conversion efficiencies of the various sub-systems. These sub-systems include the power generator, the laser and the energy coupling of the plasma. In order to assess the efficiency of the energy deposition, some authors [11] use the aerodynamic efficiency η_{ae} , defined as:

$$\eta_{ae} = \frac{U_{\infty} \Delta D}{fE} \quad (1)$$

Where U_{∞} is the upstream velocity of the flow, ΔD is the drag reduction (in Newtons), f is the repetition frequency of the laser and E is the laser energy per pulse. Due to the fact that the efficiencies of the

laser and the energy conversion from the engine can be quite low, the value of η_{ae} needs to be as high as possible to ensure that the cost of the drag reduction system does not outweigh its benefit.

A strategy to increase this efficiency is to try to change the shape of the energy deposition. Indeed, point energy deposition requires a high repetition frequency to reach a steady state. If the deposition were elongated, lower repetition frequencies might be needed and η_{ae} would increase. This idea is guided by the recent progress of femtosecond lasers, which are known to create thin ionized channels [12] [13]. These channels can be used to guide an electric discharge and there is currently an ongoing research effort to couple energy to this ionized channel using various mechanisms: more powerful nanosecond lasers [15], pulsed discharges or microwave excitation [16].

This prospect of laser-assisted linear energy deposition has led several authors to numerically address their use for drag reduction. Kremer et al have modeled linear energy depositions on the axis of supersonic cones and have shown that efficiencies between 5 and 65 can be obtained, depending on the Mach number and the shape of the energy deposition [17]. As a rule, the higher the Mach number is, the larger η_{ae} is. Sutton has analytically examined the effect of cylindrical blast waves generated upstream of fast-burning rockets and has shown that for large enough Mach numbers, long pulses can lead to fuel savings [18].

The previous studies have shown that an efficient drag reduction is feasible using a linear energy deposition upstream of the body. However, these studies focused on a single pulse event and therefore have to extrapolate to conclude on the steady state operation of the system. Reaching a steady state is important, in particular when analyzing the cumulative effect of repetitive energy deposition. In addition, another important point to assess the efficiency of the whole system is linked to the heating processes in the plasma. Indeed, only a fraction of the deposited energy is effectively used to produce the blast wave and the hot gas kernel. This fraction is driven by various loss processes in the plasma. Therefore, as in the above-mentioned works, the perfect gas assumption might overestimate the efficiency of the laser-induced drag reduction.

As a consequence, this paper focuses on the modeling of long linear energy deposition in front of a supersonic blunt body and on the corresponding numerical simulations. The two limitations discussed above are specifically addressed, first by considering a self-consistent modeling of the repetitive energy addition and, second, by using real gas properties for the flow. In order to gain insight on the applicability of the laser line energy deposition, the test model considered will have dimensions and flight conditions consistent with what can be achieved in a supersonic wind tunnel.

Virtual Spike modeling

Local Thermodynamic Equilibrium hypothesis

The modeling of the heat deposition by the laser requires the way in which the input laser energy is transferred to the gas to be considered. It will be assumed here that the energy is supplied by a filamenting femtosecond laser, combined with a secondary energy source (such as a combined nanosecond laser, or a micro-wave source).

The main energy transfers between the energy modes of the gas are shown in Figure 1. In a simplistic form, the energy transfers are as follows. During the laser breakdown and subsequent plasma heating, the power is transferred to the electrons, whose temperature increases. This rise in temperature leads to inelastic collisions, creating excited, dissociated or ionized molecules. The heavier species in the plasma are then mainly heated by inelastic collisions with the excited species. This increase in internal energy induces pressure gradients that lead to a macroscopic transfer of mass and momentum in the fluid and builds up macroscopic kinetic energy. In principle, a self-consistent modeling of a laser-induced energy deposition should take into account the breakdown phase and the following additional energy input; the various loss terms should be accounted for, such as the plasma chemistry, the radiative losses, the diffusion losses, etc. [19][20][21][22]. This approach is beyond the scope of this study. In previous works, the incoming flow was assumed to behave as a perfect gas. In this situation, the transfer between the potential energy and the microscopic kinetic energy modes is frozen. All of the energy input is used to increase the temperature. Consequently, in order to avoid unphysical temperatures, only a fraction of the energy is used [8]. This fraction is poorly known: it depends strongly on the plasma processes during the breakdown and the energy deposition.

On the contrary, another solution is to assume that the transfers between the energy modes (potential and microscopic) are so fast that the plasma created by the laser reaches thermodynamic equilibrium. In this case, the input energy is spread over all of the energy modes. This hypothesis is interesting because it gives the lower bound for the plasma temperature. Being a kind of worst case scenario, it is useful to address the question of the efficiency of the laser-induced drag reduction. It also enables a simpler modeling, since only a single fluid modeling of the plasma is needed.

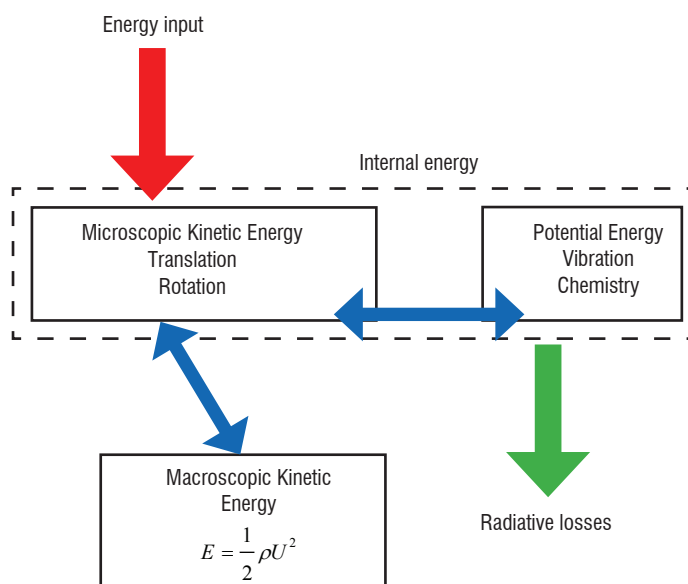


Figure 1 - Energy modes (rectangles) and energy transfers (arrows) in a gas with an external heating source Air properties

Air properties

The properties of air at local thermodynamic equilibrium are obtained from [23]. This tabulation gives these properties for a temperature up to 50,000 K and for a wide pressure range. For the purpose of our analysis, the following properties are needed: the gas molar enthalpy $h(T,p)$ and molar entropy $s(T,p)$, its heat capacity at constant pressure $c_p(T,p)$ and its molar mass $M(T,p)$. Note that the molar mass decreases at higher temperatures, because of the dissociation of N_2 and O_2 . Finally,

the transport coefficients are also needed (viscosity, conductivity). As an example, in Figure 2, the heat capacity and the thermal conductivity of air at local thermodynamic equilibrium (LTE) are given. The heat capacity shows several peaks that correspond to the dissociation of the diatomic molecules in the mixture.

Modeling of the power deposition

The laser energy deposition is modeled through a source term σ in the energy equation. Assuming that the flow is described by the Navier-Stokes equations, using temperature and pressure dependent thermophysical coefficients:

$$\begin{aligned} \frac{\partial \rho}{\partial t} + \nabla(\rho \mathbf{u}) &= 0 \\ \frac{\partial \rho \mathbf{u}}{\partial t} + \nabla(\rho \mathbf{u} \mathbf{u}) &= -\nabla p + \nabla \bar{\tau} \\ \frac{\partial \rho \left(e + \frac{1}{2} u^2 \right)}{\partial t} + \nabla \left(\rho \mathbf{u} \left(e + \frac{1}{2} u^2 \right) \right) &= -\nabla \mathbf{q} + \nabla \left(\bar{\tau} \mathbf{u} \right) \\ &\quad - \nabla(p \mathbf{u}) + \sigma \end{aligned} \quad (2)$$

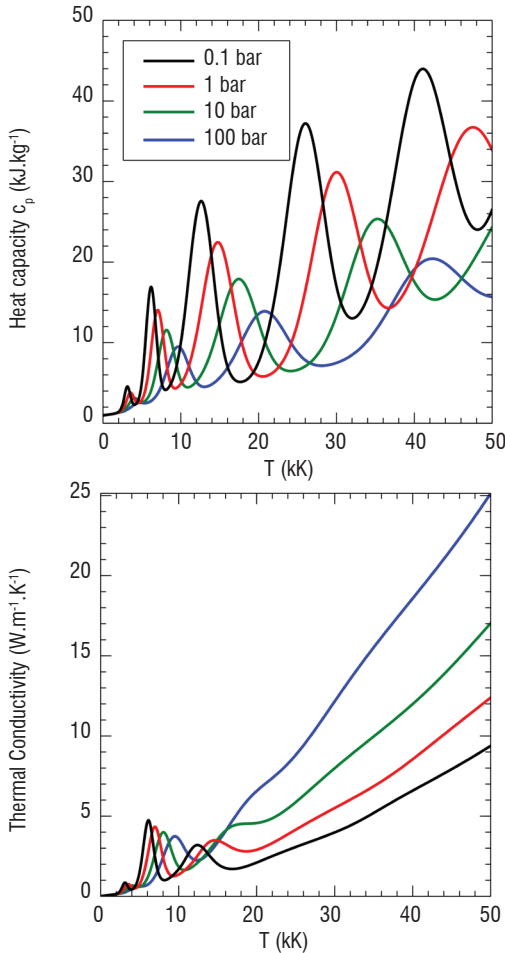


Figure 2 - Heat capacity and thermal conductivity of LTE air, for different pressures

The source term can be described as a time and space dependent function:

$$\sigma(r, z, t) = E f(r, z) g(t) \quad (3)$$

Where E is the total pulse energy, and f and g are the space and time modulation. In this study, the energy is deposited during a period of length T , in a cylinder of radius r and length L

$$g(t) = \begin{cases} \frac{1}{T} & \text{if } t \in [0, T] \\ 0 & \text{otherwise} \end{cases} \quad (4)$$

$$f(y, z) = \begin{cases} \frac{1}{\pi r^2 L} & \text{if } y \in [0, r] \text{ and } z \in [-L + z_0, z_0] \\ 0 & \text{otherwise} \end{cases} \quad (5)$$

During the energy deposition phase, inside the cylinder, the volumetric power source is $\sigma = \frac{E}{T} \frac{1}{\pi r^2 L}$.

Numerical methods

The computations in this study are performed with the CEDRE CFD code, developed at Onera [24]–[26]. The code is a multiphysics tool, including the CHARME module, a finite volume gas dynamics solver on polyhedral meshes.

The following methodology is used for this study. First, the steady-state reference flow without energy deposition is sought, using a local time step. Once the code converges to the steady solution, the heat deposition is activated and the flow time evolution is tracked using an implicit two-step Runge Kutta algorithm. For each step, a 2nd order space discretization is used; the convective part of the fluxes is computed using the Van Leer method.

The computations are performed on axisymmetric meshes, taking into account the axial symmetry of the problem. Unstructured meshes are used. They are refined close to the body, using structured patches for the boundary layer discretization. The distance to the body wall of the first cell is 4-5 μm . Assuming that the flow conditions behind the bow shock are those obtained behind a plane shock, the viscous distance y^+ of the first cell is $y^+ = 1.2-1.5$. Similarly, the region close to the body axis is refined with structured patches. In the region of the energy deposition, the cell width is 45 μm , while their length is 200 μm . The base mesh has 10^5 cells.

Results

This section presents the results of the computation. First, the test configuration and the reference flow is described. Then the effect of a single laser energy deposition is discussed, including a parametric study on the effect of the deposition duration and length. Finally, the effect of repetitive pulses is discussed.

Test model configuration and reference flow

A schematic diagram of the test model used for the study is shown in Figure 3. The test model is a standard HB-1 model [27]. The freestream conditions, as given in Table 1, reproduce typical wind-tunnel conditions achievable in the ONERA R1Ch wind tunnel.

The laser energy deposition is activated for a period T , in a cylinder of radius R and length L . The cylinder can be located upstream of the bow shock ($dx > 0$), or it can start at the stagnation point ($dx = 0$).

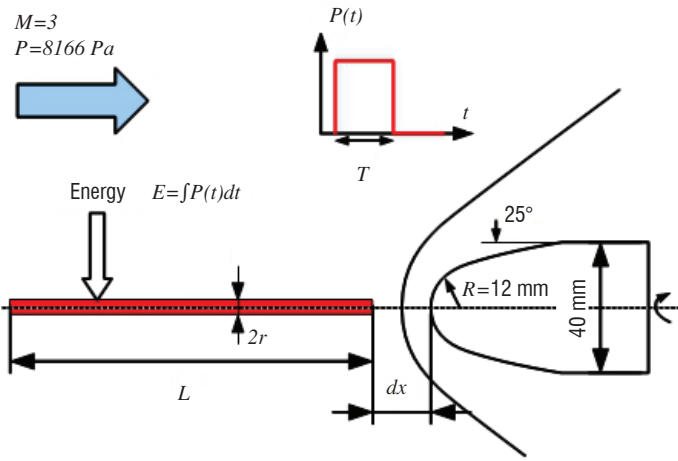


Figure 3 - Shape of the test model and location of the laser energy deposition

The parameters that control the heat deposition are the length of the filament L , its radius r , the filament standoff distance dx , the total energy released E and the duration of the deposition T .

Freestream velocity U_o	652.3 m/s
Freestream temperature T_o	118 K
Freestream pressure p_o	8166 Pa
Unit Reynolds number Re_u	$1.9 \times 10^7 m^{-1}$
Mach number M	3

Table 1 - Flow freestream conditions

Although the unit Reynolds number is above $10^7 m^{-1}$, the computation is performed assuming a laminar flow under the conditions given in Table 1. This is a simplifying assumption of this study, mainly motivated by the fact that the turbulent properties of the high temperature LTE air formed in the heated filament are difficult to model a priori. URANS models, for example, require the knowledge of turbulent coefficients suitable for the chosen turbulence model. These coefficients are quite difficult to assess for the recombining high-temperature plasma considered here. On the other hand, it is important to keep the viscous contribution, since the heated filament interaction will induce large recirculating zone, for which viscous effects are important, even though the flow is assumed to be non-turbulent.

The reference flow is shown in Figure 4. The validity of the converged solution is checked by computing the drag coefficient C_x^o and the shock standoff distance. The drag coefficient and standoff distance are compared to experimental results [28] and a correlation, as given in [29]:

$$\frac{\delta}{R} = 0.143 \exp\left(\frac{3.24}{M_o^2}\right) \quad (6)$$

Case	Drag coefficient C_x^o	Standoff distance δ (mm)
Experiment	0.70 ± 0.02	2.46 (Eq. (5))
Base mesh	0.681	2.59
Refined mesh	0.676	2.64

Table 2 – Drag coefficient and standoff distance comparison

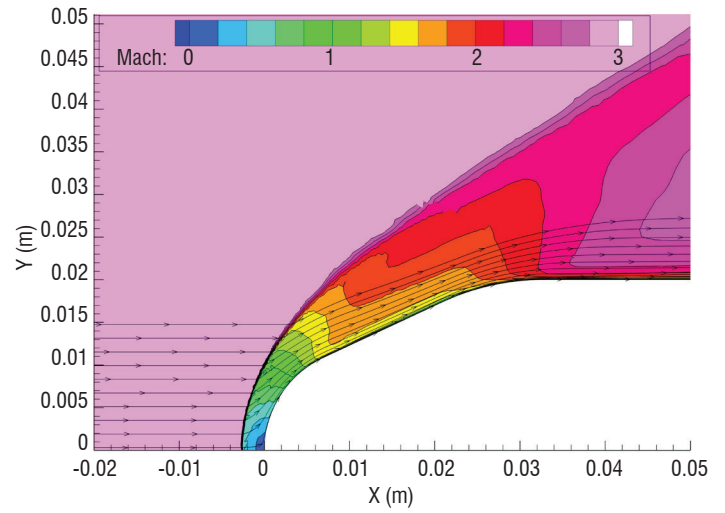


Figure 4 - Steady state flow, Mach number isocontours

Table 2 shows that the computed values for the drag coefficient are within 5% of the measured value. This computed drag falls within the experimental uncertainty of the drag measurement. The 5% discrepancy can be explained as follows: the simulations assume a laminar flow, whereas the experimental reference flow most likely transitions to the turbulent state. Hence, the friction drag is probably underestimated in the computation. The computed standoff distances are within 7% of the standoff obtained from the experimental correlation. Note that the finer mesh (cell dimension divided by two, $4 \cdot 10^5$ cells) does not yield significantly different results (0.8% change in the drag coefficient, 1.9% change in the standoff distance compared to the base mesh), suggesting that mesh convergence is obtained with the base mesh. In the following, the computations will be performed using the base mesh only.

Effect of a single pulse

An overview of the effect of a single pulse is detailed here, considering the following parameters for the energy deposition (Table 3)

Energy E	400 mJ
Deposition duration T	100 ns
Cylinder length L	8R (96 mm)
Cylinder radius r	0.4 mm
Standoff distance dx	0 mm

Table 3 - Energy deposition parameters

For the analysis of a single pulse deposition, the time evolution of the drag shown in Figure 5, Figure 6 and Figure 7 and the pressure isocontours shown in Figure 8 and Figure 9 are considered.

During the deposition stage, the motion of the gas can be neglected, because the convective timescale is much larger than the deposition duration $T \ll r/c_o$ (where c_o is the speed of sound). The equations (2) can be simplified as:

$$\rho = \rho_o, \quad \rho_o \frac{\partial e}{\partial t} = \sigma \quad (7)$$

This means that the gas density remains constant, while the internal energy increases. The energy release induces an increase in the gas pressure at the location of the deposition, while the density remains

nearly constant. This phenomenon creates a baroclinic torque at the location of the shock front, near the symmetry axis. Indeed, the energy release gives rise to a mostly radial pressure gradient, while the density gradient across the shock is axial. The misalignment of the pressure and density profile produces vorticity at the shock front location, such as $(\partial u_r / \partial z) - (\partial u_z / \partial r) < 0$. Since $u_r \approx 0$ close to the axis, this leads to $(\partial u_z / \partial r) < 0$. The flow velocity tends to decrease close to the axis. Additionally, given that the speed of sound in the heated core produced by the energy release is increased significantly, the flow becomes subsonic. This leads to the formation of a large recirculating zone ($t = 50 \mu\text{s}$), where the high pressure gas behind the shock flows upstream like a jet, following the heated core path, in a fashion similar to what is observed with the injection of a counterflowing jet in front of a blunt body [30]. Correlatively, the stagnation pressure decreases. The upstream propagation of the flow corresponds to Phase I in Figure 5, during which the drag decreases nearly linearly. Phase II starts when the counterflowing recirculating bubble reaches the upstream side of the heated core, at $t = 150 \mu\text{s}$. The upstream propagation of the jet ceases and a strong shock appears at its upstream side. During Phase III, the recirculating bubble is pushed downstream by the incoming flow. The bubble now has a toroidal shape, with a heated low pressure core. The drag drop off observed during Phase III, at $t = 375 \mu\text{s}$, is due to the low-pressure core of the vortex impinging on the body wall. This behavior is similar to that observed in [31] with an Euler computation. As the vortex passes along the body, the detached shock reforms in front of the body.

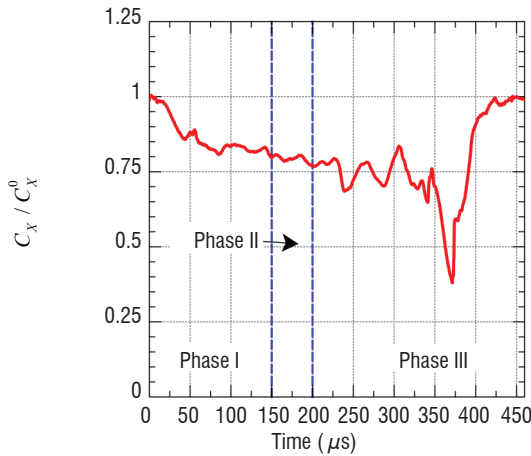
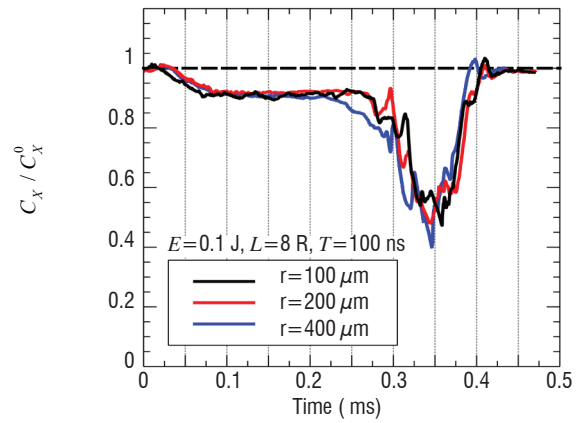


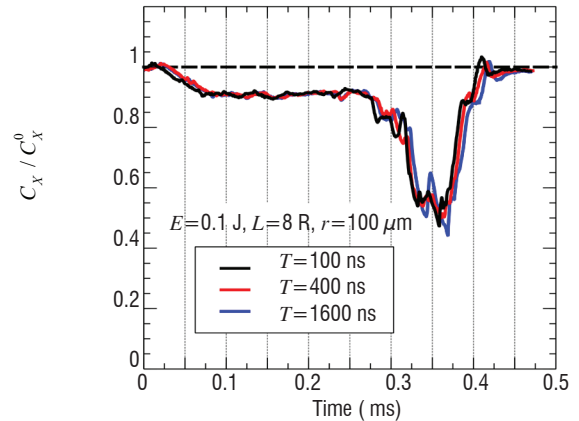
Figure 5 - Time evolution of the reduced drag coefficient. The energy deposition starts at $t=0$. The value for C_x^0 is given in Table 2 (base mesh)

Parametric study

A parametric study is performed by varying the parameters of the energy deposition. The drag evolution is not sensitive to the radius of the deposition (within the range 100-400 μm) and the duration of the deposition (within the range 100-1600 ns), as shown in Figure 6. However, it is significantly modified by the total energy input and the deposition length, as shown in Figure 7. For a constant length L , the cases for 25, 100 and 400 mJ are qualitatively similar. The higher the energy is, the longer Phase II will be, corresponding to the saturation of the counterflowing jet. The case for $E=6.25 \text{ mJ}$ is qualitatively different, because the toroidal vortex formed is small and the pressure drop at its core is insufficient to induce a large decrease in the drag. For a constant energy E and a varying length, the behavior of the drag is qualitatively the same, although the characteristic times are different. The duration of the interaction does not scale with the deposition length L . It appears that the duration of the interaction is mainly driven by the dynamics of the recirculating bubble.

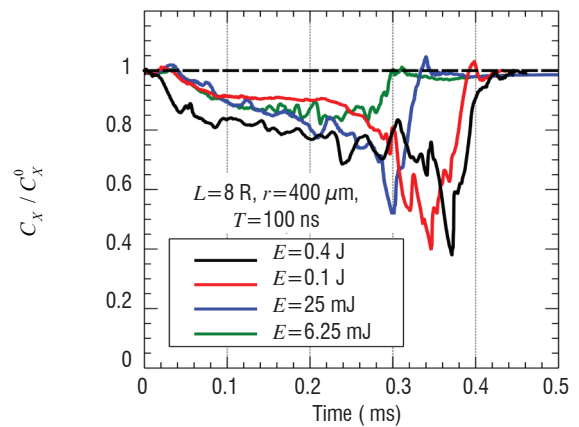


a) Effect of the deposition radius

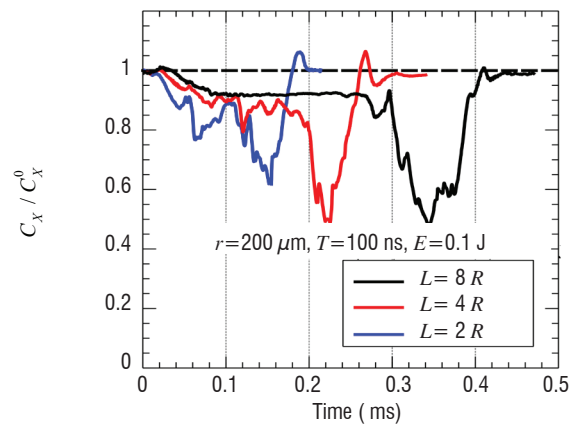


b) Effect of the deposition duration

Figure 6 - Parametric study of the drag evolution: effect of the deposition radius and duration



a) Effect of the total energy



b) Effect of the deposition length

Figure 7 - Parametric study of the drag evolution

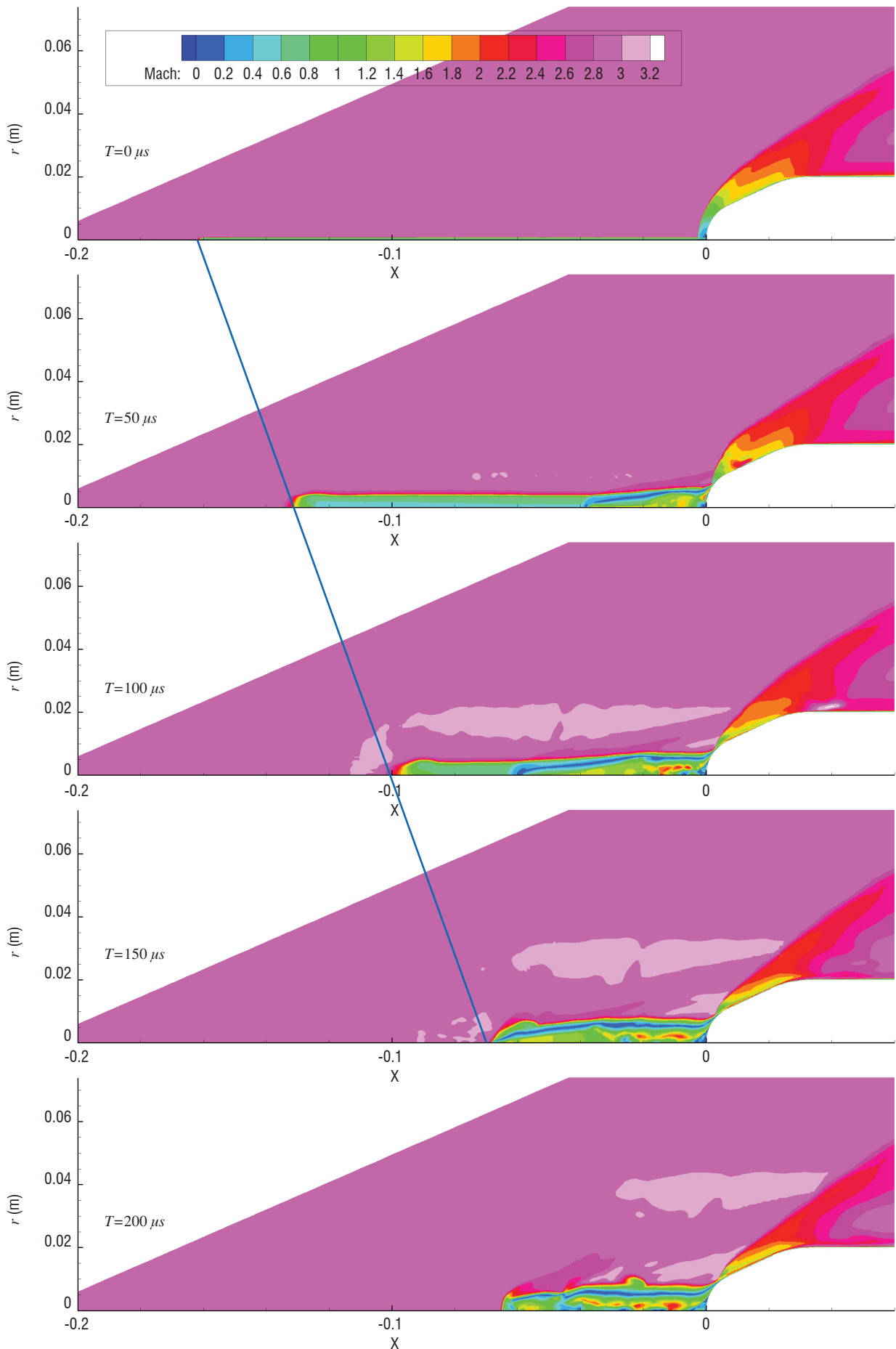


Figure 8 - Pressure contours for a single pulse

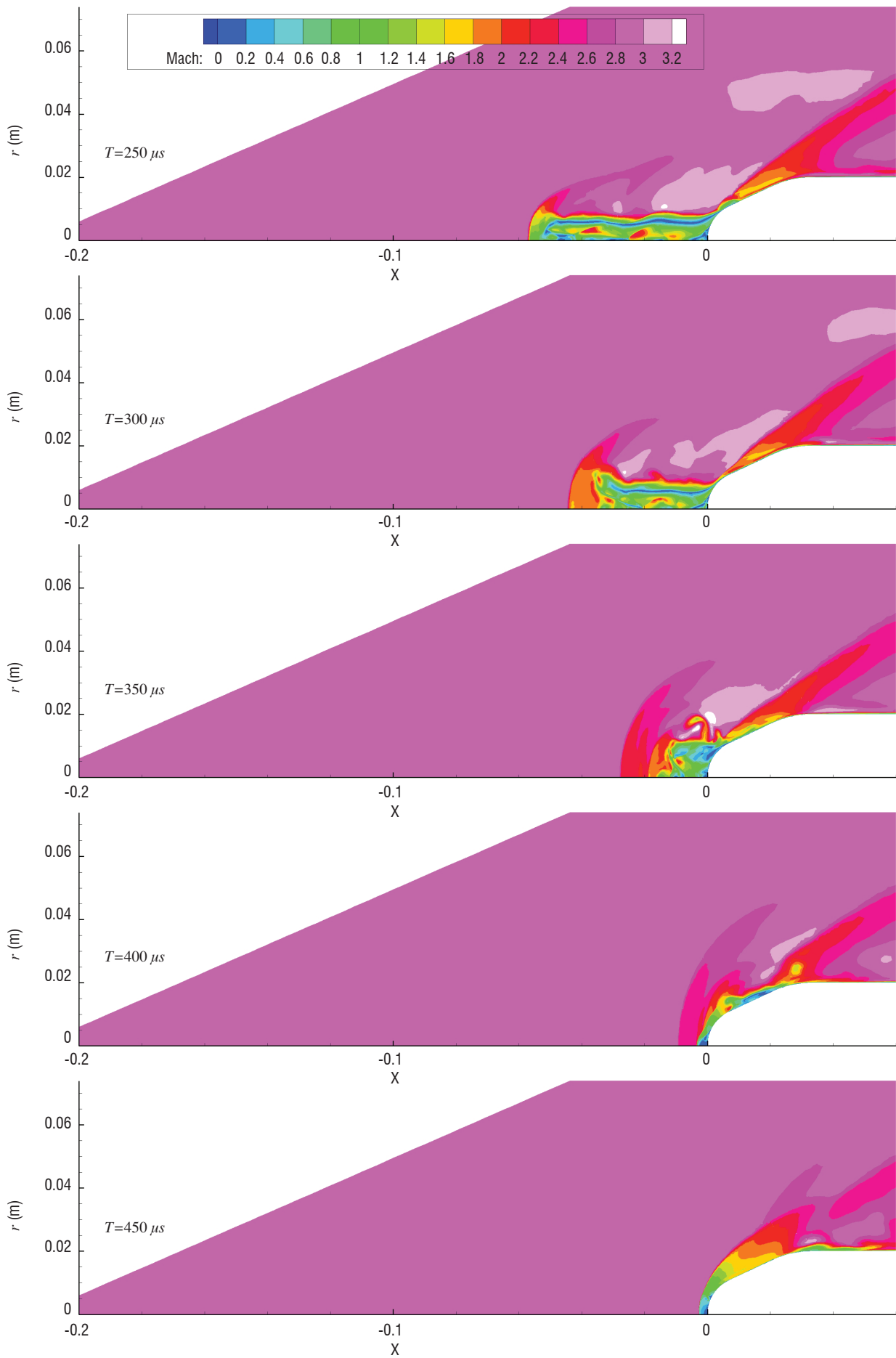


Figure 9 - Pressure contours for a single pulse

Effect of multiple pulses

When examining the effect of repetitive pulsed energy deposition, the above discussion shows that two regimes can be distinguished. In the first regime, the period of the deposition τ is longer or equal to the duration of the filament interaction, as it appears in the time evolution of the drag coefficient. In that case, the mean drag reduction is given by:

$$\langle \Delta \rangle = \frac{1}{\tau} \int_0^{\tau} \left(1 - \frac{C_x(t)}{C_x^0} \right) dt \quad (8)$$

The single pulse cases computed previously are sufficient to assess this regime. In the second regime, τ is shorter than the interaction duration. In this case, it is necessary to take into account the cumulative effect of the repeated energy deposition. The table below summarizes the cases studied for this regime.

Case	Pulse Energy $E(mJ)$	Pulse Period $\tau(ms)$	Mean Power $E/\tau(W)$
1	6.25	0.1	62.5
2	6.25	0.05	125
3	6.25	0.025	250
4	25	0.2	125
5	25	0.025	1000
6	100	0.1	1000
Continuous	X	X	125

Table 4 –Computational cases for repetitive energy deposition. The deposition duration is 100 ns.

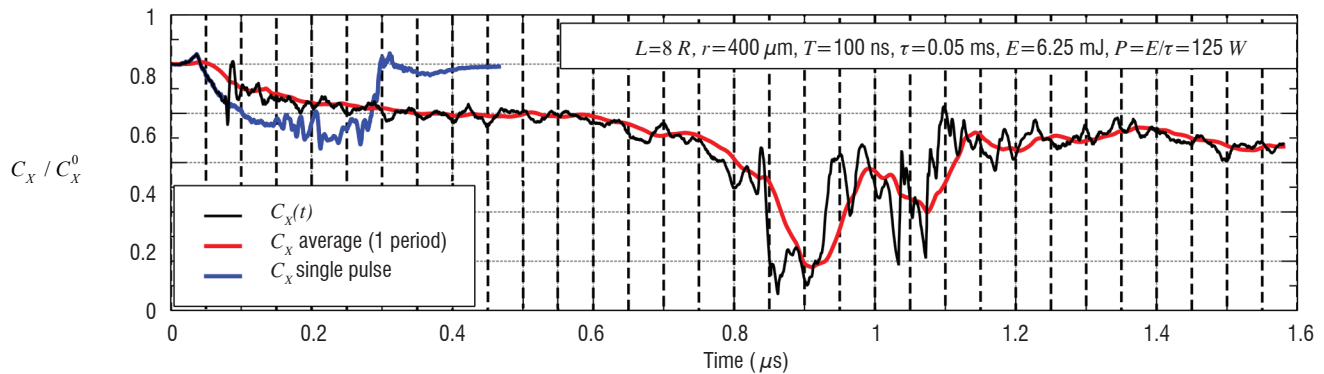


Figure 10 - Case 2, Time evolution of the drag. The dashed line marks the energy deposition time.

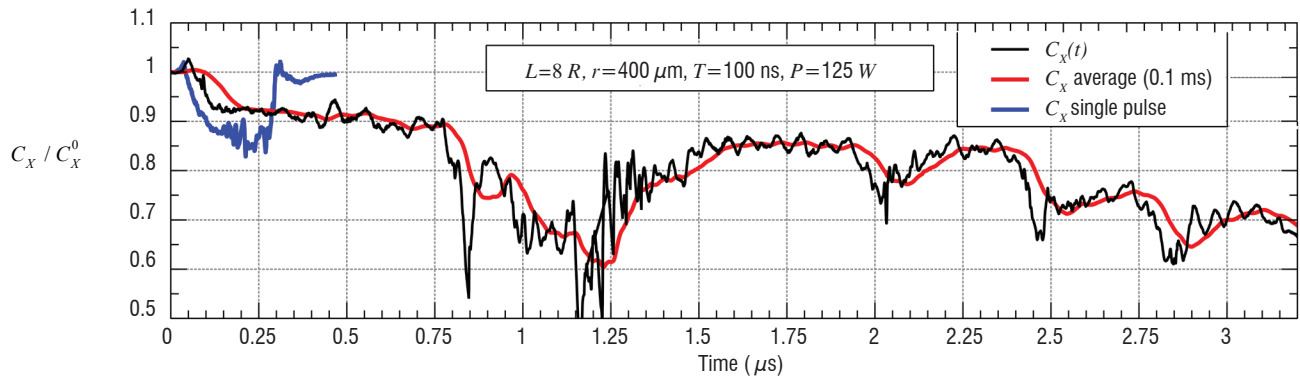


Figure 11 - Continuous deposition, Time evolution of the drag.

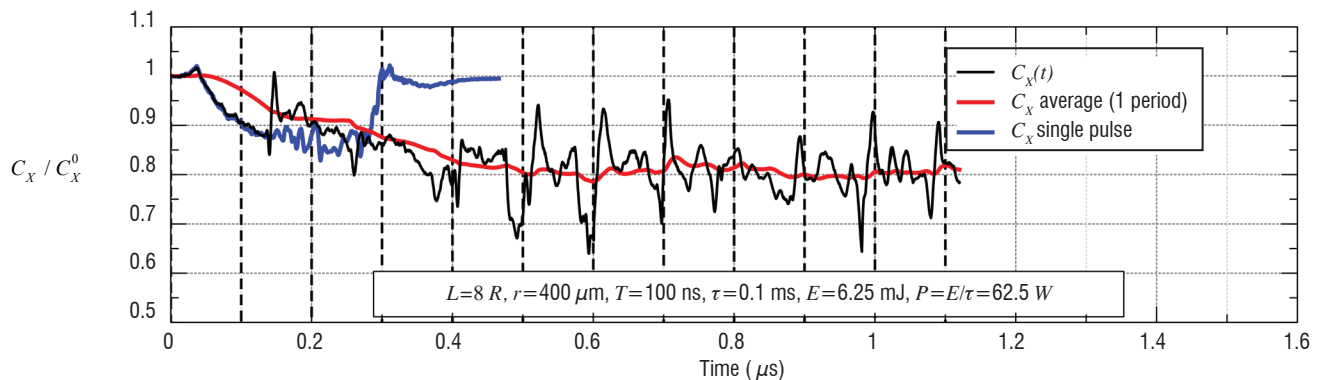
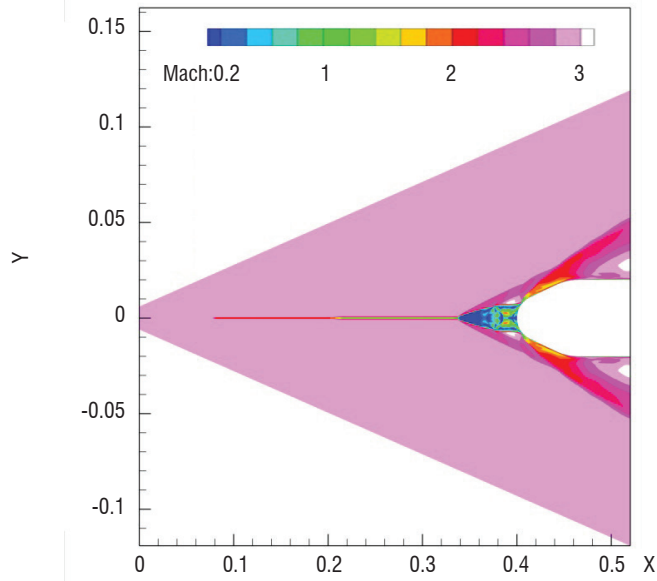


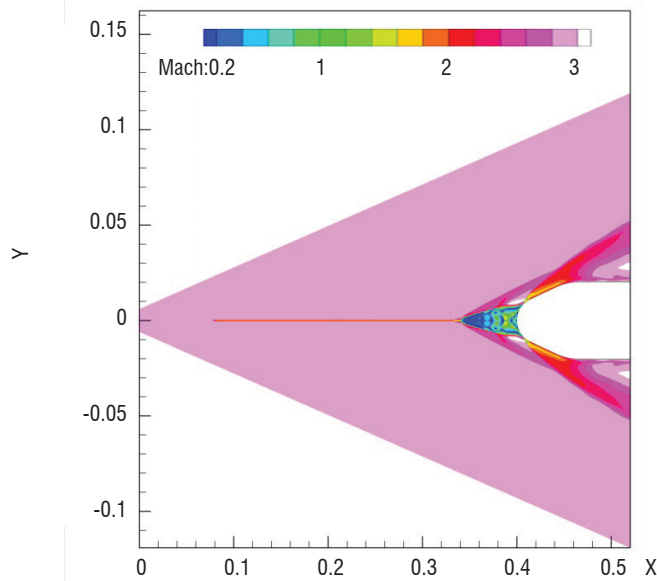
Figure 12 - Case 1, Time evolution of the drag. The dashed line marks the energy deposition time.

For each case, the computation is extended for more than 10 periods, covering at least 1 ms. A first analysis of the results shows that the flow exhibits two behaviors. The first behavior, exemplified in Figure 10, shows a pulsating flow with no stabilization. The drag shows large drop offs, with a seemingly chaotic evolution. This unsteady behavior is also observed in the case of a continuous energy deposition, as shown in Figure 11. In its second behavior, visible in Figure 12, the flow stabilizes and the mean drag reaches a nearly steady value.

Of all of the cases tested in Table 4, Cases 1 and 2 show a stabilization of the drag coefficient, correlated with the formation of a nearly steady recirculating bubble, as shown in Figure 13. The other cases do not reach a quasi-steady state in the time span of the computation. They exhibit a large recirculating bubble, as shown in Figure 14, which collapses repetitively, leading to large fluctuations of the drag coefficient. This situation is similar to what is observed for spiked blunt bodies [32] [33] [34], where pulsating regimes or steady regimes exist, depending of the reduced spike length L/D and also its shape.



(a) Case 1 : $E=6.25$ mJ, $\tau=0.1$ ms, $P=62.5$ W, $t=1.1$ ms



(b) Case 4 : $E=25$ mJ, $\tau=0.2$ ms, $P=125$ W, $t=2.2$ ms

Figure 13 - Mach number, Cases 1 and 4. A nearly steady recirculating bubble extends upstream over a diameter of approximately 0.8.

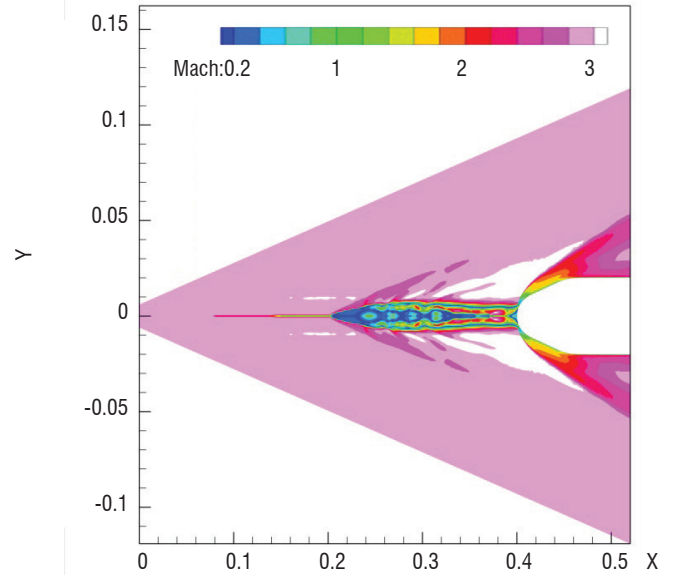


Figure 14 - Mach number, Case 2, $E=6.25$, $\tau=0.05$ ms, $P=125$ W, $t=0.6$ ms. The recirculating bubble extends upstream over approximately 2 diameters, then collapses.

Efficiency

In order to assess the energetic efficiency of a “laser spike” device, it is necessary to define the overall efficiency of the system, which is different from the aerodynamic efficiency η_{ac} defined in Eq. (1). Following [35], the overall efficiency η is defined as the ratio of the fuel mass flow rate with the system to the baseline fuel mass flow rate. Defining the baseline fuel power as $P_0 = \dot{m}_0 h_F$, where \dot{m}_0 is the fuel mass flow rate and h_F is the fuel mass enthalpy, and defining the power with the system active as $P \propto (\dot{m}_0 - \delta \dot{m} - \dot{m}') h_F$, where $\delta \dot{m}$ represents the fuel savings induced by the mean drag reduction and \dot{m}' is the fuel mass flow rate required to power the laser spike system. With this definition, the overall efficiency η of the system is given by

$$\eta = 1 - \langle \Delta \rangle + \varepsilon \frac{\eta_{pe}}{\eta_p} \quad (9)$$

Here, $\eta_{pe} = (DU_\infty) / (\dot{m}_0 h_F)$ is the propulsive efficiency of the body engine and $\eta_p = E / (\tau \dot{m}' h_F)$ is the efficiency of the laser spike system, converting the energy stored in the fuel into an actual energy deposited in the flow. This latter figure of merit includes the efficiency of the physical devices (such as the laser, the power conversion unit), and the efficiency of the physical processes (e.g., plasma induced heating of the gas). For the following analysis, $H = \eta_{pe} / \eta_p$, the figure of merit of the laser spike device. Having a large H means that the energy conversion is inefficient compared to the engine propulsive efficiency. At best, the value of H is around unity, although values in the range of 10-100 are more credible. Finally, the small parameter ε quantifies the ratio of the mean power deposited in the flow to the work of the drag force:

$$\varepsilon = \frac{E / \tau}{\frac{1}{2} \rho_\infty U_\infty^3 S C_X^0} \quad (10)$$

In order to analyze the efficiency of the drag reduction system, the two deposition regimes are considered. The first regime corresponds

Regime	Pulse Energy (mJ)	Repetition Period τ (ms)	Mean Power (W)	Mean drag reduction (Δ)	Efficiency η		
					$H=1$	$H=10$	$H=100$
I	6.25	0.3	20	9.5%	0.90	0.91	0.97
II	6.25	0.1	62.5	19%	0.81	0.83	1.02
I	25	0.325	77	13.8%	0.86	0.89	1.12
II	25	0.2	125	20%	0.80	0.84	1.22
I	100	0.4	250	14.3%	0.86	0.94	1.69

Table 5 - Efficiency of the repetitive pulsed energy deposition

to a deposition period τ equal to the interaction duration. The second regime takes into account the cumulative effect, for the two quasi-steady states previously identified. The results are given in Table 5 below, for three hypotheses for the laser spike efficiency ($H=1, 10$ and 100).

It appears first that the deposition in Regime II, where a cumulative effect is achieved, is more efficient in all cases in terms of drag reduction. In addition, in the first regime the next deposition occurs at the end of the interaction period of the previous energy release. This induces large drag fluctuations that are prejudicial from a technical point of view. Finally, in the case with $H=1$, corresponding to an efficient power conversion, the laser spike system is always efficient ($\eta < 1$). Typically, the propulsive efficiency is within the range of 0.5-0.8. In the more realistic cases ($H \geq 10$), the system is efficient as long as the laser system efficiency is not too low.

Conclusions

This study focused on the modeling of a long linear energy deposition in front of a supersonic blunt body at $M=3$. This figures the effect of a “virtual spike”, possibly obtained by the use of

femtosecond laser filaments. Single and repetitive energy depositions have been studied, considering the air plasma created as a gas at Local Thermodynamic Equilibrium. The study for a single pulse has shown that a transient drag reduction is obtained when the heated core resulting from the energy deposition interacts with the bow shock. This interaction induces a large recirculating bubble, correlated with a drop in the front pressure. This bubble evolves towards a toroidal vortex with a low pressure core, which is then convected downstream by the flow. The intensity of the drag reduction depends nonlinearly on the total energy deposition and the deposition length, while it is roughly independent of the deposition duration and its radius, within the range tested in this study. For the repetitive case, it is shown that depending on the repetition frequency, the deposition may result in the formation of a large recirculating bubble, undergoing regular collapses, or in a smaller quasi-steady recirculating bubble. This behavior is similar to what is observed for a spiked blunt body. In this case, the “length” of the spike is controlled by the mean power and repetition rate. An efficiency analysis shows that the laser spike lowers the fuel consumption by 15-20%, as long as the energy coupling efficiency of the laser system is equal to, or above, 10% of the engine propulsive efficiency ■

Acknowledgements

This study was funded by the French DGA, under the “REI, Recherche Exploratoire et Innovation” program.

References

- [1] L. N. CATTAFESTA, M. SHEPLAK - *Actuators for Active Flow Control*. Annu. Rev. Fluid Mech., vol. 43, no. 1, pp. 247–272, Jan. 2011.
- [2] E. MOREAU - *Airflow Control by Non-Thermal Plasma Actuators*. J. Phys. D: Appl. Phys., vol. 40, no. 3, pp. 605–636, Feb. 2007.
- [3] S. B. LEONOV, J. LI, S. FU - *Review of Plasma-Based Methods for High-Speed Flow Control*. vol. 498, no. 1, pp. 498–502, 2011.
- [4] L. WANG, Z. LUO, Z. XIA, B. LIU, X. DENG - *Review of Actuators for High Speed Active Flow Control*. Sci. China Technol. Sci., vol. 55, no. 8, pp. 2225–2240, May 2012.
- [5] D. KNIGHT, G. ELLIOTT, G. CANDLER, A. ZHELTOVODOV - *Localized Flow Control in High Speed flows using laser energy deposition*. CCD 2003-25, 2003.
- [6] R. G. ADELGREN, H. YAN, G. ELLIOT, and AI. - *Control of Edney IV Interaction by Pulsed Laser Energy Deposition*. AIAA J., vol. 43, no. 2, pp. 256–269, 2005.
- [7] P. K. TRET'YAKOV, A. F. GARANIN, G. N. GRACHEV, V. L. KRAINEV, A. G. PONOMARENKO, V. N. TISHCHENKO, V. I. YAKOVLEV, G. G. CHERNYI - *Control of Supersonic Flow around Bodies by Means of High-Power Recurrent Optical Breakdown*. Phys. - Dokl., vol. 41, pp. 566–567, Nov. 1996.
- [8] J.-H. KIM, A. MATSUDA, T. SAKAI, A. SASOH - *Wave Drag Reduction with Acting Spike Induced by Laser-Pulse Energy Depositions*. AIAA J., vol. 49, no. 9, pp. 2076–2078, Sep. 2011.
- [9] T. SAKAI, Y. SEKIYA, M. ROSLI, A. MATSUDA, A. SASOH - *Unsteady Interaction of Blunt Bodies With Laser Induced Plasma in A Supersonic Flow*. 39th Plasmadynamics and Lasers Conference, 2008, no. AIAA 2008–3794.

- [10] A. IWAKAWA, N. HASEGAWA, T. OSUKA, R. MAJIMA, T. SAKAI, A. SASOH - *Supersonic Drag Reduction Performance of Blunt-Body with Conical Spike using Energy Depositions*. 44th AIAA Plasmadynamics and Lasers Conference, 2013.
- [11] A. SASOH, Y. SEKIYA, T. SAKAI, J.-H. KIM, A. MATSUDA - *Supersonic Drag Reduction with Repetitive Laser Pulses Through a Blunt Body*. AIAA J., vol. 48, no. 12, pp. 2811–2817, Dec. 2010.
- [12] A. COUAIRO - *Femtosecond Filamentation in Air*. Springer series in Chemical Physics, vol. 84, pp. 235–258, 2006.
- [13] A. COUAIRO, A. MYSYROWICZ - *Femtosecond Filamentation in Transparent Media*. Phys. Rep., vol. 441, no. 2–4, pp. 47–189, 2007.
- [14] A. HOUARD, Y. LIU, A. MYSYROWICZ - *Recent Developments in Femtosecond Filamentation*. J. Phys. Conf. Ser., vol. 497, p. 012001, Apr. 2014.
- [15] B. ZHOU, S. AKTURK, B. PRADE, Y.-B. ANDRÉ, A. HOUARD, Y. LIU, M. FRANCO, C. D'AMICO, E. SALMON, Z.-Q. HAO, N. LASCoux, A. MYSYROWICZ - *Revival of Femtosecond Laser Plasma Filaments in Air by a Nanosecond Laser*. Opt. Express, vol. 17, no. 14, pp. 11450–11456, 2009.
- [16] J. B. MICHAEL, A. DOGARIU, M. N. SHNEIDER, R. B. MILES - *Subcritical Microwave Coupling to Femtosecond and Picosecond Laser Ionization for Localized, Multipoint Ignition of Methane/air Mixtures*. J. Appl. Phys., vol. 108, no. 9, p. 93308, 2010.
- [17] K. KREMEYER, K. SEBASTIAN, C.-W. SHU - *Computational Study of Shock Mitigation and Drag Reduction by Pulsed Energy Lines*. AIAA J., vol. 44, no. 8, pp. 1720–1731, 2006.
- [18] G. W. SUTTON - *Effect of Laser-Induced Upstream Cylindrical Blast Waves on a High-Velocity Rocket*. AIAA J., vol. 47, no. 5, 2009.
- [19] C. GREY MORGAN - *Laser-Induced Breakdown of Gases*. Rep. Prog. Phys., vol. 38, pp. 621–665, 1975.
- [20] N. KROLL, K. M. WATSON - *Theoretical Study of Ionization of Air by Intense Laser Pulses*. Phys. Rev. A, vol. 5, no. 4, 1972.
- [21] M. H. NIEMZ - *Threshold Dependence of Laser-Induced Optical Breakdown on Pulse Duration*. Appl. Phys. Lett., vol. 66, no. 10, p. 1181, 1995.
- [22] R. KANDALA, G. CANDLER - *Numerical Studies of Laser-Induced Energy Deposition for Supersonic Flow Control*. AIAA J., vol. 42, no. 11, 2004.
- [23] A. D'ANGOLA, G. COLONNA, C. GORSE, M. CAPITELLI - *Thermodynamic and Transport Properties in Equilibrium Air Plasmas in a Wide Pressure and Temperature Range*. Eur. Phys. J. D, vol. 46, no. 10, 2008.
- [24] A. REFLOCH, B. COURBET, A. MURRONE, P. VILLEDIEU, C. LAURENT - *CEGRE Software*. Aerosp. Lab J., no. 2, pp. 1–10, 2011.
- [25] P. CHEVALIER, B. COURBET, D. DUTOYA, P. KLOTZ, E. RUIZ, J. TROYES, P. VILLEDIEU - *CEGRE : Development and Validation of a Multiphysics Computational Software*. 1st european conference for aerospace science (EUCASS), 2005.
- [26] D. DUTOYA, L. MATUSZEWSKI - *Thermodynamics in CEGRE*. Aerosp. Lab J., no. 2, pp. 1–11, 2011.
- [27] R. CÉRÉSUELA - *Maquettes étalons HB.1 et HB.2. Caractéristiques aérodynamiques mesurées dans les souffleries de l'ONERA de Mach 2 à Mach 16.5*. ONERA-NT 123, 1968.
- [28] R. CÉRÉSUELA - *Mesure d'efforts et de pression sur la maquette balistique étalon HB2*. ONERA-NT 13/1879A 1964.
- [29] A. AMBROSIO, A. WORTMAN - *Stagnation Point Shock Detachment Distance for Flow around Spheres and Cylinders*. ARS J., vol. 32, p. 281, 1962.
- [30] V. M. FOMIN, A. A. MASLOV, N. D. MALMUTH, V. P. FOMICHEV, A. P. SHASHKIN, T. A. KOROTAVA, A. N. SHIPLYUK, G. A. POZDNYAKOV - *Influence of Counterflow Plasma Jet on Supersonic Blunt-Body Pressures*. AIAA J., vol. 40, no. 6, pp. 1170–1177, 2002.
- [31] M. GOLBABAIE-ASL, D. D. KNIGHT - *Numerical Characterization of High-Temperature Filament Interaction with Blunt Cylinder at Mach 3*. Shock Waves, vol. 24, no. 2, pp. 123–138, Aug. 2013.
- [32] A.G. PANARAS - *Pulsating Flow about Axisymmetric Concave Bodies*. AIAA J., vol. 19, no. 6, pp. 804–806, 1981.
- [33] P.-Q. ELIAS - *Effets de plasmas sur une onde de choc supersonique à Mach 3*. Thèse de doctorat en Energétique de l'Ecole Centrale Paris, 2007.
- [34] J. SRULIJES, P. GNEMMI, K. RUNNE, F. SEILER - *High-Pressure Shock Tunnel Experiments and CFD Calculations on Spike-Tipped Blunt Bodies*. 22nd AIAA Aerodynamic Measurement Technology and Ground Testing Conference, 2002.
- [35] P.-Q. ELIAS, B. CHANETZ, S. LARIGALDIE, D. PACKAN - *Study of the Effect of Glow Discharges Near a M 3 Bow Shock*. AIAA J., vol. 45, no. 9, pp. 2237–2245, 2007.

Acronyms

CFD	(Computational Fluid Dynamics)
LTE	(Local Thermodynamic Equilibrium)
URANS	(Unsteady Reynolds-Averaged Navier-Stokes)

AUTHOR



Paul-Quentin Elias is a Research Scientist at ONERA, in the Lightning & Plasma Applications Group. He holds an Engineering degree and a PhD from Ecole Centrale Paris. His main interests are the applications of cold or thermal plasmas to aerospace systems. His current activities involve the development of optical diagnostics for lightning and atmospheric pressure discharges, the development and characterization of plasma actuators for flow control applications and the testing and modeling of new low pressure plasma sources for electric propulsion. Paul-Quentin Elias has authored or co-authored 12 peer-reviewed articles, 3 invited conferences and more than 40 technical reports.

R. Jousset, S. Coumar, V. Lago
(ICARE, CNRS, Orléans)

E-mail: romain.jousset@cnrs-orleans.fr

DOI : 10.12762/2015.AL10-04

Plasmas for High Speed Flow Control

This paper presents experimental activities focused on supersonic flow control with plasma and MHD actuators. This work is carried out at ICARE, a laboratory located at the CNRS Campus in Orléans. The study of aerothermodynamic physics, one of the research fields of ICARE, is conducted with the experimental platform FAST consisting of three supersonic/hypersonic wind tunnels involved in aerothermodynamic testing for hypersonic flight and space technology.

Introduction

Flow control research in the compressible regime plays a major role in many applications, such as aerospace, defense and transportation. Over the past two decades, considerable research effort has been made on the use of plasma-based devices in high speed flow control applications, both numerically and experimentally [1-5]. Depending on the nature of the flow, ionized or neutral gas, two types of plasma-based devices can be used. In the case of neutral gas flows, plasma actuators are used and their action is based on the interaction of the electric field with the flow (EHD interaction). If the flow is already ionized, then magnetic systems are preferred and are based on the interaction of a magnetic field with the charged particles of the ionized flow (MHD interaction).

Although the ability of plasma-based devices to control high speed flows no longer needs to be demonstrated, the complexity of the wide field of competences involved in these research areas (compressible fluid mechanics, plasma discharge physics and magneto-hydrodynamics) implies that many studies must still be conducted to gain a better understanding of how and why a high speed flow is modified when plasma-based devices are used. In this respect, experimental investigations are carried out at ICARE, a CNRS laboratory located in Orléans, with the experimental platform FAST (Facilities for Aerothermodynamics and Supersonic Technologies). In particular, the studies carried out by our group focus on supersonic and hypersonic flow modifications by plasma-based devices, under rarefied conditions. Our domain of applications concerns the flight of vehicles at high altitude (i.e., low pressure) and atmospheric re-entry aerothermodynamics.

During the re-entry phase into a dense gas atmosphere, spacecraft flying at hypersonic velocities are exposed to severe conditions and the mission planning must delicately balance three requirements: deceleration, heating and accuracy of the landing. Thus, one of the promising technologies consists in using active flow control methods with plasma-based devices. This could potentially reduce the heat flux locally by increasing the shock stand-off distance, reduce the vehicle speed by increasing the wave drag and therefore the ballistic coefficient, enhance

the vehicle stability and trimming by controlling the flow leading to the simplification or elimination of the flaps, and avoid black-out transmission by using MHD to optimize communication links.

In order to improve or increase the effects of these plasma-based devices, the coupling of EHD-MHD devices could be used. Thus, electrically or magnetically generated forces act on the ionized component of the flow impacting the vehicle and can modify the shock wave shape, the shock stand-off distance, or the surface heat flux, for instance. Even though these forces act only on a small ionized part of the whole flow field, proper orientation of the field lines (electric or magnetic) applied over a partial body surface region ensures that a global body force can be exerted on the entire flow. When electrical discharges are used, substantial changes in the structure and properties of the high speed flow field have been demonstrated to occur in the vicinity of the vehicle where the actuator is located. Compared to mechanical ones, active actuators like plasma-based devices have a fast response time.

From a general point of view, a plasma actuator is a simple electrical device based on the use of a gas discharge. Among the most used types of plasma actuators, one can find those based on surface dielectric barrier discharge (dbd) with linear or serrated electrode design [6-9], direct current (dc) discharge [10-11], filamentary discharge [12], arc discharge [13] and corona discharge [14]. The main limitation in preferring the use of a particular type of plasma actuator is often driven by the flow conditions, especially the pressure condition. In rarefied flow regimes, corona and glow discharges are mainly used, with other types of plasma actuators being scarcely ever used owing to their working limitation imposed by the discharge physics itself. In the case of glow discharges working at a low pressure, the ionic wind cannot be considered to explain the observed modifications of the flow. Contrary to plasma actuators working at atmospheric pressure, the values of both the electric field and the net charge density are too low to obtain a significant EHD force and, therefore, to produce an ionic wind. Thus, under supersonic flow conditions, thermal effects, including surface and bulk (i.e., gas) heating, are commonly considered as the main physical mechanisms responsible for aerodynamic

effects [15-17]. Nevertheless, experiments still remain that can hardly be explained by thermal effects alone [17-20]. Especially, those in which a change in the discharge polarity leads to various aerodynamic effects [17, 20]. In this study, plasma flow control experiments are carried out with the MARHy wind tunnel (supersonic/hypersonic rarefied flows). The experiments began in 2004 with the Ph.D. thesis of E. Menier [21] and, as from this date, they gave rise to a better understanding of the respective contributions of the thermal effects and the purely plasma ones on the flow field modification [22, 23].

MHD prospective applications in aerodynamics were described fifty years ago by Sears [24]. Shortly after, Ziemer [25] numerically and experimentally investigated the influence of an external magnetically induced field on the shock stand-off distance, showing a notable increase with respect to the situation without magnetic induction. The bow shock wave formed in front of vehicles flying at hypersonic speeds produces a compression and a strong heating of the gas. Close to the surface, the temperature is high enough to ionize the gas, leading to a significant level of MHD interaction processes if a magnetic field is applied. MHD interaction can generate forces that enable the fluid dynamic configuration to be modified. For instance, it is possible to move the shock front away and then decrease the thermal flux toward the wall protection. Several studies have been done on this topic, such as the experimental investigations carried out by Cristofolini et al. [26] and Gülhan et al. [27], and the numerical investigations presented by Yoshino et al. [28]. For this purpose we have carried out a set of experiments with the plasma wind tunnel PHEDRA [29].

Modification of shock waves by glow discharge

The MARHy wind tunnel

The MARHy low density wind tunnel is dedicated both to academic and industrial research. A schematic view of the wind tunnel is presented in Figure 1. It consists of three parts: the settling chamber with a diameter of 1.3 m and a length of 2.0 m, the test chamber with a diameter of 2.3 m and a length of 5.0 m, and a third chamber in which a diffuser is installed. The diffuser is connected to the pumping group by a vacuum gate. A powerful pumping group with 2 primary pumps, 2 intermediary Roots blowers and 12 Roots blowers ensures the low density flow conditions in continuous operating mode. When supplied through different nozzles, the wind tunnel generates subsonic, supersonic and hypersonic flows between Mach 0.6 and Mach 22, and covers a large range of Reynolds numbers from 10^2 up to 10^5 . Figure 2 shows the working conditions of the MARHy wind tunnel, where the Reynolds number is based on a model length of 10 cm. This study was carried out with a contoured Mach 2 nozzle, giving a uniform flow distribution throughout the test section with a core 12 cm in diameter. The nominal operating conditions are summarized in Table 1.

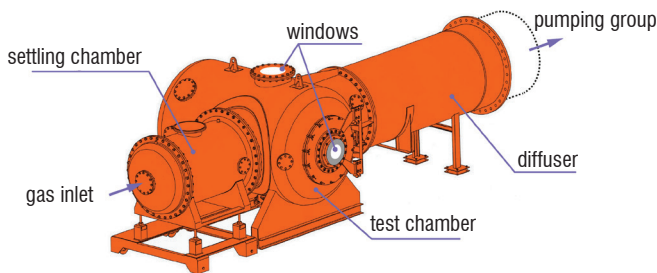


Figure 1 - Schematic view of the MARHy wind tunnel

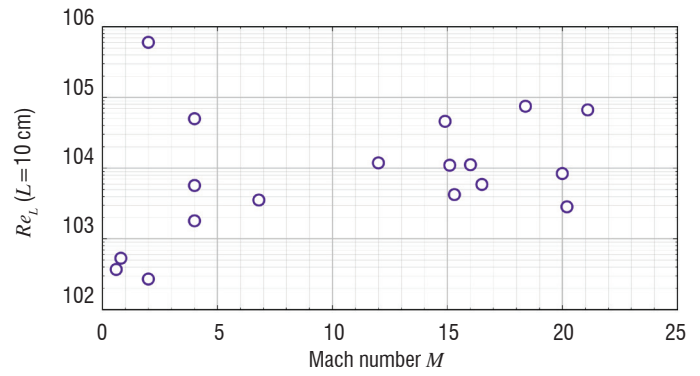


Figure 2 - Mach-Reynolds diagram for the MARHy wind tunnel

Stagnation conditions		Free stream conditions	
$p_o = 63 \text{ Pa}$	$p_i = 8 \text{ Pa}$	$\rho_i = 1.71 \times 10^{-4} \text{ kg.m}^{-3}$	
$T_o = 293 \text{ K}$	$T_i = 163 \text{ K}$	$\mu_i = 1.10 \times 10^{-5} \text{ Pa.s}$	
$\rho_o = 7.44 \times 10^{-4} \text{ kg.m}^{-3}$	$U_j = 511 \text{ m.s}^{-1}$	$\lambda_j = 0.375 \text{ mm}$	
	$M_i = 2$	$q_m = 3.34 \times 10^{-3} \text{ kg.s}^{-1}$	

Table 1 - Operating conditions

The cylinder configuration

Circular cylinder and discharge setup

The model is a circular cylinder made of alumina, with a diameter of 20 mm and a spanwise length of 80 mm (Figure 3). An aluminum electrode is flush mounted on the cylinder in the spanwise direction. It is 0.5 mm-thick, 75 mm-long and 3 mm-wide. The cylinder is mounted in the test section with its longitudinal axis perpendicular to the main flow direction. The corresponding Reynolds number is 159. The plasma is produced with a glow discharge generated by connecting the electrode to a high voltage dc power supply (Spellman SR15PN6) through a resistor ($R_s = 11 \text{ k}\Omega$). The electrode is negatively biased compared to the rest of the device (i.e., the wind tunnel metallic parts), which is grounded and collects electric charges from the plasma, ensuring the current looping. The voltage V_s is fixed by means of the power supply, which delivers the discharge current I_{HV} . The voltage applied to the electrode is V_{HV} .

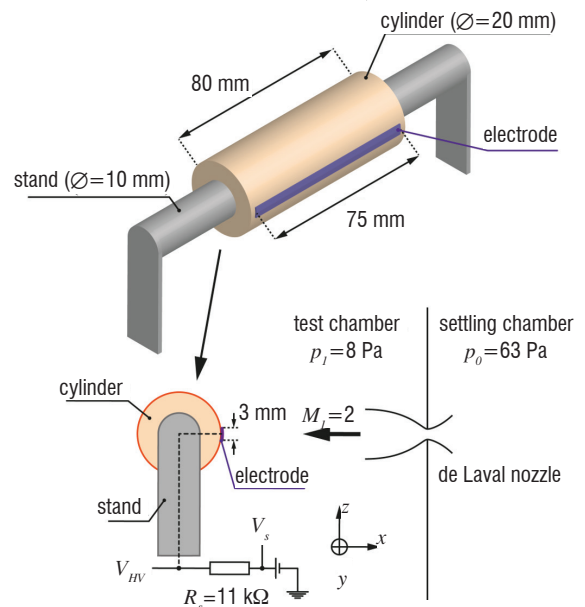


Figure 3 - Schematic representation of the cylinder

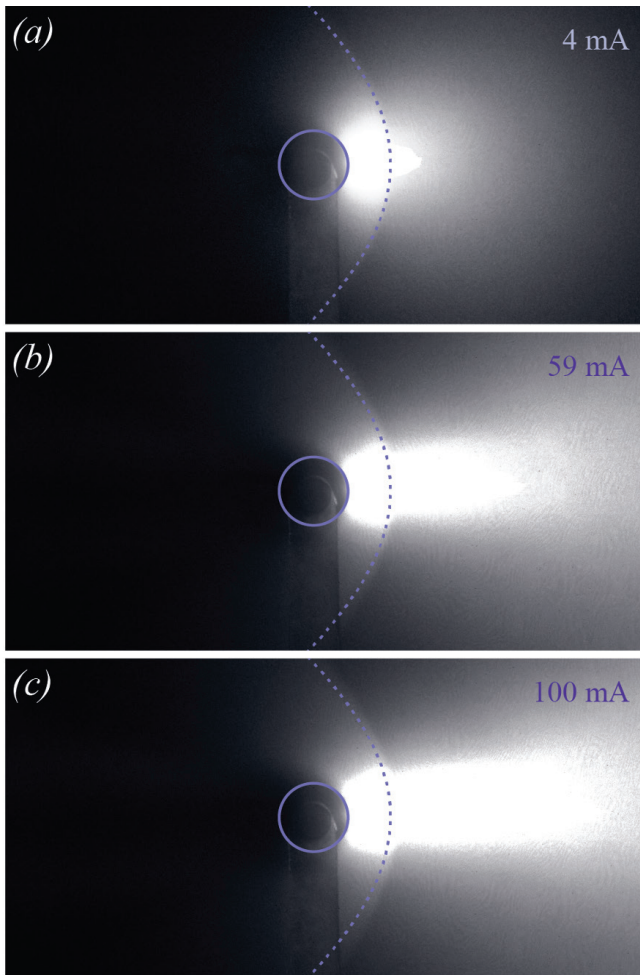


Figure 4 - Images (recorded with the iccd camera) of the flow field modified by the plasma discharge: (a) -0.46 kV and 4 mA, (b) -1.37 kV and 59 mA, and (c) -1.94 kV and 100 mA. The dotted line represents the shock wave shape of the baseline.

Modification of the flow field by the plasma discharge

Figure 4 shows the iccd images of the shock wave modified by the discharge. The natural shock wave shape is superimposed on each image, in order to facilitate comparison between the different cases. As can be observed, the plasma changes the shape of the shock wave locally, pushing it upstream of the flow. The symmetrical shape is maintained, but the "curvature" of the shock wave is slightly modified far from the stagnation line. The stand-off distance on the stagnation line is estimated, for each electrical discharge configuration, from the experimental images. Lago et al. [22] showed that the stand-off distance undergoes a linear increase with the applied voltage. In this study, the stand-off increases when the plasma is created in the region upstream and downstream from the shock wave. Thus, we can assume that the local flow properties in the vicinity of the shock wave have been modified. This approach can be compared with the one proposed by Hayes and Probstein [30], who showed that the shock stand-off distance in front of a cylinder is a function of the density ratio across the shock wave on the stagnation streamline. Three types of effects can be considered to explain why the shock wave is pushed upstream: surface heating of the electrode, volumetric heating of the gas upstream from the electrode where the plasma is present and the influence of the ionization degree. Each of these effects was studied separately, in order to quantify its respective influence on the shock wave modification.

Analysis of the plasma effects

In order to evaluate the influence of the surface and volumetric heating induced by the plasma, we have simulated these effects numerically and separately [22]. The results have shown that no thermal effects are responsible for the shock wave shape modification. These results are consistent with optical temperature measurements, which show that the gas temperature remains below 400 K (Figure 5).

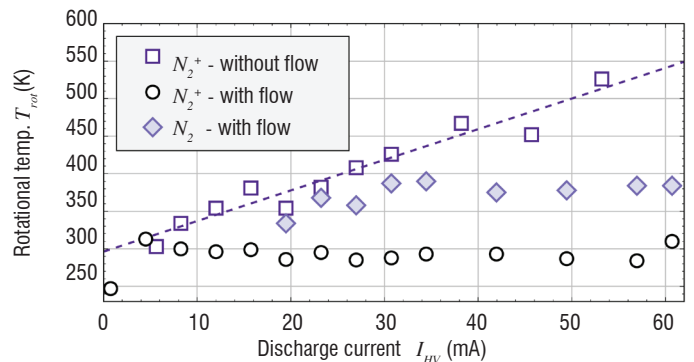


Figure 5 - Comparison between N_2 and N_2^+ rotational temperatures (i.e., gas temperature) with flow ($M_1 = 2$) and without flow versus the discharge current.

Since thermal effects are not responsible for the flow modifications observed, other properties of the plasma must be considered to explain the measurements. For this purpose, we modify the empirical relation of the shock stand-off distance Δ proposed by Ambrosio and Wortman [31], in order to express the stand-off distance as a function of the ionization degree of the plasma. If we assume that a normal shock wave is present on the stagnation streamline, then the isentropic relation gives

$$\frac{\rho_2}{\rho_1} = \frac{(\gamma+1)M_1^2}{2+(\gamma-1)M_1^2} \quad (1)$$

where M_1 is the Mach number upstream from the shock wave, γ is the isentropic exponent and ρ is the volumetric density. The subscript $_1$ is related to the upstream flow condition and the subscript $_2$ is related to the downstream condition. When the electrical discharge is switched on, the law of mass conservation can be expressed by the following relation:

$$\frac{\rho_2}{\rho_1} = \left(\frac{\rho_2}{\rho_1} \right)^* \quad (2)$$

where the superscript $*$ is related to the ionized state of the flow (i.e., a plasma is present). The isentropic exponent γ^* of a diatomic plasma in non-local thermodynamic equilibrium is determined with the following relation, proposed by Burm et al. [32]

$$\gamma^* = \frac{c_p^*}{c_v^*} \frac{2\theta + (1-\theta)}{2\theta + (1-\theta)\alpha_i + (1-\alpha_i)\alpha_i} \quad (3)$$

where α_i is the ionization degree defined as the ratio of the electron density n_e to the neutral density n_i , and $\theta = T_{gas}/T_e$ is the thermal disequilibrium between the gas temperature T_{gas} and the electron temperature T_e .

Figure 6 shows the theoretical variation of γ^* according to an ionization degree ranging from 10^{-6} to 10^{-2} , corresponding to a weakly ionized plasma. The gas temperature was fixed at $T_{gas} = 375$ K (from the results shown in Figure 5) and the electronic temperature was fixed at $T_e = 1$ eV. The isentropic exponent decreases from 1.4 (non-ionized gas) to about 1.12, and

remains almost constant for higher ionization degrees. It can be seen that the isentropic degree begins to decrease significantly for $\alpha_i > 10^{-5}$, which corroborates the hypothesis of Bletzinger et al. [2], who argued that for a very low ionization degree ($\approx 10^{-7}$) the flow modification in an ionized gas is predominantly due to thermal effects.

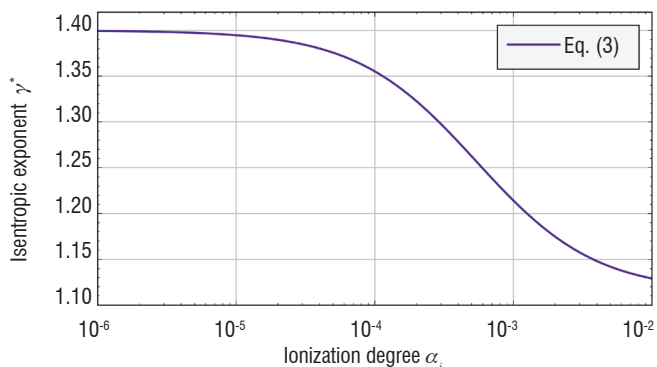


Figure 6 - Isentropic exponent of a plasma as a function of its ionization degree ($T_{gas} = 375$ K and $T_e = 1$ eV).

The upstream Mach number of the plasma state M_1^* can be calculated with Equations (1) and (2) as a function of the isentropic exponent of the plasma defined with Equation (3). For the values of γ^* plotted in Figure 6, Figure 7 shows that the plasma is responsible for a decrease in the Mach number upstream from the shock wave.

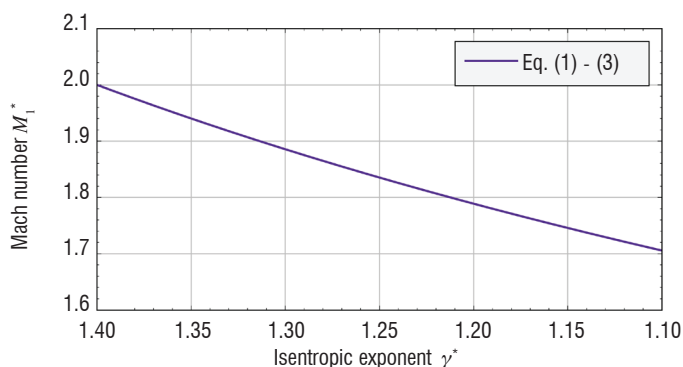


Figure 7 - Mach number of an ionized flow upstream from a normal shock wave as a function of the isentropic exponent of an ionized gas.

The stand-off distance Δ^* in an ionized gas can be calculated by modifying the empirical relation of Ambrosio and Wortmann [31] as follows:

$$\frac{\Delta^*}{R_{cyl}} = 0.386 \exp\left(\frac{4.67}{M_1^{*2}}\right) \quad (4)$$

where R_{cyl} is the cylinder radius and M_1^* is the Mach number of the ionized flow upstream from the shock wave (Figure 7). Figure 8 shows the variation in the stand-off distance for a plasma flow according to its ionization degree. The open symbols are the experimental values of Δ calculated from the iccd images for the applied voltages tested.

The values of Δ measured experimentally correspond approximately to an ionization degree ranging between 4×10^{-5} and 3×10^{-4} . These values of α_i allow the electronic density to be calculated by considering a neutral particle density behind the shock wave of $n_2 = 5 \times 10^{21} \text{ m}^{-3}$. For these values of α_i and n_2 , the electron density varies between $2 \times 10^{17} \text{ m}^{-3}$ and $1.5 \times 10^{18} \text{ m}^{-3}$, which is of the same

order of magnitude as those mentioned in the literature for this type of discharge. In addition, our measurements show that the increase in Δ is linear with I_{HV} [22], which is the same type of relation as that existing between the electronic density and the current density (i.e., the discharge current I_{HV}). The increase in Δ with the electrical parameters of the discharge is then explained by a modification of the flow conditions via a decrease in the isentropic exponent of the flow. The nature of the flow in the vicinity of the shock wave is therefore of great importance in explaining why Δ increased when the discharge was active.

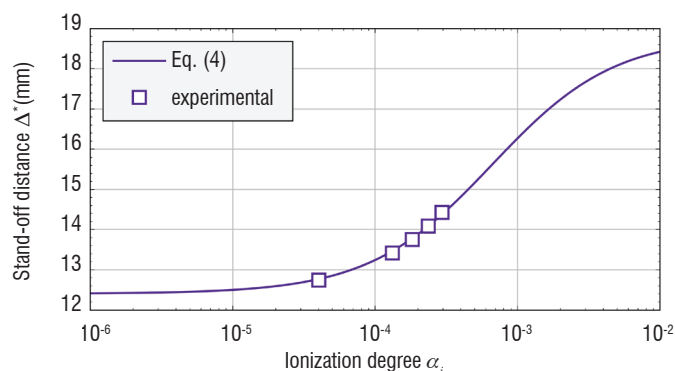


Figure 8 - Stand-off distance for a flow of ionized gas as a function of the ionization degree of the plasma. The open symbols correspond to the experimental values of Δ measured with the plasma actuator.

The flat plate configuration

Description of the flat plate and actuators

The model under investigation is a flat plate (100 mm-long, 80 mm-wide and 4 mm-thick) made of quartz, with a sharp leading edge of 15° . The flat plate is mounted in the test section, 183 mm downstream from the nozzle exit (Figure 9). The Reynolds number, based on the flat plate length L and calculated with the experimental inflow conditions (Table 1), is 794. The Knudsen number based on the same experimental conditions is 0.019, which corresponds to the slip-flow regime.

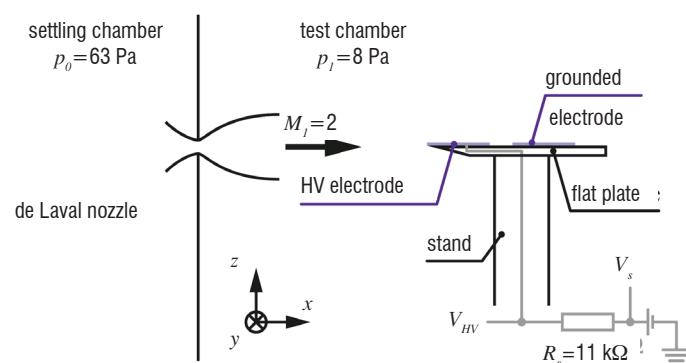


Figure 9 - Schematic view of the flat plate in the case of the plasma actuator

The plasma actuator is composed of two aluminum electrodes (80 mm-long, 35 mm-wide and $80 \mu\text{m}$ -thick), which are flush mounted on the upper surface of the flat plate (Figure 10a). The first electrode, called the active electrode, is set at the leading edge of the plate and is connected to a high voltage dc power supply (Spellman, SR15PN6) through a resistor, while the second one is grounded. The glow discharge is generated by applying a negative dc potential to the active electrode, acting as a cathode. Previous works have shown that, for this geometry, one of the effects of the plasma actuator on the flow field is caused by the heating of the surface [11]. In order

to reproduce the surface heating produced by the plasma actuator, a heating element was used. The heating actuator, namely the heater, is composed of a 0.15 mm-diameter resistance wire ($28 \Omega \cdot \text{m}^{-1}$, Cu-Ni-Mn alloy) embedded between two layers of polyimide film. The heater is flush mounted on the flat plate surface instead of the active electrode (Figure 10b). The longitudinal distribution of the resistance wire was not constant, in order to reproduce the temperature distribution measured with the plasma actuator. The heater was connected to a dc power supply (0-60 V, 0-2.5 A).

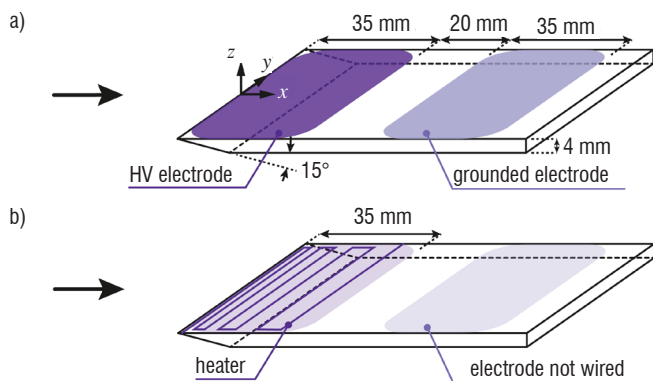


Figure 10 - Schematic views of the flat plate with: (a) the plasma actuator, and (b) the heater.

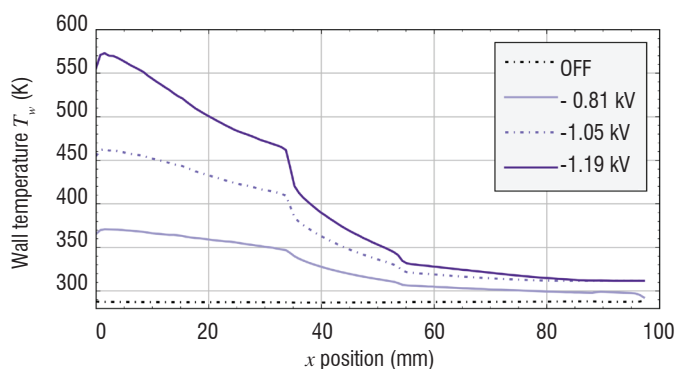


Figure 11 - Longitudinal distribution of the wall temperature along the flat plate in the case of the plasma actuator.

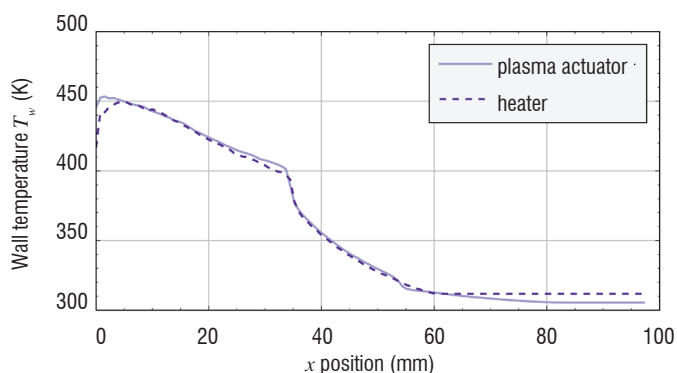


Figure 12 - Comparison of wall temperature distributions along the flat plate between the plasma actuator and the heater.

The surface heating is due to the electrode bombardment by ions and neutrals from the plasma to the wall. This type of heating mechanism is due to the electric field in the vicinity of the cathode. Given that the flat plate has a beveled leading edge, the electric field in the vicinity of the cathode varies along the X-direction. The longitudinal distribu-

tion of the surface temperature is not constant, as evidenced by the infra-red camera measurements presented in Figure 11. The temperature distribution is not homogeneous along the plate and presents the highest values close to the leading edge. The home-made heater allows this longitudinal temperature distribution to be reproduced by choosing an adequate value for the current heater I_{HE} (Figure 12). A maximum wall temperature value of $T_{w,max} \sim 510 \text{ K}$ can be reproduced with the heater.

Description of the natural flow

The flow field around the flat plate was first investigated without any actuation, corresponding to the study of the natural flow (namely, the baseline). In this case, the shock wave was experimentally visualized with the glow-discharge flow visualization technique. Figure 13 shows an image of the baseline around the flat plate, visualized with the iccd camera. This image results from the averaging and post-processing of 300 snapshots of the flow field recorded with the iccd camera. The air flows from left to right.



Figure 13 - Image of the natural flow field around the flat plate obtained with the glow-discharge flow visualization technique.

The shock wave is readily recognized on the image obtained with the iccd camera, enabling the estimation of its shape. Under our conditions, the shock wave shape for the baseline is hyperbolic and can be described by the following equation:

$$x = c_1 + c_2 \left[1 + \left(\frac{z}{c_3} \right)^2 \right]^{1/2} \quad (5)$$

where x and z are the shock wave coordinates in the Cartesian coordinate system (centered on the leading edge) and c_1 , c_2 and c_3 are the geometric coefficients of the hyperbola. The shock wave angle β corresponds to the angle of the hyperbola asymptote. The coefficients c_1 , c_2 and c_3 are estimated by fitting (least squares method) the shock wave position in the iccd images, enabling the shock wave angle to be calculated. For the baseline, the value of β is 36.77° . The shock wave is slightly detached from the leading edge of the plate because of the rarefaction effects. The order of magnitude of the shock wave stand-off distance is 1–2 mm. For the baseline, the wall temperature is homogeneous ($286.5 \text{ K} < T_w < 288.4 \text{ K}$).

Modifications induced by the plasma actuator

When the high voltage is switched on, gas above the cathode is ionized and weakly ionized plasma is created. Visually, it corresponds to the luminous area shown in Figure 14. The dark area above the cathode corresponds to the plasma sheath. The plasma discharge

induces a modification of the shock wave that is deflected outward from the flat plate surface, as illustrated in Figure 14. For the electrical configurations experimentally tested, the hyperbolic shape of the shock wave is preserved, allowing Eq. (5) to be used to estimate the shock wave angle. In addition, the order of magnitude of the shock wave stand-off distance remains within the 1–2 mm-range. Figure 15 shows the increase in the shock wave angle with the applied voltage. This variation can be approximated by the following equation

$$\beta = \beta_0 + a \left\{ 1 - \exp \left[-b \left(V_{ign} - V_{HV} \right)^n \right] \right\} \quad (6)$$

where $a = 5.89^\circ$ and $b = 2.65 \text{ kV}^{-n}$, $n = 1.28$ are the best-fit parameters and $\beta_0 = 36.77^\circ$ is the shock wave angle of the experimental baseline.

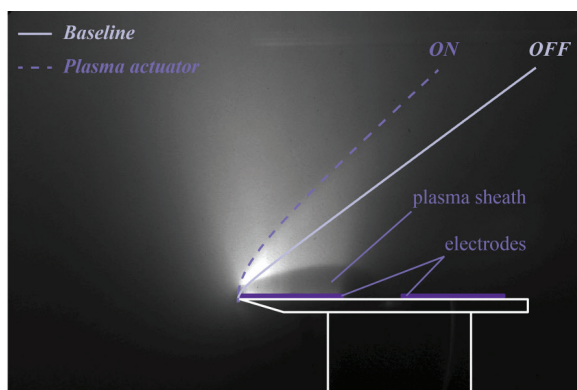


Figure 14 - Image of the flow field modified by the plasma actuator ($V_{HV} = -1.57 \text{ kV}$ and $I_{HV} = 74 \text{ mA}$)

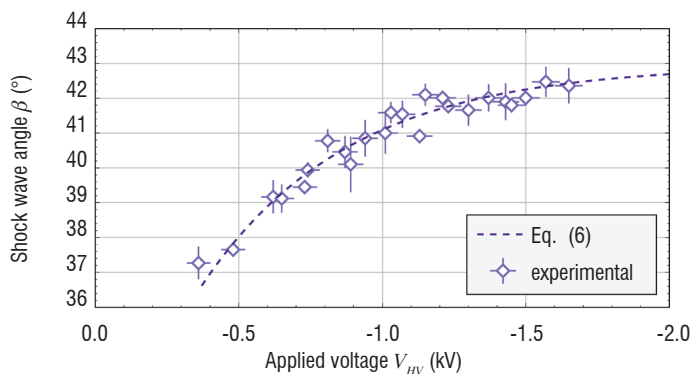


Figure 15 - Shock wave angle versus the applied voltage

Analysis of the plasma effects

In the rarefied flow regime, one of the main effects expected to be responsible for modifying the shock wave is the heating of the model surface [33], which induces a displacement effect [30]. The flow viscosity above the heater is modified, leading to an increase in the boundary layer thickness and, consequently, a shifting of the shock wave outward from the flat plate surface (i.e., β increases). In this experiment, a Pitot survey of the flow above the cathode shows the increase in the boundary layer thickness (Figure 16). At the longitudinal position $x = 17.5 \text{ mm}$ (i.e., in the middle of the cathode), the boundary layer thickness is estimated by measuring the wall-normal position of the maximum pressure. When a plasma discharge is present (with $V_{HV} = -1.47 \text{ kV}$ and $I_{HV} = 39 \text{ mA}$), the boundary layer thickness increases by 60%, showing the displacement effect induced by the plasma actuator.

Another possible effect produced by the plasma discharge is the bulk heating of the gas above the flat plate surface. In order to investigate this, temperature measurements above the cathode were performed by Menier et al. [11] with optical emission spectroscopy. These measurements were based on rotational temperature measurements from the N_2 second positive system and the N_2^+ first negative system at $\lambda = 337.14 \text{ nm}$ and $\lambda = 390.4 \text{ nm}$, respectively. The results showed that the gas temperature deduced from the rotational temperature is weakly increased by the discharge, meaning that the bulk heating is low.

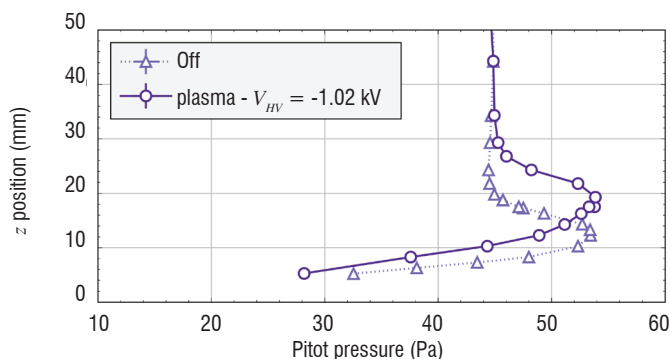


Figure 16 - Pitot pressure profiles in the wall-normal direction at $x = 17.5 \text{ mm}$ in the case of the plasma actuator

In order to differentiate the surface thermal effect from other effects purely due to the plasma discharge, experiments were carried out using the heater as actuator. Numerical simulations were performed by using the 2D compressible Navier–Stokes equations with the boundary conditions adapted to match the physical phenomena involved in the slip-flow regime, in order to simulate the surface thermal effects of the actuators [23, 34]. Figure 17 plots the shock wave angle versus the maximum surface temperature (measured close to the leading edge, Figure 11) for the two actuators (plasma and heater) and for the numerical simulation.

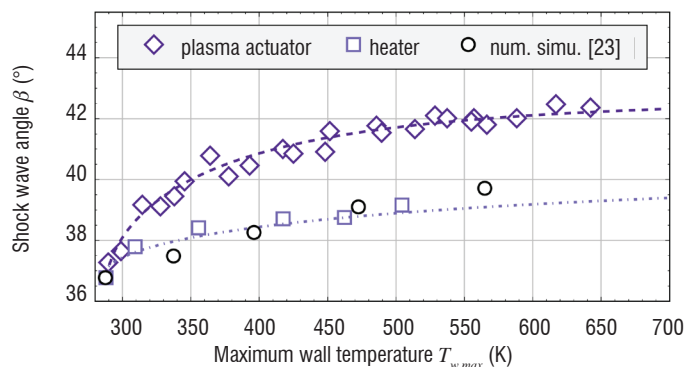


Figure 17 - Comparison of the shock wave angles measured with the two types of actuators (plasma actuator: diamond; heater: square) and calculated with the numerical simulation [23] (circle)

For any given value of $T_{w,max}$, the shock wave angle measured with the heater is lower than the value estimated with the plasma actuator. This result is confirmed by the numerical simulation, which exhibits an increase in β similar to that measured with the heater [23]. When the heating element is used, it is reasonable to assume that only a purely thermal effect at the model surface induces the flow modifications observed. In this case, the mechanism involved in the shock wave angle increase is the displacement effect. The experimental data presented in Figure 17 provide a direct estimation of the surface

heating effectiveness when the plasma actuator is used. The purely thermal effect at the flat plate surface therefore accounts for almost half of the total shock wave modification when the plasma actuator is used [23]. Moreover, the contribution of surface heating to the shock wave modification decreases with the discharge current, meaning that the efficiency of other actuation modes in the shock wave modification increases.

It is clear that the plasma actuator modifies the flow field in a way other than via a thermal effect alone at the electrode surface. In addition, previous studies [11, 12] have shown that the volumetric heating is rather low (+10 K for a plasma discharge with a power ranging between 30 W and 90 W), meaning that other effects induced by the discharge must be studied to explain the shock wave modification observed. Investigation with a cylinder has shown that the flow field is modified by a plasma actuator applied over the cylinder surface, because the ionization rate is strong enough to decrease the value of the isentropic coefficient of the gas, leading to an increase in the stand-off distance. This makes us believe that the ionization rate could play a key role in the explanation of the observed modifications over the flat plate, since the flow conditions are the same and the plasma actuator devices are similar.

Supersonic flow modification by a plasma actuator and MHD

The PHEDRA wind tunnel

This experimental investigation has been carried out in the supersonic low-pressure plasma wind tunnel PHEDRA (Figure 18). This wind tunnel is a plasma ground test platform used to simulate low-pressure flight conditions in the upper layer of planetary atmospheres.

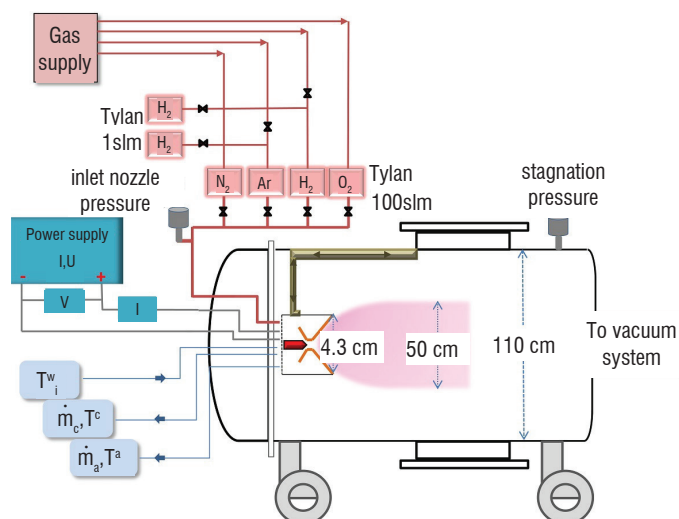


Figure 18 - General scheme of the PHEDRA wind tunnel

PHEDRA is a wind tunnel (with a length of 4.3 m and 1.1 m in diameter) where the low pressure level is maintained with a three-stage pumping group ensuring a residual pressure in the vacuum chamber of around 2 Pa during experiments. The rarefied supersonic plasma flows are produced with a dc arc jet generator. The arc is obtained between the cathode tip and the nozzle throat of the anode. The cathode is a water cooled copper support of 5 mm in diameter, rounded at the tip with a 1.6 mm-diameter zir-

conium insert, on which the cathode spot is found. The anode is convergent up to the position of the cathode tip, then straight for 6 mm with a diameter of 4 mm and then divergent. It is made of copper, with a tungsten insert in the straight 4 mm diameter segment. A vortex movement of the gas inside the arc chamber is applied to obtain stable arc conditions. The current ranges from 50 to 250 A, while the mass flow rate can be varied from 0.1 to 0.3 g.s⁻¹, thus yielding a high specific enthalpy of 5-30 MJ.kg⁻¹. All gases are supplied directly along the anode. The advantages of this type of plasma generator are the stable plasma jets with a long standing time (over a day in air) at large dimensions (500 mm-diameter and 1500 mm-length at 0.1 Torr) and low jet contamination due to the very small cathode erosion of less than 1 ng.s⁻¹ compared to the gas mass flow of at least 0.1 g.s⁻¹. The PHEDRA wind tunnel is equipped with proper instrumentation for the acquisition of the plasma operating parameters and real-time evaluation of the specific enthalpy. The operating parameters and the acquisition chain are shown in Figure 18. The experiments presented in this paper were carried out with two different gas mixtures, a mono-atomic gas with argon and a molecular one with air (80% N₂ / 20% O₂). The operating plasma conditions for each of these are listed in Table 2.

	Argon	80% N ₂ / 20% O ₂
Mass flow rate (g.s ⁻¹)	0.47	0.32
Arc current (A)	100	100
Arc voltage (V)	32	55
Specific enthalpy (MJ.kg ⁻¹)	3.2	10.6

Table 2 - Operating plasma conditions

Test models

Two test models were used in these experiments. A blunt body was aligned with the nozzle centerline for the study of the bow-shock (Configuration 1) and a flat plate was used for the study of the boundary layer (Configuration 2). The details of these configurations are illustrated in Figure 19.

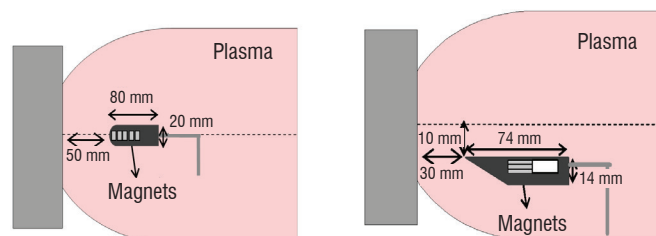


Figure 19 - Experimental configurations: blunt body (left panel) and flat plate (right panel)

The models are made of non-magnetic materials and they are inserted into the plasma flow by means of a movable support operating with an air-compressed system. For each configuration, two identical models were manufactured and mounted on the movable system, one of them carrying the permanent magnet that allows the effect of the magnetic field to be tested during the same experiment. The magnetic field is created with neodymium magnets fixed on the models. Each magnet has a square section with 10 mm sides and a 3 mm thickness, and its magnetic field strength at the surface is $B_s = 0.278$ T, perpendicular to the model surface. The magnet pieces have been superimposed to strengthen the magnetic field. Unfortunately, the heat flux leads to the loss of magnetization of the magnets, forcing us to change the magnets for each new experiment.

Results

The free stream has been characterized in previous works, in particular the velocity, temperatures and electronic parameters (n_e and T_e) of the plasma flow [29, 35, 36].

Table 3 summarizes the parameter values characterizing the plasma flow at the nozzle exit. The temperatures of the heavy species in the flow have been determined by optical spectroscopic analysis. In air plasma flows, the rotational and vibrational temperatures are obtained by fitting the N_2^+ experimental spectra with the simulated one. In argon plasma flows, the temperature was determined using the Boltzmann plot method by analyzing the atomic emission spectra.

	Argon	80% N_2 / 20% O_2
Velocity (m.s ⁻¹)	5500	6200
Temperature (K)	2300(T_{exc})	3500(T_{rot}) 9000(T_{vib})
Electron density (m ⁻³)	1.2×10^{18}	3.5×10^{18}
Electron temperature (K)	3900	10.000

Table 3 - Plasma flow parameters at the nozzle exit.

Configuration 1: blunt body

Two identical blunt bodies are used for this experiment. The model is hollow and made of alumina. Inside of one of them, a set of permanent magnets fills the cavity; inside the other one, the cavity is filled with a piece of iron. A movable arm positioning them alternately in the plasma flow during the experiments supports the blunt bodies. A position on the system can keep both of them outside of the plasma flow, to protect them from the strong heat flux. The positioning of the bodies with respect to the nozzle is adjusted by moving the plasma generator vertically and horizontally. The blunt bodies are centered according to the exit nozzle at a distance of 5 cm. Figure 20 presents a photo of the models in an argon plasma flow.

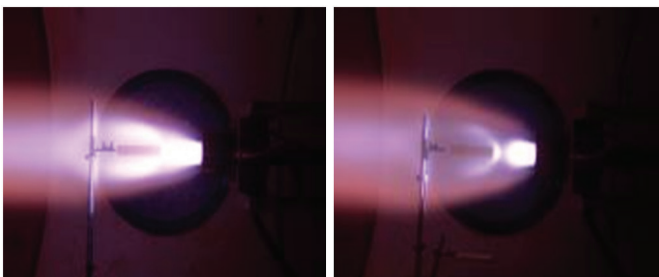


Figure 20 - Argon plasma flow around the blunt body without magnetic field (left panel) and with magnetic field (right panel)

The effect of the magnetic field can be observed clearly in Figure 20, where the bow shock around the blunt body is weaker; however, a strong radiating region remains upstream of the blunt body, and the thickness of the shock wave is slightly increased. In addition, the total diameter of the plasma flow is slightly increased because of the magnetic field. The light emitted by the excited species provides detailed information regarding the flow field. The plasma radiation is visualized with an iccd camera, which allows the analysis of the flow field behavior subject to the magnetic field effects. The images acquired in argon and air plasma flows are

presented in Figures 21 and 22, respectively. In the case of air plasma, the strong influence of the magnetic field upstream of the blunt body, producing a strong attraction of the plasma and increasing the radiation emission in this region, is particularly noteworthy.

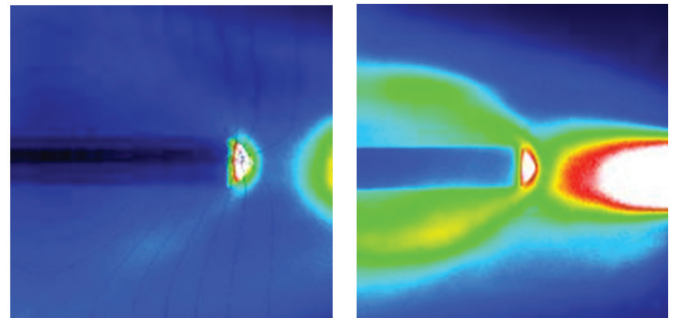


Figure 21 - Iccd images of the flow field obtained in argon around the blunt body without magnetic field (left panel) and with magnetic field (right panel)

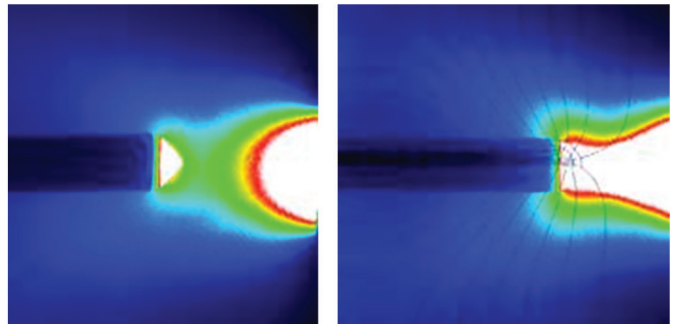


Figure 22 - Iccd images of the flow field obtained in air plasma around the blunt body without magnetic field (left panel) and with magnetic field (right panel)

The temperature of the plasma in the bow shock region was determined from spectroscopic measurements. The influence of the magnetic field produces a decrease by 30% in the argon temperature in the bow shock region, because the determined temperature is $T = 2160$ K without magnet and $T = 1511$ K with the magnet, with an estimated accuracy of 2%. In air plasma flows, the rotational and vibrational temperatures were obtained from the N_2^+ spectral emission in the bow shock region. The global intensity emission increases with the effect of the magnetic field. In the region of the bow-shock formed in front of the blunt body without magnetic field, the rotational and vibrational temperatures are equal to 4000 K while the vibrational temperature increases up to 5300 K with the presence of the permanent magnets inserted in the blunt body, representing an increase by 37% with an accuracy of 5%. Measurements of the electron density and temperature around each blunt body are carried out with a plane electrostatic probe positioned 20 mm upstream of the blunt body and at a height of 4 mm. The probe current is modified by the presence of the magnetic field, making the ion current higher and the electron current lower. The same behavior is observed in air plasma. In both cases, argon and air plasma flows, the magnetic field produces a decrease by 52.7% and 79% in the electron density, respectively, and an increase by 38% and 42% in the electron density, respectively. The electrostatic probe was replaced by a Pitot tube, in order to measure the total pressure in the same location as the electron parameters. Values also show a decrease in the total pressure of 8.4% and 9.5% in argon and air plasma, respectively, around the blunt body equipped with the permanent magnets.

Configuration 2: flat plate

The other configuration investigated in this work concerns the flow field around a flat plate and the modification of the boundary layer induced by the presence of a magnetic field perpendicular to the flat plate surface.

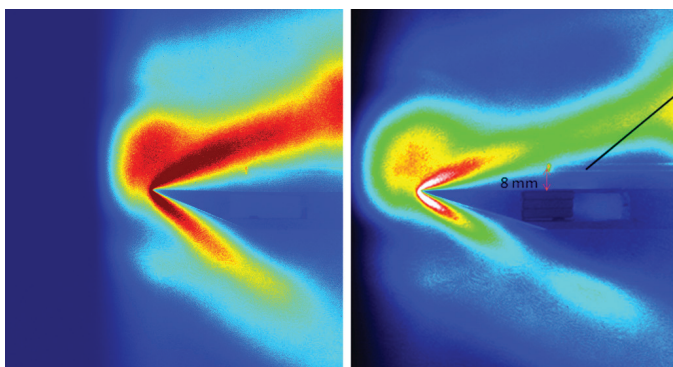


Figure 23 - LCCD images of the flow field obtained in argon around the flat plate without magnetic field (left panel) and with magnetic field (right panel)

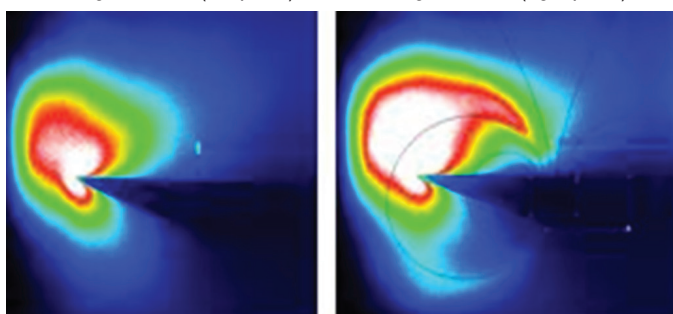


Figure 24 - LCCD images of the flow field obtained in air plasma around the flat plate without magnetic field (left panel) and with magnetic field (right panel)

The flow field modification in argon plasma flows is presented in Figure 23, which shows that the boundary layer is affected in the region above the magnet. The light intensity emitted from excited species decreases in a zone where the magnetic field lines are more or less perpendicular to the surface plate. The electron density and temperature were estimated from the Langmuir probe measurements performed at distances of 8 mm and 16 mm from the surface of the flat plate. The flow at 8 mm is not affected by the magnetic field and the electron value parameters confirm this observation. However, at 16 mm, where the boundary layer is strongly affected, the electron density decreases by 13% while the electron temperature increases by 32%.

In air plasmas, the flow field around the flat plate is quite different and the modification produced by the magnetic field does not have the same behavior as in argon plasmas, as can be observed in Figure 24. The plasma follows the magnetic field, creating a circular zone that seems to be more luminous and presents higher electron density and temperature.

This experimental work has shown substantial modifications of the plasma flow field interacting with relatively low magnetic field values and shows that the modifications strongly depend on the plasma nature ■

Acknowledgements

Romain Jousso's fellowship is provided by the Investissement d'Avenir program of the French Government: Laboratoire d'Excellence CAPRYSES (Grant No. ANR-11-LABX-0006-01). Additional funding is provided by the Région Centre with the PASS grant (Convention No. 00078782).

References

- [1] V.M. FOMIN, P.K. TRETYAKOV, J.P. TARAN - *Flow Control Using Various Plasma and Aerodynamics Approaches (short review)*. *Aerosp. Sci. Technol.* 8(5):411–21 (2004)
- [2] P. BLETZINGER, B.N. GANGULY, D. VAN WIE, A. GARSCADDEN - *Plasmas in High Speed Aerodynamics*. *J. Phys. D: Appl. Phys.* 38(4):R33–57 (2005)
- [3] E. MOREAU - *Airflow Control by Non-Thermal Plasma Actuators*. *J. Phys. D: Appl. Phys.* 40(3):R605–36 (2007)
- [4] S.B. LEONOV - *Review of Plasma-Based Methods for High-Speed Flow Control*. *AIP Conf. Proc.* 1376:498–502 (2011)
- [5] L. WANG, Z.B. LUO, Z.X. XIA, B. LIU, X. DENG - *Review of Actuators for High Speed Active Flow Control*. *Sci. China Tech. Sci.* 55(8):2225–40 (2012)
- [6] J.R. ROTH - *Aerodynamic Flow Acceleration Using Paraelectric and Peristaltic Electrohydrodynamic Effects of a one Atmosphere Uniform Glow Discharge Plasma*. *Phys. Plasmas* 10(5):2117–26 (2003)
- [7] C.L. ENLOE, T.E. MCLAUGHLIN, R.D. VAN DYKEN, K.D. KACHNER, E.J. JUMPER, T.C. CORKE - *Mechanisms and Responses of Single Dielectric Barrier Plasma Actuator: Plasma Morphology*. *AIAA J.* 42(3):589–94 (2004)
- [8] R. DURSCHER, S. ROY - *Three-Dimensional Flow Measurements Induced from Serpentine Plasma Actuators in Quiescent Air*. *J. Phys. D: Appl. Phys.* 45(3):035202 (9 pp.) (2012)
- [9] R. JOUSSOT, A. LEROY, R. WEBER, H. RABAT, S. LOYER, D. HONG - *Plasma Morphology and Induced Airflow Characterization of a DBD Actuator with Serrated Electrode*. *J. Phys. D: Appl. Phys.* 46(12):125204 (12 pp.) (2013)
- [10] R.L. KIMMEL, J.R. HAYES, J.A. MENART, J. SHANG - *Effect of Surface Plasma Discharges on Boundary Layers at Mach 5*. *AIAA Paper No.* 2004-509 (2004)
- [11] E. MENIER, L. LEGER, E. DEPUSSAY, V. LAGO, G. ARTANA - *Effect of a dc Discharge on the Supersonic Rarefied Air Flow Over a Flat Plate*. *J. Phys. D: Appl. Phys.* 40(3):695–701 (2007)
- [12] S.B. LEONOV, D.A. YARANTSEV - *Near-Surface Electrical Discharge in Supersonic Airflow: Properties and Flow Control*. *J. Propul. Power* 24(6):1168–81 (2008)

- [13] P. GNEMMI, C. REY - *Plasma Actuation for the Control of a Supersonic Projectile*. J. Spacecraft Rockets 46(5):989–98 (2009)
- [14] P.Q. ELIAS, B. CHANETZ, S. LARIGALDIE, D. PACKAN, C. LAUX - *Mach 3 Shock Wave Unsteadiness Alleviation Using a Negative Corona Discharge*. AIAA J. 46(8): 2042-9 (2008)
- [15] V.E. SEMENOV, V.G. BONDARENKO, V.B. GILDENBURG, V.M. GUBCHENKO, A.I. SMIRNOV - *Weakly Ionized Plasmas in Aerospace Applications*. Plasma Phys. Contr. F. 44(12B):B293–305 (2002)
- [16] J. MENART, J. SHANG, C. ATZBACH, S. MAGOTEAUX, M. SLAGEL, B. BILHEIMER - *Total Drag and Lift Measurements in a Mach 5 Flow Affected by a Plasma Discharge and a Magnetic Field*. AIAA Paper No. 2005–947 (2005)
- [17] A. KLIMOV, V. BITYURIN, Y. SEROV - *Non-Thermal Approach in Plasma Aerodynamics*. AIAA Paper No. 2001–348 (2001)
- [18] V.A. BITYURIN, A.I. KLIMOV - *Non-Thermal Plasma Aerodynamics Effects*. AIAA Paper No. 2005–978 (2005)
- [19] S.B. LEONOV, D.A. YARANTSEV, V.G. GROMOV, A.P. KURIACHY - *Mechanisms of Flow Control by Near-Surface Electrical Discharge Generation*. AIAA Paper No. 2005–780 (2005)
- [20] J. SHIN, V. NARAYANASWAMY, L.L. RAJA, N.T. CLEMENS - *Characterization of a Direct-Current Glow Discharge Plasma Actuator in Low-Pressure Supersonic Flow*. AIAA J. 45(7):1596–605 (2007)
- [21] E. MENIER - *Influence d'une décharge électrique continue sur un écoulement supersonique raréfié*. Ph.D. thesis, Université d'Orléans, France (2007)
- [22] V. LAGO, R. JOUSSOT, J.D. PARISSÉ - *Influence of the Ionization Rate of a Plasma Discharge Applied to the Modification of a Supersonic Low Reynolds Number Flow Field Around a Cylinder*. J. Phys. D: Appl. Phys. 47(12):125202 (13 pp.) (2014)
- [23] R. JOUSSOT, V. LAGO, J.D. PARISSÉ - *Quantification of the Effect of Surface Heating on Shock Wave Modification by a Plasma Actuator in a Low-Density Supersonic Flow Over a Flat Plate*. Exp. Fluids 56(5):102 (18 pp.) (2015)
- [24] W. SEARS - *Magnetohydrodynamic Effects in Aerodynamic Flows*. ARS J. 29(6):397-406 (1959)
- [25] R.W. ZIEMER - *Experimental Investigation in Magneto-Aerodynamics*. ARS J. 29(9):642-7 (1959)
- [26] A. CRISTOFOLINI, C.A. BORGHI, M. CARRARO, G. NERETTI, L. BIAGIONI, G. FANTONI, A. PASSARO - *Experimental Investigation on the MHD Interaction Around a Sharp Cone in an Ionized Argon Flow*. AIAA paper N° 2006-3075 (2006)
- [27] A. GÜLHAN, B. ESSER, U. KOCH, F. SIEBE, J. RIEHMER, D. GIORDANO, D. KONIGORSKI - *Experiments on Heat-Flux Mitigation by Electromagnetic Fields in Ionized Flows*. AIAA paper N° 2009-3725 (2009)
- [28] T. YOSHINO, T. FUJINO, M. ISHIKAWA - *Possibility of Thermal Protection in Earth Re-Entry Flight by MHD Flow Control with Air-Core Circular Magnet*. IEEE T. Electr. Electr. Eng. Vol. 4, No. 4, 2009, pp. 510-517.
- [29] V. LAGO, E. TINON - *Experimental Investigation of Supersonic Plasmas Flow Fields Modification by Magnetic Fields*. AIAA paper N° 2012-5869 (2012)
- [30] W.D. HAYES, R.F. PROBSTEIN - *Hypersonic Flow Theory*. Vol. I Inviscid flows. Academic Press, New York (1966)
- [31] A. AMBROSIO, A. WORTMAN - *Stagnation Point Shock Detachment Distance for Flow Around Spheres and Cylinders*. ARS J. 32(2): 281-1 (1962)
- [32] K.T.A.L. BURM, W.J. GOEDHEER, D.C. SCHRAM - *The Isentropic Exponent in Plasmas*. Phys. Plasmas 6(6):2622–7 (1999)
- [33] I. ADAMOVICH, I. CHOI, N. JIANG, J. KIM, S. KESHAV, W. LEMPERT, E. MINTUSOV, M. NISHIHARA, M. SAMIMY, M. UDDI - *Plasma Assisted Ignition and High-Speed Flow Control: Non-Thermal and Thermal Effects*. Plasma Sources Sci. T. 18(3):034018(13 pp.) (2009)
- [34] R. JOUSSOT, V. LAGO, J.D. PARISSÉ - *Efficiency of Plasma Actuator Ionization in Shock Wave Modification in a Rarefied Supersonic Flow Over a Flat Plate*. AIP Conf. Proc. 1628:1146-53) (2014)
- [35] P. TARDY, M.A. DUDECK - *Magnetohydrodynamic Velocimetry of a Low-Pressure Plasma Jet*. Rev. Sci. Instrum. 63(8):3985-8 (1992)
- [36] V. LAGO - *Mesures des températures électronique et rotationnelle dans des jets supersoniques des plasmas d'air et d'azote*. Ph.D. thesis, Université Paris XI, France (1993)

Acronyms

MHD	(magnetohydrodynamics)
EHD	(electrohydrodynamics)
dbd	(dielectric barrier discharge)
dc	(direct current)
iccd	(intensified charge-coupled device)
CFD	(computational fluid dynamics)



Romain Jousso obtained his Master's degree in Physics and Applications from the Univ. of Orléans (France) in 2007 and received his Ph.D. in Plasma Physics in 2010 from the same institution. Since 2013, he has been working as a postdoctoral fellow at ICARE (CNRS) in Orléans. His research interests include experimental investigations on flow control by plasma actuators. His current studies involve the study of various types of discharges applied to subsonic flows and supersonic rarefied flows.



Sandra Coumar graduated from EPF and is currently doing her Ph.D. on the FAST platform (Facilities for Aerothermodynamics & Supersonic Technologies) at ICARE (CNRS) in Orléans. Her work concerns the physical mechanisms induced by plasma actuators applied to rarefied and supersonic flow control.



Viviana Lago holds the position of Research Engineer since 1996 at the CNRS at the Laboratoire d'Aérothermique and then at ICARE in Orléans where she is the scientist manager of the 'Fast' platform: Facilities for Aerothermo-dynamics and Supersonic Technologies. She graduated from Paris XI University in Fundamental Physics in 1990. She obtained the Ph.D. in 1993 from the Université Paris XI, Orsay specialized in 'Gas and Plasmas Physics', and the Research Habilitation Degree in 2013 at the Univ. of Orléans. Her research fields concern experimental investigations on: plasma physics, rarefied gas dynamics, re-entry and hypersonic aerodynamics, thermo-chemical non-equilibrium flows and high-temperature thermo-chemistry and plasma flow control applied to super/hypersonic flows. She is a member of the 3AF Aerodynamic Committee and a member of the 3AF 'Groupe Régional Centre'.

G. Dufour, F. Rogier
(ONERA)

E-mail: Guillaume.Dufour@onera.fr

DOI : 10.12762/2015.AL10-05

Numerical Modeling of Dielectric Barrier Discharge Based Plasma Actuators for Flow Control : the COPAIER/CEDRE Example

Numerical simulation of active flow control using plasma actuators is dependent upon the development of models accounting for the effects of the actuators on the flow. These can be obtained either by using experimental results coupled with strong assumptions regarding the plasma force distribution, or through numerical simulation. The objective of this paper is to investigate the characteristics of DBD plasma source terms obtained using direct numerical simulation. Using ONERA's in-house plasma solver COPAIER, we propose an insight of a complete chain of numerical models, ranging from the plasma discharge description to the computation of a DBD-induced ionic wind.

Introduction

Flow control with active actuators requires efficient, robust, easy to integrate and low energy consumption devices. Among these, Dielectric Barrier Discharge (DBD) actuators have already demonstrated their efficiency in delaying flow separation or turbulence effects [5]. Following these promising results, some numerical studies have been conducted in order to estimate the effects of such actuators in other situations and also to try to determine their best locations and operating conditions [6]. As far as flow control is concerned, these numerical simulations involving plasma actuators are mainly focused on the aerodynamical effects and, in order to model the plasma actuator, simplified source term expressions are used, with regard to both the geometrical and temporal aspects. Indeed, in such studies, the effects of Dielectric Barrier Discharges are mainly considered to be localized in a small rectangular area around the tip of the exposed electrode and the total exerted force is assumed to be uniformly distributed within this volume. The mean value of the source term is then fixed using some experimental measurements [5]. As for exploring the time-modulation of the actuator effects, periodic Heaviside-shaped functions are considered, the only remaining parameters being the duty cycle and the operating frequency [6]. In order to obtain a more accurate source term describing the plasma actuator, it can be reconstructed from the Navier-Stokes equations using experimental measurements, such as the gas velocity distribution, and some simplifying assumptions such as neglecting the pressure gradient [9]. Another idea is to completely model the discharge numerically and then to estimate the electric force exerted by the plasma on the flow from the computed

electric field, the charged species densities and their velocities. Such numerical simulations are particularly challenging and some strategies, such as asynchronous [3] or implicit [14] [15] [16] ones, have been tested in order to tackle these multiscale problems.

In this paper we will investigate how this last approach is developed within the plasma solver COPAIER developed at ONERA, focusing on a particular sinusoidal DBD actuator. In a first section, we will describe the physical model used for the plasma. Then, in a second part, the numerical hurdles inherent to this model will be presented, as well as the numerical methods used in COPAIER, in order to overcome them. In a third section, the specific test-case of DBD actuation will be presented, as well as its numerical discretization. The dynamics of its discharge will be explained thoroughly in the next part. Then, the estimate of the electric force will be discussed in a fifth section. Finally, in the last two parts, the coupling of the COPAIER solver with the in-house Navier-Stokes solver CEDRE is presented and the effect of the time resolution of the source term will be investigated.

Plasma Model

The simulation of the dynamics of all of the species composing the plasma is based on the resolution of conservation equations for the densities of the species taken into account. These equations can be written in the generic form:

$$\partial_t n_i + \nabla_x \cdot (n_i v_i) = S_i$$

where n_i is the density of the i -th species and v_i is its velocity. The right-hand term S_i describes the kinetic source term accounting for the creation (or destruction) of the charged species. The velocities should, in theory, be obtained by solving a similar equation for the momentum. Nevertheless, the inertia of charged particles being very low, the COPAIER solver assumes that the velocity is given by a mobility law depending on the local flow velocity and Electric Field. This mobility law is written as follows:

$$v_i = U_g + \mu_i E + D_i \frac{\nabla_x n_i}{n_i}$$

where U_g is the surrounding flow velocity, E is the electric field and μ_i and D_i are respectively the mobility and diffusion coefficients of the considered species. As for the Electric Field, E , it is assumed to be the solution of a Poisson equation.

$$-\nabla \cdot (\varepsilon E) = \rho \quad ; \quad E = -\nabla \varphi$$

$$\rho = \sum_i n_i q_i$$

where ρ is the volumic charge induced by the charged species, ε is the local permittivity of the material and φ is the Electric Potential. It is assumed that the boundary conditions allowing the Poisson equation to be solved are either of Dirichlet type (anode and cathode) or of Neumann type (exterior boundaries).

The source term S_i describes the kinetics responsible for the creation of the charged species. Numerous kinetics models exist for atmospheric plasma discharges, involving different numbers of species [8]. In order to limit the number of species and reactions to be considered, some studies consider plasma discharges in nitrogen where the kinetics can be described using two reactions and three species only. However, one key-point of discharges in air is the possibility of creating negative ions by attaching electrons to dioxygen, which is not possible using only nitrogen. Although the user of the COPAIER solver could define a set of hundreds of species and reactions to model the kinetics, he would face major problems due to a heavy computational load, so it is of prime importance to limit the complexity of this part. Thus, henceforth we will consider, as proposed by J.-P. Boeuf in [2], a reduced model for the kinetics, composed of electrons and three species N_n , N_p and N_m , standing respectively for the neutral, positive and negative ions. The set of reactions to be considered can then be limited to only four, as described in the following Table 1.

Name	Description	Coeff.
Ionisation	$N_n + e \rightarrow N_p + 2e$	k_i
Attachment	$N_n + e \rightarrow N_m$	k_a
Electron-ion Recombination	$N_p + e \rightarrow N_n$	k_R
Ion-ion Recombination	$N_p + N_m \rightarrow N_n$	k_R

Table 1 - Reduced kinetics

It must be noted that these coefficients depend on the local electric field. In particular, no ionization occurs if the electric field magnitude is lower than the breakdown value for air. The BOLSIG+ solver [4] provides values for all coefficients (ionization, attachment, etc.) for

both nitrogen and dioxygen. The values for the coefficients associated with the reactions defined here are then calculated so that they are consistent with the composition of N (20% dioxygen and 80% nitrogen) and can be found in [17].

For the kind of discharge that we are interested in, it has already been shown that the photoionization process does not play an important role and may instead induce a higher computational burden [13]. Its interest is limited to the spontaneous creation of electrons out of neutral particles in order to guarantee a minimum density of electrons available for the ionization process. In this model, this phenomenon is not considered and, instead, a minimum density has been introduced for each species. Practically, this minimum has not been reached during our simulations.

Furthermore, some specific phenomena must be considered for the plasma dynamics. These are of two kinds: the first is the secondary emission of electrons at both the cathode and dielectric surface. Denoting the positive and electronic fluxes at these surfaces by J_+ and J_e respectively, there is a secondary emission coefficient g , depending on the material of the surface, such that $J_e = -\gamma \cdot J_+$. Obviously, when an AC voltage is used, the stressed electrode plays the role of an anode and a cathode alternatively. It must be noted that in the anode alternative, the incoming positive ion flux is assumed to be zero so that no secondary emission occurs during this phase.

The other phenomenon describes the fact that some charged species can be trapped on the surface of a dielectric material and then act as a surface charge for the Poisson equation. This induces a discontinuity for the electric field in the direction normal to the surface of the dielectric material:

$$[[\varepsilon E \cdot \vec{n}]] = \sigma$$

Finally, the electric force exerted on the fluid can be modeled using the electric field and the densities of the charged species. It can be written as:

$$F = \sum_i n_i q_i E$$

Solving this model is challenging, since it is heavily multiscale in both space and time; this point has already been reported in other references, with similar models and setups; see for example [3], [14], [15] or [16]. In these studies, these problems have been tackled either by using specific numerical approaches (asynchronous or implicit schemes) or by focusing on lower voltages and/or higher frequencies. We will recall here the main reasons explaining why this problem is multiscale. Firstly, more than the obvious scale difference between the actuator size (some centimeters) and the characteristic length of the flow when dealing with drag reduction (about one meter or more), the plasma model introduces its own scale differences in size and, as a consequence, in time. In order to illustrate this point, let us consider the case of electron dynamics. We first must remark that the Electric Field generated has a singular point near the tip of the stressed electrode (illustrated in Figure 5), introducing steep variations over very small distances. Describing this effect accurately thus requires the consideration of very small characteristic lengths, even smaller than the anode thickness, which is of about 70 micrometers. Moreover, given that the electronic mobility is dependent on the electric field value, their drift velocity is large in this area. The characteristic time associated with the transport phenomenon can then be

defined as the ratio between the characteristic length and the velocity, leading to characteristic times as small as some picoseconds. Nevertheless, this multiscale aspect is not limited to the tips of the stressed electrodes. Indeed, when the densities of charged species are high enough, the effect of the local charge on the electric field must be considered, introducing a new characteristic length, known as the Debye length:

$$\lambda_D = \sqrt{\frac{\epsilon k_B T_e}{n_e q_e^2}}$$

For atmospheric plasma discharges such as those that we are interested in, for an electronic temperature around 10000 K and an electronic density that can be as high as 10^{18} m^{-3} , the Debye length can shrink rapidly down to one micrometer, introducing a three order scale difference between the geometry of the electric field and the actuator size, which is generally millimetric. Other phenomena, such as ion kinetics, also have characteristic times depending on the electric field values, although their dynamics might not be the most constraining ones. The table below sums up the different time scales that we have to deal with when trying to simulate an atmospheric plasma discharge.

Phenomenon	Characteristic time
Transport of electrons	From 1 ns to 1 ps
Electric field variations	From 1 μs to 0.01 ns
Kinetics	From 0.1 to 10 μs
Transport of heavy species (ions)	From 0.1 to 1 ns
Plasma dynamics	From 0.01 to 0.1 ms
Ionic wind	About 1 ms

Table 2 - Characteristic times for a plasma discharge

Numerical methods used in COPAIER

Turning to numerical models, the multi-scale aspect discussed in the model translates into two different notions, which are the mesh size and the time step. As regards the first one of these, a refined mesh must be used, at least locally, in order to accurately solve the electric field profile. Nevertheless, in order to correctly describe the experimental set-up, the size of the computational domain must remain large enough, which can lead to computations involving a huge number of unknowns if the mesh size is almost constant.

In order to overcome this difficulty, the COPAIER solver is able to simultaneously use two types of meshes. On the one hand, a structured mesh based on quadrangles can be used where precision is needed. It is well-known in the Applied Mathematics community that structured meshes allow for better (precision-wise) and often faster numerical results, but also introduce numerous unneeded mesh cells where mesh refining is concerned. On the other hand, an unstructured triangle-based mesh enables complex actuator geometries to be taken into account and also enables less-refined mesh zones to be easily defined, in order to limit the number of Degrees of Freedom (DOFs). This aspect is illustrated in Figure 4.

For the time step, the major hurdle is to deal with the multi-scale aspect of the model. The simplest way to tackle this would obviously be to numerically solve all phenomena using the most constrained time step. Unfortunately, some equations, such as the Poisson equation for the Electric Field, require relatively high computational times so this approach would not be able to provide numerical results within a reasonable time. As a consequence, a different approach has been chosen in COPAIER. As explained previously, the numerical model for plasma discharges can be split into three different parts (drift-diffusion, kinetics and the Poisson equation). Each of these will then be dealt with using a specific numerical method, which allows for adapted time-integration strategies such as sub-cycling (for the phenomena with the smallest time steps) and splitting methods. For this last point, given that all of the numerical methods used in COPAIER are second-order accurate in time, the Strang splitting strategy, which guarantees a second-order accurate coupling, has been used. We will now briefly explain the various numerical methods used to solve all of the equations of the plasma model.

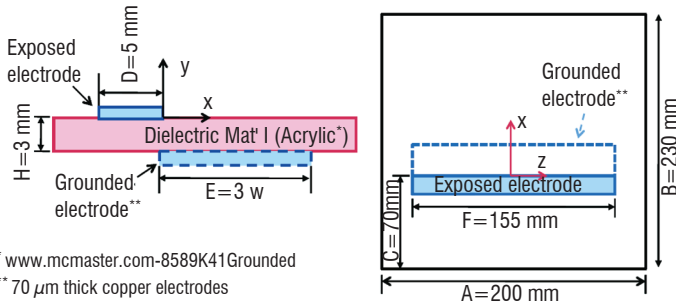
In order to solve the drift-diffusion equation, a Finite Volume approach, which is well-suited when dealing with conservation equations, has been chosen. More precisely, the fluxes at each edge of the mesh are estimated using a MUSCL reconstruction, ensuring a second-order (space-wise) approximation [18]. This kind of method requires an estimate for the gradient of the density profile. When the mesh is unstructured, a dual-mesh algorithm using the Green formula to estimate the gradient is implemented. The time-integration part is performed using the Heun Method, which is known to be conditionally stable (the time step must comply with the classic CFL condition) and also second-order accurate in time.

The Finite Element Method has been used to solve the Poisson equation. In order to remain consistent with the accuracy provided by the numerical scheme used for the transport of the species, a P1-Finite Element formulation has been implemented for the unstructured mesh, while a Q1 formulation has been used for the structured part of the mesh. In order to limit the computational burden imposed by this method when refined meshes are used, a non-overlapping Schur method has been developed. It relies on a decomposition of the rigidity matrix, allowing the values of the potential on the nodes corresponding to the interface between the structured and unstructured meshes to first be determined. It must be noted that this requires either solving a linear system of size N_{interf} (i.e., the number of nodes on the interface) at each time step, or inverting the Schur matrix (of size N_{interf}^2). The efficiency of this algorithm is then lessened when the interface size grows, which should limit its use to 2D meshes. Given that the structure of the Schur matrix does not change over time, a LU decomposition is performed (only once, as a preprocessing task), in order to compute its inverse. Another matrix inversion is needed at every time step, when computing the electric field within each domain. Depending on the size of the mesh, either a direct LU decomposition or an iterative Conjugate Gradient Method can be used.

Finally, considering the kinetics dynamics, a second-order explicit Runge-Kutta method has been developed. This method is based on the estimation of a maximum time step ensuring the positivity of the components of the kinetics.

Numerical computation of a plasma actuator effect: a DBD Test-case

In this section, we will present the numerical computation of the electric force induced by a DBD-type discharge. The test-case that has been chosen corresponds to an experimental setup proposed by S. Roy [1] and illustrated in Figure 1.



* www.mcmaster.com-8589K41Grounded
** 70 μm thick copper electrodes

Figure 1 - Experimental Set-Up

Such a configuration is an interesting one to model numerically, since it has been extensively studied and its working frequency is quite high so the periodic behavior of the actuator is reached within a short time. This last point is of prime importance, since it allows us to perform numerical computations of this periodic behavior while limiting the associated computational cost.

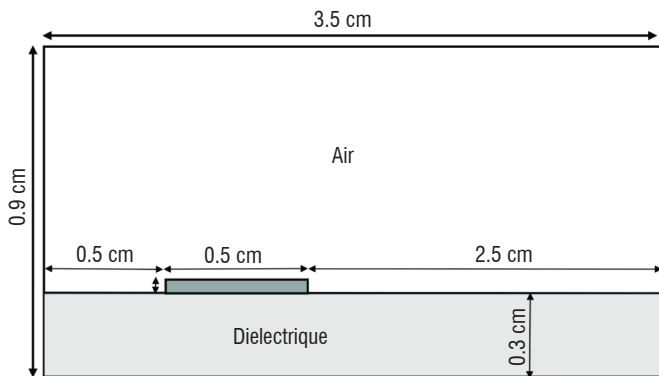


Figure 2 - Computational Domain

The experimental setup can be described numerically using a 2D computational domain defined as in Figure 2. It must be noted that the cathode does not appear on this figure; this is motivated by the absence of plasma in the area near the cathode. Thus, describing the volumic cathode would require small mesh cells where no plasma dynamics would occur.

The effect of the cathode is instead taken into account by using a Dirichlet boundary condition on the part of the lower domain boundary corresponding to the location of the cathode. The potential profile shown in Figure 3 matches the results already presented by

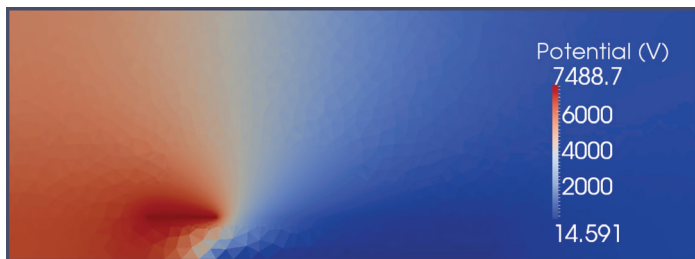


Figure 3 - Potential profile

Unfer et al in [3] for a Laplacian potential for the same configuration, which shows that this representation indeed provides a correct electric field.

The phenomena discussed in Part 2, such as the secondary emission and the electric field discontinuity at the boundary of the dielectric, are included through an identification of all the mesh edges corresponding to the surface of the dielectric or the anode. For each edge, the “incoming” flux of charged species is used either for computing the contribution of the secondary emission (modification of the flux for the electrons) or to update the accumulated charge on the surface of this part of the dielectric. The total charge on the dielectric can then be calculated at every time step through a sum of all of the charges contained within the “dielectric edges”.

With this model, the mesh used focuses on the part where precision is needed, more specifically near the surface of the dielectric and in the vicinity of the tip of the anode. In order to contain the computational cost as much as possible, the size of the mesh cells increases quickly as the distance to the anode grows. Such a strategy is well-suited for our numerical resolution of the Poisson equation. Indeed, as stated before, Neumann boundary conditions have been used for the exterior boundary, so that the profile of the computed electric field can be significantly modified if the size of the computational domain is not large enough. The use of an unstructured mesh allows us to define a computational domain large enough to neglect the effect of the Neumann condition (see again Figure 3) on the results, while limiting the number of degrees of freedom.

The structured part of the mesh contains the area where the electric field singularity is located, as is shown in Figure 5 and Figure 6, where the electric field is represented near the anode with the mesh used.

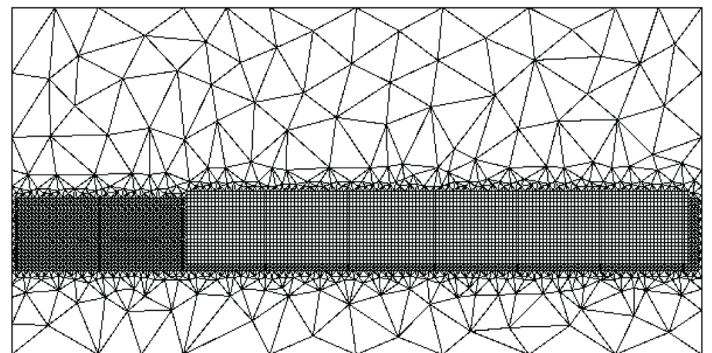


Figure 4 - Example of mesh refinement

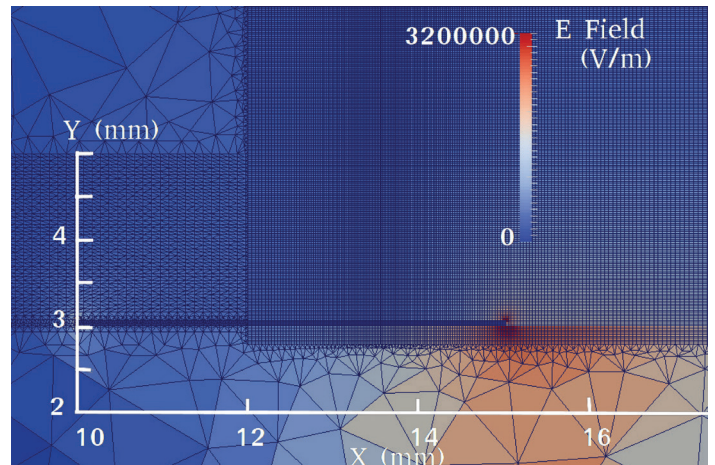


Figure 5 - Example of an electric field profile and mesh

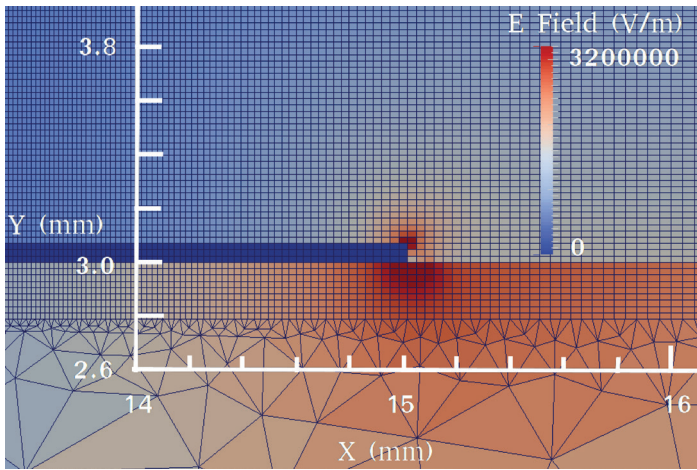


Figure 6 - Electric field singularity and mesh (zoom)

The model for the kinetics has already been discussed in Section 2. The discharge is assumed to occur in air at atmospheric pressure and ambient temperature. The accumulation of charged species at the surface of the dielectric material is taken into account. The applied potential has an amplitude of 10.5 kV, which corresponds to 21 kV peak-to-peak (ptp).

Physical parameters	
Signal shape	Sinusoidal
Applied voltage (ptp)	21 kV
Frequency	14 kHz
Relative permittivity (dielectric)	$\epsilon_r = 3$
Secondary emission coefficient	$\gamma = 10^{-4}$

The use of a structured mesh allows the precision of the results to be preserved, while limiting the number of cells used. It must be noted that the minimum mesh size corresponds to the discretization of the anode width and leads practically to dimensions comparable to the minimum Debye length attained during the discharge. This ensures that the electric field will be correctly solved even when the plasma is established.

Numerical parameters	
total number of cells	15192
Total number of edges	27361
Min mesh size	10 μm
Min time step	5.10 ⁻¹² s
Physical time simulated	300 μs

As for the initial condition, only the density profiles have to be given. We assumed that the densities of the charged species are all constant within the computational domain and an arbitrary low value of 10⁻⁹.m⁻³ has been used. The neutral density is the one measured in air at atmospheric pressure and ambient temperature, which is 2.5.10²⁶.m⁻³. The charge on the surface of the dielectric is assumed to be zero at the beginning. Practically, our computations using several different values showed that the effects of the initial conditions remain limited to the dynamics of the first period of the discharge. The COPAIER

solver version used in to simulate this test-case is single-threaded. This computation took about a week to complete, on an Intel quad-core 2.66 GHz workstation equipped with 8 GB of RAM.

Discharge Dynamics

After the first period, the discharge dynamics enters a periodic regime, with the same period T of the actuation ($T = 1/14000$ s), which can be split into four different steps. In a first part, the voltage applied to the anode rises and as soon as the Voltage breakdown value is reached, the process of ionization begins, yielding a cloud of high positive ions densities.



Figure 7 - Positive ion density – streamer beginning time = $3T + T/10$

This streamer propagates along the dielectric material while charging its surface, as represented in Figure 7 and Figure 8. Given that the density level variations may reach several orders of magnitude, the quantity represented in these figures is the logarithm of the density.

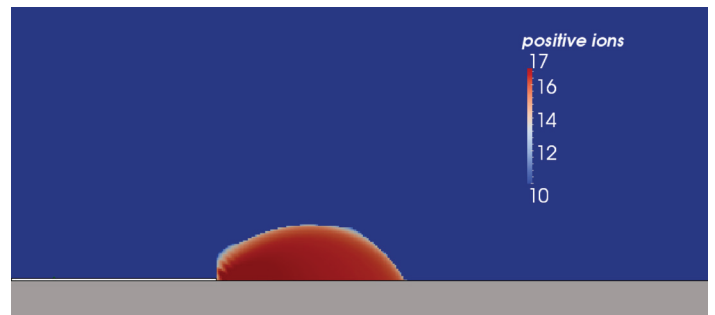


Figure 8 - Positive ions - maximum streamer extension time = $3T + T/4$

Please note that in all of the figures, the anode and dielectric part are indicated respectively by the grey and (thin) white areas, but they can also be inferred from the cloud profile: the dielectric lies at the bottom of the cloud, while the downstream tip of the anode is located at the very bottom-left corner of the cloud. This streamer leads to a modification of the electric field, as shown in Figure 9 (in this figure, only the anode and the dielectric surface have been specified). The electric force created in this phase has the shape of the ionic cloud. The density of the force is expressed in N.m⁻³ in Figure 10.

Then, after the voltage peak, the electric field decreases rapidly until its value is driven by the local charge instead of by the voltage applied to the anode, as seen in Figure 9. During this phase, the cloud of positive ions moves a little backwards toward the anode, which is represented in Figure 11.

In a third phase, the discharge enters a negative regime as the applied voltage becomes negative. During this part, the behavior of the

discharge differs significantly from that occurring during the positive part. Indeed, as the electric field reaches the breakdown value, the ionization always creates both positive ions and electrons, but the latter is no longer absorbed by the anode and instead travels very quickly towards the positive part of the dielectric surface. As a by-product, a lot of negative ions are created along the way by the electrons. Due to the high velocity of the electrons, this effect happens several times during this phase, generating pulses of high electronic and negative ion densities within low densities zones. In Figure 12 the negative ion density (on a logarithmic scale) during one pulse is represented; the production of negative ions has ended near the anode and the negative ions are attracted towards the positive area of the dielectric.

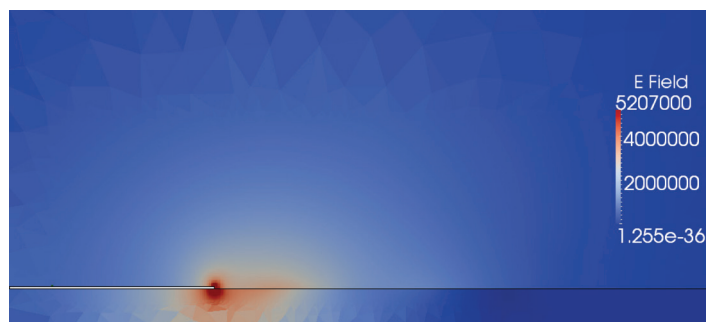


Figure 9 - E. field: (V/m): dielectric charge effect - time = $3T + T/2$



Figure 10 - Force magnitude profile in the positive part of the discharge - time = $3T + T/4$

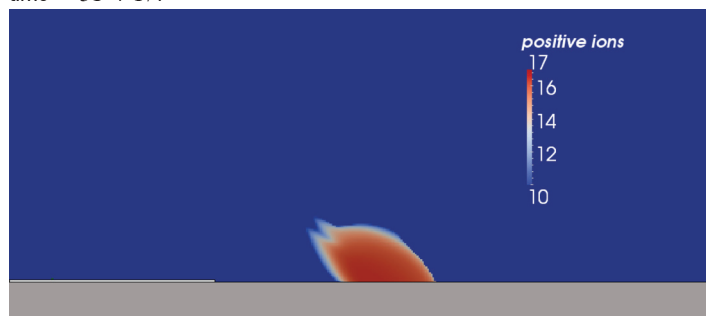


Figure 11 - Positive ions attracted back to the anode - time = $3T + 3T/8$



Figure 12 - Negative ion density - time = $3T + 3T/4$

During this step, the electric force exerted on the flow is located closer to the tip of the anode and its duration is limited to that of each pulse. In Figure 13, the force profile during one of these pulses is represented. It can be noted that the maximum value is still comparable to that obtained during the positive part, but on a much smaller scale. In this image, the two main contributions of the pulsed aspect to the electric force can be seen. Indeed, the small and intense one near the electrode tip represents the creation of the electronic high density zone, while the more diffuse part corresponds to the lesser important and slower part of the force created by the negative ions generated along the trajectory of the electrons.

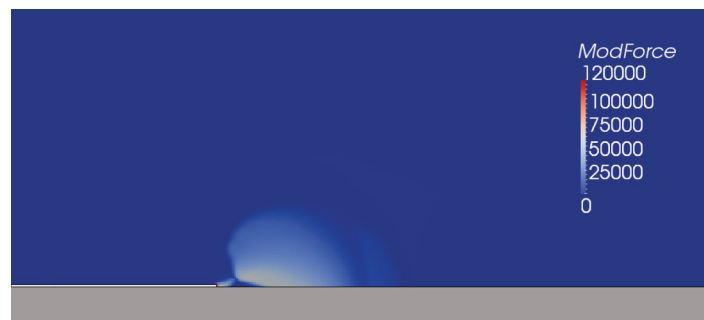


Figure 13 - Force magnitude profile during the negative part - time = $3T + 3T/4$

Finally, in a fourth phase, the potential again rises towards zero. The ionic cloud vanishes either into the anode, or by charging the dielectric surface negatively. A new cycle can then begin.

Electric force estimates

The representation of the electric force term proves to be difficult if performed both in time and space. Indeed, as stated in the previous section, the amplitude of the electric force varies very rapidly (by several orders of magnitude) both in time and space. In order to gain a proper understanding of its dynamics, we have chosen to represent either its time or space variations. More precisely, we will be interested in both of the following quantities, the first one being:

$$F_t(t) = \int_{\Omega} F(t, x) dx$$

where Ω is the whole computational domain; this represents the time variations of the total force generated by the actuator. The other term is written as

$$F_x(x) = \frac{1}{T} \int_{kT}^{(k+1)T} F(t, x) dt$$

where T is the period of the actuator; this represents the spatial distribution of the mean (in time) force exerted by the actuator on the flow. This last term is represented in Figure 14 and shows that the main part of the actuator effect on the flow will be located within the first millimeters, near the downward tip of the anode.

The time evolution of the total force exerted by the actuator follows a periodic pattern, except for the very first period of actuation. This can be seen in Figure 15, where the first four periods of the computed electric force are represented. In this figure, the blue line represents the force module while the green and red lines respectively stand for the parallel (x -) and normal (y -) forces. The evolution of these

quantities is consistent with the discharge dynamics, since we have two main behavior types. The first is a smooth curve, which is generated by the positive streamer described in the previous section, while the second shows a series of peaks, which correspond to the electronic pulses generated during the negative part of the discharge.

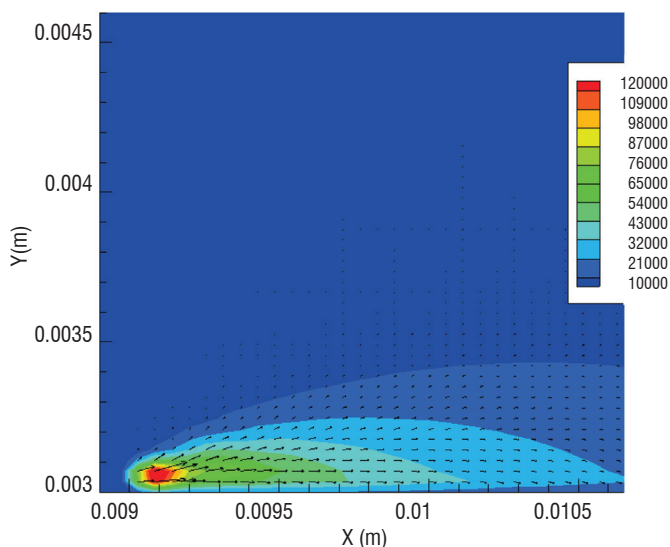


Figure 14 - Electric force profile: mean value over one period of actuation

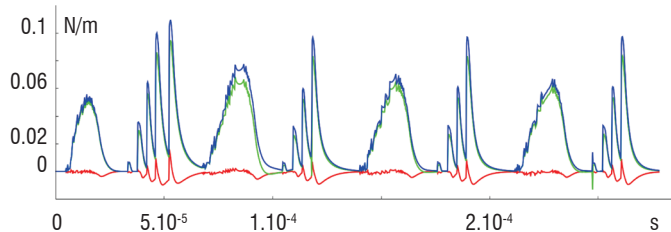


Figure 15 - Total force dynamics (N/m), first four periods at 14 kHz

The difference in the first period lies in the force exerted during the positive phase of the discharge. It can easily be explained by the initial conditions used for the numerical simulation. Indeed, at the beginning of the simulation, the densities of all species are assumed to be constant over the computational domain and the charge at the surface of the dielectric is set to zero. In fact, after the first period, the dielectric surface has a negative charge because the applied potential begins a new period, yielding higher values for the electric field generated near the tip of the anode and an earlier start of the streamer, allowing for a very important electric force being exerted on the gas.

The total deposited charge on the surface of the electrode is represented in Figure 16 and indeed shows a periodic behavior after the first two periods of the actuator. It can also be noted that the negative charge deposited during the negative part of the cycle is slightly greater than the positive one, but with a shorter duration. Given that our model is 2D and does not model the actual length of the anode, this charge is expressed in C/m (charge by unit of anode length).

We are interested in the evolution of the force during one period. In Figure 17 the force computed for the fourth period of the actuator is represented.

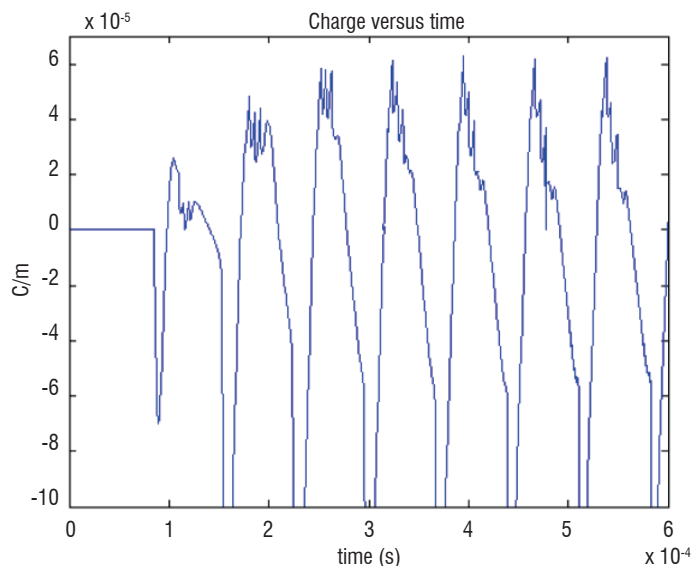


Figure 16 - Charge deposited on the surface of the dielectric material

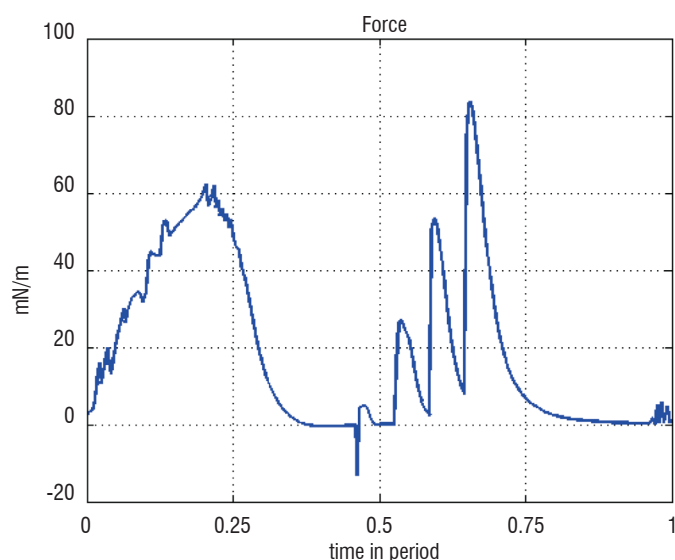


Figure 17 - Force exerted during the fourth period

We observe that the total force is mostly created during the positive part of the cycle, while the streamers triggered later in the negative part seem to hold only a minor contribution. In fact, the positive cycle describes a regime of glow discharge and the negative one is formed of successive streamers triggered at different times, depending strongly on the slope of the applied potential.

The total force generated corresponds to the mean value calculated in one period

$$F_{TOT} = \frac{1}{T} \int_{kT}^{(k+1)T} \int_{\Omega} F(t, x) dt dx$$

For our test-case, the computed value for this set-up is about 19 mN/m and the experimental value given by Durscher and Roy [1] is around 20 mN/m. Hence, the discrepancy between measurement and modeling is here less than 1mN/m, which is a good estimation, given the (relatively) low level of complexity of the modeling.

Having such a numerical model allows for a parametric study to determine the trends of the discharge dynamics and characteristic when the applied voltage or the frequency are changed.

In Figure 18 the average force time-profiles for both 7 kHz and 14 kHz actuators are represented. The dynamics of both discharges remain similar with the smooth positive part and the pulsed negative one. In terms of amplitude, it can be noted that a higher frequency yields a higher force term.

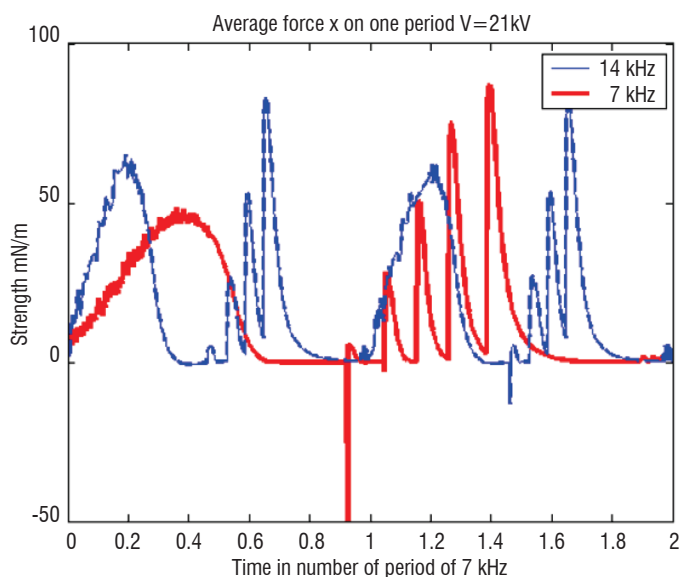


Figure 18 - Total force dynamics 14 kHz, 7 kHz

Conversely, in Figure 18, both of the average force time-profiles for two different voltages are represented. Unsurprisingly, a higher voltage creates a higher force term. It can also be noted that increasing the voltage also increases the number of pulses during the negative part of the discharge.

A parametric study of the total force variation with respect to the operating voltage has been performed. The frequency is set to 14 kHz.

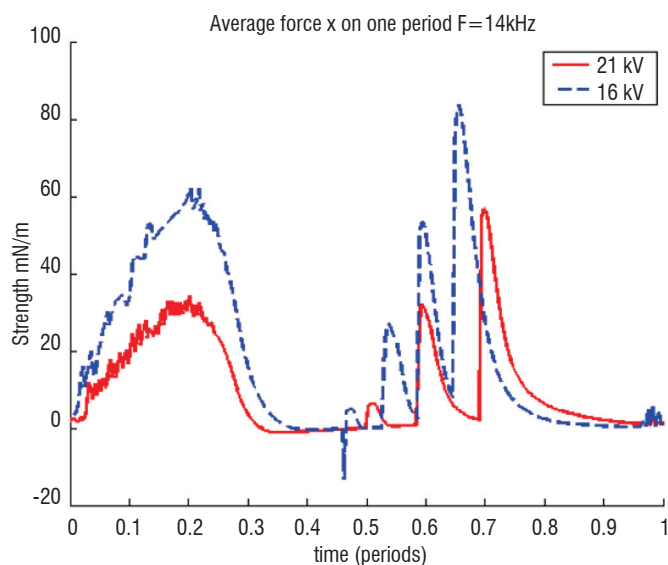


Figure 19 - Total force dynamics 16kV 21 kV

In Figure 20, the total body force for voltages ranging from 14kV to 28kV is shown. When comparing these values with the experimental results

of S. Roy [1], we observe a small discrepancy in the total body force (less than 1mN/m) for voltages of around 21kV and a larger one for low voltages. The evolution of the force with the applied voltage seems to follow the well-known “exponential law” (F of order $V^{3/2}$, represented with a red line in Figure 20), at least for low voltages. In the range of high voltages (larger than 26 kV), the body force seems to reach a threshold. This effect, numerically observed for voltages up to 32 kV (not represented here), still needs further computations, although this phenomenon has been noticed by many experimentalists in other configurations. For example, the induced velocity does not increase with the voltage for a high enough voltage [11]. This fact has also been noted by the group of J.P. Boeuf [7], which suggests that the induced velocity will eventually reach a limit.

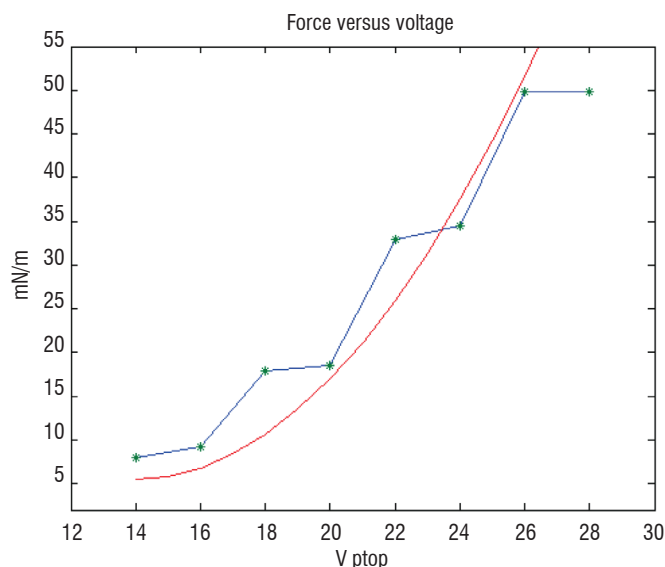


Figure 20 - Mean total force vs. applied voltage

Ionic wind estimate

In order to compare our numerical results with experimental data, we need to estimate the ionic wind generated by the discharge. For this purpose, the actuator effect will be modeled as a momentum source term in a Navier-Stokes solver. The ONERA in-house Navier-Stokes solver CEDRE [12] has been used to compute the flow created by the DBD-discharge. This flow computation corresponds to a typical flat plate case. The actuator characteristics are kept unchanged with a 21 kV (ptp) sinusoidal potential at a 14 kHz frequency.

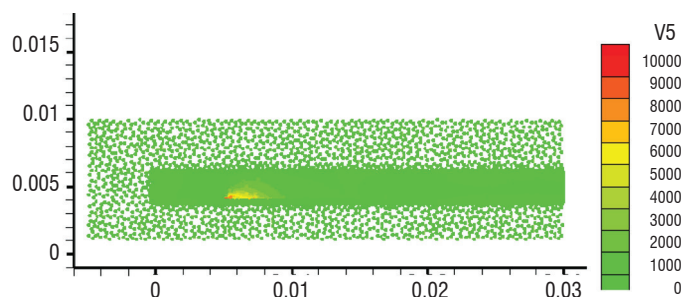


Figure 21 - Source term ($N/m^3/s$) as seen by CEDRE

The electric force, as it appears in its periodic regime, has been computed by the plasma solver COPAIER and averaged over one period. It is then introduced as a time-wise constant source term, while it varies

in space, as shown in Figure 10. More precisely, the Navier-Stokes solver considers a P1-reconstruction of the source term, which is given as point-located values. In order to avoid errors in the total force due to this interpolation, a very dense set of points has been used near the tip of the electrode. This is illustrated in Figure 21.

The computations were performed using a turbulent k- ω model, which provides a better description of the wall-jet nature of the flow [10]. The computation is an unsteady one, but what we are aiming at is a steady-state flow profile, so that this can be compared with the experimentally measured profiles.

The results are shown in Figure 22 and Figure 23 respectively for the x-component and y-component of the ionic wind velocity.

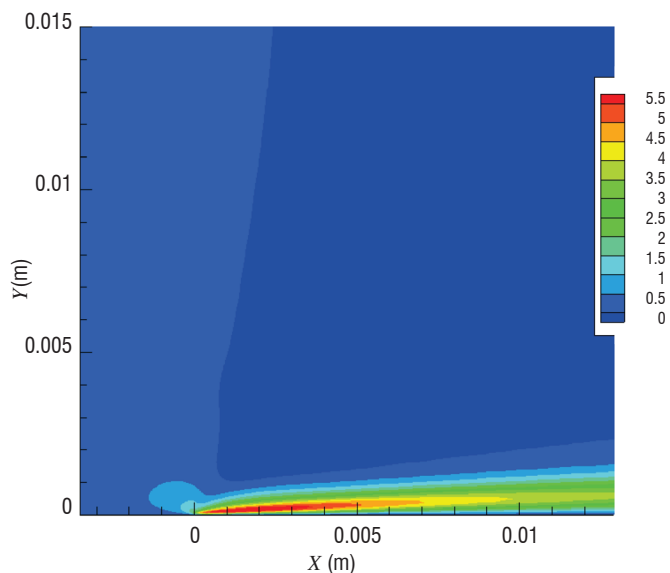


Figure 22 - Parallel (x-) velocity profile

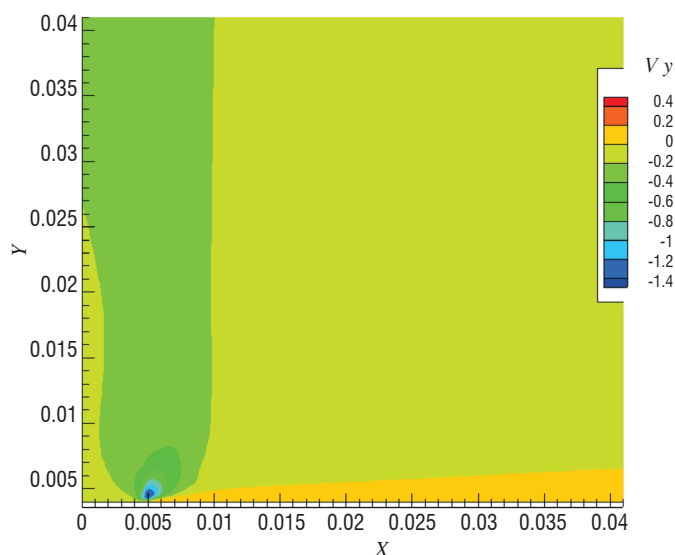


Figure 23 - Orthogonal (y-) velocity profile

In these figures, it may be noted that the ionic wind maximum parallel velocity is of about 6 m.s⁻¹ and is reached near the tip of the anode, where the electric force source term is the most important. The perpendicular velocity is negative and its maximum amplitude is of about

1.8 m.s⁻¹, which is reached a little over the exposed electrode. This zone corresponds to a suction zone.

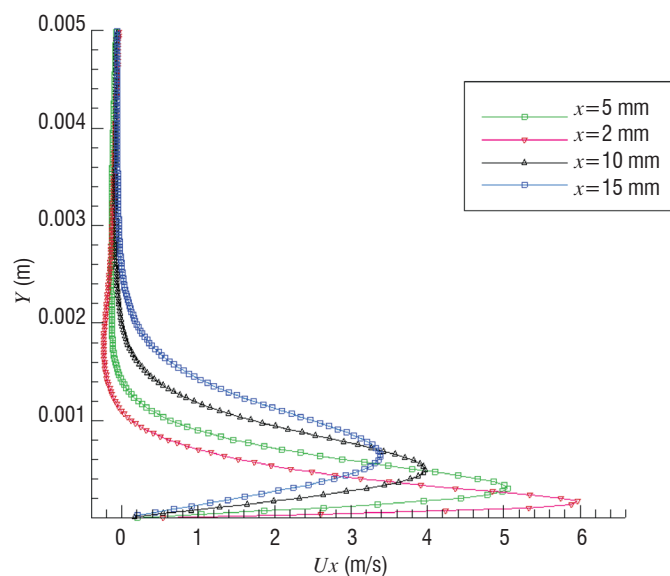


Figure 24 - Velocity y-profile for various positions downstream

The profiles of the parallel component U_x of the velocity at various locations downstream from the tip of the anode are represented in Figure 24. The effect of the actuator fades as the distance increases. These numerical results can be compared with the experimental measurements of ionic wind velocities from Durscher and Roy in [1]. The location of the probe is 15 mm downstream from the tip of the anode.

It can be seen in Figure 25 that the shape of the experimental and computed curves is similar, but the “width” of the wind created experimentally seems to be larger than that computed. While the order of magnitude for the velocity is correct, the difference between the maximum values remains significant (about 5 m/s for the experiment against 3.5 m/s for the computation).

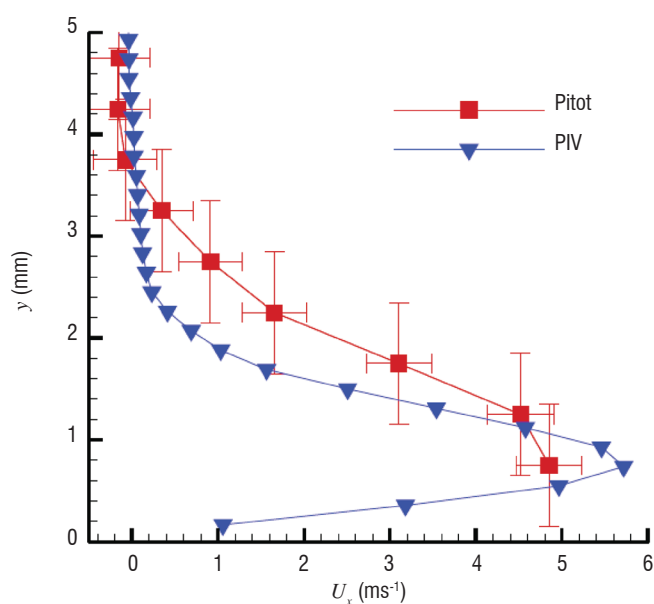


Figure 25 - Experimental velocity y-profile, probe at location $x=15$ mm, from S. Roy et al [1]

Ionic wind profile: influence of the temporal dynamics of the source term

In the previous section, the effect of the actuator on the flow has been assumed to remain constant, given the short period of the actuator. Nevertheless, the time-profile of the space-integrated electric force shown in Section 5 indicates that the actual effect of the actuator does not exactly consist in a continuous medium-amplitude effect, but rather in short pulses of a high amplitude force. In order to investigate the possibility of coupling between the time-dynamics of the actuator and the aerodynamics, allowing for a better efficiency of the ionic wind generation, another computation has been set-up.

In this numerical test, the source term is no longer assumed to be constant in time, but rather is approximated using a piecewise-constant function. We then define a sequence of ten different source-term profiles, each one representing the mean effect of the actuator during a tenth of an actual period. They are defined as follows:

$$F_x^k(x) = \frac{10}{T} \int_{2T+(k-1)\frac{T}{10}}^{2T+k\frac{T}{10}} F(t,x) dt$$

Obviously, this piecewise approximation preserves the mean force value over one period, so that this test-case can be compared force-wise with that described in Section 7. It must be noted that, as stated in the introduction of this paper, many numerical experiments have already been conducted in order to determine the effect of the duty

cycle of a plasma actuator on the aerodynamics [6]. The study proposed here differs significantly from these by modifying both the temporal and spatial distribution of the force source term created by the actuator. More precisely, instead of just adjusting the amplitude of the source term, the changes of its shape throughout the actuator period are also taken into account, performing the complete simulation of the discharge. However, in order to save computational time, the objective remains to use a source term pre-processed by the COPAIER solver, so complete coupling with the fluid solver as in [16] is not considered.

In Figure 26, Figure 27 and Figure 28 the velocity fields and profiles at different times within an actuation period are represented, after the periodic regime of both the actuator dynamics and the flow evolution are reached. The position of the anode tip is indicated with a white line and the width of the image corresponds to 10 millimeters.

In the first of the three figures, the velocity field is that created during the previous periods of actuation and the action of the actuator for the considered period has not yet begun. The velocity of the flow near the tip of the anode shows low values.

In the second figure of the set, a high velocity “bubble” has appeared due to the action of the positive part of the discharge; its effect is mainly located near the anode. As explained previously, the effect of the negative part of the discharge shows a lower relative effect and just allows the transport of the “bubble” downstream to be accompanied.

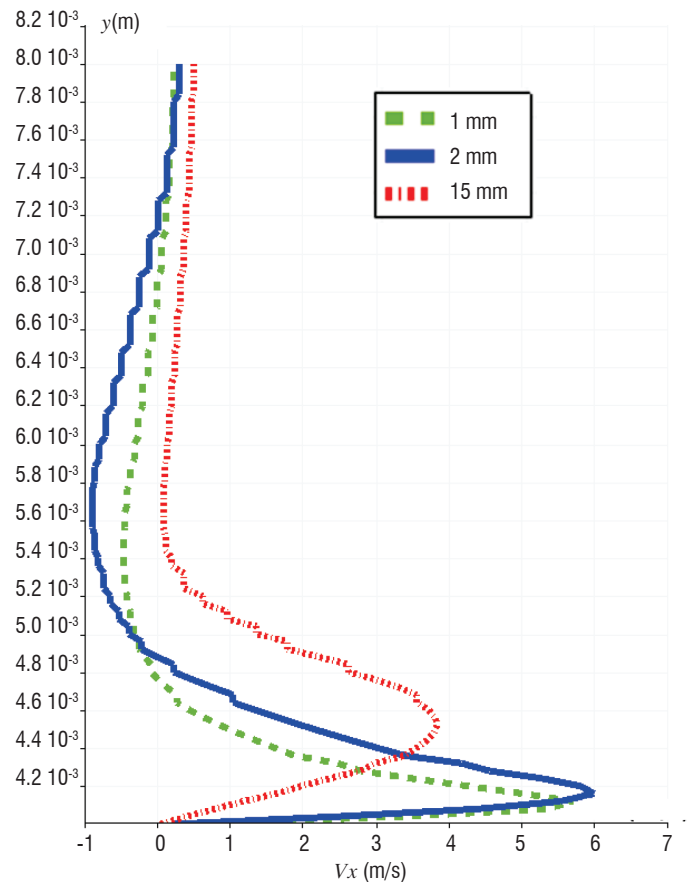
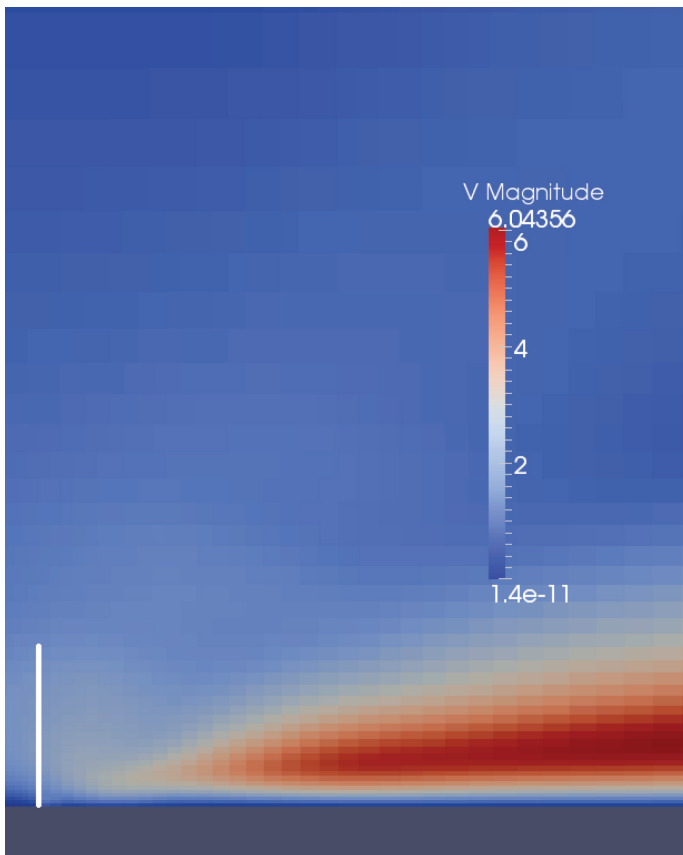


Figure 26 - Velocity field at $t = 400T$

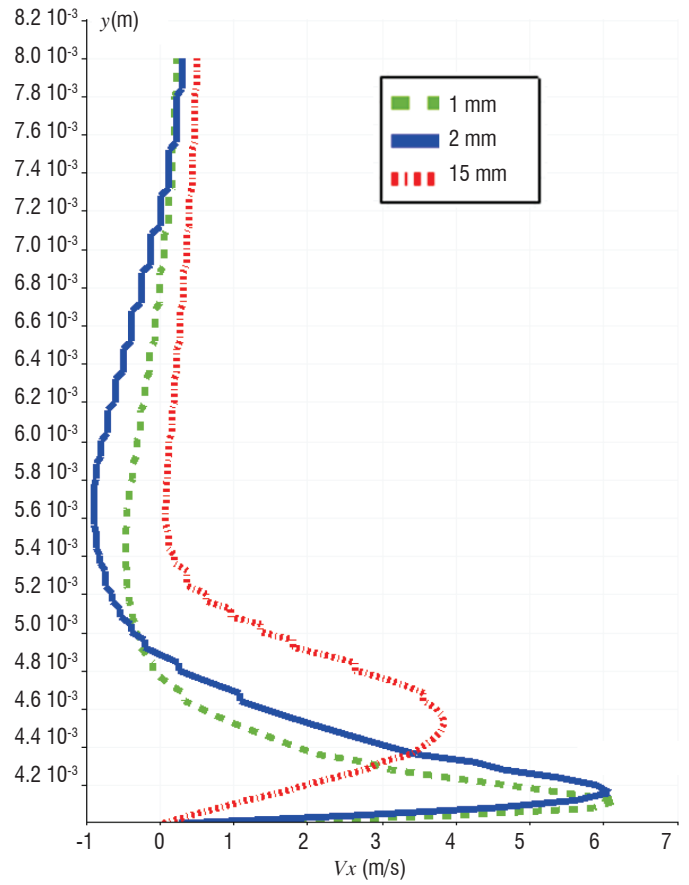
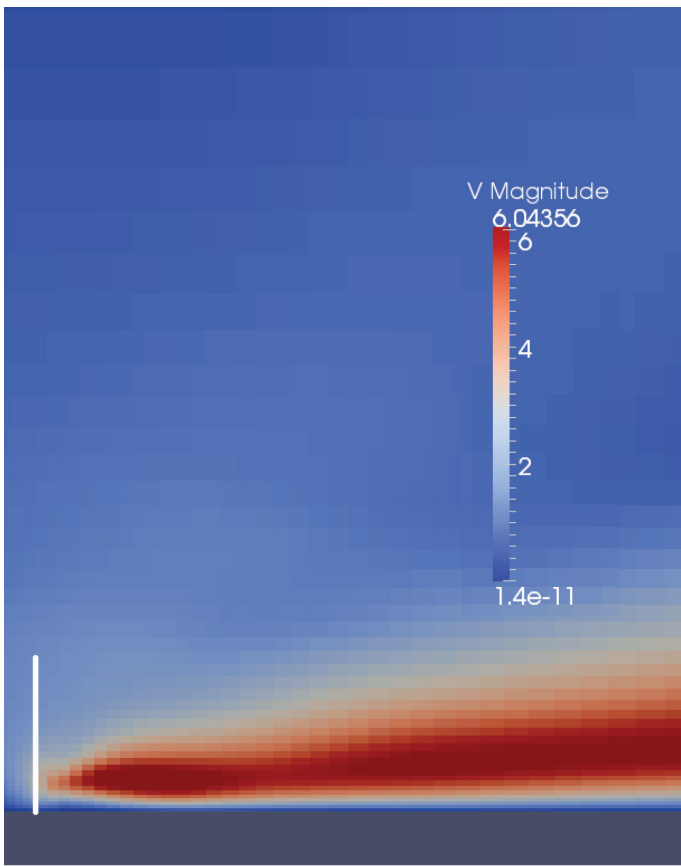


Figure 27 - Velocity field at $t=400T+T/3$

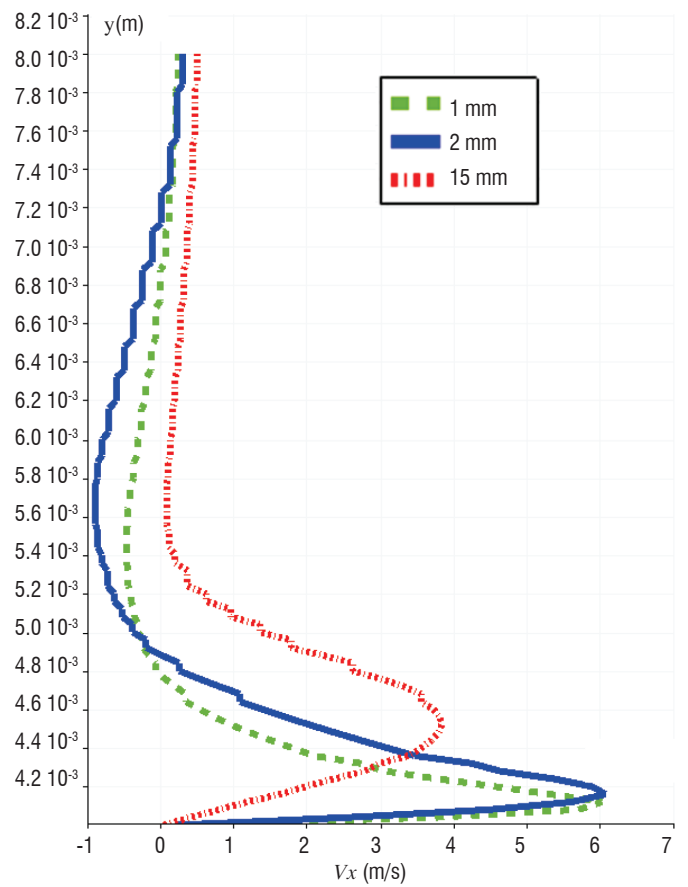
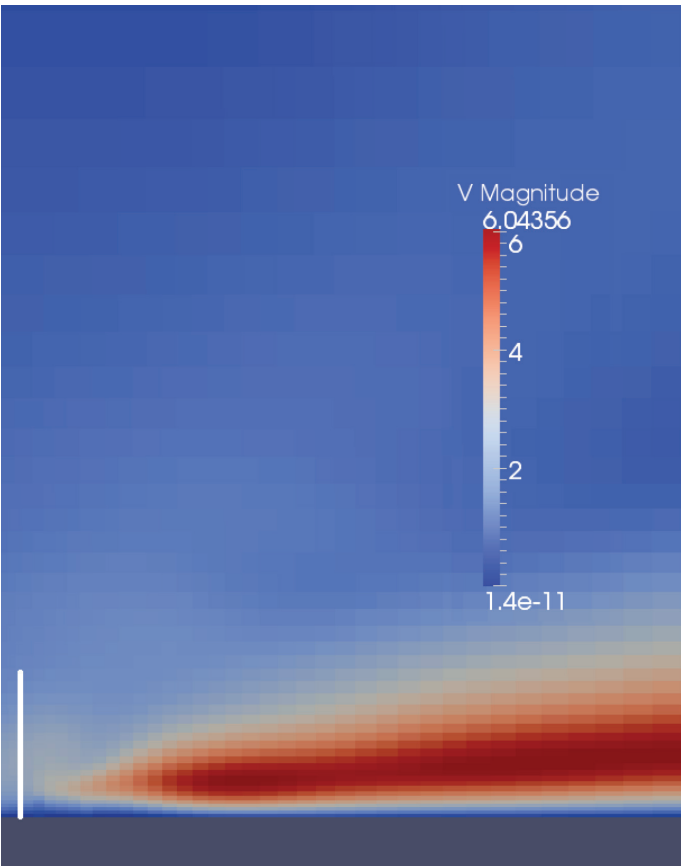


Figure 28 - Velocity field at $t=400T+2T/3$

In the third figure, the merging of the bubble with the already established velocity field can be seen.

As a consequence of this behavior, the velocity y-profiles (curves in the right hand side of the figures) will show different dynamics depending on their distance to the actuators. If the point of measure is far enough from the downstream tip of the anode, the profile will mainly remain unchanged by the effect of the actuator. When considering close enough points of measure (e.g., 1 mm and 2 mm), it can be seen that the profile shows small but still significant differences depending on the part of the actuator period that we are considering. If the shape remains globally the same, the maximum value attained varies (from about $5.7 \text{ m}\cdot\text{s}^{-1}$ to $6.2 \text{ m}\cdot\text{s}^{-1}$ for the 1 mm curve), due to the transport of the “high velocity bubble”. Once this effect has become diffused within the established velocity field, no further dynamical effect is visible.

These preliminary results hint at a new aspect of the definition of the body force term created by a plasma actuator. Indeed, when compared to a constant mean-valued functioning of the actuation, the coupling between the complete dynamics of the actuator and the flow dynamics modifies the velocity field near the anode and leaves it unchanged further away. It can then be inferred that trying to determine a constant value of the electric force using velocities either measured far away from the anode or averaged may lead to inaccurate results.

Moreover, when averaging the velocity field over time, it can be seen that the area where the maximum velocity is attained is no longer located at the very tip of the anode, but rather slightly downstream (Figure 29). This “shift”, which has already been observed in experimental velocity profiles [9], could then be explained by the temporal dynamics of the source term. This point will be further investigated in future studies by considering test-cases involving lower frequencies (and higher voltages, in order to preserve the order of magnitude of the force).

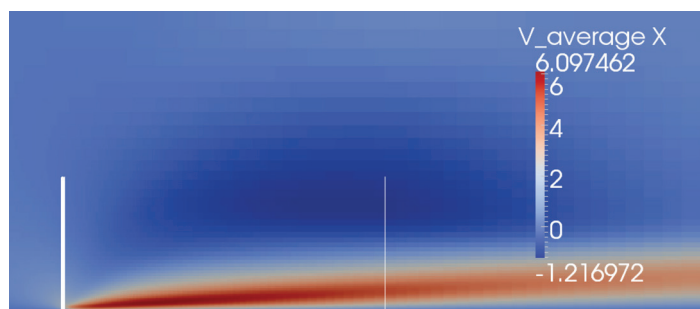


Figure 29 - Time-averaged velocity field

Conclusions

The COPAIER solver enables complete 2D numerical simulations of plasma discharges to be made. The physical model takes into account complex kinetics mechanics, as well as the interaction of the charge species dynamics with the electric field. It has then been shown on a sinusoidal DBD test-case that the effect of the actuator tends toward a periodic behavior and the importance of the dielectric charge for the cycle has been demonstrated. The computed total force proves to be a good estimate when compared to the experimental results and the parametric studies show the same trends as those experimentally observed. However, the flow computations using the computed source term reveal some discrepancies with the experimental results of DBD-induced ionic wind velocities, particularly when considering the maximum velocity attained by the flow. Nevertheless, the ability to use the numerical computations performed with COPAIER to investigate the coupling between the aerodynamics and the dynamics of the plasma discharge has been demonstrated. In particular, estimating the body force term using only velocity measurements away from the tip of the anode may not be representative of the actuator effect and may lead to incorrect results when trying to extrapolate the effects of the actuator for different voltages or frequencies, emphasizing the need for further numerical and experimental studies, in particular at lower frequencies ■

Acknowledgements

We would like to thank S. Roy (Department of Mechanical and Aerospace Engineering, University of Florida) for fruitful discussions about the definition of the DBD numerical test-case. We also would like to thank F. Chedevergne, F. Vuillot and K. Kourtzanidis (ONERA) for their help in the definition of the Navier-Stokes computations using CEDRE. This work was partially funded within the framework of the internal SAHA project at ONERA.

References

- [1] R. DURSCHER, S. ROY - *Evaluation of Thrust Measurement Techniques for Dielectric Barrier Discharge Actuator*. Experiments in Fluids, Vol. 53, No. 4, 2012, pp. 1165-1176.
- [2] J.P. BOEUF, L. PITCHFORD - *Electrohydrodynamic Force and Aerodynamic Flow Acceleration in Surface Dielectric Barrier Discharge*. Journal of Applied Physics, Vol. 97, No. 10, 2005.
- [3] T. UNFER, J.P. BOEUF, F. ROGIER, F. THIVET - *An Asynchronous Scheme with Local Time Stepping for Multi-Scale Transport Problems: Application to Gas discharges*. Journal of Computational Physics, Vol. 227, No. 2, 2007, pp. 898-918.
- [4] BOLSIG+, <http://www.bolsig.laplace.univ-tlse.fr/>
- [5] J.R. AHOLT - *Computational Investigation of Plasma Actuator as an Active Flow Control Strategy of Laminar Separation Bubbles*. MasterThesis, Missouri University of Science and Technology, 2011.
- [6] T.K. WEST, S. HOSDER - *Numerical Investigation of Plasma Actuator Configurations for Flow Separation Control at Multiple Angles of Attack*. 6th AIAA Flow Control Conference, New Orleans, 2012.
- [7] J. BOEUF, Y. LAGMICH, L. PITCHFORD - *Contribution of Positive and Negative Ions to the Electrohydro-Dynamic Force in a Dielectric Barrier Discharge Plasma Actuator Operating in Air*. Journal of Applied Physics, Vol. 106, No. 2, 2009.

- [8] I.A. KOSSYI, A.Y. KOSTINSKY, V.P. SILAKOV, T. UNFER, J. BOEUF - *Kinetic Scheme of the Non-Equilibrium Discharge in Nitrogen-Oxygen Mixtures*. Plasma Sources Science and Technology, Vol. 1, No. 207, 1992, pp. 207-220.
- [9] N. BENARD, A. DEBIEN, E. MOREAU - *Time-Dependent Volume Force Produced by a Non-Thermal Plasma Actuator from Experimental Velocity Field*. Journal of Physics D Applied Physics, Vol. 46, No. 24, 2013.
- [10] K. KOURTZANIDIS - *Numerical Simulation of Plasma Actuators for Flow Control*. 51st AIAA Aerospace Sciences Meeting, Texas, USA, 2013.
- [11] M. FORTE, J. JOLIBOIS, J. PONS, E. MOREAU, G. TOUCHARD, M. CAZALENS - *Optimization of a Dielectric Barrier Discharge Actuator by Stationary and Non-Stationary Measurements of the Induced Flow Velocity: Application to Airflow Control*. Experiments in Fluids, Vol. 43, No. 6, 2007, pp. 917-928.
- [12] A. REFLOCH, B. COURBET, A. MURRONE, P. VILLEDIEU, C. LAURENT, P. GILBANK, J. TROYES, L. TESSÉ, G. CHAINERAY, J.B. DARGAUD, E. QUÉMERAIS, F. VUILLOT - *CEDRE Software*. Aerospace Lab Journal Issue 2 - March 2011
- [13] J.C. MATEO-VELEZ - *Modélisation et simulation numérique de la génération de plasma dans les décharges couronnées et de son interaction avec l'aérodynamique*. PhD. Thesis, Université Toulouse III, France, 2006.
- [14] A.V. LIKHANSKII, M.N. SHNEIDER, S.O. MACHERET, R.B. MILES - *Modeling of Dielectric Barrier Discharge Plasma Actuator in Air*. Journal of Applied Physics, Vol. 103, 2008
- [15] D. BREDEN, K. MIKI, L.L. RAJA - *Self-Consistent Two-Dimensional Modeling of Cold Atmospheric-Pressure Plasma Jets/Bullets*. Plasma Sources Science and Technology, Vol. 21, 2012
- [16] A.V. LIKHANSKII, M.N. SHNEIDER, D.F. OPAITS, R.B. MILES, S.O. MACHERET - *Numerical Modeling of DBD Plasma Actuators and the Induced Air Flow*. 38th AIAA Plasmadynamics and Lasers Conference, Miami, June 2007
- [17] Y. LAGMICH - *Diagnostic et modélisation d'une décharge à barrière diélectrique pour le contrôle d'écoulement*. PhD. Thesis, Université Toulouse III, France, 2006.
- [18] R.J. LEVEQUE - *Finite Volume Methods for Hyperbolic Problems*. Cambridge University Press 2002.

Nomenclature

E	Electric Field (V/m)
U_g	Gas velocity (m/s)
F	Frequency of the discharge (Hertz)
V_o	Voltage applied to the exposed electrode
k_B	Boltzmann Constant
PIV	Particle Image Velocimetry
T_e	Electronic Temperature (K)
v_i	Velocity of the species "i" (m/s)
V_b	Voltage breakdown of the air gap (Volt)

AUTHORS



François Rogier : Senior researcher, in charge of the Mathematical Modeling and Numerical Simulation (M2SN) research unit of the Department of Modeling and Information Processing at ONERA. He graduated from École Centrale de Paris in 1984 and he obtained his PhD in Applied Mathematics in 1989 at Pierre et Marie Curie University. He joined ONERA in 1989 and has led the M2SN research unit since 2004. He has worked in many numerical analysis fields (domain decomposition methods, kinetic theory), as well as in plasma modeling, for more than ten years.



Guillaume Dufour is a researcher working in the Mathematical Modeling and Numerical Simulation (M2SN) research unit of the Department of Modeling and Information Processing at ONERA. He received the Agrégation (civil service competitive examination for positions in public education) in Mathematics and the Magistère Degree from École Normale Supérieure de Lyon, France, in 2001 and 2002 respectively. He obtained his PhD in Applied Mathematics from the University of Toulouse in 2005. Since 2006, he has been working at ONERA and is involved in research and development of mathematical models for plasmas, in both an atmospheric and space context. His research interests include mathematical modeling and numerical analysis of fluid models for complex discrete systems, with applications to various areas of physics and informatics (aerodynamics, plasmas, networks, etc.).

F. Chedeveigne, G. Casalis, O. Léon,
M. Forte, F. Laurendeau, N. Szulga,
O. Vermeersch, E. Piot
(ONERA)

E-mail: Francois.Chevevergne@onera.fr

DOI : 10.12762/2015.AL10-06

Applications of Dielectric Barrier Discharges and Plasma Synthetic Jet Actuators at ONERA

This paper focuses on two plasma actuators, developed at ONERA: the DBD actuator (Dielectric Barrier Discharge) and the PSJ actuator (Plasma Synthetic Jet). At the DMAE (Modeling for Aerodynamics and Energetics Department), DBD actuation is investigated for laminar/transition purposes. The results presented deal with 2D configurations including both experimental and modeling works. As regards the activities on the PSJ actuator, most of the work is dedicated to the detailed characterization of the general physics involved in such an actuator. Similarly to the DBD activities, both experimental and modeling investigations are performed in order to be able to develop efficient control strategies using the PSJ actuator.

Introduction

Over the last two decades, increasing efforts have been made with regard to plasma-based flow and flight control research activities. While some applications decreased in popularity, a considerable potential appeared in small-scale plasma actuators. Contrary to more conventional devices, plasma actuators have no moving parts and offer the possibility of a very fast response in time. The two primary mechanisms of plasma-based flow control include the generation of body forces and thermal effects. In the first category, a non-thermal plasma actuator, called a DBD (Dielectric Barrier Discharge) actuator, has been extensively studied. It is based on the generation of a non-equilibrium surface discharge that results in a body-force parallel to the wall in which the device is inserted. In the second category, the Applied Physics Laboratory of Johns Hopkins University initially developed the SparkJet actuator, which generates a discharge in a small cavity covered by a millimeter nozzle protruding from the wall. A thermal plasma is produced in order to locally increase the pressure and temperature of the surrounding gas in the cavity, inducing the formation of a synthetic jet through the nozzle.

ONERA has developed plasma actuators of both types over the last decade, namely DBD and PSJ (Plasma Synthetic Jet) actuators. Several applications have been explored for these actuators, ranging from transition delay to flow separation control, through jet noise reduction. All of them concern subsonic flows. For transition or separation applications, flows exhibit small to moderate Reynolds numbers, up

to 1.3 M, corresponding to low Mach numbers. However, for jet noise reduction applications, Mach numbers up to 0.9 have been investigated using the PSJ actuator. Although tangible results have already been obtained with regard to this variety of applications, the fine characterization and the understanding of the mechanisms that drive the effect of those actuators on flows is an essential ingredient to prepare advanced strategies involving active flow control.

This article is a synthesis of the work done at ONERA on these two actuators, focusing on their experimental characterization and on the models developed to simulate their effects on flows.

DBD actuator

An example of a relatively simple plasma actuator is provided by the so-called Dielectric Barrier Discharge (DBD) actuator. Up to now, the DBD actuator considered in the Department has been constituted of two copper electrodes adhered to each face of a dielectric material. An alternating high voltage is applied to one electrode, whereas the other one is grounded. The resulting electric field in the vicinity of the electrodes enables the ionization of the ambient air. Then, the charged particles drift under the effect of the electric field, inducing a local body force (also called “ionic wind”), parallel to the surface of the dielectric. Over the last two decades, many studies have been conducted in order to establish the electrical and mechanical characteristics of this actuator. Most of them are summarized in a recent review from Bénard and Moreau [1].

This ionic wind can be used to control the flow around various aerodynamic configurations. For example, within the European project PLASMAERO [1], the DBD actuator technology has been tested for delaying the boundary layer separation occurring on a NACA15 airfoil mounted with high positive incidence (12.5°) without sweep. Three successive single DBD actuators were mounted next to the wall on the suction side of the model and have been operated separately or simultaneously in order to assess the benefit of a multi-DBD actuation. The results have shown that operating the three actuators simultaneously was more efficient than using a single DBD actuation. During this series of experiments, performed at the Pprime Institute, it has been possible to delay the separation position up to 30% of the chord with multi-DBD actuation. The same experiment has been conducted with PSJ actuators and showed a maximum delay of 45% of the chord.

Another possible use of the DBD actuator currently under investigation in the DMAE, is the control of the laminar-turbulent transition location. In fact, delaying transition over the wings of civil aircraft could be a possible way of reducing fuel consumption by reducing the skin friction drag. This application has been successfully demonstrated on a flat plate, see [3-5], and on an airfoil, see [6-7], for two dimensional configurations and velocities with magnitudes up to 40 m/s.

In addition to these experimental investigations, various numerical approaches have also been conducted, in order to derive a mathematical model for the body force induced by a DBD plasma actuator and to implement it in various fluid solvers (boundary layer codes or RANS codes, for example). These body-force models can be classified into two main categories: phenomenological models, which rely on plasma physics [8-10] and empirical models, which are generally based on velocity measurements in the vicinity of the plasma actuator in quiescent air [11]. However, these empirical models depend strongly on the actuator considered, and particularly on various geometric or electric parameters, leading in practice to new models for each specific DBD actuator.

The remaining part of this section is devoted to the description of recent activities performed at the DMAE on the laminar-turbulent transition delay using a DBD actuator.

Steady and unsteady effect of a DBD actuator

A sketch of a typical DBD actuator used at the DMAE is given in Figure 1, together with its installation on a flat plate.

In this example, both electrodes have the same width and are made from the usual copper tape. The air-exposed electrode is located upstream from the one that is grounded, in order to induce a body force in the main-stream direction. In this case, a dielectric insert made of PMMA with 2 mm thickness is used and the actuator is located at $x=470$ mm from the leading edge.

In order to understand the effect of the DBD plasma actuator in the vicinity of the electrodes, the results obtained from a previous study [12] with a similar aerodynamic configuration are worthy of interest. Figure 2 shows the time evolution of the longitudinal velocity component downstream from a DBD actuator when the latter is turned on. In this case, the velocity was measured using Laser Doppler Anemometry (LDA) at $y=1$ mm from the wall and at $x=10$ mm from the downstream edge of the air-exposed electrode. The main flow was seeded with mineral oil particles and the magnitude of the free-stream velocity was very low (3 m/s), resulting in data rates of about 10 kHz.

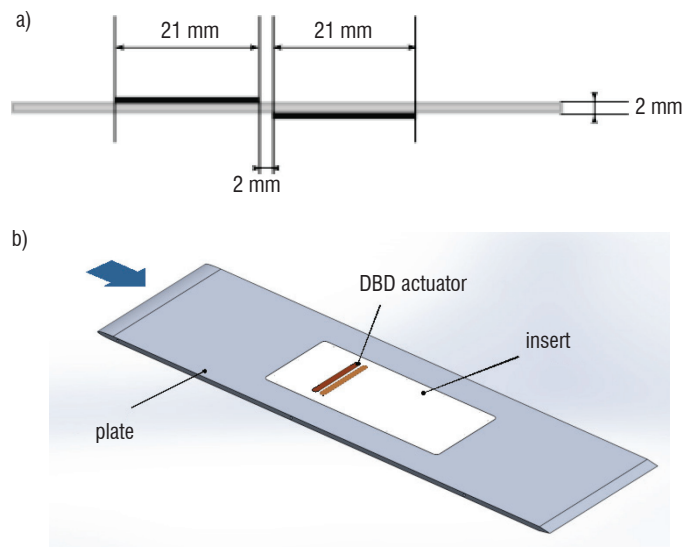


Figure 1 - Cross-section view of a typical DBD actuator used in the DMAE (a) and a flat plate model equipped with one of them (b)

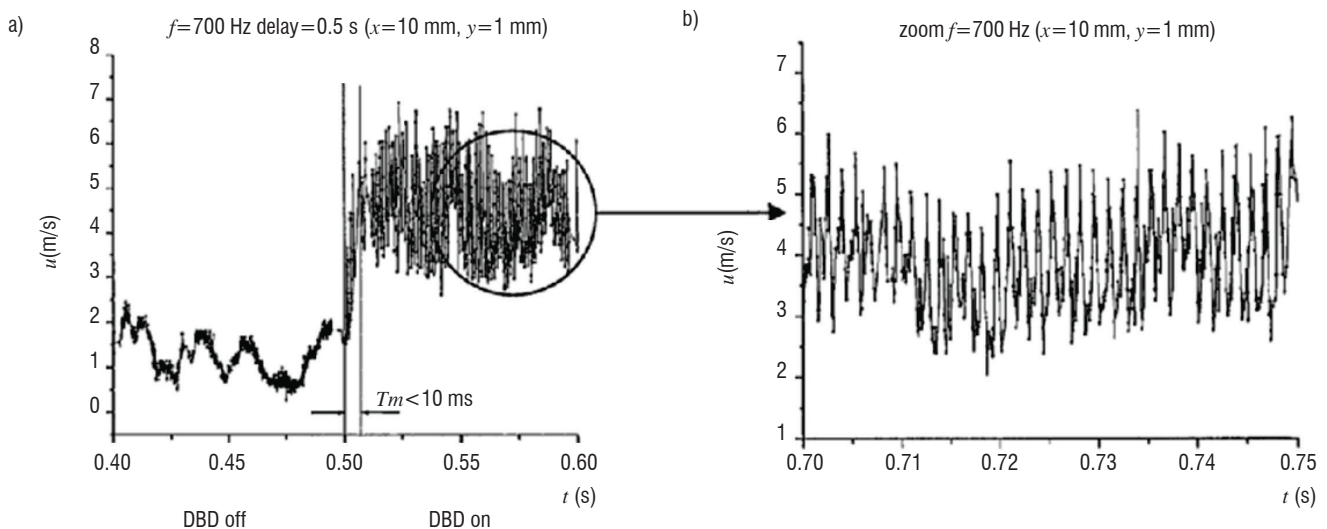


Figure 2 – Time evolution of the longitudinal velocity component downstream from a DBD plasma actuator (a) and with a smaller time scale (b) I, from [12]

Figure 2(a) shows a clear increase in the magnitude of the mean velocity (from 1.5 m/s up to 5 m/s) a few milliseconds after the actuator is turned on. As explained previously, the DBD induces a body force parallel to the wall, which results in a steady wall jet of a few meters per second (often called “ionic wind”). Nevertheless, this steady effect is superimposed with an unsteady effect visible in Figure 2(b), which shows the time evolution of the velocity when the actuator is turned on, and with a smaller time scale. Velocity fluctuations are clearly visible at the same frequency (700 Hz) as the high voltage signal used to supply the actuator. In fact, as has been demonstrated by many authors [1], the DBD actuator induces an unsteady body force at the frequency of the high voltage signal, mainly due to the different discharge regimes between the positive and the negative half cycles.

In the case of a two-dimensional boundary layer, the natural transition is induced by the spatial growth of unsteady instability modes, the well-known Tollmien-Schlichting (TS) waves. If we want to achieve a delay of the transition location, the goal is to decrease this spatial growth or to damp the TS waves. Basically, two approaches are possible to attain this goal: on the one hand, steady actuation is used to modify the mean velocity profile, in order to make the boundary layer more stable. On the other hand, unsteady actuation is used to directly counteract the instabilities. The DBD actuator has the ability of delaying transition by means of either steady or unsteady actuation, as this actuator is able to induce either a quasi-steady or unsteady body force (depending on the electrical parameters of the high-voltage signal) [13]. Most of the results presented in this paper about transition delay are linked with the first approach: stabilization of the boundary layer using the quasi-steady body force induced by the actuator. “Quasi-steady” means that the frequency of the high voltage signal has to be chosen properly at a sufficiently high value, in order to ensure that the unsteady effect will not excite the TS waves, resulting in a promotion of the transition. Thus, only the quasi-steady body force will be considered in the following, assuming that the frequency of the DBD actuator is higher than the most amplified TS frequencies.

Flat plate case

The model shown in Figure 1 is mounted in the TRIN2 wind tunnel of the DMAE, with a free-stream velocity of 35 m/s. This facility features a low turbulence level ($Tu \sim 1.5 \times 10^{-3}$) and is well suited for transition experiments (transitional N-factor ~ 7). Assuming the development of a Blasius boundary layer, the linear stability

theory, which agrees with time-resolved hot-wire measurements, shows that the most unstable TS frequencies range from 600 Hz to 1000 Hz. As a consequence, the frequency of the DBD input signal is set at 3 kHz, a value that is sufficiently above the TS frequencies to assume that only a quasi-steady body force will play a major role. The latter adds momentum inside the boundary layer (in the same direction as that of the main flow) and modifies the mean velocity profile in such a way that it is more stable with respect to the instability TS modes, leading to a transition delay (similarly to when suction is applied) with a global benefit in terms of friction drag.

The study presented in this paper has two main objectives: the first is to establish a model of the body force induced by the DBD actuator and assess the efficiency of the set-up with respect to the laminar-turbulent transition position. The longitudinal velocity component is usually determined by hot-wire measurements inside the boundary layer. However, this kind of measurement is not possible very close to the actuator, because of the interactions between the discharge and the hot-wire probe. Therefore, it has been decided to perform LDA measurements in the vicinity of the actuator. Figure 3 gives an example of such velocity measurements, just above the downstream edge of the air-exposed electrode ($x=470$ mm) without and with actuation for two different values of the electrical power consumption.

Velocity profiles obtained from LDA measurements are represented, compared to the local Blasius boundary-layer profile. These are in very good agreement when the DBD is not active (left graph of Figure 3). When the actuator is turned on, the longitudinal velocity is increased in the boundary layer close to the wall, approximately in the first half of the boundary layer thickness. These measurements clearly show the effect of the steady body force induced by the actuator inside the boundary-layer. The next step is to measure the transition location, in order to assess whether the boundary layer is stabilized by this DBD actuation.

Figure 4 shows the longitudinal evolution of the velocity fluctuations inside the boundary layer at a constant height ($z=1$ mm) above the wall, obtained from hot-wire measurements. This plot presents the same three cases as Figure 3. The transition location is characterized by a sudden increase in the velocity fluctuation, as the boundary-layer regime changes from laminar to turbulent.

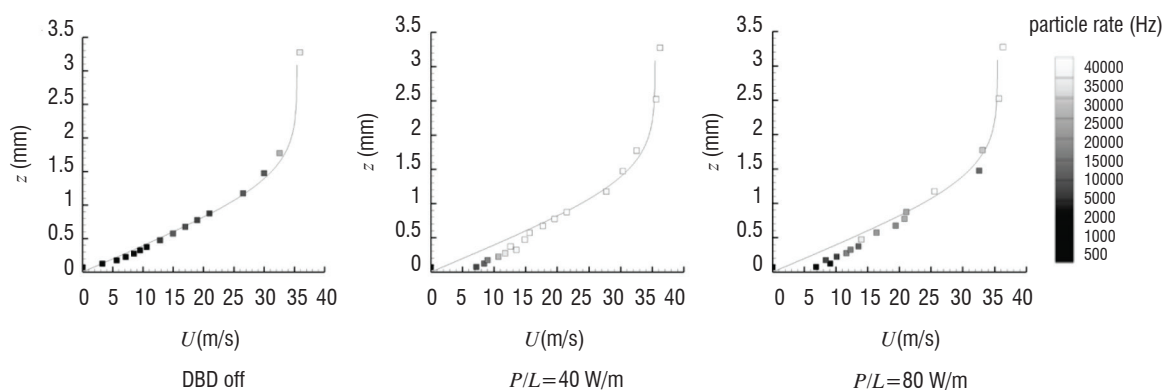


Figure 3 - LDA measurements of the longitudinal velocity just above the DBD actuator in comparison with a Blasius boundary-layer profile (full line) without and with DBD actuation

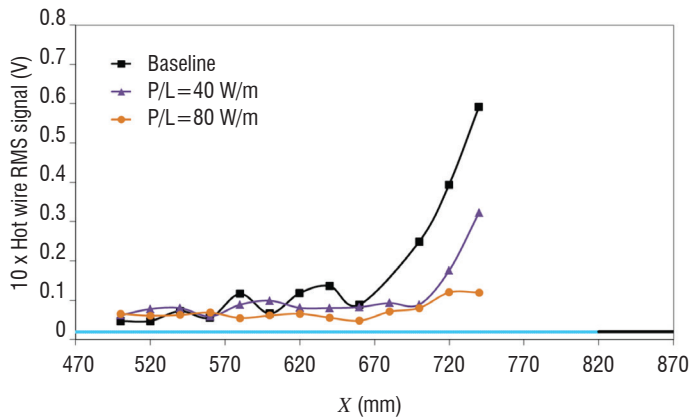


Figure 4 - Longitudinal evolutions of the velocity fluctuations inside the boundary layer without and with DBD actuation

The natural transition location (without actuation) is measured at $x=670$ mm. When the actuator is turned on, the transition location is progressively shifted downstream when the power consumption of the actuator is increased. For the lowest power consumption, the transition location is delayed by roughly 35 mm, and by more than 80 mm in case of the highest power value. These measurements prove that the local modification of the velocity profiles induced by the actuator (shown in Figure 3) enables the stabilization of the boundary layer and a delay in the transition.

2D airfoil case

The same kind of DBD actuator has also been installed on an airfoil model based on an ONERA-D profile, as presented in Figure 5 (left). The goal of this study was to assess the ability of the actuator to control the transition on a more realistic aerodynamic configuration, for which the boundary layer develops with a non-zero pressure gradient. The model is mounted inside the TRIN1 wind tunnel of the DMAE with an incidence of 1.5° in an unswept configuration. Longitudinal hot-wire measurements have been performed inside the boundary layer at a constant height above the wall, similarly to the measurements presented in Figure 4, and for a free-stream velocity of 21 m/s. The longitudinal evolutions of velocity fluctuations are shown in Figure 5 (right), without and with actuation, for a DBD actuator located at $x/c=33\%$.

The results presented in Figure 5 (right) are very similar to those shown in Figure 4: the transition is progressively shifted downstream when the actuator is turned on and when the electrical power is increased. A maximum transition delay of 6% of the chord has been measured for the highest power consumption value.

This experiment has been reproduced numerically, using the experimental pressure distribution to perform boundary-layer computations and linear stability analysis. A model of the body force induced by the DBD actuator has been implemented in a boundary-layer code, so as to study the influence of the plasma actuator on the stability of the boundary layer. An example of a numerical result is shown in Figure 6, which presents the chordwise evolutions of the N-factors (chordwise integration of amplification rate) for various instability frequencies without (left) and with (right) actuation, using similar conditions as for the experiment.

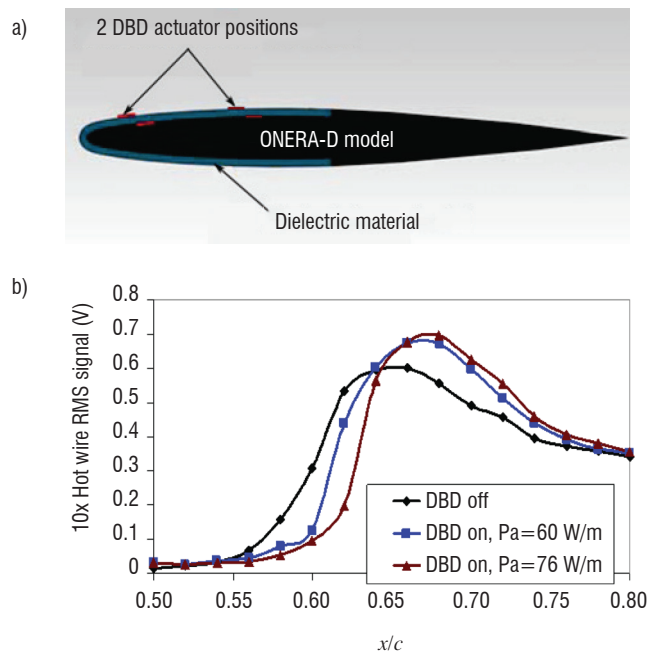


Figure 5 - (a) Cross-sectional view of the ONERA-D model equipped with DBD actuators (b) longitudinal evolutions of velocity fluctuations inside the boundary layer without and with DBD actuation

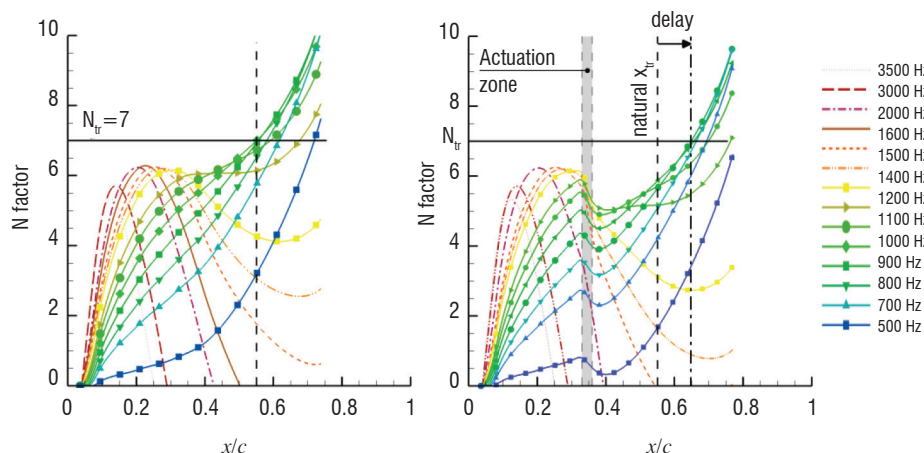


Figure 6 - Linear stability analysis of the boundary layer developed on the ONERA-D model for the baseline case (left) and with DBD actuation (right - $P_a=60$ W/m) for a free-stream velocity of 21 m/s

Using the natural transition location obtained from the experiment ($x_{tr}/c=56\%$ in Figure 5), the left part of Figure 6 enables the value of the transitional N-factor ($N_t=7$) to be determined, which corresponds to the transition threshold in the well-known eN method [14]. Then, using the body force model, the manipulated boundary layer was computed and the corresponding stability analysis has been plotted in Figure 6 (right). The stabilizing effect on the TS waves is clearly visible, since all of the N-factor curves are decreasing in the region of the plasma-induced body force, resulting in a transition delay of 8% of the chord. The numerical results slightly overestimate the experimental delay.

Current work and perspectives

With the perspective of delaying the laminar-turbulent transition along the wings of realistic transportation airplanes, another issue is to deal with crossflow instabilities. Indeed, given that real wings have a non-zero sweep angle, the boundary layer is 3D and the mean velocity profile in the direction perpendicular to the external streamlines – the so-called crossflow direction – exhibits an inflection point inside the boundary layer. This induces a strong disturbance called the crossflow (CF) instability, which occurs close to the leading edge for accelerated mean flows. For this particular instability, both unsteady and steady modes can be spatially amplified in the streamwise direction. The steady crossflow instability amplitudes are strongly related to the roughness of the surface on which the considered boundary layer is developing. Finally, two approaches are currently being investigated in order to control the crossflow induced transition: the first is to modify the mean crossflow velocity profile inside the boundary layer; the second is to use nonlinear interactions between several crossflow instabilities.

The first approach has been investigated for many years using wall suction. The mean velocity profile modified by suction is more stable with respect to the instability modes, inducing a delay of the transition location. This idea has been tested in-flight by several industrial aircraft manufacturers and has proven to be very efficient for transition delay. However, all of the devices used to create the suction are quite expensive to implement in practice, so alternative ways must also be assessed. The DBD actuator seems to be a promising way: given that the intensity of the mean CF velocity profile is not very high, it can reasonably be affected by the body force induced by this kind of plasma actuator. Of course, the direction of the induced body force must be chosen properly, so as to reduce the magnitude of the inflexional CF mean velocity profile.

The second possible approach is to use the DBD actuator to mimic micron-roughness elements, in order to induce a non-linear interaction between the artificial CF modes and the natural modes leading to transition. Previous experiments performed in the US [15] and in the DMAE [16] show that using artificial roughness elements regularly stuck in a line parallel and close to the leading edge, forces the steady CF instability vortices, with the spanwise wavelength corresponding the spacing between two consecutive roughness elements. Then, the trick consists in exciting a slightly amplified CF mode in such a way that a non-linear interaction modifies the mean velocity profile, which becomes more stable with respect to the most amplified CF modes. This idea has been successfully implemented experimentally but the size of the roughness elements must be chosen very accurately. The

advantage of using DBD actuators instead of these roughness elements is that the amplitude of the body force can be adjusted.

Both ways are currently being investigated within the framework of the BUTERFLI European Project, in cooperation with Russia.

Plasma Synthetic Jet actuator

For several years, the DMAE [17,18], in collaboration with the CNRS LAPLACE laboratory [19,20], has developed the Plasma Synthetic Jet (PSJ) actuator, shown in Figure 7, which is similar to the SparkJet actuator [21]. This is a compact actuator designed to be integrated into a wall and dedicated to flow control applications. It consists of a cylindrical cavity whose dimensions do not exceed a few millimeters. A convergent nozzle is added to produce a jet, as explained in the following, which interacts with the external flow. The exhaust orifice has a diameter of 1 mm. Two electrodes are located inside the cavity and are connected to an electric circuit. Figure 8 shows a diagram of the actuator and the electric circuit. The latter can be decomposed into two parts: the charge circuit consisting of a high voltage pulse generator, a resistance R_c and a capacitor C , and the discharge circuit consisting of the same capacitor and the electrodes. At the beginning of a cycle, the capacitor is discharged and a high voltage pulse is produced by the power supply. The voltage at the capacitor increases up to the breakdown voltage value of the air surrounding the electrodes. At this instant, an electric arc is produced between the electrodes. Due to the Joule effect, the resulting plasma arc transfers energy to the air inside the cavity. The temperature and the pressure increase inside the cavity. A jet is then generated through the nozzle. Afterwards, a natural suction phase occurs, driven by simple pressure recovery, and the cycle can be repeated. Thus, the PSJ actuator works as a zero net mass flux device. When the actuation frequency is high enough, the operation of the PSJ during a cycle is influenced by the previous cycle. In this case, at the breakdown instant, the air inside the cavity is not at rest. Also, the temperature of the air inside the cavity, the walls and the electrodes may remain high. The energy deposition is modified by these high-frequency effects, as well as the dynamics within the cavity. As a consequence, when the frequency is high enough, the jet generated is different from that generated by the PSJ working in a single-pulse or low-frequency mode.



Figure 7 – Photograph of a PSJ actuator

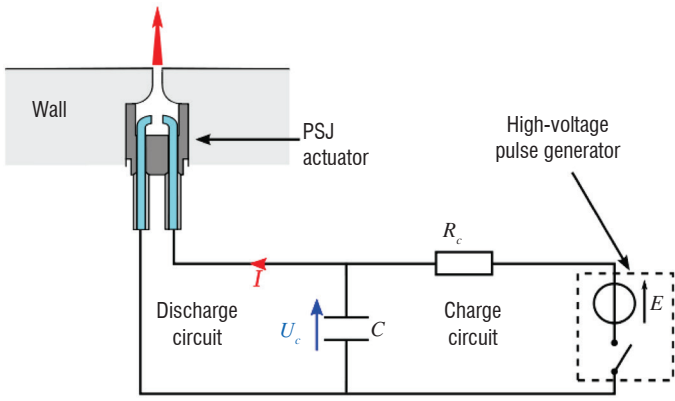


Figure 8 – Diagram of the PSJ actuator inserted into a wall, defining the boundary of a flow, and its electric power supply

Experimental characterization

A significant number of experimental characterizations have been conducted at the DMAE on the jet produced by a PSJ actuator, either with or without a flow on the surface of the wall in which it is inserted. While the experiments bringing into play a flow have shown the capability of the actuator to alter and control its dynamics, this section is focused on the characterizations performed in a quiescent environment. Indeed, in order to build an accurate model of the PSJ actuator, a first necessary step is to capture the dynamics of the synthetic jet without any external influences.

Electrical measurements

In order to characterize the electric discharge that drives the energy deposition inside the cavity of the PSJ actuator, and thus ultimately the dynamics of the synthetic jet, measurements of the capacitor voltage U_c and the current in the discharge circuit I were performed with a PSJ actuator working at a repetition rate of 1Hz. This frequency is sufficiently low to consider the actuator as working in a single-pulse mode. An example of the signals obtained for a capacitance $C = 12.2$ nF is provided in Figure 9. The voltage across the capacitor initially follows the expected charging of the RC series circuit previously described in Figure 8. The discharge circuit being open, the current is null. At about $t = 11.5 \mu\text{s}$, electrical breakdown occurs and the plasma generated between the electrodes closes the discharge circuit: the voltage across the capacitor U_c and the discharge intensity I then describe underdamped oscillatory responses, indicative of a spark discharge [19,22]. Based on a large number of measurements, we showed that a simple and relevant electrical model of the discharge can be constructed to reproduce the major characteristics of the current during the energy deposition phase of the PSJ actuator. This electrical model of the discharge is shown in Figure 10. Particularly, it can be assumed that the total equivalent resistance R and inductance L are constant during the discharge. This model will serve as a physically-based input for unsteady simulations of the actuator relying on the methodology proposed by Laurendeau et al [23], and sheds light on the major electrical parameters driving the discharge, which it is important to account for in future design improvements of the actuator.

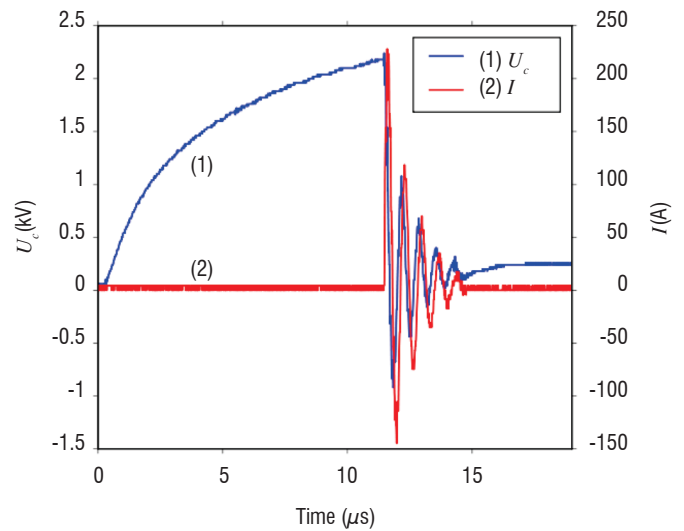


Figure 9 - Capacitor voltage U_c and current in the discharge circuit I measured during one actuation cycle with an effective capacitance $C = 12.2$ nF

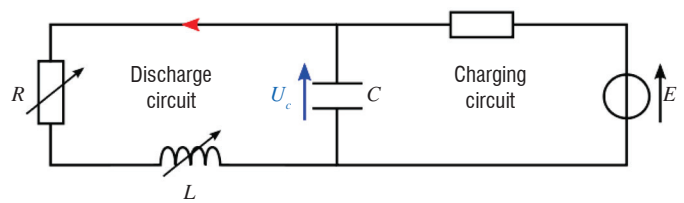


Figure 10 - Equivalent electrical model of the PSJ actuator power supply during the arc discharge, where R and L respectively refer to the total resistance and inductance in the discharge circuit induced by the wires and plasma

Schlieren visualizations

A first aerodynamic characterization of the synthetic jet produced in a quiescent environment was performed using Schlieren visualizations. Such visualizations are aimed at providing a qualitative description of the density gradients in a given direction, integrated along the path of the rays of light. Examples of Schlieren visualizations obtained for a capacitance of 30 nF are provided in Figure 11. A phase-averaging procedure was used, in order to provide the mean jet topology at given instants during its development. The phase-averaging process is performed using the breakdown instant as the reference instant. As observed in these figures, the phase-averaged synthetic jet is composed of a train of vortex rings, convected at different velocities and interacting with one another. The generation of these vortex rings is tightly linked to the dynamics of the pressure waves generated inside the cavity of the actuator during the energy deposition phase.

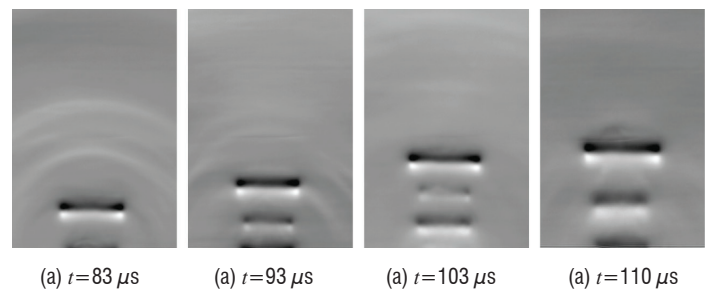


Figure 11 - Phase-averaged Schlieren visualizations obtained for an installed capacitance $C=30$ nF, at various instants t from the breakdown instant.

Particle Image Velocimetry

A more quantitative characterization was then conducted for the synthetic jet produced by the actuator, through Particle Image Velocimetry (PIV). A diagram of the setup used is shown in Figure 12. Performing a high-quality PIV measurement of such a synthetic jet requires some challenges to be overcome, particularly regarding the seeding of the jet [24] and the evaluation of the sources of uncertainty. Indeed, first with regard to the seeding, the air inside the cavity of the actuator cannot be seeded directly for geometrical reasons and the particles tend to be naturally expelled from the synthetic jet. Although the vortex rings drag particles in the jet core, this results in poorly seeded areas in instantaneous PIV images. However, through a phase-averaged approach it can be expected to provide sufficient information to yield a satisfactory averaged description of the complete jet velocity field. This approach was thus selected for these measurements. Second, regarding the sources of uncertainty in such measurements, various parameters must be accounted for. The major parameters identified were the location of the laser sheet (about 0.4 mm thick) with respect to the actuator exit orifice (diameter of 1 mm), the position of the wall on the images and the dispersion of the velocity calculated by the PIV algorithm. The uncertainty analysis conducted [25] then allows these measurements to be compared with simulations of the actuator.

An example of the PIV measurements obtained with an effective capacitance value $C = 10.2$ nF is shown in Figure 13. In this figure, the evolution of the axial velocity, the radial velocity and the vorticity are presented for 3 consecutive instants measured as from the breakdown instant. With this capacitance, phase-averaged axial velocities up to 120 m/s are reached

on the jet axis. The generation of a train of vortex rings can be observed on the vorticity maps, with the circled numbers localizing the different rings. As observed with the Schlieren visualizations, the vortex rings interact, but at different instants due to the difference in capacitance values.

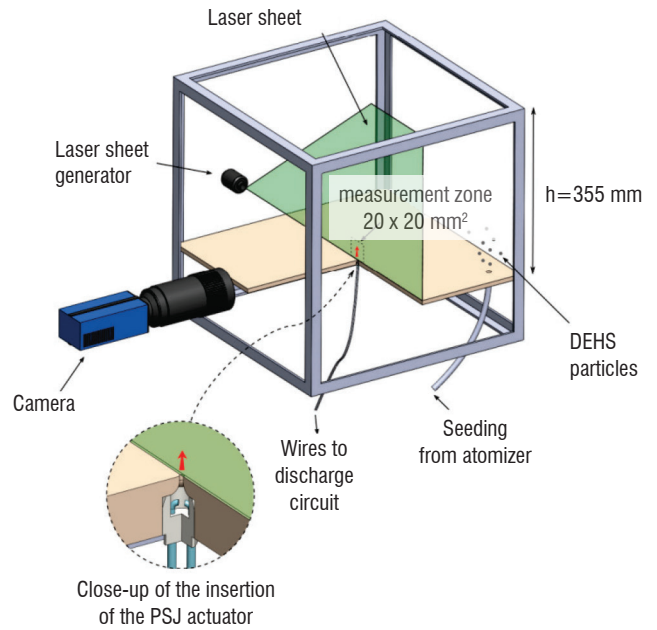


Figure 12 – Diagram illustrating the PIV setup and the flow visualization chamber; a quarter of the floor in which the PSJ actuator is inserted was removed for clarity

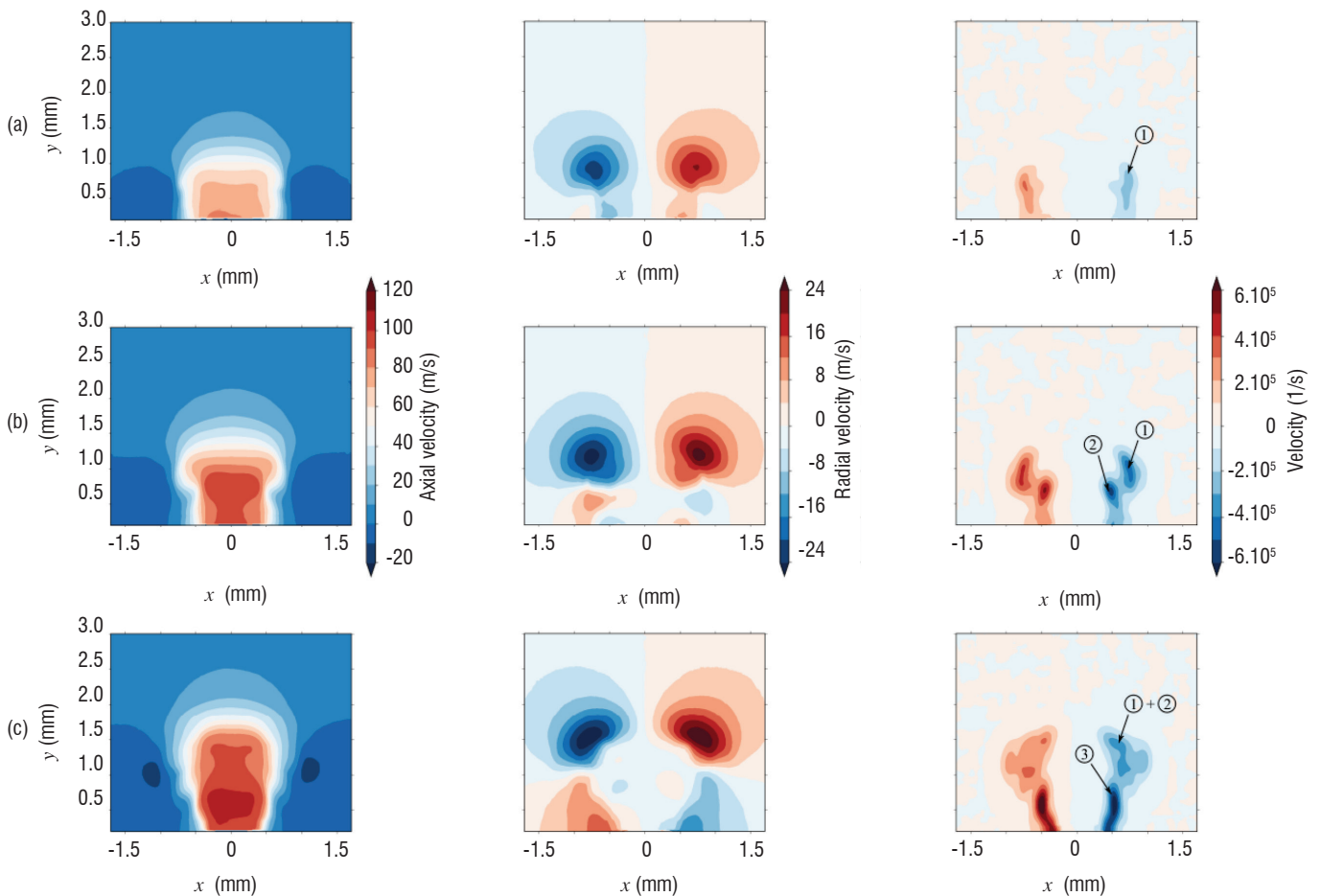


Figure 13 – Contour maps of the phase-averaged axial velocity (left column), radial velocity (center column) and vorticity (right column), obtained for an effective capacitance $C=10.2$ nF, at various instants in the jet development: (a) $t = 56.3 \mu\text{s}$, (b) $t = 66.1 \mu\text{s}$, (c) $t = 76.1 \mu\text{s}$. On the vorticity maps, the circled numbers highlight specific vorticity regions identified as vortex rings.

LES methodology

Contrary to DBD models, for which non-equilibrium plasma physics is required, the PSJ actuator induces plasma, for which the LTE (Local Thermodynamic Equilibrium) hypothesis can be formulated. Such an assumption eases the development of a dedicated model since the flow and the plasma can be considered as a unique mixture driven by a real gas law. Thus, following the work initiated by Sary et al [26], the spark discharge is modeled through energy source terms depending on time and space, and introduced into a large eddy simulation. The current intensity being known, whether from direct measurement or through an equivalent RLC circuit [14], the source term S is written as:

$$S = \sigma E^2$$

where σ is the electric conductivity and E is the electric field:

$$E = \frac{I}{\int_0^{r_{arc}} 2\pi r \sigma dr}$$

The discharge canal is assumed to be cylindrical, with a radius r_{arc} . Due to the high temperature generated by the energy deposition, a real gas model is adopted for air in the computation. The model selected is that proposed by D'Angola et al [27], for which, for example, the electric conductivity is a function of the pressure and the temperature. Thus, the source term S is coupled to the Navier-Stokes solver for the gas, which provides the spatial distribution and the temporal evolution of the pressure and the temperature. From these data, the source term is evaluated in the fluid domain and added to the energy equation.

The CEDRE code [28] from ONERA is a multi-physics platform that contains several solvers, all coupled together. The source term S is computed from a solver called COPAIER, included in the CEDRE code, and coupled to the unstructured Navier-Stokes solver called CHARME. In order to compute the synthetic jet produced by the energy deposition inside the cavity, Large Eddy Simulations (LES) are carried out. The cavity, including the electrodes, is meshed with about one million cells, as shown in Figure 14, whereas the outer region in which the jet expands typically contains 5-10 million cells.

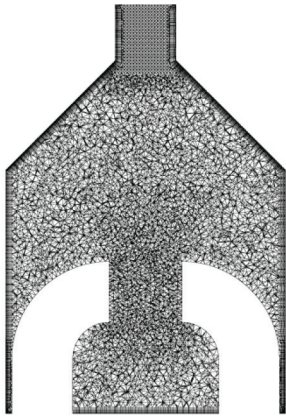


Figure 14 - Typical mesh inside the PSJ cavity

Excellent agreement with measurements from Hardy et al [8] has been obtained by Laurendeau et al [23]. Comparisons of the jet front evolution and jet topology have proven the relevance of the proposed methodology. Recently, further validation of the energy deposition model has been achieved using the PIV measurements. Figure 15 compares velocity fields obtained from PIV and from the LES at the same instant after the breakdown.

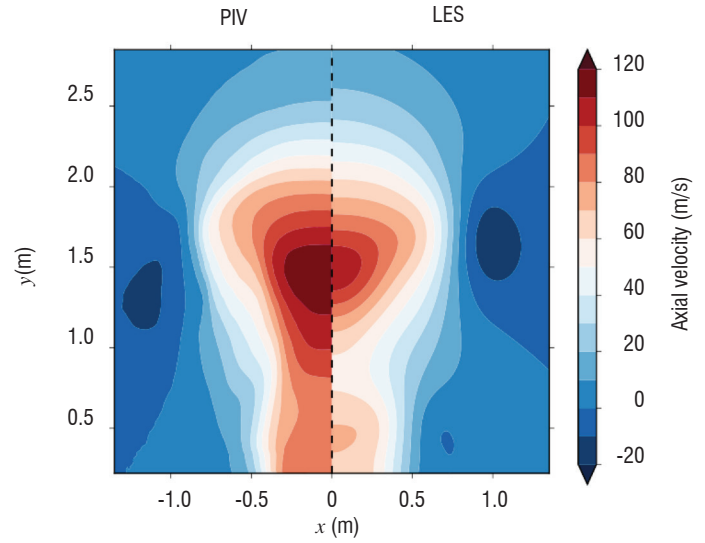


Figure 15 - Axial velocity fields V_y generated with a capacitance value $C = 10.2$ nF. Left: phase-averaged velocity measured by PIV at $t = 86.1 \mu\text{s}$. Right: velocity yielded by LES at $t = 86.1 \mu\text{s}$ after the breakdown.

The general topology of the synthetic jet is well recovered and the velocity magnitudes are also fairly well reproduced. Main discrepancies appear in zones where the confidence level is rather low for PIV measurements [25].

Conclusion

For several years, ONERA has investigated both DBD and PSJ plasma actuators. Two different objectives have been targeted: the transition location delay for a DBD actuator and the separation reduction or delay for a PSJ actuator. The ONERA approach consists in a dual investigation relying on both dedicated experimental work and CFD simulations. For the DBD actuator only a heuristic model is under development at the DMAE, with the goal of implementing it in CFD codes. On the other hand, a detailed model of the PSJ actuator is being investigated, using LES simulations. A very good agreement has been obtained when comparing the results of the simulations with PIV measurements, inducing a reasonable trust in the energy deposition model. The next step will consist in deriving a simple model of the flow at the exhaust of the PSJ actuator, this model being then implemented in CFD codes for practical applications of flow active control. Using both experiments and numerical simulations, Onera intends to implement control strategies based on these plasma devices in complex and realistic aerodynamic configurations ■

Acknowledgements

First investigations regarding the plasma actuators in DMAE have been performed in the European project PLASMAERO. Most of the presented results come from the PhD works of Natacha Szulga and Francois Laurendeau, both granted by DGA and ONERA.

References

- [1] N. BENARD, E. MOREAU - *Electrical and Mechanical Characteristics of Surface AC Dielectric Barrier Discharge Plasma Actuators Applied to Airflow Control*. Experiments in Fluids 55:1846 (2014)
- [2] M. FORTE, A. DEBIEN, D. CARUANA, N. BENARD, PH. BARRICAU, CH. GLEYZES, E. MOREAU - *Mid-Chord Separation Control Using PSJ and DBD Plasma Actuators*. ERCOFTAC Bulletin, vol. 94, pp. 41-46, March (2013).
- [3] S. GRUNDMANN, C. TROPEA - *Experimental Transition Delay Using Glow-Discharge Plasma Actuators*. Experiments in Fluids 42(4):653-657 (2007).
- [4] R. JOUSSOT, R. WEBER, A. LEROY, D. HONG - *Transition Control Using a Single Plasma Actuator*. International Journal of Aerodynamics, 3 (2013).
- [5] A. DUCHMANN, S. GRUNDMANN, C. TROPEA - *Delay of Natural Transition with Dielectric Barrier Discharges*. Experiments in Fluids 54(3):1-12 (2013).
- [6] A. SÉRAUDIE, O. VERMEERSCH O., D. ARNAL - *DBD Plasma Actuator Effect on a 2D Model Laminar Boundary Layer*. Transition delay under ionic wind effect. AIAA Applied Aerodynamics Conference (2011).
- [7] A. DUCHMANN, B. SIMON, C. TROPEA, S. GRUNDMANN - *Dielectric Barrier Discharge Plasma Actuators for In-Flight Transition Delay*. AIAA Journal 52(2):358-367 (2014).
- [8] W. SHYY, B. JAYARAMAN, A. ANDERSSON - *Modeling of Glow Discharge-Induced Fluid Dynamics*. Journal of applied physics 92(11):6434-6443 (2002).
- [9] K.P. SINGH, S. ROY - *Force Approximation for a Plasma Actuator Operating in Atmospheric Air*. Journal of Applied Physics 103(1):0133051-0133056 (2008).
- [10] T. UNFER, J.P. BOEUF - *Modeling and Comparison of Sinusoidal and Nanosecond Pulsed Surface Dielectric Barrier Discharges for Flow Control*. Plasma Physics and Controlled Fusion 52:124019 (2010).
- [11] J. KRIEGSEIS, C. SCHWARZ, C. TROPEA, S. GRUNDMANN - *Velocity-Information-Based Force-Term Estimation of Dielectric-Barrier Discharge Plasma Actuators*. Journal of Physics D: Applied Physics 46(5):055202. (2013).
- [12] M. FORTE, L. LEGER, J. PONS, E. MOREAU, G. TOUCHARD - *Plasma Actuators for Airflow Control: Measurement of the Non-Stationary Induced Flow Velocity*. Journal of Electrostatics, 63(6), 929-936 (2005).
- [13] A. KURZ, S. GRUNDMANN, C. TROPEA, M. FORTE, A. SÉRAUDIE, O. VERMEERSCH, D. ARNAL, N. GOLDIN, R. KING - *Boundary Layer Transition Control Using DBD Plasma Actuators*. AerospaceLab Journal Issue 6, AL06-02 (2013).
- [14] A. SMITH, N. GAMBERONI - *Transition, Pressure Gradient and Stability Theory*. Douglas Aircraft Co. Rept. ES 26388, El Segundo, California (1956).
- [15] W.S. SARIC, A.L. CARPENTER, H. REED - *Passive Control of Transition in Three-Dimensional Boundary Layers, with Emphasis on Discrete Roughness Elements*. Phil. Trans. R. Soc. A 369:1352-1364 (2011).
- [16] O. VERMEERSCH, D. ARNAL, E.I. ALAH, L. DIN - *Transition Control by Micron-Sized Roughness Elements: Non-Linear Stability Analyses and Wind Tunnel Experiments*. International Journal of Engineering Systems Modelling and Simulation 5(1-3/2013):84 (2013).
- [17] P. HARDY, PH. BARRICAU, A. BELINGER, D. CARUANA, J.P. CAMBRONNE, CH. GLEYZES - *Plasma Synthetic Jet for Flow Control*. 40th Fluid Dynamics Conference and Exhibit, AIAA 2010-5103 (2010).
- [18] D. CARUANA, F. ROGIER, G. DUFOUR, CH. GLEYZES - *The Plasma Synthetic Jet Actuator, Physics, Modeling and Flow Control Application on Separation*. AerospaceLab Journal Issue 6, AL06-10 (2013).
- [19] A. BELINGER, P. HARDY, PH. BARRICAU, J.P. CAMBRONNE, D. CARUANA - *Influence of the Energy Dissipation Rate in the Discharge of a Plasma Synthetic Jet Actuator*. J Phys D Appl Phys 44:365-201 (2011).
- [20] A. BELINGER, P. HARDY, N. GHERARDI, N. NAUDE, J.P. CAMBRONNE, D. CARUANA - *Influence of the Spark Discharge Size on a Plasma Synthetic Jet Actuator*. IEEE T Plasma Sci 39:2334-2335 (2011).
- [21] K. GROSSMAN, B. CYBYK, D. VANWIE - *Sparkjet Actuator for Flow Control*. 41st Aerospace Sciences Meeting and Exhibit, AIAA 2003-57 (2003).
- [22] W.D. GREASON - *Methodology to Study the Resistance of a Spark Discharges*. IEEE T Ind Appl 35(2):359-365 (1999).
- [23] F. LAURENDEAU, F. CHEDEVERGNE, G. CASALIS - *Transient Ejection Phase Modeling of a Plasma Synthetic Jet*. Physics of Fluids 26(12):125,101 (2014).
- [24] T.M. REEDY, N.V. KALE, J.C. DUTTON, G.S. ELLIOT - *Experimental Characterization of a Pulsed Plasma Jet*. AIAA Journal 51(8):2027-2031 (2013).
- [25] F. LAURENDEAU, O. LÉON, F. CHEDEVERGNE, G. CASALIS - *PIV and Electric Characterization of a Plasma Synthetic Jet Actuator*. 45th AIAA Fluid Dynamics Conference, AIAA 2015-2465 (2015).
- [26] G. SARY, G. DUFOUR, F. ROGIER, K. KOURTZANIDIS - *Modeling and Parametric Study of a Plasma Synthetic Jet for Flow Control*. AIAA Journal Vol 52 ,no 8, pp 1591-1603 (2014).
- [27] A. D'ANGOLA, G. COLONNA, C. GORSE, M. CAPITELLI - *Thermodynamic and Transport Properties in Equilibrium Air Plasma in a Wide Pressure and Temperature Range*. Eur. Phys. J. D, vol 46, pp 129-150 (2007).
- [28] A. REFLOCH, B. COURBET, A. MURRONE, PH. VILLEDIEU, C. LAURENT, P. GILBANK, J. TROYES, L. TESSÉ, G. CHAINERAY, J.B. DARGAUD, E. QUÉMERIS, F. VUILLOT - *CEDRE Software*. AerospaceLab Journal Issue 2, AL02-11 (2011).

Acronyms

DBD	(Dielectric Barrier Discharges)
PSJ	(Plasma Synthetic Jet)
RANS	(Reynolds Averaged Navier-Stokes)
LDA	(Laser Doppler Anemometry)
TS	(Tollmien-Schlichting)
CF	(Crossflow)
PIV	(Particle Image Velocimetry)
LES	(Large Eddy Simulations)
CFD	(Computational Fluid Dynamics)

AUTHORS



François Chedevergne graduated from ISAE SUPAERO, France, and received his PhD degree in Fluid Mechanics in 2007. He is in charge of the modeling of the PSJ actuator developed at ONERA. He is also involved in the development of the ONERA code CEDRE, concerning all aspects related to turbulence modelling.



Grégoire Casalis is the Scientific Deputy Director of the Department Modelling in Aerodynamics and Energetics of ONERA. He is Professor at ISAE-Supaero and has been the director of the Doctoral School "Aeronautics-Astronautics". His scientific topics are related to flow stability, from generic configurations (laminar boundary layer) to complex ones (internal solid rocket motor flow).



Olivier LÉON graduated from École Centrale de Lyon, France, and simultaneously obtained his M.Sc. degree in Aerospace Engineering from the Pennsylvania State University, USA, in 2009. He obtained his Ph.D. degree in Fluid Mechanics in 2012 from Toulouse University. His research interests include fluid dynamics metrology and flow control using plasma actuators.



Maxime Forte graduated from Ecole Nationale Supérieure de Mécanique et d'Aérotechnique (ENSMA - French engineering school specialized in space and aeronautics) in 2004 and received his PhD in Fluid Mechanics from the University of Poitiers in 2007. He joined ONERA in 2010 and works as a research scientist in the Aerodynamics and Energetics Modeling Department in Toulouse. His research interests include experimental investigations on boundary-layer transition (flow control, tripping criteria and new devices for transition detection).



François Laurendeau obtained his engineering degree from SUPAERO in 2013. He is currently a PhD student at Onera. His work, co-financed by the Direction Générale de l'Armement, deals with the unsteady simulations and the PIV characterizations of the Plasma Synthetic Jet actuator.



Natacha Szulga graduated from ISAE-ENSICA in 2013 and is now a PhD student at ONERA-DMAE. Her current work deals with boundary layer transition control by means of DBD actuation and is funded by ONERA and DGA (Délégation Générale de l'Armement).



Olivier Vermeersch graduated from École Nationale Supérieure de Mécanique et d'Aérotechnique (ENSMA - French engineering school specialized in space and aeronautics) in 2006 and received his PhD in Fluid Mechanics from the University of Toulouse in 2009. Since then, he has worked as a research scientist in the Aerodynamics and Energetics Modeling Department of Onera. His research interests include boundary-layer stability computations and control of the laminar/turbulent transition with different kinds of actuation (micro-sized roughnesses, plasma actuators).



Estelle Piot graduated in 2005 from Ecole Polytechnique in Paris, and received her PhD in Fluid Mechanics from the University of Toulouse/Supaéro in 2008, for studies of boundary layer instabilities. Since then, she has been a research engineer at ONERA, in charge of aeroacoustics characterization and optical measurements in flow ducts. In 2014, she became the head of Instability, Transition and Acoustics research unit.

T. Ombrello

(U.S. Air Force Research Laboratory)

N. Popov

(Moscow State University)

E-mail: timothy.ombrello.1@us.af.mil

DOI : 10.12762/2015.AL10-07

Mechanisms of Ethylene Flame Propagation Enhancement by $O_2(a^1\Delta_g)$

Recently estimated and updated quenching rates of $O_2(a^1\Delta_g)$ by H and H_2 have been added to a known and validated combustion mechanism to predict enhancement of C_2H_4 flame propagation in the presence of $O_2(a^1\Delta_g)$. The results of experiments that targeted the isolated enhancement of $O_2(a^1\Delta_g)$ on C_2H_4 flame propagation were used as a means to compare the effects of different chain-initiation, chain-branching, and quenching rates. The ratio of chain-branching to quenching rates of 0.25 to 0.33 for $H+O_2(a^1\Delta_g)$ was found to accurately predict the enhancement trends found in the C_2H_4 flame propagation experiments. The results suggest that flame propagation enhancement of hydrocarbon fuels may not be strongly dependent on the reactions of intermediate hydrocarbon fragments with $O_2(a^1\Delta_g)$ since the dominant pathways may solely lie with primary radicals such as H.

Introduction

Understanding in the field of plasma-assisted combustion has advanced considerably over the past decade, showing significant enhancement and making mainstream practical applications increasingly more realistic [1-3]. Many of the applications are motivated by the need for higher performance and more efficient combustion systems ranging from small internal combustion engines to high-speed air-breathing propulsion devices. These systems can require ignition at low temperatures, within restricted residence times, burning outside normal flammability limits, and flame stabilization in high-speed flows. Therefore, there has been significant effort focused on attempting to gain a fundamental understanding of the mechanisms of plasma-assisted combustion. This has naturally motivated investigations that identify and target specific plasma-produced species and enhancement pathways by decoupling the potential thermal, kinetic, transport, and hydrodynamic effects.

One of the areas of research that has emerged with regard to decoupling the plasma-flame interaction in order to understand combustion enhancement is to produce specific species via a plasma discharge and examine their effects on flame propagation. Since the propagation of a flame is driven by how the reactants are conditioned and brought to sufficiently high temperatures allowing for rapid oxidation, thermal conduction and radical diffusion upstream are vital. Therefore there is the potential to affect flame propagation rates by either providing a source of heat or by modifying the kinetics to increase chemical heat release in the lower temperature preheat portions of a flame. The application of plasma touches upon both of these enhancement mechanisms by producing species in the reactants somewhere

upstream that will allow for modification of kinetics in the early stages of the flame. For example, the low temperature preheat zone will significantly benefit from the activation of new kinetic pathways through the introduction of specific species that affect chain-initiation and chain-branching reactions. This in turn couples with the enhanced early reactivity and heat release that ultimately results in a more rapid propagating or stable flame. For this to be accomplished, the species causing the enhancement need to survive until the flame front, and therefore results in either in situ production for short lifetime species, or potential remote production for longer lifetime species. This creates a challenge as to discerning where and how the species are produced, and therefore properly defining the boundary conditions for modelling. An attractive plasma-produced species that can be produced and introduced to a flame for enhancement is $O_2(a^1\Delta_g)$, the first electronically excited state of O_2 . While $O_2(a^1\Delta_g)$ is typically produced among many other plasma species that have the potential to enhance a flame, one of the key points is that $O_2(a^1\Delta_g)$ requires very low excitation levels with only 0.98 eV/molecule. Therefore, it has the potential to be generated across a wide range of systems. More importantly, $O_2(a^1\Delta_g)$ has very high reactivity. For example, take one of the most important chain-branching reactions in combustion systems,



If the O_2 in the system is excited to the first electronic level, $O_2(a^1\Delta_g)$, it is shown in figure 1 that the reaction rate becomes significantly faster (up to 6 orders of magnitude), especially at temperatures below 1000 K. Furthermore, if only 1% of the O_2 is converted to $O_2(a^1\Delta_g)$, there remains an order of magnitude increase in the reaction rate at temperatures as high as 1000 K. Therefore, if plasma can activate the

oxidizer of a combustion system to produce $O_2(a^1\Delta_g)$, there is great potential to enhance the overall combustion process with small energy input through chain-branching because of the high chemical selectivity and radical production. Furthermore, $O_2(a^1\Delta_g)$ has a significantly long radiative lifetime (> 4000 s) because of a spin forbidden transition to the ground state [4]. Therefore, it can be produced remotely, quantitatively measured, and transported to a flame, allowing for a clear definition of the boundary conditions for any experiment, and therefore subsequent modelling efforts.

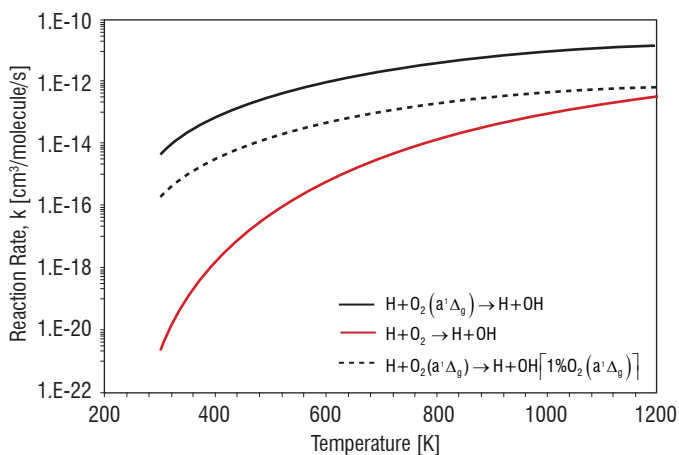


Figure 1 – Calculated reaction rate as a function of temperature for H with O_2 and $O_2(a^1\Delta_g)$ [5, 6]

Because of the potential benefits of $O_2(a^1\Delta_g)$, there have been many works targeting an understanding of the enhancement mechanism using a variety of fuels [7-15]. The experiments and kinetic models have shown that the induction and ignition delay times can be reduced significantly and the laminar flame speeds can be enhanced. Initially Basevich *et al.*, apparently for the first time, used the reactions involving $O_2(a^1\Delta_g)$ to explain flame speed enhancement in H_2/O_2 mixtures after the excitation of O_2 by a discharge [7]. The oxygen flow was excited by a DC discharge ($I=5-85$ mA), and then H_2 was added to the flow. The obtained mixture was ignited by a pulsed spark discharge with subsequent measurements of normal flame velocity and the axial profile of translational gas temperature. For discharge currents exceeding 17 mA, the flame velocity almost doubled, while the increase in the translational gas temperature did not exceed 5-10 K. The results of the simulations in reference [5] confirmed the assumption that the impact of a glow discharge in O_2 on the flame velocity was likely associated with the effect of $O_2(a^1\Delta_g)$ molecules.

Kozlov *et al.* [11] also investigated flame propagation enhancement by performing numerical simulations of H_2/O_2 flames with the addition of $O_2(a^1\Delta_g)$ under the conditions of the experiments in reference [7]. The results showed that a 10% conversion of O_2 to $O_2(a^1\Delta_g)$ gave more than a 50% increase in the laminar flame velocity. Lean mixtures were enhanced more than stoichiometric and rich mixtures because of the chain-initiation and chain-branching reactions involved. It should be noted though that gas heating may not be neglected with such a significant concentration of $O_2(a^1\Delta_g)$. With having 10% of the O_2 excited to $O_2(a^1\Delta_g)$, its thermalization exceeds a temperature change of 100 K for a stoichiometric H_2/O_2 mixture and greater than 300 K for a lean ($\phi = 0.1$) H_2/O_2 mixture.

Bourig *et al.* extended the numerical modeling by investigating flame propagation, as well as flame stabilization by $O_2(a^1\Delta_g)$ [15]. More recently, Starik *et al.* numerically examined the effects of $O_2(a^1\Delta_g)$ on CH_4 -air flame propagation with a detailed kinetic mechanism

developed [13]. Similar to previous investigations, the flame propagation enhancement was up to 40% for fuel rich mixtures and up to 70% for fuel lean mixtures with 10% conversion of O_2 to $O_2(a^1\Delta_g)$. Nevertheless, there was a lack of clean experiments for detailed comparisons of the enhancement, and therefore left question as to how valid the enhancement predictions were.

Recent advancements in experiments have provided some data on the individual effects of $O_2(a^1\Delta_g)$ on flame propagation. In the previous work of Ombrello *et al.* [16], experiments were designed and conducted to isolate $O_2(a^1\Delta_g)$ from other excited species for transport to sub-atmospheric pressure lifted tribrachial flames. The details of the experiments can be found in reference [16], and therefore only a brief description is given here for clarity of the motivation. The experimental set-up, shown in figure 2, consisted of a high velocity (20-40 m/s) 1.04 mm diameter C_2H_4 fuel jet within a low velocity (0.15-0.2 m/s) 90 mm diameter O_2/Ar co-flow to make the burner, which was placed in a variable pressure chamber. This burner configuration created a mixing layer with a stoichiometric contour where the premixed flame head was always anchored, followed with a diffusion flame tail (shown in the right inset in figure 2). Because of the slow laminar boundary layer development and the velocity and concentration gradients created, the lifted flame height was very sensitive to the changes in flame speed, and therefore provides favorable flame geometry for the direct observation of flame speed enhancement. Therefore, for a fixed flow field, the flame was located in a stationary position where the lifted flame speed at the premixed flame head was balanced with the local flow velocity. If the flame speed was increased because of the presence of plasma species, the liftoff height decreased to re-establish a local dynamic balance between the flame speed and flow velocity. Importantly, since the fuel and oxidizer were not mixed far upstream of the flame, there was very short residence time for the fuel and oxidizer to react in the cold flow, isolating the enhancement effects to be directly from reactions in the flame zone and not far upstream in the cold un-reacted flow.

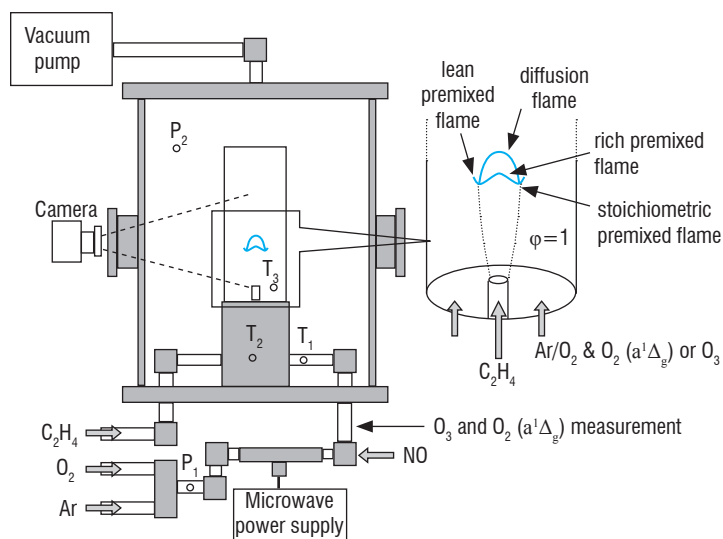
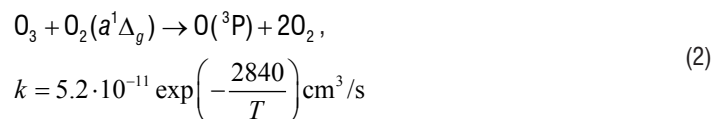


Figure 2 – Set-up for experiments in reference [16]

Upstream of the burner, the O_2/Ar mixture was excited with a self-sustained microwave discharge which produced excited Ar, as well as multiple oxygen containing species such as O, O_3 , $O_2(v)$, $O(^1D)$, $O(^1S)$, $O_2(a^1\Delta_g)$, and $O_2(b^1\Sigma_g^-)$. Pressures and reactant flow rates were chosen to provide long residence times (0.91-1.68 s) between the discharge and burner to allow for quenching and recombination of most species except O_3 and $O_2(a^1\Delta_g)$. These two species could be

selectively quenched with the addition of NO in the plasma afterglow. Without NO injection, the $O_2(a^1\Delta_g)$ was quenched via reaction with O and O_3 . With NO injection, the O and O_3 were catalytically removed and the $O_2(a^1\Delta_g)$ concentration was preserved. Additionally, the NO did not have any effect on the flame speed with the concentrations that were injected.

The isolation of $O_2(a^1\Delta_g)$ from all other plasma species was vital to develop an understanding of the kinetic pathways involved because of the strong combustion enhancement from other species, such as O and O_3 , as well as their ability to rapidly quench $O_2(a^1\Delta_g)$. For example, the reaction of [17]:



rapidly quenches $O_2(a^1\Delta_g)$ and produces atomic oxygen, potentially in the high temperature region in a flame front. The atomic oxygen can then take part in critical chain chemical reactions which significantly increase flame propagation speeds.

Therefore, with the plasma turned on and off, with and without NO injection, the isolated effects of O_3 and $O_2(a^1\Delta_g)$ on flame speed were observed by changes in flame liftoff height. Significantly, the results were the first isolated enhancement effects of $O_2(a^1\Delta_g)$ on C_2H_4 flame speed, with clear correlations between increased change in flame liftoff height (and hence increase in flame speed) with increased $O_2(a^1\Delta_g)$ concentration. Interestingly, the results (shown in figure 3) revealed that approximately 500 parts per million (ppm) of O_3 produced the same amount of flame speed enhancement as approximately 5500 ppm of $O_2(a^1\Delta_g)$. Since the flame speed enhancement kinetics with O_3 is fairly well known, it can be used as a metric for comparison to flame speed enhancement kinetics with $O_2(a^1\Delta_g)$. This is a key point that is vital to the discussion to follow in this paper.

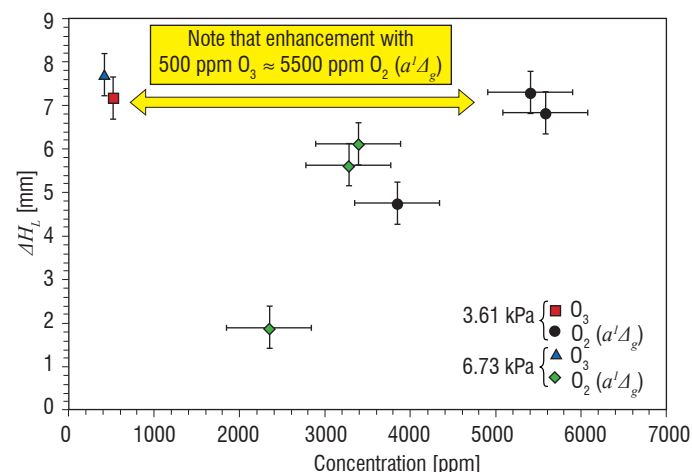


Figure 3 – Experimental results of flame liftoff change with $O_2(a^1\Delta_g)$ and O_3 concentration. The error bars denote the experimental uncertainties in the concentrations and change in flame liftoff height [16]

The goal of the present work was to use the experimental data shown in figure 3 from reference [16] as a target to assess the sensitivity of chain-initiation, chain-branching, and quenching rates of $O_2(a^1\Delta_g)$ on C_2H_4 flame speed enhancement. The roles of specific reactions are sought in order to better understand and validate the flame speed enhancement kinetics with the presence of $O_2(a^1\Delta_g)$.

Initial Simulations and Kinetics

Originally in reference [16], simulations were performed in an attempt to explain the flame speed enhancement and understand the mechanisms involved with the presence of $O_2(a^1\Delta_g)$. To accomplish this, a kinetic sub-mechanism was added to a validated combustion mechanism [18] and simple one-dimensional flame simulations [19] were performed. The tribrachial flames that were used in the experiments of reference [16] are established in the mixing layer between the fuel and the oxidizer. Even though there is a non-premixed boundary condition for the reactants, the leading edge and stabilization point of the flame is premixed and at a stoichiometric equivalence ratio [20-25]. Therefore simple one-dimensional premixed stoichiometric freely propagating flame simulations can be performed and used for valid comparison. The one-dimensional laminar flame speed can be converted to the tribrachial flame speed by the square root of the unburned to the burned density ratio [20]. Through the original calculations in reference [16], it was found that there was a significant mismatch in enhancement between $O_2(a^1\Delta_g)$ and O_3 compared to the experiments. In the experiments, approximately 500 ppm of O_3 was yielding the same change in flame liftoff height (and hence increase in flame speed) as approximately 5500 ppm of $O_2(a^1\Delta_g)$ (see figure 3), whereas the simulations were showing significantly elevated levels of enhancement with $O_2(a^1\Delta_g)$ (~5%) as compared to O_3 (~1%) (figure 4). Since the kinetics are simple and fairly well known for O_3 , there was concern that the $O_2(a^1\Delta_g)$ mechanism was in error. Specifically, the thought was that $O_2(a^1\Delta_g)$ quenching reactions were missing, leading to higher concentrations surviving throughout the early stages of the flame and hence elevated levels of flame propagation enhancement.

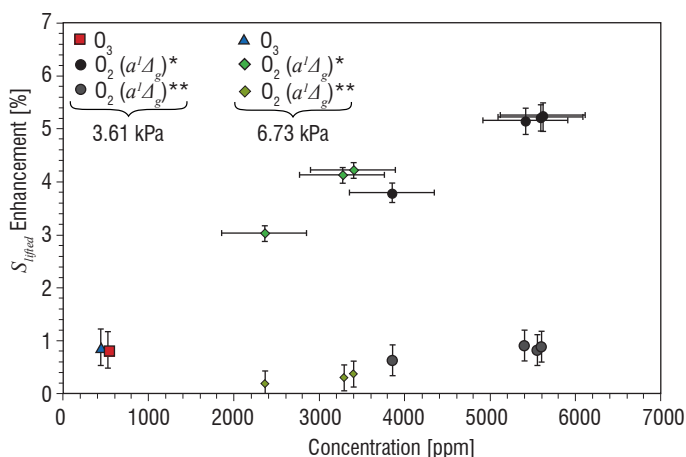
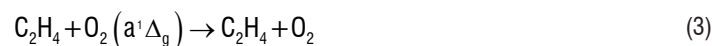


Figure 4 – Computational results of lifted flame speed enhancement with $O_2(a^1\Delta_g)$ and O_3 using the original kinetics (*) and the inclusion of the estimated fictitious collisional quenching rate of C_2H_4 with $O_2(a^1\Delta_g)$ to fit trend of experimental results (**)[16]

To rectify, there was emphasis placed on the quenching of $O_2(a^1\Delta_g)$ via the fuel, C_2H_4 . Unfortunately, there was a lack of temperature dependent quenching rate data of $O_2(a^1\Delta_g)$ by hydrocarbon species that was suspected to be the main cause for the discrepancy. The only rates that could be found were at 298 K [26]. Therefore, a temperature dependent quenching reaction rate was estimated for



in order to explain the mismatch in enhancement as compared to the experiment. Since the temperature dependence of $O_2(a^1\Delta_g)$ quenching

by other parent fuels, such as H_2 , are approximately Arrhenius,[27] it was assumed that C_2H_4 might also follow. Therefore, originating with the quenching rate of $O_2(a^1\Delta_g)$ at 298 K given in reference [27], a temperature dependent rate was found that would explain the discrepancy between the experimental results in reference [16] and the original kinetics. The estimated rate is shown in figure 5, and the results of the calculated flame speed enhancement are shown in figure 4. While the enhancement by $O_2(a^1\Delta_g)$ could be decreased to the levels of O_3 as shown in the experiments with the estimated rate for (3), it was unrealistic and therefore motivated more detailed studies into the kinetics.

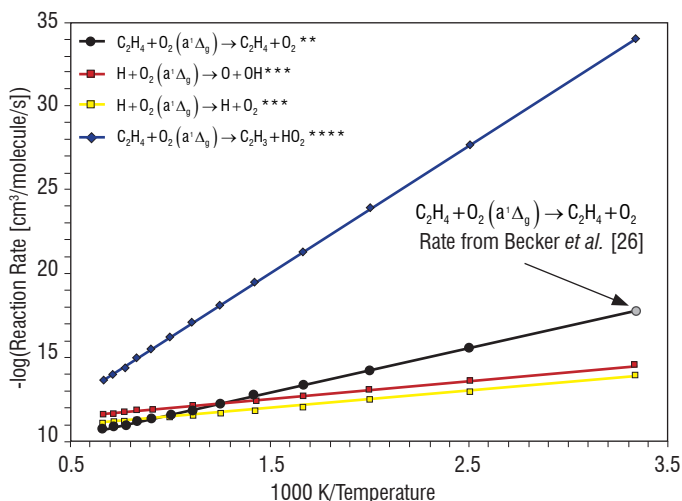


Figure 5 – Arrhenius temperature dependent collisional and reactive quenching rates of $O_2(a^1\Delta_g)$ by H and C_2H_4 . Estimated quenching rate of C_2H_4 with $O_2(a^1\Delta_g)$ to fit trend of experimental results (**), rate from reference [28] (***), and rate from reference [13] (****)

Simulations with Updated Kinetics

Recently there have been advancements in the kinetic understanding of $O_2(a^1\Delta_g)$ based upon the collective interpretation of many experimental and computational studies. One temperature dependent reaction rate of importance to a C_2H_4 fueled system that was shown in reference [13] is



While this reaction has the potential to affect $O_2(a^1\Delta_g)$ concentration and the overall reaction mechanism (see figure 5), simulations showed that it had no effect on the flame speed enhancement.

The focus of another recent work dealing with the enhancement kinetics via $O_2(a^1\Delta_g)$ was on H_2/O_2 reactants for simplicity and greatest comparison to experimental results [28]. It was found that in order to explain a wide range of experimental observations, there was an error in $O_2(a^1\Delta_g)$ quenching. In short, this meant that the original kinetics used in the simulations shown in figure 4 were overestimating the enhancement compared to the experiments. The focus of the discrepancy was on the balance between the chain-initiation and quenching pathways of H_2 with $O_2(a^1\Delta_g)$ and the chain-branching and quenching pathways of H with $O_2(a^1\Delta_g)$ via the reactions:



The concern was that the weighting of the chain-initiation and chain-branching pathways were higher than they should be, and therefore would lead to significantly elevated levels of flame enhancement. Specifically, the balance between (7) and (8) was suspect because of how critical $H + O_2$ is to all combustion systems. The result of the study [28] showed that the ratio of chain-branching to quenching (7/8) should not be greater than 0.25. In order to provide some level of experimental validation, a comprehensive numerical study of the ignition of H_2/O_2 mixtures for the experimental conditions of [29] was carried out by Chukalovsky *et al.* [30]. Similarly, it was shown that the probability of the chain-branching to the collisional quenching pathway (7/8) decreased to approximately 0.11 at high temperature. This weighting of the quenching reaction versus the branching reaction was a departure from previous thoughts on the kinetics, and since these two reactions are so dominant in all combustion systems, it was prudent to assume that they might have implications beyond just H_2/O_2 systems, specifically for hydrocarbon fuels.

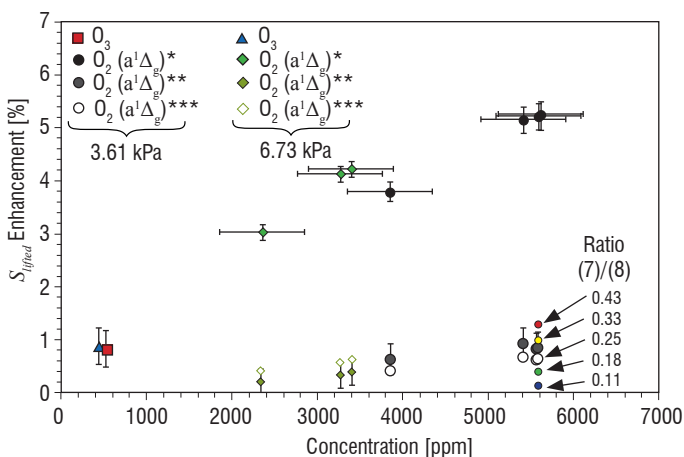


Figure 6 – Computational results of lifted flame speed enhancement with $O_2(a^1\Delta_g)$ and O_3 using the original kinetics (*), the inclusion of the fictitious rate for reaction (3) [16] (**), and the updated kinetics with H and H_2 from reference [28] (***)

The experimental and simulation results from reference [16] were then revisited with the knowledge garnered in the H_2/O_2 reactant study. Since it was clear that the fictitious reaction of $O_2(a^1\Delta_g)$ quenching via C_2H_4 (3) was able to explain the discrepancy, it was compared to the updated reactions of (7) and (8) across the temperature range experienced in a flame. The results are shown in figure 5. The collisional quenching rate (8) is very comparable to the fictitious rate of (3) at temperatures above 700 K, which is in the regime that would most affect the early stages of the flame.

The flame propagation enhancement was then computed using the updated kinetics and removing (3) to see if it also explained the discrepancy compared to the experiments. Figure 6 shows the results of using the updated rates for $O_2(a^1\Delta_g)$ involved in chain-branching

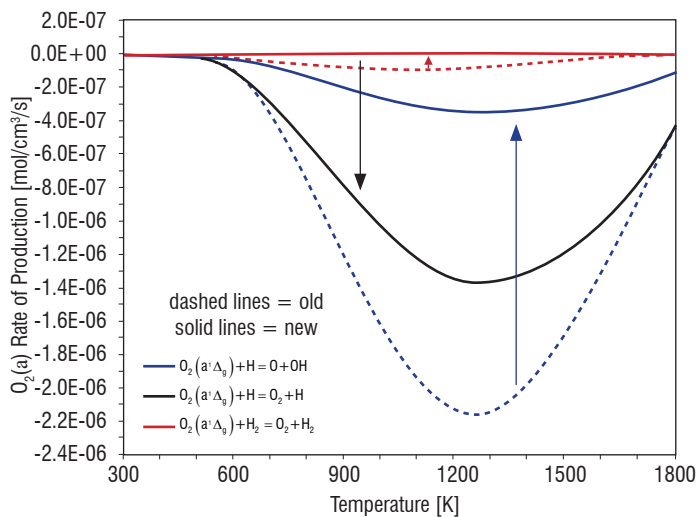


Figure 7 – Computed rate of production of $O_2(a^1\Delta_g)$ versus temperature showing the major consumption pathways of $O_2(a^1\Delta_g)$ with the original and updated H and H_2 kinetics

and collisional quenching with the suggested (7/8) ratio of 0.25 from reference [28]. The new ratio gives computed flame speed enhancement that nearly matches the experimental trends, as well as when using the fictitious reaction (3). This clearly shows that the collisional quenching reaction of (8) plays a critical role in explaining the enhancement for the C_2H_4 fueled system. Additional simulations were performed with varying the ratio of (7/8) from 0.11 to 0.43. The results showed that a ratio of 0.25 to 0.33 provided a comparable level of enhancement via $O_2(a^1\Delta_g)$ to match O_3 .

A more detailed investigation of the kinetic processes involved was achieved by examining the rate of production of $O_2(a^1\Delta_g)$. This allowed for an understanding of what the differences were in terms of the reactions with $O_2(a^1\Delta_g)$ with the original and updated kinetics. The major pathways with H and H_2 are shown in figure 7. The differences can be seen in the decreased importance of (6) and (7), but increased reactivity via (8). The shifting of importance of the reaction makes sense since H is present in the early stages of the flame because of back diffusion from the high-temperature reaction front.

When compared to the past kinetics with the fictitious rate for (3) in figure 8, it became more apparent why the updated kinetics correctly captured the effect on the flame enhancement. In the past work of reference [16] the fictitious rate for (3) had a peaked consumption

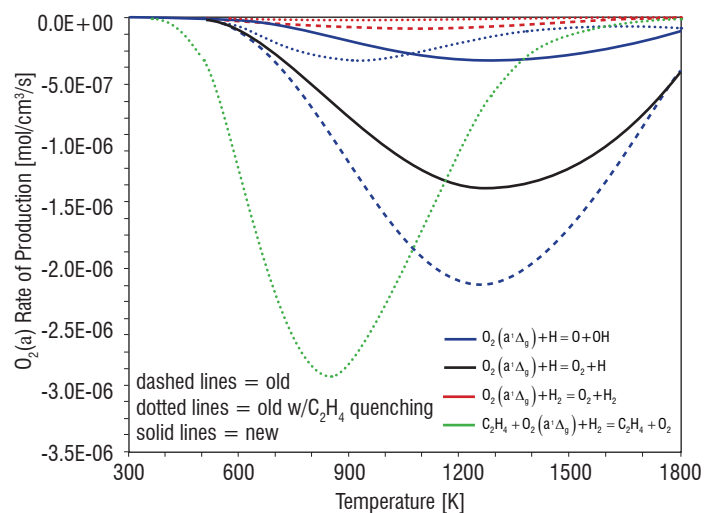


Figure 8 – Computed rate of production plot of $O_2(a^1\Delta_g)$ versus temperature showing the major consumption pathways of $O_2(a^1\Delta_g)$ with the past and updated kinetics

rate at much lower temperatures than reasonable because of having to compensate for the elevated branching rates via (7). The updated kinetics suppressed the chain-branching reaction (7) and increased the quenching reaction (8), resulting in a more accurate and realistic explanation of the enhancement.

Summary and Conclusions

It has become evident through the inclusion of recently updated kinetics that careful attention needs to be paid to the balance between chain-initiation, chain-branching, and quenching rates when interrogating $O_2(a^1\Delta_g)$. Specifically, since the H atom is one of the most dominant and important intermediate radicals in all combustion systems, its contribution to collisional quenching needs to be heavily weighted and considered for an accurate description of any combustion enhancement mechanisms. The results of new H and H_2 kinetics with $O_2(a^1\Delta_g)$ has provided a more accurate explanation of the flame propagation enhancement of C_2H_4 by $O_2(a^1\Delta_g)$. The implications are far ranging, indicating that the development of the kinetics involved in the enhancement of hydrocarbon fuels may not have to include intermediate hydrocarbon fragment reactions with $O_2(a^1\Delta_g)$ to accurately predict flame propagation enhancement. The dominant pathways may solely lie with primary radicals such as H ■

References

- [1] A. STARIKOVSKIY and N. ALEKSANDROV – *Plasma-Assisted Ignition and Combustion*. Progress in Energy and Combustion Science, Vol. 39, pp. 61-110, 2013.
- [2] S. M. STARIKOVSKAIA – *Plasma Assisted Ignition and Combustion: Nanosecond Discharges and Development of Kinetic Mechanisms*. Journal of Physics D: Applied Physics, Vol. 47, pp. 353001, 2014.
- [3] I. V. ADAMOVICH and W. R. LEMPert – *Challenges in Understanding and Development of Predictive Models of Plasma Assisted Combustion*. Plasma Physics Controlled Fusion, Vol. 57, pp. 014001, 2015.
- [4] A. A. IONIN, I. V. KOCHETOV, A. P. NAPARTOVICH and N.N. Yuryshv – *Physics and Engineering of Singlet Delta Oxygen Production in Low-Temperature Plasma*. Journal of Physics D: Applied Physics, Vol. 40, R25-R61, 2007.
- [5] V. Ya. BASEVICH and A. A. BELYAEV – *Evaluation of Hydrogen-Oxygen Flame Velocity Increase at Singlet Oxygen Addition*. Chemical Physics Reports, Vol. 8, pp. 1124, 1989.
- [6] L. IBRAGIMOVA, G. SMEKHOV and O. SHATALOV – *Recommended Rate Constants of Chemical Reactions in an H_2 - O_2 Gas Mixture with Electronically Excited Species $O_2(^1A)$, $O(^1A)$, $OH(^2\Sigma)$ Involved*. Institute of Mechanics of Lomonosov, Moscow State University, 2003.
- [7] V. Y. BASEVICH and S. M. KOGARKO – *To Mechanism of the Influence of Glow Discharge Products on the Hydrogen-Oxygen Flame Velocity in Conditions of Inflammation Peninsula*. Kinetics and Catalysis, Vol. 7, pp. 393, 1966.

- [8] G. D. SMEKHOV, L. B. IBRAGUIMOVA, S. P. KARKACH, O.V. SKREBKOV and O. P. Shatalov – *Numerical Simulation of Ignition of Hydrogen-Oxygen Mixture in View of Electronically Excited Components*. High Temperature, Vol. 45, n° 3, pp. 395-407, 2007.
- [9] O. V. SKREBKOV and S. P. KARKACH – *Vibrational Nonequilibrium and Electronic Excitation in the Reaction of Hydrogen with Oxygen Behind a Shock Wave*. Kinetics and Catalysis, Vol. 48, n° 3, pp. 367-375, 2007.
- [10] A. M. STARIK and N.S. TITOVA – *Kinetics of Detonation Initiation in the Supersonic Flow of the $H_2 + O_2$ (air) Mixture in O_2 Molecule Excitation by Resonance Laser Radiation*. Kinetics and Catalysis, Vol. 44, n° 1, pp. 28-39, 2003.
- [11] V.E. KOZLOV, A. M. STARIK and N. S. Titova – *Enhancement of Combustion of a Hydrogen-Air Mixture by Excitation of O_2 Molecules to the Singlet State*. Combustion, Explosion, and Shock Waves, Vol. 44, n° 4, pp. 371-379, 2008.
- [12] A. M. STARIK, V. E. KOZLOV and N. S. TITOVA – *On Mechanisms of Flame Velocity Increase Upon Activation of O_2 Molecules in Electrical Discharge*. Journal of Physics D: Applied Physics, Vol. 41, 125206, 2008.
- [13] A. M. STARIK, V. E. KOZLOV and N. S. TITOVA – *On the Influence of Singlet Oxygen Molecules on the Speed of Flame Propagation in Methane-Air Mixture*. Combustion and Flame, Vol. 157, n° 2, pp. 313-327, 2010.
- [14] A. S. SHARIPOV and A. M. STARIK – *Kinetic Mechanism of $CO-H_2$ System Oxidation Promoted by Excited Singlet Oxygen Molecules*. Combustion and Flame, Vol. 159, n° 1, pp. 16-29, 2012.
- [15] A. BOURIG, D. THÉVENIN, J. P. MARTIN, G. JANIGA and K. ZÄHRINGER – *Numerical Modeling of H_2-O_2 Flames Involving Electronically-Excited Species $O_2(a^1\Delta_g)$, $O(^1D)$ and $OH(^2\Sigma^+)$* . Proceedings of the Combustion Institute, Vol. 32, pp. 3171-3179, 2009.
- [16] T. OMBRELLO, S. H. WON, Y. JU and S. WILLIAMS – *Flame Propagation Enhancement by Plasma Excitation of Oxygen. Part II: Effects of $O_2(a^1\Delta_g)$* . Combustion and Flame, Vol. 157, pp. 1916-1928, 2010.
- [17] J. I. STEINFELD, S. M. ADLER-GOLDEN and J. W. GALLAGHER – *Critical Survey of Data on the Spectroscopy and Kinetics of Ozone in the Mesosphere and Thermosphere*. Journal Physical Chemistry Reference Data, Vol. 16, n° 4, pp. 911-951, 1987.
- [18] H. WANG, X. YOU, A. V. JOSHI, S. G. DAVIS, A. LASKIN, F. EGOLFOPOULOS and C. K. LAW – *USC Mech Version II. High-Temperature Combustion Reaction Model of $H_2/CO/C_1-C_4$ Compounds*. http://ignis.usc.edu/USC_Mech_II.htm, May 2007.
- [19] PREMIX from the CHEMKIN package, Reaction Design, 6440 Lusk Boulevard, Suite D-205, San Diego, CA 92121. <http://www.reactiondesign.com>.
- [20] S. H. CHUNG – *Stabilization, Propagation and Instability of Tribrachial Triple Flames*. Proceedings of the Combustion Institute, Vol. 31, n° 1, pp. 877-892, 2007.
- [21] J. LEE, S. WON, S. JIN and S. CHUNG – *Lifted Flames in Laminar Jets of Propane in Coflow Air*. Combustion and Flame, Vol. 135, n° 4, pp. 449-462, 2003.
- [22] J. JU and Y. XUE – *Extinction and Flame Bifurcations of Stretched Dimethyl Ether Premixed Flames*. Proceedings of the Combustion Institute, Vol. 30, pp. 295-301, 2005.
- [23] Y. XUE and Y. JU – *Combustion Science and Technology*. Vol. 178, pp. 2219-2247, 2006.
- [24] M. KIM, S. WON and S. CHUNG – *Effect of Velocity Gradient on Propagation Speed of Tribrachial Flames in Laminar Coflow Jets*. Proceedings of the Combustion Institute, Vol. 31, pp. 901-908, 2007.
- [25] G. RUETSCH, L. VERVISCH and A. LINAN – *Effects of Heat Release on Triple Flames*. Physics of Fluids, Vol. 7, pp. 1447-1454, 1995.
- [26] K. H. BECKER, W. GROTH and U. SCHURATH – *The Quenching of Metastable $O_2(a^1\Delta_g)$ and $O_2(b^1\Sigma_g^-)$ Molecules*. Chemical Physics Letters, Vol. 8, pp. 259-262, 1971.
- [27] P. BORRELL and D.S. RICHARDS – *Quenching of Singlet Molecular Oxygen, $O_2(a^1\Delta_g)$ and $O_2(b^1\Sigma_g^-)$, by H_2 , D_2 , HCl and HBr* . Journal of the Chemical Society: Faraday Transactions 2, Vol. 85, n° 9, pp. 1401-1411, 1989.
- [28] N. A. POPOV – *Effect of Singlet Oxygen $O_2(a^1\Delta_g)$ Molecules Produced in a Gas Discharge Plasma on the Ignition of Hydrogen-Oxygen Mixtures*. Plasma Sources Science and Technology, Vol. 20, n° 4, 2011.
- [29] V. V. SMIRNOV, O. M. STELMAKH, V. I. FABELINSKY, D. N. KOZLOV, A. M. STARIK and N. S. TITOVA – *On the Influence of Electronically Excited Oxygen Molecules on Combustion of Hydrogen-Oxygen Mixture*. Journal of Physics D: Applied Physics, Vol. 41, pp. 192001, 2008.
- [30] A. A. CHUKALOVSKY, K. S. KLOPOVSKY, M. A. LIBERMAN, Y. A. MANKELEVICH, N. A. POPOV, O. V. PROSHINA and T. V. RAKHIMOVA – *Study of Singlet Delta Oxygen $O_2(a^1\Delta_g)$ Impact on H_2-O_2 Mixture Ignition in Flow Reactor: 2D Modeling*. Combustion Science and Technology, Vol. 184, n° 10-11, pp. 1768-1786, 2012.

AUTHORS



Timothy Ombrello earned his Ph.D. in Mechanical and Aerospace Engineering from Princeton University in 2009 and is currently a Research Aerospace Engineer in the High Speed Systems Division at the U.S. Air Force Research Laboratory. His interests lie in performing research and crafting techniques to enhance reactivity for more rapid ignition and more robust flame propagation and stabilization, from fundamental bench-top to supersonic wind tunnel experiments.



Nikolay Popov received his Ph.D. in Plasma Physics from Moscow Radio-Technical Institute, Russian Academy of Science, Moscow in 1990 and Dr. of Sciences degree from Moscow State University in 2010. He is currently a Lead Scientific Researcher in Skobel'tsyn Institute of Nuclear Physics, Moscow State University. His interests lie in numerical studies of non-equilibrium processes in gas discharge plasma, plasma chemistry, and plasma assisted ignition and combustion.

Konstantin V. Savelkin
Dmitry A. Yarantsev

(Joint Institute for High Temperatures, Russian Academy of Sciences, 125412 Moscow, Russia)

Sergey B. Leonov

(Joint Institute for High Temperatures, Russian Academy of Sciences, 125412 Moscow, Russia)
 (Department of Aerospace and Mechanical Engineering, University of Notre Dame, Notre Dame, IN, 46556, USA)

E-mail : leonov.1@nd.edu

DOI: 10.12762/2015.AL10-08

Experiments on Plasma-Assisted Combustion in a Supersonic Flow: Optimization of Plasma Position in Relation to the Fuel Injector

The results of an experimental study of plasma-induced ethylene ignition and flameholding in a supersonic model combustor are presented in the paper. The experimental combustor has a cross-section of 72 mm (width) x 60 mm (height) and length of 600 mm. The fuel is directly injected into the supersonic airflow through wall orifices. The flow parameters are: Mach number $M=2$, static pressure $P_{st}=160-250$ Torr, stagnation temperature $T_0=300$ K and total air flow rate $G_{air} \leq 0.9$ kg/s. The near-surface quasi-DC electrical discharge is generated by a series of flush-mounted electrodes, providing an electrical power deposition of $W_{pl}=3-24$ kW. The scope of the experiments includes the characterization of the discharge interacting with the main flow and fuel injection jet, a parametric study of ignition and flame front dynamics and a comparison of three plasma generation schemes: the first two examine upstream and downstream locations of plasma generators in relation to the fuel injectors. The third pattern follows a novel approach of a combined mixing/ignition technique, where the electrical discharge is distributed along the fuel jet, starting within the fuel injector. The last pattern demonstrates a significant advantage in terms of the flameholding limit. The experiments are supported by gas temperature and H_2O vapor concentration measurements by Tunable Diode-Laser Absorption Spectroscopy (TDLAS). The technique studied in this work has weighty potential for high-speed combustion applications, including cold start/restart of scramjet engines and support of the transition regime in a dual-mode scramjet and during off-design operation.

Introduction

Ignition and stabilization of combustion in supersonic flows at low and moderate entry total enthalpies is a problem of major fundamental and applied importance in the development of hypersonic vehicles. The use of gaseous plasma generated in electrical discharges for the stabilization of supersonic combustion is one of the most promising approaches. Compared to a basic scramjet layout, the scheme with plasma assistance delivers more freedom in the choice of the geometric configuration, due to the replacement of a mechanical flameholder with a highly effective electrically driven apparatus. Prospectively, the use of this method could lead to a reduction in total pressure losses under non-optimal conditions, to the enhancement of operation stability and, consequently, to expanding the limitations in scramjet operability.

The concept of Plasma-Induced Ignition and Plasma-Assisted Combustion is considered on the basis of three main ideas: the gas heating/non-equilibrium excitation by the discharge, fuel-air mixing in-

tensification and flow structure control in the vicinity of the reaction zone. Over the years, many studies have been conducted to develop an alternative plasma-based ignition system that could consistently and reliably ignite non-stoichiometric mixtures at a wide range of pressures and temperatures [1-3]. Most plasma technologies rely on a high energy density electrical discharge to ionize the mixture and initiate combustion due to a thermal/chemical activation of the fuel or air/fuel mixture [3-5]. Likewise, the experimental studies were performed under conditions that are typical for scramjet operation [6-10]. A basic geometric configuration was used for the duct, which includes a backward wallstep or contoured cavity. Factually, plasma is used as an igniter of a combustible mixture in a low-speed zone. At the same time, previous experiments with this configuration, where an electric discharge is used with a plane wall arrangement [11-12], demonstrate the feasibility of plasma application as an effective igniter, mixer and flameholder in a supersonic combustor without the help of any mechanical obstacles.

Another pole of the problem is highly non-equilibrium chemical kinetics, which may help to reduce plasma power for the fuel-oxidizer mixture ignition, due to variable selectivity of chemical reaction pathways. Significant progress in this domain over the last 15 years is apparent [3-5, 13-15]. It has been shown that a dramatic reduction in the ignition time up to orders of magnitude occurs at premixed conditions, including a range of gas temperatures that is specifically important for scramjet technology, $T_o=500-900\text{ K}$. Despite being very promising, such an approach seems to be of little practicality for high-speed engines with direct fuel injection. Under most conditions, the main limiting factor is rather slow mixing, resulting in a strong fuel/oxidizer ratio gradient across the combustion chamber. The most challenging issue in this case is the proper location of a typically non-uniform discharge in a shear layer between the fuel jet and the surrounding airflow.

A novel pattern of plasma-fuel interaction is examined in this paper and is compared to previously tested configurations, where plasma is generated in the air in front of the fuel injection [11-12, 16]. In the current scheme, electric discharge is partially located inside of an injection orifice, chemically pre-processing the fuel and accelerating the mixing due to the introduction of strong thermal inhomogeneity into the flow field. The idea exploits the effect of discharge specific localization in the shear layer with a gradient concentration of two gases [17]. For future research, such an approach appears to be quite prospective to promote mixing and flameholding in a supersonic combustor.

Experimental apparatus and diagnostics

The experiments were performed in a supersonic blow-down wind tunnel PWT-50H [11 12], the schematic drawing of which is shown in figure 1. In this configuration, the test section operates as a supersonic combustor, with the fuel injectors and electrical discharge generator flush-mounted on a plane wall [18], as shown tentatively in figure 1b. The combustor cross-section is $Y \times Z = 72\text{ mm}$ (width) $\times 60\text{ mm}$ (height), with a length of $X = 600\text{ mm}$. In order to avoid thermal choking during fuel ignition, the test section has a 10° expansion angle downstream of the injectors on the opposite (bottom) wall to the cross-section of $Y \times Z = 72\text{ mm} \times 72\text{ mm}$. The experimental conditions are as follows: initial Mach number $M=2$; static pressure $P_{st}=160-250\text{ Torr}$; air mass flow rate $G_{air}=0.6-0.9\text{ kg/s}$; fuel (ethylene) mass flow rate $G_{C_2H_4}=1-8\text{ g/s}$; duration of steady-state aerodynamic operation $t \leq 0.5\text{ s}$. The PWT-50H high-speed combustion facility test section is equipped with 3 pairs of 100 mm diameter windows placed in the side walls of the duct for optical access. The first pair of windows is located near the upstream side of the combustor and provides optical access to the plasma-fuel-flow interaction area. The second pair of windows is placed downstream, with a 65 mm gap between the two pairs of windows. The third pair of windows is typically used for TDLAS measurements, as has been done in our previous work [16]. Instrumentation includes the pressure measuring system, the schlieren system, a UV/visible optical emission spectrometer, current and voltage sensors, a Tunable Diode Laser Absorption Spectroscopy (TDLAS) apparatus for water vapor temperature/concentration measurements, a 5-component exhaust flow chemical analyzer, high-speed cameras and operation sensors.

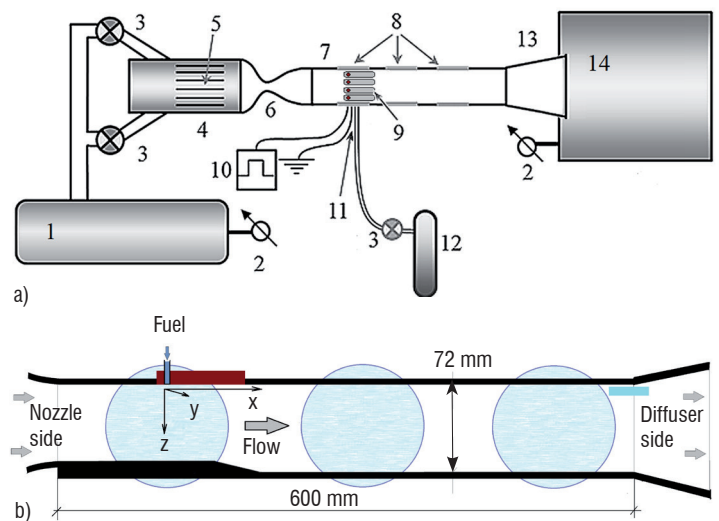


Figure 1 - Schematic drawing of the PWT-50H experimental facility.
a) General layout : 1- high pressure tank ; 2 - operation gauges ; 3 - solenoid valves ; 4 - plenum section ; 5 - honeycomb ; 6 - nozzle ; 7 - test section ; 8 - optical access windows ; 9 - plasma-injector modules ; 10 - high-voltage power supply ; 11 - fuel ports / discharge connectors ; 12 - fuel tank ; 13 - diffuser ; 14 - low-pressure tank.
b) Test section wall profile : optical windows are indicated by circles, the location of the plasma-injector modules is shown by a rectangle in the top wall of the test section.

Three basic schemes were examined for the injectors and plasma generator arrangement, as shown in figure 2.

Scheme N° 1

Electrodes located upstream of the fuel injectors. Plasma is generated mostly in air and then interacts with the injected fuel [12].

Scheme N° 2

Electrodes located downstream from the fuel injectors. An electrical discharge is generated in non-uniform air-fuel composition [16].

Scheme N° 3

The electrical discharge collocates with the fuel jet [24].

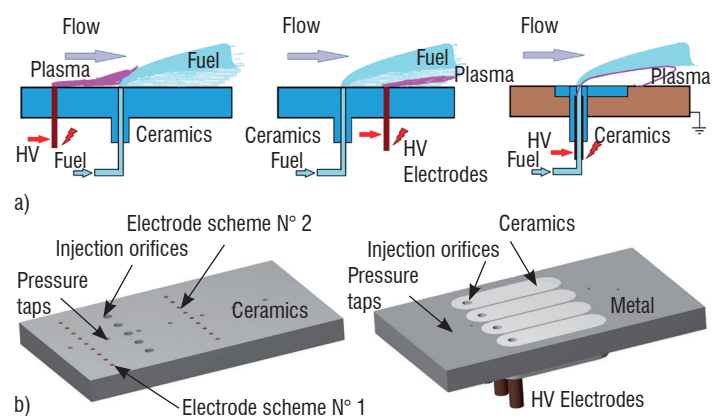


Figure 2 - Schematic drawing of three basic layouts for the fuel injectors and electrode arrangement.

a) : 3D view of two insertions used during testing.

b) : the left image is for Scheme N° 1 and Scheme N° 2 ; the right image is for Scheme N° 3.

In the first two patterns, the fuel is injected through 5 circular ($d=3.5$ mm) orifices all in a row across the span, as shown in figure 2b. The row of injectors is located at 20 mm downstream from the first row of electrodes and 30 mm upstream from the second one. The fuel mass flow rate was balanced between the orifices using a fuel plenum. The duration of the discharge was in the range 70-120 ms; typically it was 100 ms. Fuel injection was started 20 ms after the discharge initiation. Usually, the fuel injection continued for 10-20 ms after the discharge, in order to observe whether the flame was held or extinguished. The injection could be organized downstream or upstream from the discharge zone by switching between two rows of electrodes. For the third scheme, four injection-ignition modules (PIM) were installed in the combustor with the same fuel injection and plasma operation time diagram. The high-voltage electrode (anode) is integrated into the fuel injector. For this, a metal tube is inserted into a ceramic injection orifice. The distance between the end of the tube and the duct wall surface, $ZI \leq 10$ mm, is long enough to ensure significant impact of the discharge on the fuel flow prior to its injection into the main airflow.

The custom-made power supply used in these experiments is designed to operate with a steep falling voltage-current characteristic and individual control of each output channel. Control of output power is performed by varying the internal resistance of the power supply. Under typical experimental conditions, the power supply operates in nearly current-stabilized mode. Voltage across the gap and discharge current are measured using a Tektronix P6015A high-voltage probe and Agilent 1146A current probe during the run for each module, which enables the discharge power coupled to the individual PIM to be calculated.

The facility is equipped with a NetScanner 9116 static pressure scanner with 16 static pressure sensors, B1 - B16, a stagnation pressure sensor $P_{P_{tot}}$, and a pressure in vacuum tank sensor P_{ip} . Schlieren visualization was used as the main tool to study the dynamics of the flow structure modification during fuel ignition induced by the plasma. The high-resolution schlieren system uses a high-power pulsed diode laser (pulse duration $t_{exp} = 100$ ns) and a framing camera (frame rate of up to 1000 frames per second, Basler A504K). The plasma luminescence emission spectra were recorded by the Lot-ORIEL spectrometer with an Andor CCD camera. The spectral dispersion is 0.035 nm/pixel and the spectral resolution is $\Delta\lambda = 0.13$ nm. The spectroscopic system collects plasma emissions from a cylindrical volume with a diameter of 10 mm aligned in the Y direction from window to window. During the operation, the spectrometer records an emission spectrum every 10 ms.

Near-surface quasi-DC electrical discharge characterization in a high-speed flow

Typical photographs of the discharge appearance, taken during operation in Scheme N°.1 and Scheme N°.3, without and with fuel injection, are presented in figure 3. In Scheme N°.2 the discharge without injection looks very similar to Scheme N°.1. Hydrocarbon fuel injection leads to a significant increase in the discharge luminescence in the interaction zones, mostly due to strong CN and C2 molecular band amplification. The total discharge power in all cases was $W_{pl} = 6-24$ kW. Both the discharge voltage and current were oscillating because of discharge filament length variations, within a range

of $U_{pl} = 0.7-2$ kV and $I_{pl} = 2-7$ A, respectively. Prior to fuel injection, the discharge power was distributed equally between the electrodes.

Characterizing the discharge parameters and dynamics, the description below is focused on Scheme N°. 3. The detailed data for the discharge in Modes N°.1 and N°.2 are presented in the publications [12, 16, 18]. At the beginning of the plasma filament development, a breakdown occurs along the path inside the injector and a short gap between the injection orifice and a grounded metal wall upstream from the injector. After this, the filaments are convected by the flow downstream from the injector, ending at the grounded wall downstream from the ceramic inserts, shown in figure 2. After this occurs, the plasma filaments extend downstream over a distance of up to 100 mm, close to the surface of the ceramic insert. The location of the filament ends at the grounded wall oscillates at a frequency of $F = 10-20$ kHz. The filament behavior changes significantly after fuel injection. Specifically, plasma emission intensity increases and the plasma filaments move away from the surface

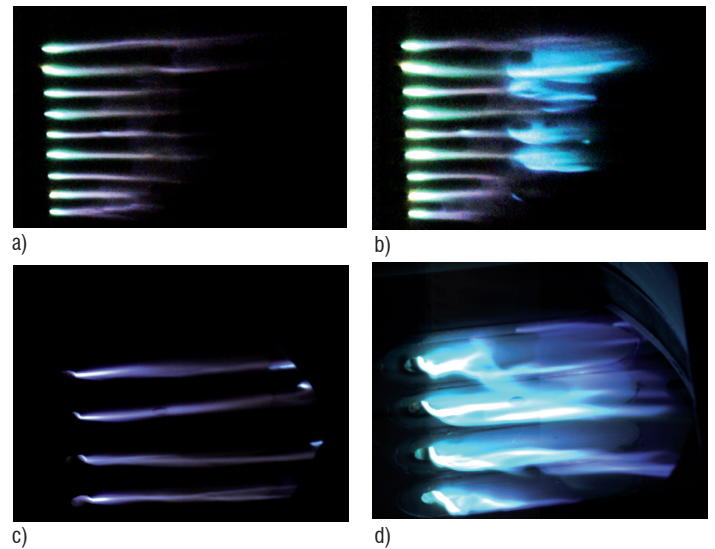


Figure 3 - Photographs of an electrical discharge in the combustion chamber, with an exposure time of $t = 100$ μ s (compare to figure 2b for details). Scheme N°.1: (a) no ethylene injection ; (b) ethylene injection enabled. Scheme N°.3: (c) no ethylene injection ; (d) ethylene injection enabled.

The typical dynamics of time-resolved discharge power for 4 individual modules is shown in figure 4(a). Despite the large magnitude of the high-frequency oscillations, the time-averaged power values are quite stable and repeatable from run to run. It is also seen that the value of the discharge power varies during the run. Fuel injection and ignition lead to an increase in the discharge power in the central modules, due to a significant extension of the length of plasma filaments and the resultant rise of gap voltage, as shown in figure 4(b). At a certain value of the fuel injection flow rate, the intense heat release in chemical reactions in the near-centerline zone of the combustor induces flow separation near the duct corners, which consequently reduces the length of the lateral plasma filaments, as well as the discharge power in the lateral modules. The discharge power can be regulated by varying the average output current of the power supply. It should be noted that the power deposition is not proportional to the average discharge current, because increasing the current somewhat reduces the gap voltage. The operation characteristics of individual PIM modules depend to some extent on whether the adjacent modules are powered or not, especially for the lateral modules.

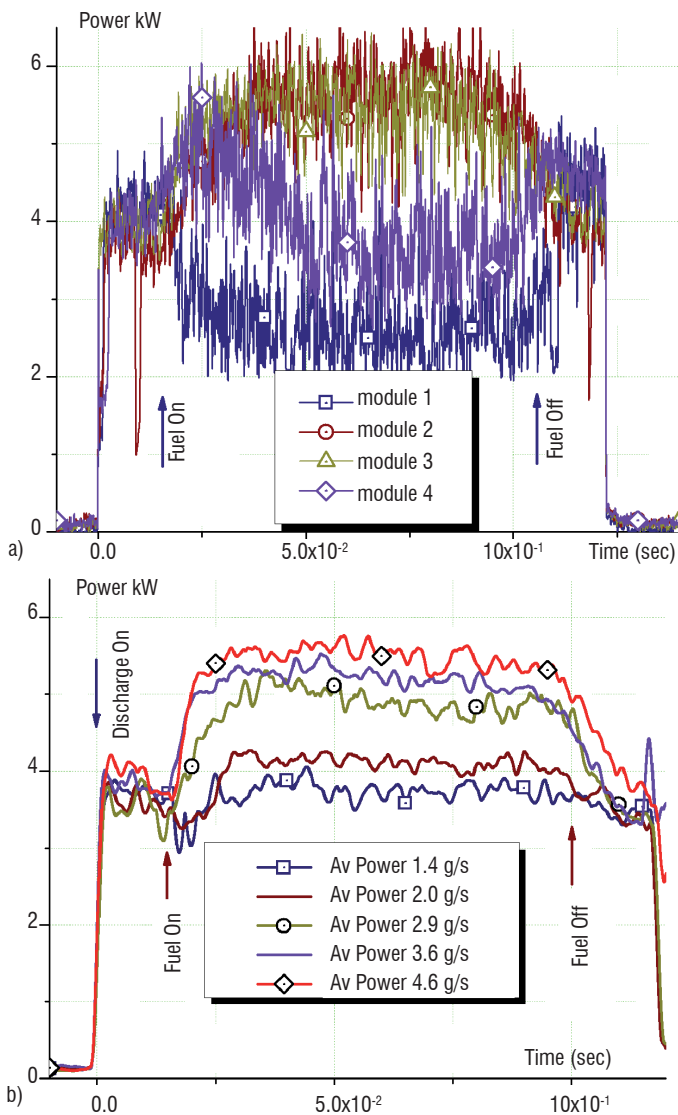


Figure 4 - (a) Discharge power dynamics and distribution among the PIM modules, calculated from voltage and current measurements. $G_{C_2H_4}=3$ g/s ; averaged current $I_{pl}=4A$. (b) Discharge power in Module N°. 3 vs. fuel injection flow rate. A low-pass filter is applied to reduce high-frequency oscillations.

A composite optical emission spectrum of the plasma, obtained by integrating the emission from the plasma-fuel-flow interaction area, $x=20-30mm$, $y=0-10$ mm, is shown in figure 5. Analysis of the spectra shows that, in the presence of the hydrocarbon fuel, three different types of species are detected: hydrocarbon/carbon fragments, chemical reaction products resulting from the interaction of hydrocarbon plasma and air, and excited air species (mainly N_2). The species with the highest emission intensity include atomic hydrogen, carbon and oxygen (O atom triplet line at $\lambda=777$ nm outside of the spectral range of figure 5), hydrogen molecule H_2 , as well as C_2 , CN , OH and CH radicals. Neglecting continuum emission, the molecular bands of the CN radical violet system, $CN(B^2\Sigma \rightarrow X^2\Sigma)$ and C_2 Swan bands contribute up to 50% of the integrated emission intensity. These spectra indicate intense chemical transformations in the flow, including the generation of active radicals in electronically excited states. The emission spectra were used to evaluate plasma parameters in a zone near the base of the fuel injection jet. A second positive system of molecular nitrogen, $N_2(C^3\Pi_u, v'=0 \rightarrow B^3\Pi_g, v''=0)$ band at $\lambda=337.1$ nm, was used to infer the rotational-translational temperature in the plasma [19], $T_r=3000 \pm 500$ K, which is strongly weighted toward

the peak temperature in the plasma filament. The H atom Balmer series lines are very intense, with the H_α line at $\lambda=656.3$ nm being the strongest in this case. Electron density in the plasma was extracted from the H_α spectral line shape [20, 21], since the Stark effect is the dominant mechanism of line broadening under these conditions. Electron density near the base of the fuel injection jet is inferred to be $n_e=(4.51.0)10^{15}$ cm⁻³.

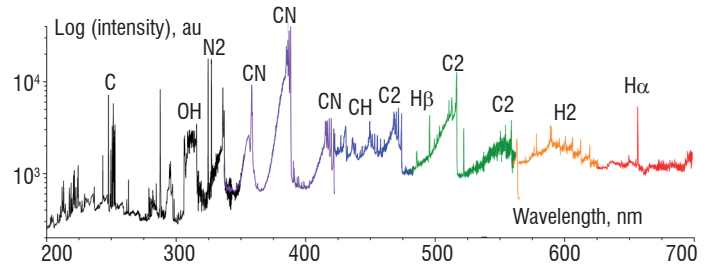


Figure 5 - Survey optical emission spectrum obtained from the ethylene-air-flow-plasma interaction region. The spectrum incorporates seven overlapping spectra, obtained separately under the same conditions. Discharge current $I_{pl}=2-4A$, ethylene injection jet $G_{C_2H_4}=0.5-1$ g/s from each module in $M=2$ airflow, $P_{st}=180-220$ Torr. Major emission lines and bands are labeled.

The mechanism of plasma interaction with a jet of fuel injected into the airflow is of major importance for the dynamics of ignition and flameholding under these conditions. From a comparison of the images in figure 3c and figure 3d, it is apparent that plasma emission, which serves as an indicator of energy loading by the discharge (i.e., indicating the presence of both an electric field and discharge current), essentially follows the fuel jet. The effect of the electrical current convecting with the flow has been previously observed in a near-surface transverse filament discharge between two pin electrodes in Mach 2 airflow [18, 22]. In Mach 2.8 airflow, a near-surface transverse DC discharge filament between two electrodes extended in the flow direction convected in the boundary layer at a velocity of approximately 60% of the free stream velocity [23]. A quantitative prediction of the discharge behavior in the fuel injection flow under these conditions can be obtained using a plasma fluid model, incorporating equations for electron and ion densities and the Poisson equation for the electric field, as discussed in detail in [24]. Quantitatively, the filament shape and discharge current path through the fuel injection jet, reacting mixing layer and the air flow is controlled by the trade-off between at least two factors, (i) the maximum value of the effective ionization coefficient, i.e., the difference between the ionization and attachment coefficients, $\alpha(E/N) - \eta(E/N)$, and (ii) the maximum effect of convection by the flow.

Experimental results on Plasma-assisted combustion : effect of fuel mass flow rate and discharge power

Figure 6 presents typical data for the wall pressure distribution in the case of Schemes N°.1 and N°. 2, when the electrode system and fuel injectors are not combined into a single module. The discharge generation without fuel injection slightly affects the pressure distribution, increasing the pressure in the immediate vicinity of the electrode system. When the fuel injection is turned on, the pressure increases slightly in the zone close (downstream) to the injector for the first scheme and close to the plasma area for the second scheme. This increase is associated with the fast reactions of fuel partial oxidation by atomic oxygen O . Other reaction branches are related to

electronically / vibrationally excited nitrogen (N_2^*) and other active species generated in air plasma. In the case of a second scheme, highly reactive species and radicals, such as H , CH and C_2H_3 are involved in the initial fast chemical processes as well. The products of these fast plasma-chemical reactions are accumulated in the associated separation bubble and then are blown down by a core flow. The main chemical power release occurs after fuel mixing with core air in the second combustion stage [11], rather than downstream from the place of plasma generation. In figure 6, this zone is located at $x > 120$ mm. The schlieren image in figure 7a depicts this zone very well ; it is labeled as the "Flame front". At low plasma power $W_{pl} < 8$ kW, the second combustion stage may not be carried out at all. Two effects are responsible for this : (a) insufficient fuel activation by the discharge and (b) insufficient fuel-air mixing enhanced by the plasma. Numerical modeling [25], including plasma-chemical kinetics and mixing processes, indicates that the second effect may be dominant.

Under "optimal" conditions for Scheme N° 2, the zone of intensive chemical reactions moves upstream and stabilizes near the plasma location. This regime is seen in figure 6 for an ethylene mass flow rate $G_{C_2H_4} = 2.1$ g/s . When the flame front is stabilized (during steady-state flameholding), the combustion process appears to progress slowly in the axial direction, due to gradual mixing of fuel and air. The chemical energy release during combustion elevates the pressure and forms a wedge-shape combustion zone, with its average angle increasing as combustion intensifies. The associated oblique shock wave angle increases accordingly. It should be noted that this zone is observed during operation in Scheme N° 1 as well; however, the electrical power has to be rather high for this effect to appear, $W_{pl} > 20$ kW. If $G_{C_2H_4} > 3$ g/s, the zone of high energy release moves downwards gradually.

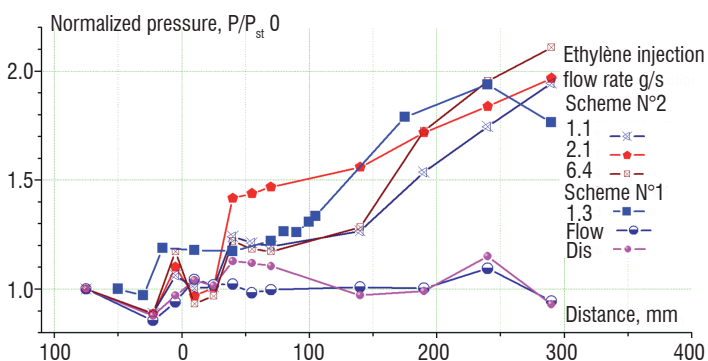


Figure 6 - Normalized wall pressure P/P_{st} distribution during plasma-assisted combustion for Scheme N° 1 and Scheme N° 2. Total discharge power $W_{pl} = 9-12$ kW. The caption numbers indicate an ethylene mass flow rate $G_{C_2H_4}$ in g/s; points labeled "Flow" were obtained without fuel injection, with the discharge turned off; points labeled "Dis" were obtained without fuel injection, with the discharge turned on.

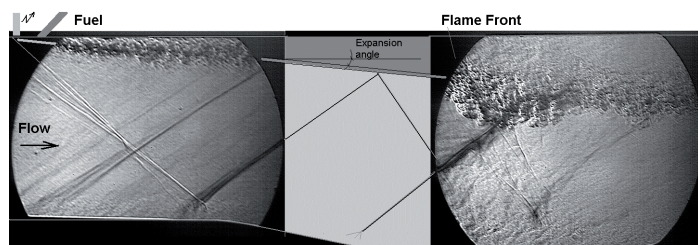
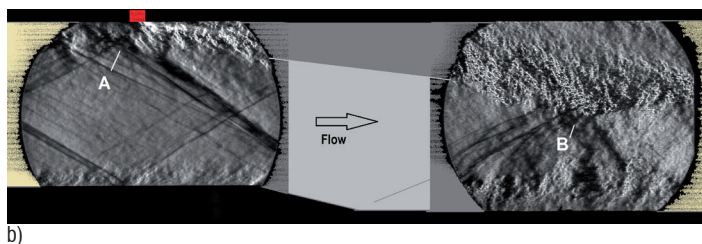


Figure 7 - Composite schlieren image illustrating the flow structure in the test section. It consists of a pair of images taken through two different windows during different runs, combined into one. Black areas show the contour of combustor walls; the electrode positions and point of fuel injection are indicated. The extent of the wedge-like combustion zone between the two windows is interpolated in gray. (a) Scheme N° 1 : ethylene injection mass flow rate $G_{C_2H_4} = 1.3$ g/s. (b) Scheme N° 3 : ethylene injection mass flow rate $G_{C_2H_4} = 3$ g/s.

A series of experiments was performed on ethylene ignition and flameholding by means of the electrical discharge collocated to the fuel injection jet, described above as Scheme N° 3. The following test parameters have been varied : (1) fuel injection flow rate, within a range of $G_{C_2H_4} = 1 - 8$ g/s ; and (2) discharge time-averaged current (i.e., discharge power). First of all, it has been determined that ignition and flameholding are observed over a much wider range of parameters compared to the previously tested configurations for Schemes N° 1 and N° 2, with the electric discharge located both upstream and downstream from the fuel injection port.

Typical schlieren images for Scheme N° 3 are shown in figure 7(b), illustrating the flow structure during combustion. When the discharge is enabled, the location of the plasma filament near the injection orifice becomes visible due to oblique shock generation. The oblique shock wave interacts with an expansion wave generated by angle step expansion of the bottom test section wall (see figure 7b) and then with a compression wave generated there when the flow velocity vector is reversed. Flow separation near the side wall at the PIM location is also evident. A further increase in the fuel mass flow rate would result in the separation zone moving upstream, thus increasing the oblique shock wave angle and eventually leading to thermal choking of the duct.

The other side of the electrical discharge effect on combustion is the enhancement of air-fuel mixing in high-speed flows. Both direct and indirect plasma-flow interaction mechanisms are responsible for this effect. First, plasma-based heating generated in the flow acts as a "gradual" obstacle, generating a vortex flow similar to a Karman vortex trail. An additional, direct, plasma effect is caused by strong modulation of the power deposition in the electric discharge, which results, depending on the discharge location, in boundary or shear layer tripping. As seen in figure 4a, the instantaneous discharge power modulation is up to $\sim 50\%$ of the average power value; the frequency of the modulation is 10-20 kHz. An indirect mixing enhancement mechanism is carried out through the Richtmyer-Meshkov instability, appearing in flows with non-collinear density and pressure gradients. This leads to the formation of deterministic vortex-dominated and, subsequently, small-scale stochastic perturbations resulting in turbulent mixing [25-26]. Two regions of the flow field, labeled as A and B in figure 7b, are of particular interest. In region A, shock waves caused by the test section wall imperfections and originating upstream from the field of view interact with the fuel jet with a high density gradient, caused by plasma-induced non-uniform heating. In region B, the shock wave is caused by the wall wedge and is amplified by a strong shock coming from the PIMs. At the beginning of the PIM operation, this shock impacts the heated near-wall fuel jets, thus enhancing the mixing processes.



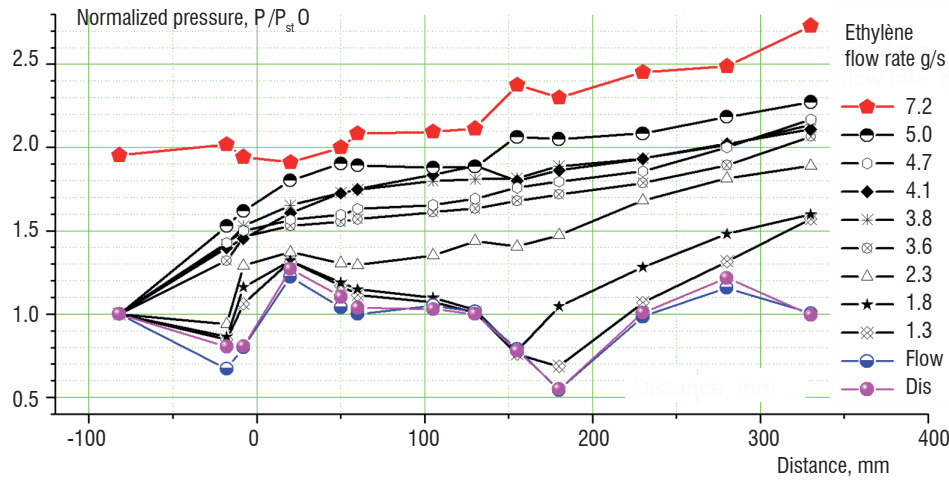


Figure 8 - Normalized pressure $P/P_{st,0}$ profiles along the combustor vs. fuel mass flow rate : Scheme N°. 3, total discharge power $W_{pl} = 16-18 \text{ kW}$. Compare to figure 6 for Schemes N°. 1 and N°. 2.

In figure 8, pressure distributions measured along the test section are plotted vs. the fuel mass flow rate. At high enough values of the discharge power and fuel injection mass flow rate, a significant increase is observed in the wall pressure over a wide range of fuel flow rates. In lean mixtures, ignition is detected downstream, as far as $x > 250 \text{ mm}$ from the location of the plasma/airflow/fuel injection interaction region (this is not visible in the schlieren images). As the fuel injection flow rate is increased, the flame front moves forward and gradually occupies the entire combustor downstream from the injector location. Operating at a fuel mass flow rate above $G_{C_2H_4} \approx 6 \text{ g/s}$ may lead to thermal choking in this combustor geometry. Increasing the duct expansion angle may resolve this problem

Data on TDLAS measurements

The DLAS measurements were performed in typical operation modes : $M=2$, $P_{st}=150 \text{ Torr}$; the plasma power was $W_{pl}=10-16 \text{ kW}$, the ethylene mass flow rate was “optimal” for each operation scheme: $G_{C_2H_4}=1.3-1.6 \text{ g/s}$ for Scheme N°. 1, $G_{C_2H_4}=1.8-2.1 \text{ g/s}$ for Scheme N°. 2 and $G_{C_2H_4}=2-2.5 \text{ g/s}$ for Scheme N°. 3. The data on the Z-distribution (cross-flow) of the gas temperature in one of the cross-sections $x=130 \text{ mm}$ are shown in figure 9. The spectral interval of a single diode laser (DL) scan was about 0.9 cm^{-1} . Four absorption lines fall within the interval. Depending on the temperature of the probing zone, the relative intensities of the lines vary significantly. The algorithm for the data processing and evolving the parameters of the probed gas flow are described in a previous publication [27]. Each point in the figure was obtained during an individual run of the facility. The values of the temperature inferred from both slopes coincide reasonably well. The accuracy of the measurements could be estimated at $\Delta T = \pm 30 \text{ K}$. Note, the measured temperature is line-averaged on the DL beam pass from wall to wall. In the case of a non-homogeneous distribution of the gas parameters in the reacting zone, a contribution of each individual area is weighted in accordance with the water vapor concentration. This turns the estimation of the maximal gas temperature values into a non-trivial problem.

The result of the measurements indicates a substantial difference in a maximal temperature value and a hot zone thickness depending on the plasma-flow-fuel interaction scheme applied. In the case of upstream plasma generation, the reaction zone is thin compared to that in Schemes N°. 2 and N°. 3. The maximal value of the Y-averaged gas temperature has been observed to be also much lower in this case. The distribution patterns are different as well. Scheme N°. 3, where plasma collocates with the fuel injection jet, demonstrates the highest gas temperature amplitude and a rather thick hot zone in the Y direction. A qualitatively similar result was obtained for a water vapor concentration distribution measured by TDLAS.

Averaged temperature, K

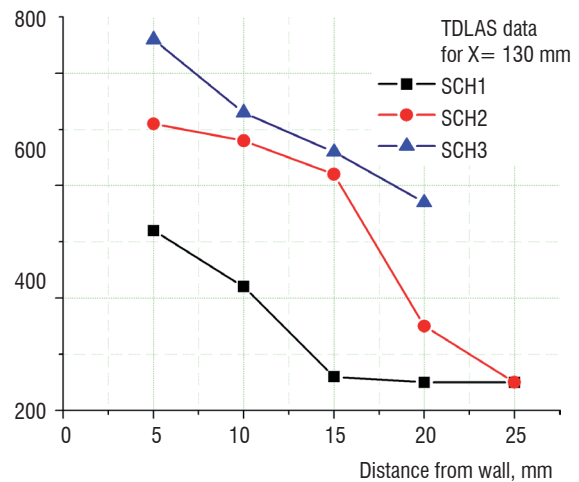


Figure 9 - Temperature of the water vapor distribution cross-flow, measured by TDLAS in a cross-section at $x=130 \text{ mm}$ from the point of fuel injection. Comparison of the three schemes.

Discussion

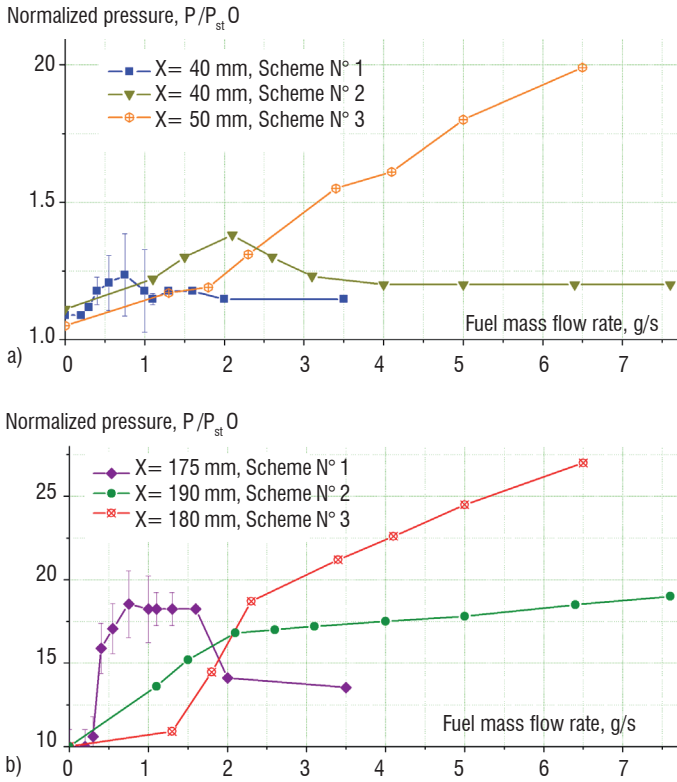


Figure 10 - Comparison of the pressure data depending on the fuel mass flow rate, obtained for the configuration with discharge generation upstream from the fuel injector, downstream from the fuel injector and for a collocated scheme. The flow parameters ($M=2$, $P_{st}=150-200$ Torr) and discharge power ($W_{pl}=12-18$ kW) are similar in all cases; the axial location X is measured from the fuel injection cross-section. (a) location of the measuring points in proximity of the fuel injector $x=40-50$ mm; (b) in the downstream zone $x=175-190$ mm.

Figure 10 shows a striking difference between the performance of the three schemes applied for plasma-based ignition and flameholding: the previously used schemes with plasma generation upstream [12] and downstream from the fuel injection port [16] and the last scheme with collocated plasma generation and fuel injection, combined into a single unit [24]. The Scheme N° 1 exhibits a more effective ignition under fuel-lean conditions, i.e., at low fuel flow rates. However, the last configuration, Scheme N° 3, shows a much better performance under fuel-rich conditions, where Scheme N° 1 is limited to partial oxidation with a fairly insignificant increase in the pressure. The lean combustion limit for the last configuration is $G_{C_2H_4} > 1$ g/s, while for the previous Scheme N° 1 it was $G_{C_2H_4} < 0.4$ g/s.

In the last experiments with Scheme N° 3, increasing the ethylene flow rate results in a more pronounced pressure rise (i.e., in more intense combustion), which was not the case for the previously tested Configuration N° 1. To interpret this difference, two key points need to be made: (1) in Scheme N° 1, the discharge was sustained in air, while in this scheme it is sustained in the fuel (inside the injection orifice), as well as in the fuel-air mixture; and (2) the flow structure in this Configuration N° 3 is significantly different. Specifically, the near-surface quasi-DC discharge used in Scheme N° 1 produces a “closed” flow separation zone (a separation bubble) downstream

from the discharge, with high concentrations of chemically active species, such as atomic oxygen (O) and electronically/vibrationally excited nitrogen (N_2^*). The fuel, after being injected into this zone, has a sufficiently long residence time to mix with plasma-activated air and ignite. After ignition, the volume of this zone increases and forms an extended subsonic flow zone without obvious reattachment downstream. A further increase in the fuel mass flow rate results in extremely fuel-rich conditions in the separation zone, with subsequent flame extinction/blow-off. Under these conditions, the residual pressure increase indicates a partial oxidation of fuel by active species generated by the discharge. In contrast to this pattern, in Scheme N° 3 the discharge is localized along the fuel injection jet, which generates reactive species and radicals, such as H , CH , C_2H_3 , etc..., by electron impact and enhances mixing by convecting the unstable plasma filament with the injection jet. Based on these results, it appears that filament convection with the flow becomes significant only at a sufficiently high fuel injection speed, comparable with the main airflow velocity. This explains why ignition is not observed under fuel-lean conditions (see figure 10).

Conclusions

The paper discusses the experimental results on plasma-assisted supersonic combustion and flameholding recently obtained at the high-speed combustion facility PWT-50H, using flush-mounted discharge modules. The use of this method may potentially lead to a reduction in the total pressure losses when operating the combustor under non-optimal conditions, enhancement of operation stability and, consequently, the expansion of the air-breathing corridor of the scramjet operation range. The concept of plasma-assisted combustion includes not only accelerating ignition, but also mixing enhancement when operating under non-premixed conditions and flame stabilization (flameholding). This paper presents experimental results showing a significant performance enhancement based on plasma-flow interaction physical mechanisms, which were not understood previously.

The comparison of previously used schemes with the upstream and downstream generation of plasma in relation to the place of fuel injection and the novel scheme of a combined electric discharge/fuel injection module, with the high-voltage electrode placed inside the fuel injection orifice, is depicted in this work. In the last scheme, referred to as Scheme N° 3, after breakdown is achieved, the discharge current path follows the fuel injection jet due to convective entrainment of the plasma by the flow. The axial part of the plasma filament is localized inside the fuel-air mixing layer. The plasma filaments are extended by the fuel injection flow, penetrate into the main airflow and end far downstream, which is critically important for fuel-air mixing acceleration.

Stable flameholding has been observed over a wide range of fuel injection mass flow rates. The critical importance of the plasma module and combustor geometry, as well as that of key operation parameters such as total discharge power, $W_{pl} > 10$ kW and fuel mass flow rate $G_{C_2H_4} > 1$ g/s, has been demonstrated. It is also important that these experiments illustrate possible ways for further improvement of this technique, including the use of contoured injector orifices for supersonic injection and a power supply with a modified voltage-current characteristic. Finally, the new scheme demonstrates a significant advantage in terms of flameholding limits, compared to previously tested configurations ■

Acknowledgments

This work was supported by the AFOSR (contract monitor: Dr. Chipping Li) and the AFORL (contract monitor : Dr. Campbell Carter). The authors would like to thank Prof. Igor Adamovich (OSU) and Dr. Vladimir Sabelnikov (ONERA) for multiple discussions and Alec Houpt for his help with the text editing. The authors are grateful to the ISAN team, headed by Prof. Mikhail Bolshov, which performed the TDLAS measurements.

Acronyms

PIM (Plasma-based Injection-Ignition Module)
PWT-50H (Pulse Wind Tunnel of JIHT RAS)
TDLAS (Tunable Diode Laser Absorption Spectroscopy)

References

- [1] E.T. CURRAN - *Scramjet Engines: the First Forty Years*. J. Propul. Power 17 (6), (2001) 1138–1148.
- [2] J. C. B. MACKEAND - *Sparks and Flames: Ignition in Engines : An Historical Approach*. Tyndar Press, 1997.
- [3] A. STARIKOVSKIY, N. ALEKSANDROV - *Plasma-Assisted Ignition and Combustion*. Progress in Energy and Combustion Science, Volume 39, Issue 1, February 2013, Pages 61–110.
- [4] I.V. ADAMOVICH, I. CHOI, N. JIANG, J.-H KIM, S. KESHAV, W.R. LEMPERT, E. MINTUSOV, M. NISHIHARA, M. SAMIMY, and M. UDDI - *Plasma Assisted Ignition and High-Speed Flow Control: Non-Thermal and Thermal Effects*. Plasma Sources Science and Technology, vol. 18, 2009, p. 034018.
- [5] S.M. STARIKOVSKAIA - *Plasma Assisted Ignition and Combustion*. J. Phys.D: Applied Physics, 2006, vol.39, R265-R299.
- [6] M.C. BILLINGSLEY, W.F. O'BRIEN, J.A. SCHETZ - *Plasma Torch Atomizer-Igniter for Supersonic Combustion of Liquid Hydrocarbon Fuels*. AIAA Paper 2006-7970.
- [7] H. DO, M.A. CAPPELLI, M.G. MUNGAL - *Plasma Assisted Cavity Flame Ignition in Supersonic Flows*. Combust. Flame 157 (9) (2010) 1783–1794.
- [8] L.S. JACOBSEN, C.D. CARTER, T.A. JACKSON, et al. - *Plasma-Assisted Ignition in Scramjets*. J. Propul. Power 24 (4) (2008) 641–654.
- [9] K. TAKITA, K. SHISHIDO, K. KURUMADA - *Ignition in a Supersonic Flow by a Plasma Jet of Mixed Feedstock Including CH₄*. Proc. Combust. Inst. 33 (2) (2011) 2383–2389.
- [10] FEI LI, XI-LONG YUA, YING-GANG TONG, YAN SHEN, JIAN CHEN, LI-HONG CHEN, XIN-YU CHANG - *Plasma-Assisted Ignition for a Kerosene Fueled Scramjet at Mach 1.8*. Aerospace Science and Technology 28 (2013) 72–78.
- [11] S. LEONOV, D. YARANTSEV, V. SABELNIKOV - *Electrically Driven Combustion near the Plane Wall in a Supersonic Duct*. Progress in Propulsion Physics, Advances in Aerospace Science, EUCASS book series, Vol 2, 2011, pp. 519-530.
- [12] S. LEONOV, C. CARTER, D. YARANTSEV - *Experiments on Electrically Controlled Flameholding on a Plane Wall in Supersonic Airflow*. Journal of Propulsion and Power, 2009, vol.25, N°2, pp.289-298.
- [13] Z. YIN, I.V. ADAMOVICH, and W.R. LEMPERT - *OH Radical and Temperature Measurements During Ignition of H₂-Air Mixtures Excited by a Repetitively Pulsed Nanosecond Discharge*. Proceedings of the Combustion Institute, vol. 34, 2013, pp. 3249–3258.
- [14] W. SUN, M. UDDI, T. OMBRELLO, S.H. WON, C. CARTER, Y. JU - *Effects of Non-Equilibrium Plasma Discharge on Counterflow Diffusion Flame Extinction*. Proceedings of the Combustion Institute 33 (2), 3211-3218, 2011.
- [15] I. N. KOSAREV, V. I. KHORUNZHENKO, E. I. MINTOUSOV, P. N. SAGULENKO, N. A. POPOV, S. M. STARIKOVSKAIA - *A Nanosecond Surface Dielectric Barrier Discharge at Elevated Pressures: Time-Resolved Electric Field and Efficiency of Initiation of Combustion*. Plasma Sources Science & Technology, vol. 21, N° 4, 2012.
- [16] A. FIRSOV, S. LEONOV, D. YARANTSEV et al - *Temperature Measurement in Plasma-Assisted Combustor by TDLAS*. Paper AIAA 2012-3181.
- [17] S. B. LEONOV, A. A. FIRSOV, YU. I. ISAENKOV et al. - *Plasma-Based Fast Mixing and Ignition in Supersonic Flow*. Paper AIAA 2011-2327.
- [18] S. B. LEONOV AND D. A. YARANTSEV - *Near-Surface Electrical Discharge in Supersonic Airflow: Properties and Flow Control*. Journal of Propulsion and Power, vol. 24, 2008, pp. 1168-1181.
- [19] C. O. LAUX, T. G. SPENCE, C. H. KRUGER and R. N. ZARE - *Optical Diagnostics of Atmospheric Pressure Air Plasmas*. Plasma Sources Sci. Technol. 12 (2003) 125–138.
- [20] M. A. GIGOSOSY and V. CARDENOSOZ - *New Plasma Diagnosis Tables of Hydrogen Stark Broadening Including Ion Dynamics*. J. Phys. B: At. Mol. Opt. Phys. 29 (1996) 4795–4838.
- [21] H. R. GRIEM - *Stark Broadening of the Hydrogen Balmer- α Line in Low and High Density Plasmas*. Contrib. Plasma Phys. 40 (2000), pp.46-56.
- [22] A. A. FIRSOV, M. A. SHURUPOV, D. A. YARANTSEV, S. B. LEONOV - *Plasma-Assisted Combustion in Supersonic Airflow : Optimization of Electrical Discharge Geometry*. Paper AIAA-2014-0988.
- [23] C.S. KALRA, S.H. ZAIDI, R.B. MILES, and S.O. MACHERET - *Shockwave–Turbulent Boundary Layer Interaction Control Using Magnetically Driven Surface Discharges*. Experiments in Fluids, vol. 50, 2011, pp. 547–559.
- [24] K.V. SAVELKIN, D.A. YARANTSEV, I.V. ADAMOVICH, and S.B. LEONOV - *Ignition and Flameholding in a Supersonic Combustor by an Electrical Discharge Combined with a Fuel Injector*. Published online in Combustion and Flame, 2014, <http://dx.doi.org/10.1016/j.combustflame.2014.08.012>.
- [25] M. A. DEMINSKY, I. V. KOCHETOV, A. P. NAPARTOVICH, S. B. LEONOV - *Modeling of Plasma Assisted Combustion in Premixed Supersonic Gas Flow*. International Journal of Hypersonics, Volume 1, N° 4, December 2010, pp. 5-15.
- [26] A. A. ZHELTOVODOV and E. A. PIMONOV - *Using a Localized Pulse Periodic Energy Supply for Intensification of Mixing of Parallel Compressible Flows*. Technical Physics Letters, 2013, Vol. 39, N° 11, pp. 1016–1018.
- [27] M. A. BOLSHOV, Y. A. KURITSYN, V. V. LIGER, V. R. MIRONENKO, S. B. LEONOV, D. A. YARANTSEV - *Measurements of the Temperature and Water Vapor Concentration in a Hot Zone by Tunable Diode Laser Absorption Spectrometry*. Appl. Phys. B Lasers and Optics (2010), v.100, N° 2, 397-407.



Konstantin Savelkin graduated from Moscow Aviation Institute with a degree in radioelectronics equipment in 1986. Now he works as leading engineer in Joint Institute for High Temperatures Russian Academy of Science, Department of Plasma Aerodynamics and Combustion Control. He designs and assembles the power sources for different types of plasma generators as well as maintains wind tunnel experimental facility.



Dmitry Yarantsev graduated from Moscow Power Engineering Institute (Technical University) with a master degree in nuclear power plants and thermonuclear facilities in 2001. Now he works as research scientist in Joint Institute for High Temperatures Russian Academy of Science, Department of Plasma Aerodynamics and Combustion Control. He develops diagnostic techniques and performs experimental research in the field of plasma assisted combustion in high speed flow and flow control by plasma.



Sergey B. Leonov works as a Research Professor in University of Notre Dame, USA, Aerospace and Mechanical Engineering Department. He graduated from the Moscow State University, 1981, and received PhD degree in mechanics of gases and plasma from the Baltic State University, in 1991. In 2006 he has got the degree of Doctor of Science in physics and mathematics. Since 1998 he is Head of Laboratory and since 2009 is Head of Department in the Joint Institute for High Temperature Russian Academy of Sciences. Since 2009 he is a Professor in Moscow Open University. In 2013-2014 he is a Visiting Professor in The Ohio State University, USA, Mechanical and Aerospace Engineering Department. The main subjects of his interest are experimental plasma aerodynamics, plasma assisted combustion, plasma diagnostics, gasdynamics and aerodynamics, weakly ionized plasma generation.

S. Bentaleb, N. Blin-Simiand,
 P. Jeanney, L. Magne, N. Moreau,
 S. Pasquiers, P. Tardiveau
 (Université Paris-Sud and CNRS
 Université Paris-Saclay)

E-mail: stephane.pasquiers@u-psud.fr

DOI : 10.12762/2015.AL10-09

Ignition of Lean Air / Hydrocarbon Mixtures at Low Temperature by a Single Corona Discharge Nanosecond Pulse

A great number of experimental studies have demonstrated that non-thermal plasmas produced by high voltage pulse discharges, running at a given pulse repetition frequency, are able to ignite air / hydrocarbon mixtures at a low initial temperature and atmospheric pressure. In this paper, we show that ignition can also be achieved using a single nanosecond pulse corona discharge generated under a very strong overvoltage. Experiments were conducted in air / propane and air / n-heptane mixtures. For such a discharge, ignition of n-heptane requires less released electrical energy than propane and lean mixtures can be completely burnt with reasonable energy values of several tens of mJ. Extended flame kernels or several points of ignition can be induced. For n-heptane, we have developed a simplified combustion model using a reduced mechanism, enabling us to suggest a kinetic explanation for ignition at a low temperature. In particular, it appears that oxygen atoms produced in the plasma induce a significant reduction of the ignition time. This model lays the foundation for a more complete study, including the production of other active species by the discharge, such as the first excited state of the oxygen atom, or even dissociation products of the hydrocarbon molecule following electron collisions or quenching of the nitrogen excited states.

Introduction

Combustion control and ignition using cold and non-thermal plasmas has become a major topic of interest over the past ten years or so [1, 28-31], and more specifically the use of discharges generated under strong overvoltages for automobile atmospheric engine applications [7, 24, 36]. Due to strong environmental constraints for automobile exhaust gases, engines to be developed in the future must run on lean air / gasoline mixtures, or mixtures diluted with burnt gases. In both cases, the optimization of ignition devices is required, since classical spark gaps become inefficient under these conditions. In this context, the generation of non-equilibrium plasmas in large volumes, with high densities of active species, and the ability to induce rapid gas heating is challenging. Among the various types of electrical discharges studied, the pulsed corona generated under a very strong overvoltage has recently demonstrated promising characteristics for ignition issues at low initial temperatures (close to 300 K) of air-based gas mixtures at high pressure (at least one atmosphere) [3, 16, 33, 34]. This discharge should also be useful for the ignition of mixtures with a reduced oxygen concentration (less than 20%) at a pressure lower

than one atmosphere and thus may be interesting for aeronautical applications. Another concept is the use of a discharge to produce excited molecular oxygen species to be then injected into the combustible mixture [27].

It was shown that the plasma produced by a single nanosecond pulsed overvoltage in a point-to-plane configuration can be used to ignite various kinds of quiescent air / fuel (propane C_3H_8 , n-heptane $n-C_7H_{16}$) mixtures [3, 16, 33]. Diffuse and large plasma is able to develop in atmospheric air [34, 35]. This diffuse pattern is created by a multi-avalanche overlapping process. Space charge mechanisms and screening effects responsible for streamer inception and multi-channel generation are weaker, since the applied electric field increases very fast over the entire gap. The addition of propane into air induces a significant effect of diffuse discharge constriction very near the anode and its filamentation within the other part of the gap [3, 4, 16]. However, the discharge is able to ignite mixtures along paths between the two electrodes and not only at the pin, which leads to a specific cylinder-shaped flame propagation instead of a classical spherical one [5, 6, 16].

Several results emphasize the possible advantages of such an igniter, compared to classical spark gap devices. First, very lean air / propane and air / n-heptane mixtures can be completely burnt with reasonable released electrical energies of several tens of mJ. Sparks remain inefficient at very low equivalence ratios. Second, nanosecond discharges can induce extended flame kernels or several points of ignition. Spark gap ignition will always remain much localized at a single point. The consequences are faster combustion and less misfiring. Third, ignition times are reduced with non-equilibrium discharges. A thermal spark promotes neutral heating by maintaining the electrical current over a long period, but it is less efficient in the end. For example, T. Shiraishi et al [24] compared the ignition of iso-octane by a streamer discharge and by a thermal arc, and showed that the use of the non-thermal plasma is more efficient, in particular with a shorter ignition time, than the arc, whereas the arc current is maintained for a greater amount of time.

Decomposition mechanisms of hydrocarbons in the plasma phase deserve to be studied in more detail. In particular, data regarding the production of radicals or molecules (cross-sections and reaction coefficients) following dissociative excitations by electronic collisions or by quenching of the nitrogen excited states are rather scarce. The data proposed by other scientific communities must be clearly validated using dedicated experiments and by comparison with detailed kinetic modeling. Kinetic schemes developed for cold combustion should be taken into account in the interpretation of experimental results, including the effect of peroxy radicals, which are efficient combustion chain propagators through the generation of the hydroxyl radical. Experimental and numerical studies should be extended to heavy hydrocarbons, in order to simulate actual fuels, for example n-heptane or iso-octane (gasoline engines), aromatics and saturated monocyclic hydrocarbons (kerosene in aeronautical applications).

The mechanisms involved in the combustion of propane have been the subject of numerous studies [8, 10, 11, 26]. However, few things are known about combustion control and ignition of air / propane mixtures by non-thermal plasmas [12, 13, 18, 22]. Evidently, oxidation reactions of hydrocarbon molecules by oxygen atoms and by hydroxyl radicals should play a role in the ignition process, but such reactions are not so efficient at low temperatures for saturated compounds. Obviously a complete understanding of the ignition phenomenon requires a clear knowledge of the kinetic decomposition mechanisms of the hydrocarbon molecules in the plasma [19], as well as the production processes of the hydroxyl radical, which is more reactive with hydrocarbons than the oxygen atom is at a low temperature. Under conditions of a uniform plasma and electric field amplitude similar to that created during the diffuse corona discharge, a recent kinetic modeling by E. Filimonova [9] shows that the discharge stimulates the development and increases the intensity of a cool flame in an air / propane mixture. It sharply reduces the cool flame ignition time, as well as the total induction time. The rapid formation of propyl-peroxy radicals $C_3H_7O_2$ and propyl hydro-peroxide C_3H_7OOH in large concentrations is promoted, leading to a partial release of chemical enthalpy due to the organic peroxide decomposition. As a result, the discharge promotes faster oxidation of the mixture at initial temperatures in the range 500-800 K to the point of hot ignition occurrence (typically $T > 1000$ K). In other words, an air / fuel mixture is

heated within the range of temperatures where the high temperature oxidation mechanism occurs with a higher rate compared to that of the auto-ignition case [9].

Studies using heavy fuels instead of small hydrocarbons (C1–C5) are not extensive [24, 25]. Recently, S. Nagaraja et al [17] numerically investigated the effect of a non-equilibrium plasma produced by a dielectric barrier discharge running at a high HV-pulse repetition frequency (60 kHz) on the ignition properties of n-heptane diluted in dry air at a reduced total pressure of 0.2 atm and with an equivalence ratio and initial temperature in the range of 0.5-1.5 and 550-650 K respectively. For this molecule, low-temperature chemistry plays a critical role. It is shown that O, H atoms and OH radicals produced by the plasma initiate and accelerate the H abstraction of fuel molecules (RH) and reduce the induction time of the exothermic cycle $RH \rightarrow R \rightarrow$ peroxy $RO_2 \rightarrow OROOH$ by a factor of ten [17].

This paper gives, in a first part, an overview of experimental results obtained in our laboratory on the ignition of air / propane and air / n-heptane mixtures at a low temperature (ambient, close to 300 K) and atmospheric pressure, by a single corona discharge nanosecond pulse. In a second part, we present the results of a 0D-kinetic modeling, giving insight about the role of the oxygen molecule dissociation with regard to the ignition time in air / n-heptane. Such a model helps in the understanding of the ignition processes involved in corona discharges under strong overvoltages.

The nanosecond corona discharge and ignition of air / fuel mixtures

The experimental set-up and the associated diagnostics have been described in detail in previous publications [3, 4, 16, 33-35]. A positive high voltage (up to 50 kV) is applied between a parabolic pin electrode and a grounded plane over a single nanosecond range pulse with a short rise time of 2 ns. Changing the distance between the electrodes (within the range of 1-2 cm) and changing the HV-pulse length (10-60 ns) enables the electrical energy released into the gas (10-120 mJ) to be changed. This energy is determined by time integration of the electrical power given by the current-voltage product. The technique used for measuring the discharge current and voltage has been given by P. Tardiveau et al [34]. The plane is grounded through a 0.2 Ohm low inductance resistive shunt. Precise and time resolved current measurements can be performed with this coaxial type shunt without any electromagnetic disturbance. On the other hand, the voltage is recorded at the end of the HV-generator line using a home-made capacitive coaxial probe. This probe is completely integrated into the line, in order to have a high bandwidth and to not disturb the discharge. Signals are recorded on a 500 MHz bandwidth digital oscilloscope with a 4 Gs s^{-1} sampling frequency per channel.

The intense electric field (higher than 1 kV/cm near the tip, corresponding to a reduced field E/N greater than 400 Td, N being the total molecule density at 1 bar and 20°C) induced within the electrode gap promotes the development of a particular regime of atmospheric pure air discharge [34, 35]: it spreads over the entire electrode gap in a completely diffuse way, leading to a large volume of plasma. This diffuse regime tends to disappear in mixtures containing low hydrocarbon (HC) percentages and a multi-channel pattern develops, as shown in Figure 1 [3, 4, 16].

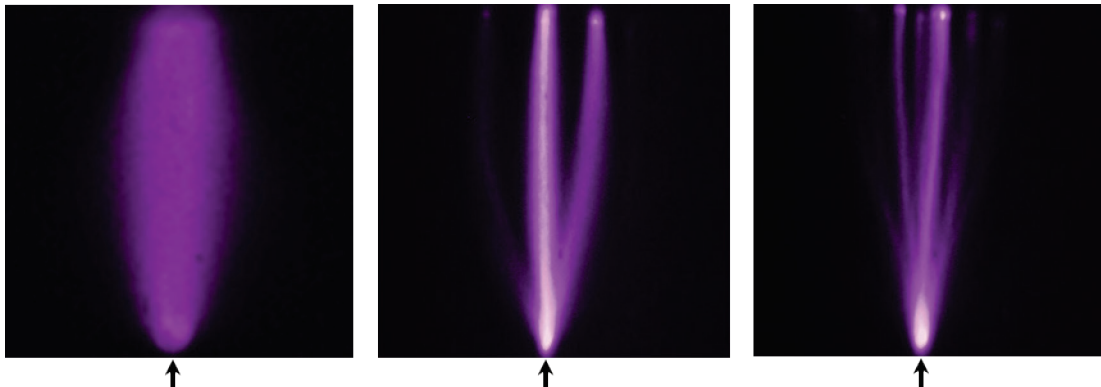


Figure 1 - Diffuse nanosecond discharge in pure air (left) and filamentation effect in air / propane (middle) and air / n-heptane (right) mixtures with 6 % of hydrocarbon. The arrow gives the location of the pin HV electrode.

We define the ignition threshold energy as the minimum electrical energy that the discharge must release into the mixture in order to ignite it and to induce flame propagation and complete combustion of the entire volume. Figure 2 shows how this minimum changes with the HC concentration. For stoichiometric mixtures (equivalence ratios equal to 1, for 4% of propane or for 1.9 % of heptane), this is around 17 mJ whatever the kind of hydrocarbon. It increases with lower equivalence ratios and this effect is much more significant for propane. The ignition of lean mixtures remains possible down to the low flammability level (2.1% for propane, 1.1% for n-heptane), but complete combustion cannot be achieved below 2.4% of propane, whatever the energy of the discharge. It is clear that ignition of the lean air / n-heptane mixture is much easier than for the air / propane one.

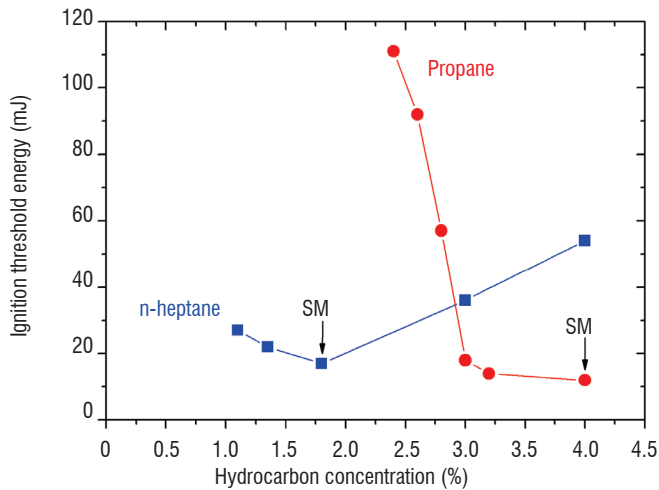


Figure 2 - Minimum energy for ignition as a function of propane and n-heptane concentrations (HV-pulse amplitude: 45 kV, HV-pulse length: 13 ns, electrode gap: 1.6 cm). SM: Stoichiometric mixture. Initial temperature: 300 K.

For low discharge energy (about 10 mJ) or low equivalence ratios, there is a single point ignition located at the tip of the anode and it leads to a classical spherical flame. However, in the case of a stoichiometric air / propane mixture, the increase of the energy up to 80 mJ leads to ignition all along the plasma channel. This can be identified in Figure 3A by the blue light in the first picture. If the energy density is high enough, the discharge can induce a kind of cylindrical flame and, in the first two pictures of Figure 3A, the cylindrical kernel is overlapped by two brighter flame kernels, starting at each electrode and leading to a rather complex flame structure. In the case of a stoichiometric air / n-heptane mixture, this cylindrical shape is no longer observed and only the two-point ignition remains, as shown in

Figure 3B. Two quasi-spherical kernels grow from the electrodes and merge together.

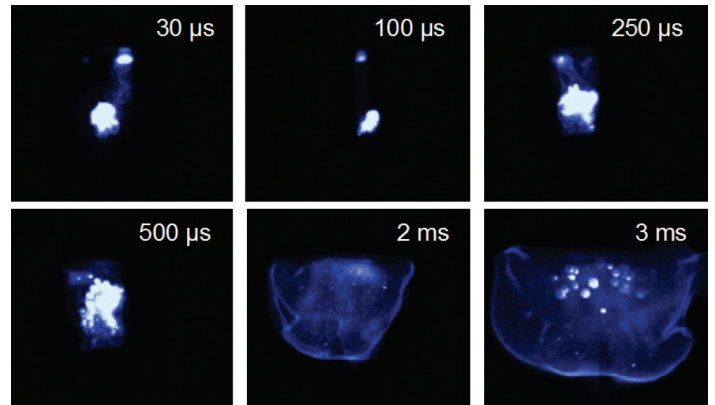


Figure 3a - Ignition along a plasma channel and cylindrical propagation in a stoichiometric air / propane mixture (Electrode gap: 1.6 cm, discharge energy: 85 mJ). Initial temperature: 300 K.

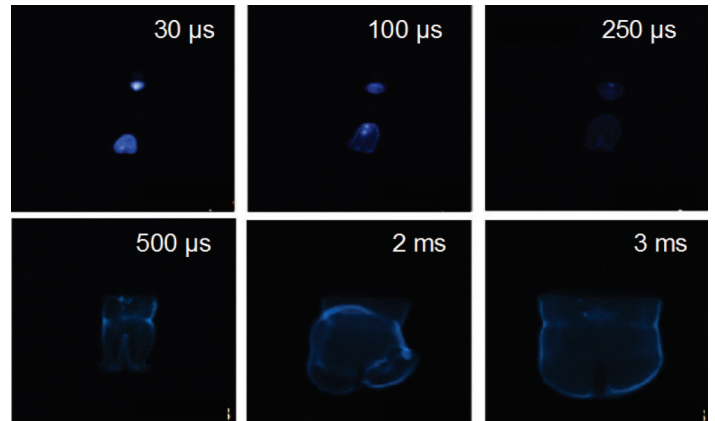


Figure 3b - Ignition along a plasma channel and cylindrical propagation in a stoichiometric air / n-heptane mixture (Electrode gap: 1.1 cm, discharge energy: 80 mJ). Initial temperature: 300 K.

The flame front speed is not dependent on the amount of electrical energy released into the gas and is only governed by combustion kinetics. However, the time needed to burn the whole amount of gas is dependent on this amount and, more precisely, on the local energy density. If the density is high enough over a long distance, as observed in propane at high energies, the initial flame kernel becomes longer and globally increases the rate of combustion. For stoichiometric conditions, the times required to achieve complete combustion can be reduced by twice as much as those obtained with spherical flames. This is also true for the double point ignition in heptane.

In the case of single point ignition, the times required for complete combustion of the gas mixture enclosed in the discharge chamber are given in Figure 4. Complete combustion is achieved more rapidly with n-heptane than with propane. This is due to higher combustion temperatures (2200 K) being reached with n-heptane, inducing higher drive speeds of the expanded burnt gases. However, this effect is strongly attenuated with increasing equivalence ratios.

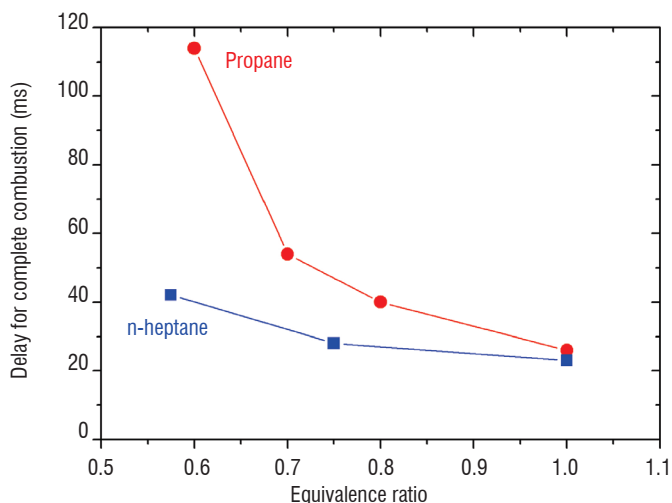


Figure 4 - Time needed to burn the entire mixture for various equivalence ratios (single point ignition).

P. Tardiveau et al [33] showed also that discharge filamentation had an effect on ignition. Ignition will be promoted by thinner plasma channels, where the energy density is higher. The constriction of filaments is more pronounced with n-heptane, but the gap distance is also a deciding parameter. The ability of the discharge to ignite air / HC mixtures, even at low equivalence ratios, is strongly correlated to the energy density that the discharge is able to release into the gas. When the experimental parameters are adjusted to make the discharge more filamentary, and then to increase the energy density, ignition is easier and combustion is faster [3, 33].

Lower concentrations of HC and shorter gap distances make the discharge more diffuse and the plasma channel radii larger, which reduces the energy density and does not promote ignition. Thus, it is necessary to increase the amount of electrical energy to make the combustion successful. Likewise, propane makes the discharge more diffuse. Apart from the specific kinetic properties of the two hydrocarbons, this should contribute to the fact that the ignition threshold energy is higher at a low equivalence ratio with propane than it is with n-heptane.

The diameter of the plasma channels is a key parameter that determines ignition. If it is too large, ignition becomes more difficult, or even impossible, whatever the energy released. In other words, it is more efficient for ignition to increase the energy density by varying the thinness of the plasma channels than by injecting more energy. This is an experimental finding deduced from a great number of fast imaging measurements. However, ignition always starts very close to the electrodes, at points where the electrical power density is higher.

The single nanosecond pulsed discharge is too short in time to heat the mixture by Joule effect. A nanosecond ultra-fast heating mechanism, involving the quenching reaction of nitrogen excited states on oxygen molecules, has been considered for other kinds of nanosecond

discharge [2, 21]. However, spontaneous Raman spectroscopy measurements carried out on this discharge with 1.7% of propane (below flammability limit) and an energy of 30 mJ, tend to show that the temperature in the post-discharge at 1 mm from the tip remains under 500K [16]. Therefore, the reasons for ignition should be found partly in an efficient production of active radicals, such as O(³P) and OH.

Kinetic interpretation of the ignition of the air / n-heptane mixture

The effects of O(³P) radicals on the ignition of air / n-heptane mixtures were investigated with a simplified kinetic model of combustion [3]. Of course, other species are produced during the discharge, owing to electron collisions on molecules constituting the mixtures, in particular the first excited state of the oxygen atom, O(¹D), various excited states of N₂ and O₂ (among which those that are metastable constitute an important energy reservoir), organic fragments (radicals and molecules) of the hydrocarbon, which could also come from the N₂ metastable quenching processes, etc. In our first approach, the goal is to highlight the role of the oxygen molecule dissociation yield producing O(³P) and to reveal specific kinetic routes for a low value of the initial temperature. Future work should be devoted to the role of species other than O(³P).

Together with specific reactions for air plasma [14] (but without electronically excited and ionized species), we used the low temperature reduced mechanism proposed by N. Peters et al [20], which includes the formation of ketohydroperoxydes following isomerization of the peroxy radicals. 37 species and 99 reactions were taken into account in all.

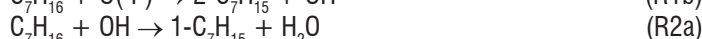
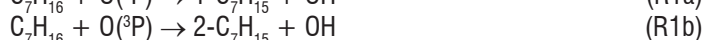
The model couples all balance equations for species densities to the temperature equation given by:

$$\frac{dT}{dt} = \frac{\sum_k^{N_i} H_k \times [\dot{X}_k]}{\sum_k^{N_i} C_{\bar{u}} \times [X_k]} \quad \text{with} \quad [\dot{X}_k] = \frac{d[X_k]}{dt} \quad (1)$$

where $[X_k]$ is the density, H_k is formation enthalpy and C_{pk} is the heat capacity at constant pressure for each species k . The heat capacities and enthalpies are given by:

$$\frac{C_{pk}}{R} = \sum_{n=1}^5 a_{nk} T^{n-1} \quad \text{and} \quad \frac{H_k}{RT} = \sum_{n=1}^6 \frac{a_{nk} T^{n-1}}{n} + \frac{a_{7k}}{T} \quad (2)$$

where the polynomial coefficients values a_{nk} were taken from H. Seiser et al [23]. This model enables the time evolution of the temperature and species to be calculated, under atmospheric pressure, for equivalent ratios Φ , ranging from 0.5 to 1.5 and initial temperatures ranging from 350 K to 750 K. Besides oxidation by molecular oxygen, we took into account initiation reactions between n-heptane and O(³P) or OH radicals:



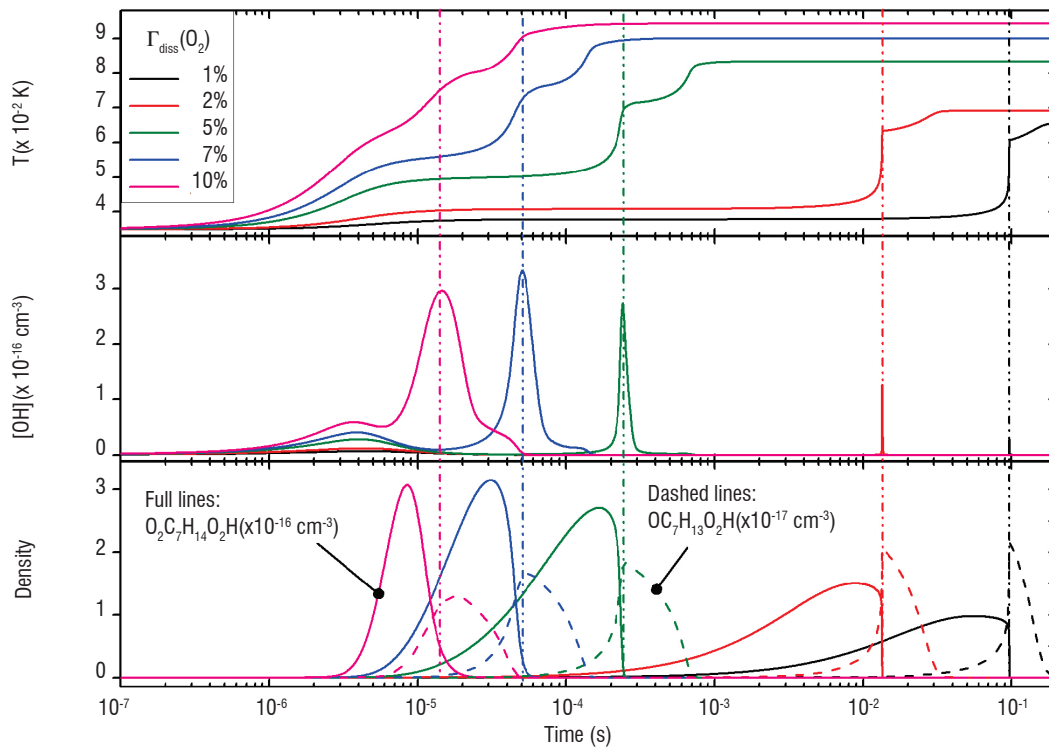


Figure 5 - Calculated time evolutions of radicals (hydroxide OH and hydroperoxy heptyl peroxy $O_2C_7H_{14}O_2H$) and molecular ketohydroperoxide ($OC_7H_{13}O_2H$) densities, and of temperature. Initial temperature: 350 K. O_2 dissociation yields $\Gamma_{diss}(O_2)$: given in the upper diagram.

The mechanism includes isomerization of peroxy radicals $C_7H_{15}O_2$ (resulting from the reaction of heptyl radicals 1- or 2- C_7H_{15} with O_2) forming hydroperoxy heptyl radicals, (R3), which leads to hydroperoxy heptyl peroxy radicals by reaction with molecular oxygen, (R4):



By decomposition, this radical leads to the formation of an OH radical and heptyl ketohydroperoxide $OC_7H_{13}O_2H$. This ketohydroperoxide acts as a degenerate branching agent yielding hydroxyl and ketoheptyl radicals, (R5):



The decomposition of ketoheptyl radicals is also taken into account, (R6):



Molecular oxygen dissociation by electron collisions and quenching of the nitrogen excited states are an O-atom density source; this is why O_2 dissociation yields $\Gamma_{diss}(O_2)$ ranging from 0.1 % to 10 % were considered as input data. Figure 5 shows the results obtained with an initial temperature $T_{ini} = 350$ K and for a stoichiometric mixture ($\Phi = 1$).

Calculations were made for several O_2 dissociation yields, i.e., for several initial densities of $O(^3P)$. It can be seen that this yield has a strong influence, even though the maximum value chosen for our computations is rather moderate compared to some values published in the literature. Indeed, for a voltage pulse of 25 kV with a duration of 25 ns, operating at a repetition frequency of 10 Hz applied to the pin, the measurements performed by A. Lo et al [15] show that the O_2 dissociation reaches

almost 33% on the discharge axis, in agreement with the result of 50% given by G. Stancu et al [32] for a 10 kHz repetitive nanosecond pulsed discharge, in a pin-to-pin geometry. However, for the air / n-heptane mixture, the results plotted in Figure 5 emphasize that only 10% of the oxygen molecule dissociation leads to a strong reduction of the time required for a significant increase in the temperature.

The hydroxyl radical time evolution shows two peaks. One, between 3 and 4 μs , whatever the O_2 dissociation yield, increases with this dissociation rate. This first increase of OH, linked to the initiation process, comes from the balance between its generation by the reaction between n-heptane and the oxygen atom, (R1a) and (R1b), and its consumption, (R2a) and (R2b), which occurs mainly by reaction with n-heptane at this time.

The second peak in the OH time evolution is higher, and its time of occurrence is even shorter the higher the initial atomic oxygen density is. This increase is linked to the formation of heptyl ketohydroperoxide $OC_7H_{13}O_2H$ resulting from the decomposition reaction of the hydroperoxy heptyl peroxy radicals $O_2C_7H_{14}O_2H$, which generates one OH radical. Moreover, by reaction (R5), $OC_7H_{13}O_2H$ is also a source of OH.

In Figure 5, a rapid increase in the temperature is observed, along with the second OH peak and the ketoperoxide peak. This time, corresponding to the maximum OH density, was chosen to determine the ignition time. It is identified by the vertical dotted-dashed lines in each diagram.

The computed ignition time as a function of the initial temperature for two equivalence ratios, 0.5 and 1, and two oxygen dissociation yields, 0.1 % and 5.0 % is shown in Figure 6. For a given initial temperature, the time required for ignition to occur decreases when $\Gamma_{diss}(O_2)$ increases from 0.1 % to 5 %.

Also, for the two dissociation rates, the ignition time decreases when the initial temperature increases. Moreover, increasing the equivalent ratio from 0.5 to 1 entails a slight decrease in the ignition time. Note that for very short times, less than $2 \mu\text{s}$, the two OH density peaks described in Figure 5 are not resolved in time. This prevents the determination of the ignition delay as defined above. In this case, this time is chosen corresponding to the maximum density of OH.

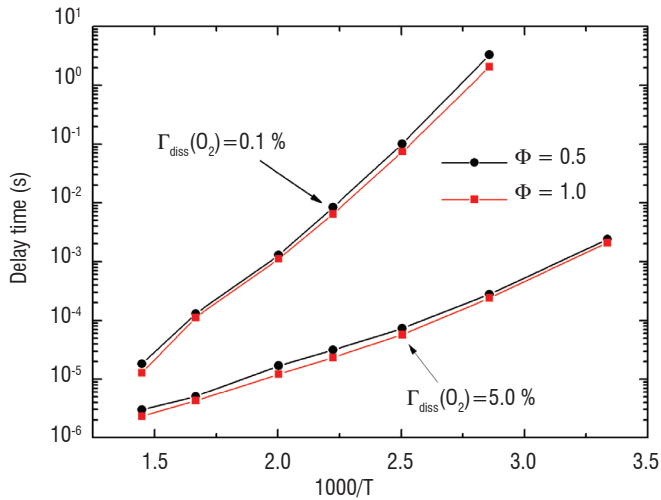


Figure 6 - Computed time required for the ignition of the air / n-heptane mixture as a function of the initial temperature (in K) for two values of the equivalence ratio Φ and of the dissociation percentage Γ_{diss} of the oxygen molecule.

Conclusion

The cold and non-equilibrium plasma generated by a single nanosecond pulsed overvoltage can be used to ignite various kinds of quiescent air / fuel mixtures. It shows several advantages, compared to classical spark gap devices: ignition of lean mixtures with low

electrical energy consumption, extended flame kernels or several points of ignition and reduction of the ignition time.

A comparative study between propane and n-heptane emphasizes that less energy is required to ignite n-heptane and more specifically at low concentrations. The time required for the air / n-heptane mixture to burn completely is also reduced compared to propane for an equivalence ratio lower than one. Modeling shows that the oxygen atoms produced in the plasma appear to be a key species for these phenomena and, in the case of n-heptane, ketohydroperoxides, which are efficient combustion chain propagators through the generation of the hydroxyl radical, play a major role in the triggering of the combustion by the low temperature discharge.

Some of these results may be considered interesting for engineers working on the optimization of ignition devices, owing to the increasingly more important environmental constraints. As regards automobile engines, the implementation of a nanosecond corona discharge device on a spark plug has already been done some years ago [7] leading to the consideration of promising development.

As regards the interpretation of measurements, future work should be devoted to the role of species other than the oxygen atom in its ground state for the ignition of the air / n-heptane mixture. In particular, the production of the excited state $O(^1D)$ by the discharge deserves to be taken into account, because this state is much more reactive with hydrocarbons than $O(^3P)$. In addition, the development of a physical model describing the temporal evolution of the local reduced electric field E/N in the pin-to-plate gap, and consequently the spatial distribution of the energy deposition in the nanosecond corona discharge, should be of great interest if the reduced kinetic scheme proposed can be included in such a model. Such a physical model is particularly important, in order to correctly predict the local densities of the reactive species produced and thereafter the ignition of the combustible mixture at various locations between the electrodes ■

References

- [1] I. ADAMOVICH, I. CHOI, N. JIANG, J-H. KIM, W. LEMPET, E. MINTUSSOV, M. NISHIHARA, M. SAMINY, M. UDDI - *Plasma Assisted Ignition and High-Speed Flow Control: Non-Thermal and Thermal Effects*. Plasma Sources Sci. Technol., Vol. 18, 034018 (13pp), 2009.
- [2] N. ALEKSANDROV, S. KINDUSHEVA, M. NUDNOVA, A. STARIKOVSKII - *Mechanism of Ultra-Fast Heating in a Non-Equilibrium Weakly Ionized Air Discharge Plasma in High Electric Fields*. J. Phys. D: Appl. Phys., Vol. 43, 255201 (19pp), 2010.
- [3] S. BENTALEB - *Etude du déclenchement de combustion de mélanges air-propane et air-heptane par décharge mono-impulsionnelle nanoseconde*. Ph.D. thesis, Univ. Paris-Sud XI, Orsay, France, 2012.
- [4] S. BENTALEB, P. TARDIVEAU, N. MOREAU, P. JEANNEY, F. JORAND, S. PASQUIERS - *Filamentation of a Nanosecond Pulse Corona Discharge in Air-Propane Mixtures at Atmospheric Pressure*. IEEE Trans. Plasma Sci., Vol. 39, 2236-2237, 2011.
- [5] S. BENTALEB, P. TARDIVEAU, N. MOREAU, F. JORAND, S. PASQUIERS - *Energy Release of a Nanosecond Pulse Corona Discharge in Atmospheric Air-Propane Mixtures for Ignition Purposes*. Proc. 63rd GEC, Paris, France, 37, 2010.
- [6] S. BENTALEB, P. TARDIVEAU, N. MOREAU, F. JORAND, S. PASQUIERS - *Cylindrical Flame Kernel and Flame Propagation Induced in Air-Propane Mixtures by a Single Corona Discharge*. 6th International Workshop and Exhibition on Plasma Assisted Combustion (IWEPAC), Heilbronn am Neckar, Germany, 2010.
- [7] E. DOMINGUES, M. BUREY, B. LECORDIER, P. VERVISCH - *Ignition in an SI Engine Using Nanosecond Discharges Generated by a Spark Gap Plasma Igniter (SGPI)*. Society of Automotive Engineers, SAE paper 2008-01-1628 (8pp), 2008.
- [8] R. FAIRLY, J. GRIFFITHS, K. HUGHES, H. PEARLMAN - *Cool Flames in Space: Experimental and Numerical Studies of Propane Combustion*. Proc. Combust. Instit., Vol. 30, 1057-1064, 2005.
- [9] E. FILIMONOVA - *Discharge Effect on the Negative Temperature Coefficient Behaviour and Multistage Ignition in C3H8-Air Mixture*. J. Phys. D: Appl. Phys., Vol. 48, 015201 (16pp), 2015.
- [10] S. GALLAGHER, H. CURRAN, W. METCALFE, D. HEALY, J. SIMMIE, G. BOURQUE - *A Rapid Compression Machine Study of the Oxidation of Propane in the Negative Temperature Coefficient Regime*. Combust. Flame, Vol. 153, 316-333, 2008.

- [11] K. HUGHES, J. GRIFFITHS, M. FAIRWEATHER, A. TOMILN - *Evaluation of Models for the Low Temperature Combustion of Alkanes Through Interpretation of Pressure-Temperature Ignition Diagrams*. Phys. Chem; Chem. Phys., Vol. 8, 3197–3210, 2006.
- [12] Y. KIM, V. FERRERI, L. ROSOCHA, G. ANDERSON, S. ABBATE, K-T. KIM - *Effect of Plasma Chemistry on Activated Propane/air Flames*. IEEE Trans. Plasma Sci., Vol. 34, 2532–2535, 2006.
- [13] I. KOSAREV, N. ALEKSANDROV, S. KINDYSHEVA, S. STARIKOVSKAIA, A. STARIKOVSKII - *Kinetics of Ignition of Saturated Hydrocarbons by Nonequilibrium Plasma: C₂H₆- to C₅H₁₂-Containing Mixtures*. Combust. Flame, Vol. 156, 221–233, 2009.
- [14] I. KOSSYI, A. KOSTINSKY, A. MATVEYEV, V. SILAKOV - *Kinetic Scheme of the Non-Equilibrium Discharge in Nitrogen-Oxygen Mixtures*. Plasma Sources Sci. Technol., Vol. 1, 207–220, 1992.
- [15] A. LO, A. CESSOU, P. VERVISCH - *Space and Time Analysis of the Nanosecond Scale Discharges in Atmospheric Pressure air: II. Energy Transfers During the Post-Discharge*. J. Phys. D: Appl. Phys., Vol. 47, 115202 (9pp), 2014.
- [16] N. MOREAU - *Décharge nanoseconde dans l'air et en mélange air/propane. Application au déclenchement de combustion*. PhD thesis, Univ. Paris-Sud XI, Orsay, France, 2011.
- [17] S. NAGARAJA, W. SUN, V. YANG - *Effect of Non-Equilibrium Plasma on Two-Stage Ignition of n-Heptane*. Proc. Combust. Inst., Vol. 35, 3497–3504, 2015.
- [18] S. PANCHESHNYI, D. LACOSTE, A. BOURDON, C. LAUX - *Ignition of Propane-Air Mixture by a Repetitively Pulsed Nanosecond Discharge*. IEEE Trans. Plasma Sci., Vol. 34, 2478–2487, 2006.
- [19] S. PASQUIERS, S. BENTALEB, P. JEANNEY, N. BLIN-SIMIAND, P. TARDIVEAU, L. MAGNE, K. GADONNA, N. MOREAU, F. JORAND - *Towards a Kinetic Understanding of the Ignition of Air-Propane Mixture by a Non-Equilibrium Discharge: the Decomposition Mechanisms of Propane*. Int. J. Aerodyn., Vol. 3, 135-158, 2013.
- [20] N. PETERS, G. PACZKO, R. SEISER, AND K. SESHADRI - *Temperature Cross-Over and Non-Thermal Runaway at Two-Stage Ignition of n-Heptane*. Comb. Flame, Vol. 59, 38-59, 2002.
- [21] N. POPOV - *Fast Gas Heating in a Nitrogen–Oxygen Discharge Plasma: I. Kinetic Mechanism*. J. Phys. D: Appl. Phys., Vol. 44, 285201 (16pp), 2011.
- [22] L. ROSOCHA, D. COATES, D. PLATTS, S. STANGE - *Plasma-Enhanced Combustion of Propane Using a Silent Discharge*. Phys. Plasmas, Vol. 11, 2950–2956, 2004.
- [23] H. SEISER, H. PITSCHE, K. SESHADRI, W. PITZ, H. CURRAN - *Extinction and Autoignition of n-Heptane in Counterflow Configuration*. Proc. Combust. Inst., Vol. 28, 2029-2037, 2000. UCRL-WEB-204236 Review and release date: May 19, 2004.
- [24] T. SHIRAIISHI, T. URUSHIHARA, M. GUNDERSEN - *A Trial of Ignition Innovation of Gasoline Engine by Nanosecond pulsed Low Temperature Plasma Ignition*. J. Phys. D: Appl. Phys., Vol. 42, 135208 (12pp), 2009.
- [25] B. SHUKLA, V. GURURAJAN, K. EISAZADEH-FAR, B. WINDOM, D. SINGLETON, M. GUNDERSEN, F. EGOLFOPOULOS - *Effects of Electrode Geometry on Transient Plasma Induced Ignition*. J. Phys. D: Appl. Phys., Vol. 46, 205201 (9pp), 2013.
- [26] J. SIMMIE - *Detailed Chemical Kinetic Models for the Combustion of Hydrocarbon Fuels*. Prog. Energy Comb. Sci., Vol. 29, 599–634, 2003.
- [27] V. SMIRNOV, O. STELMAKH, V. FABELINSKY, D. KOSLOV, A. STARIK, N. TITOVA - *On the Influence of Electronically Excited Oxygen Molecules on Combustion of Hydrogen–Oxygen Mixture*. J. Phys. D: Appl. Phys., Vol. 41, 192001 (6pp), 2008.
- [28] S. STARIKOVSKAIA - *Plasma Assisted ignition and Combustion*. J. Phys. D: Appl. Phys., Vol. 39, R265–R299, 2006.
- [29] S. STARIKOVSKAIA - *Plasma-Assisted Ignition and Combustion: Nanosecond Discharges and Development of Kinetic Mechanisms*. J. Phys. D: Appl. Phys., Vol. 47, 353001 (34pp), 2014.
- [30] A. STARIKOVSKII - *Plasma Supported Combustion*. Proc. Combust. Inst., Vol. 30, 2405–2417, 2005.
- [31] A. STARIKOVSKII, N. ALEKSANDROV - *Plasma-Assisted Ignition and Combustion*. Prog. Energy Comb. Sci., Vol. 39, 61-110, 2013.
- [32] G. STANCU, F. KADDOURI, D. LACOSTE, C. LAUX - *Atmospheric Pressure Plasma Diagnostics by OES, CRDS and TALIF*. J. Phys. D: Appl. Phys., Vol. 43, 124002 (10pp), 2010.
- [33] P. TARDIVEAU, S. BENTALEB, P. JEANNEY, F. JORAND, S. PASQUIERS - *Comparative Study of Air-Propane and Air-Heptane Mixtures Ignition by Nanosecond Pulsed Discharges*. Int. J. Plasma, Environ. Sci. Technol., Vol. 6, 130-134, 2012.
- [34] P. TARDIVEAU, N. MOREAU, S. BENTALEB, C. POSTEL, S. PASQUIERS - *Diffuse Mode and Diffuse-to-Filamentary Transition in a High Pressure Nanosecond Scale Corona Discharge under High Voltage*. J. Phys. D: Appl. Phys., Vol. 42, 175202 (11pp), 2009.
- [35] P. TARDIVEAU, S. PASQUIERS - *Diffuse and Streamer Discharges at Intermediate Pressures*. In Runaway electrons preionized diffuse discharges, Ch.9, Ed. V. Tarasenko, Nova Science Publishers, Series Electrical Engineering Developments, 2014.
- [36] F. WANG, J. LIU, J. SINIBALDI, C. BROPHY, A. KUTHI, C. JIANG, P. RONNEY, M. GUNDERSEN - *Transient Plasma Ignition of Quiescent and Flowing Air/Fuel Mixtures*. IEEE Trans. Plasma Sci., Vol. 33, 844-849, 2005.

Acronyms

HC	(hydrocarbon)
HV	(high voltage)



Sabrina Bentaleb was a PhD student working at LPGP under the supervision of Pierre Tardiveau, on the nanosecond corona discharge and its application to the ignition of air / n-heptane mixtures.



Nicole Blin-Simiand finished her PhD thesis in physical chemistry in 1987 at Pierre et Marie Curie University in Paris. She joined the CNRS in 1988 and studied low temperature oxidation of hydrocarbons (the role of peroxidic species). Since 2000, she has been appointed at LPGP to work on the chemical processes involved in high pressure non-thermal plasmas.



Pascal Jeanney is an Assistant engineer at LPGP. He is specialized in optical systems and devices, with complementary competencies in electrical engineering.



Lionel Magne graduated from the South Paris University (Paris 11) in 1988 and achieved his PhD degree in 1992 at LPGP. He joined the CNRS in 1992 to work on the kinetics of low pressure pulsed discharges in reactive molecular gas mixtures. Since 2000 he has been involved in research on pollution control and the ignition of combustion by non-thermal plasmas. His activity is particularly focused on time resolved spectroscopic diagnostics (laser, absorption) on radicals and atomic species and the development of kinetic models.



Nicolas Moreau was a PhD student working at LPGP under the supervision of Stéphane Pasquiers, on the nanosecond corona discharge and its application to ignition of air / propane mixtures.



Stéphane Pasquiers graduated from the South Paris University (Paris 11) in 1985 and achieved his PhD degree in 1987 at LPGP. He joined the CNRS in 1988 to work on high power XeCl lasers energized by photo-triggered discharges and thereafter on HF/DF lasers (discharge equilibrium and stability, plasma kinetics and chemistry). At the present time, his main scientific interests, for various applications, are: pulsed discharge physics at high pressure (0.1–10 bars), non-thermal plasma kinetics in atmospheric gases, decomposition processes and kinetics of hydrocarbons and VOCs.



Pierre Tardiveau achieved his PhD degree in physics from the South Paris University (Paris 11) in 2002. He is now an associate professor working at LPGP on the characterization of pulsed discharges in dense and inhomogeneous media and their application to air treatment and combustion. He is strongly involved in the study of nanosecond pulse corona discharges generated under a very strong overvoltage.